Fall 2011

Numerical study of two-phase air-water interfacial flow: plunging wave breaking and vortex-interface interaction

Bon Guk Koo
University of Iowa

NUMERICAL STUDY OF TWO-PHASE AIR-WATER INTERFACIAL FLOW: PLUNGING WAVE BREAKING AND VORTEX-INTERFACE INTERACTION

by

Bon Guk Koo

An Abstract

Of a thesis submitted in partial fulfillment
of the requirements for the Doctor of
Philosophy degree in Mechanical Engineering
in the Graduate College of
The University of Iowa

December 2011

Thesis Supervisors: Professor Frederick Stern
Adjunct Assistant Professor Jianming Yang

ABSTRACT

Two different air-water interfacial flows are studied including plunging wave breaking and flow past a vertical surface-piercing circular cylinder using complementary CFDShip-Iowa version 6 including Cartesian grid solver and orthogonal curvilinear grid solver.

The plunging wave-breaking process for impulsive flow over a bump in a shallow water flume has been simulated using the exact experimental initial and boundary conditions. The overall plunging wave breaking process is described with major wave breaking events identified: jet plunge, oblique splash and vertical jet. These major events repeat up to four times before entering the chaotic breaking. The simulations show a similar time line as the experiments consisting of startup, steep wave formation, plunging wave, and chaotic wave breaking swept downstream time phases. Detailed wave breaking processes are discussed along with the experimental results.

The simulations show differences and similarities with other experimental and computational studies for wave breaking in deep water and sloping beaches. The geometry and conditions in the present study are relevant to ship hydrodynamics since it includes effects of wave-body interactions and wave breaking direction is opposite to the mean flow.

Large-eddy simulation with the Lagrangian dynamic subgrid-scale model has been performed to study the flow past a surface-piercing circular cylinder for Re and Fr effect. The flow features near the air-water interface show significant changes with different Reynolds numbers from sub-critical to critical regime. It is shown that the interface makes the separation point more delayed for all regime of Re. Remarkably

reduced separated region below the interface is observed for critical Re regime and it is responsible for much reduced wake and recirculation region behind the cylinder and it recovers in the deep flow.

At different Fr, significant changes are shown on the air-water interface structures. At lower Fr, relatively smaller bow waves are observed in front of the cylinder with Kelvin waves behind the cylinder. For higher Fr, the bow wave increases remarkably with the larger wake region and deeper depression and it breaks with similar features of plunging breakers. Much more small air-water interface structures including splashes and bubbles are observed behind the cylinder. It is hard to distinguish the Kelvin waves behind the cylinder due to much larger free-surface oscillations and turbulence. As Fr increases, the Kelvin wave angle decreases and deeper and narrower depression region behind the cylinder are observed. The flow features around the cylinder are significantly changed due to this cavity region behind the cylinder.

Abstract Approved: _____
Thesis Supervisor

_____
Title and Department

_____
Date

_____
Thesis Supervisor

_____
Title and Department

_____
Date

NUMERICAL STUDY OF TWO-PHASE AIR-WATER INTERFACIAL FLOW: PLUNGING WAVE BREAKING AND VORTEX-INTERFACE INTERACTION

by

Bon Guk Koo

A thesis submitted in partial fulfillment
of the requirements for the Doctor of
Philosophy degree in Mechanical Engineering
in the Graduate College of
The University of Iowa

December 2011

Thesis Supervisors: Professor Frederick Stern
Adjunct Assistant Professor Jianming Yang

Graduate College
The University of Iowa
Iowa City, Iowa

CERTIFICATE OF APPROVAL

PH.D. THESIS

This is to certify that the Ph.D. thesis of

Bon Guk Koo

has been approved by the Examining Committee
for the thesis requirement for the Doctor of Philosophy
degree in Mechanical Engineering at the December 2011 graduation.

Thesis Committee: _____
Frederick Stern, Thesis Supervisor

_____
Jianming Yang, Thesis Supervisor

_____
James Buchholz

_____
Pablo Carrica

_____
George Constantinescu

To my beloved wife and two daughters, Sekyoung Choi, Ashley H. Koo, Emily H. Koo

ACKNOWLEDGMENTS

I would like to express the deepest appreciation to my advisor, Professor Frederick Stern, who had supported me throughout my thesis with his patience and knowledge. I would also like to give my thanks to my co-advisor, Dr. Jianming Yang. This thesis would not have been possible without their guidance, support, and constructive discussions. I would also like to convey my sincere gratitude to my advisory committee members, Professors James Buchholz, Pablo Carrica, George Constantinescu, and H.S. Udaykumar. I would like to specially mention the help that I received from Dr. Zhaoyuan Wang and Dr. Jungsoo Suh for numerical simulations.

I would like to express my appreciation to Professor Ho Hwan Chun in Pusan National University who inspired me to study for Ph.D. I am grateful to my Korean colleagues in IIHR, especially, Dr. Bongchul Seo, Dr. Hyunse Yoon, Dr. Dongjin Yeo, and Sungmo Yeon for the great time we shared together in Iowa.

I am indebted to my parents, my mother-in-law, and my brother for their love, support, and encouragement. I would like to express my special love and gratitude to my wife, Sekyoung, my two daughters, Ashley (Hayoon) and Emily (Hyewon), who accepted my absences from home-life, but also supported and motivated through the hard times.

This work is sponsored by the US Office of Naval Research through research grant N00014-01-1-0073 and N00014-06-1-0420 under the administration of Dr. Patrick Purtell. The numerical simulations were performed using DoD HPC resources.KOSEF (Korea Science and Reserch Foundation) also sponsored this work.

ABSTRACT

Two different air-water interfacial flows are studied including plunging wave breaking and flow past a vertical surface-piercing circular cylinder using complementary CFDShip-Iowa version 6 including Cartesian grid solver and orthogonal curvilinear grid solver.

The plunging wave-breaking process for impulsive flow over a bump in a shallow water flume has been simulated using the exact experimental initial and boundary conditions. The overall plunging wave breaking process is described with major wave breaking events identified: jet plunge, oblique splash and vertical jet. These major events repeat up to four times before entering the chaotic breaking. The simulations show a similar time line as the experiments consisting of startup, steep wave formation, plunging wave, and chaotic wave breaking swept downstream time phases. Detailed wave breaking processes, including wave profile at maximum height, first plunge, entrapped air bubble trajectories and diameters, kinetic, potential, and total energy, and bottom pressures are discussed along with the experimental results.

The simulations show differences and similarities with other experimental and computational studies for wave breaking in deep water and sloping beaches. The geometry and conditions in the present study are relevant to ship hydrodynamics since it includes effects of wave-body interactions and wave breaking direction is opposite to the mean flow.

Large-eddy simulation with the Lagrangian dynamic subgrid-scale model has been performed to study the flow past a surface-piercing circular cylinder for Re and Fr effect. The flow features near the air-water interface show significant changes with different Reynolds numbers from sub-critical to critical regime. It is shown that the interface makes the separation point more delayed for all regime of Re. Remarkably reduced separated region below the interface is observed for critical Re regime (drag

crisis) and it is responsible for much reduced wake and recirculation region behind the cylinder and it recovers in the deep flow.

At different Fr, significant changes are shown on the air-water interface structures. At lower Fr, relatively smaller bow waves are observed in front of the cylinder with Kelvin waves behind the cylinder and small amount of free-surface roughness and turbulence are also seen in the wake region. For higher Fr, the bow wave increases remarkably with the larger wake region and deeper depression and it breaks with similar features of plunging breakers. Much more small air-water interface structures including splashes and bubbles are observed behind the cylinder. It is hard to distinguish the Kelvin waves behind the cylinder due to much larger free-surface oscillations and turbulence. As Fr increases, the Kelvin wave angle decreases and deeper and narrower depression region behind the cylinder are observed. The flow features around the cylinder are significantly changed due to this cavity region behind the cylinder.

TABLE OF CONTENTS

LIST OF TABLES

LIST OF FIGURES

CHAPTER 1

INTRODUCTION

1.1 Background and motivation

Two-phase air-water interfacial flows arise in natural world, physical and biological sciences and in many areas of modern technology and engineering applications. Especially in ship hydrodynamics, the interface between air and water has been received a lot of attention and examples include breaking wave impact on ships and offshore structures.

Wave breaking is an important subject of studies in geophysics and ocean, coastal and marine engineering and wave breaking is one of common examples of two-phase flows. However, it has not been fully understood yet. Wave breaking plays a number of important roles in air-sea interaction including limiting the height of the surface waves, generating ocean currents, enhancing mass, momentum, and energy transfer between the air and water, dissipating surface wave energy, generating vorticity, turbulence and wave-induced vibration, entraining air and generating white water. Wave breaking can occur in both deep water and shallow water regions of the oceans and can thus affect ships and coastal structures. The mechanism of wave breaking process needs to be better understood, especially to improve the design of ships and offshore structures that are exposed to extreme conditions.

The flow past a surface-piercing circular cylinder is another example of two-phase flows and wave-body interactions which has received less attention in spite of its importance in various coastal engineering applications such as offshore structures and surface vessels. The flow is known to show different complex structures in the vicinity of the cylinder; a bow wave appears at the front, which then spills over the cylinder to generate the near wake. The bow wave itself can breakup and develop into a fountain at higher flow velocities. A Kelvin surface wake is generated behind the cylinder, which

fans out to the far distance rear. Although a few experimental and numerical studies on the flow around a surface- piercing cylinder are available in the literature, the effects of the interface on the force distributions on the body, vortex generation and turbulent structures, and air-water inerface structures, especially, their changes with the Reynolds and Froude numbers are not well understood. A better understanding of these effects is also important for the cases when vortex- and wave-induced vibrations of the cylinder are to be considered.

1.2 Objectives and Approach

This thesis discusses two different interface flows; plunging wave breaking downstream of a bump in a shallow water flume and flow around a vertical surface-piercing circular cylinder. The overall goal of this dissertation is to improve the understanding of the dynamics of interfacial flows using complementary CFD approach.

The present numerical studies are motivated to study breaking waves using the exact experimental initial and boundary conditions and validate the capability of CFDShip-Iowa Version 6, a sharp interface Cartesian grid solver for two-phase incompressible flows (Yang and Stern, 2009; Wang et al., 2009). Since plunging is the most dramatic wave breaking phenomena which are characterized by an ample amount of air entrapment and generation of turbulence and vorticity, the present research focuses on providing a detailed quantitative description of the overall plunging wave breaking process through numerical simulations, which experimental studies are unable to show quantitatively due to the experimental limitations such as resolution problems and capability of the experiment facilities.

The flow past surface-piercing circular cylinder is numerically investigated using the orthogonal curvilinear grid solver of CFDShip-Iowa version 6 (Suh et al., 2011) to study systematically the origin of the surface current, i.e., the outward transverse velocity at the interface, a series of simulations with different Reynolds and Froude numbers. The

effects of Re/Fr on the flow, including forces/pressure/shear-stress distributions, turbulent structures, vortex shedding, and vorticity transport have been investigated.

1.3 Outline

This thesis is divided into five chapters. Chapter 2 discusses mathematical modeling and numerical methods for Cartesian grid and orthogonal curvilinear grid solvers. Chapter 3 discusses impulsive plunging wave breaking downstream of a bump in a shallow flume using numerical simulations, including wave breaking process, air entrainments, jet characteristics, energy dissipations, etc. In this chapter, brief experimental studies (Kang et al., 2011) are also presented. In addition to chapter 3 where only fine grid solutions are presented, results from other grids and solvers are discussed in Appendix A and B. Chapter 4 focuses on the two-phase flow past a vertical surface-piercing circular cylinder and discusses the flow features on the force distributions on the cylinder, vortex generation and turbulent structures, and vortex shedding with the change of the Reynolds and Froude numbers. Chapters 3 and 4 are self-contained and divided into subsections with introduction, literature reviews, simulation conditions, results and discussion, and conclusions and future work. Finally, Chapter 5 summarizes overall conclusions.

CHAPTER 2

COMPUTATIONAL METHODS

2.1 Overview of CFDShip-Iowa Version 6

CFDShip-Iowa version 6, a Cartesian grid solver for the large-eddy simulation (LES) of two-phase incompressible flows recently developed at IIHR, is used in the current study. This solver is based on the work of Yang and Balaras (2006), in which a sharp interface immersed boundary method, has been developed to handle complex immersed stationary/moving boundaries on Cartesian grids, and has been extensively expanded to fit the need of ship hydrodynamics applications. In this solver, the interface was represented by the level set (LS) method, which is later extended by Wang et al. (2009) using a coupled level set and volume-of-fluid (CLSVOF) method. A ghost fluid methodology is adopted to handle the jump conditions across the interface, where the density and surface tension effect are treated in a sharp way while the viscosity is smeared by a smoothed Heaviside function. A sharp embedded boundary method is used to handle complex immersed boundaries on Cartesian grids. Various upwind convection schemes including quadratic upwind interpolation for convective kinematics (QUICK) and weighted essentially non-oscillatory (WENO) have been implemented. High Performance Computing (HPC) components include a semi-coarsening multigrid Poisson solver using HYPRE library, a parallel tridiagonal system solver for the inversion of momentum equations, domain decomposition in all three directions, and parallel I/O based on MPI2.

Recently, CFDShip-Iowa version 6 has been extended to the mathematical model and numerical method in the orthogonal curvilinear coordinates by Suh et al. (2011) and it is used in the simulation of the two–phase flow past a vertical surface-piercing circular cylinder, which is discussed in the chapter 4. Summary of this extended CFDShip-Iowa version 6 will be discussed in later section.

2.2 Mathematical methods of Cartesian Grid Solver

2.2.1 Governing Equations and Interface Jump Conditions

Incompressible viscous flows of two immiscible fluids, e.g., air and water, are governed by the Navier-Stokes equations:

$$\frac{\partial \mathbf{u}}{\partial t} + \mathbf{u}\cdot\nabla\mathbf{u} = \frac{1}{\rho}\nabla\cdot\left(-p\mathbf{I}+\mathbf{T}\right)+\mathbf{g} \tag{2.1}$$

$$\nabla\cdot\mathbf{u} = 0 \tag{2.2}$$

where t is the time, $\mathbf{u}$ is the velocity vector, p is the pressure, $\boldsymbol{I}$ is the unit diagonal tensor, ρ is the density, $\mathbf{g}$ represents the gravity acceleration, and $\mathbf{T}$ is the viscous stress tensor defined as

$$\mathbf{T} = 2\mu\mathbf{S} \tag{2.3}$$

with μ the dynamic viscosity and $\mathbf{S}$ the strain rate

$$\mathbf{S} = \frac{1}{2}\left[\nabla\mathbf{u}+\left(\nabla\mathbf{u}\right)^{T}\right] \tag{2.4}$$

where the superscript T represents transpose operation.

Since the fluid properties are discontinuous across the interface, which is a function of time and space, density and viscosity are also functions of time and space and only known with given interface position. Their definitions will be deferred after the introduction of interface representation using level set.

Since the fluids considered here are viscous and no phase change occurs, the velocity across the interface Γ is continuous:

$$\left[\mathbf{u}\right] = 0, \tag{2.5}$$

where [ ] denotes the jump at the interface, i.e., $f_L^I - f_G^I$ for a variable f with superscript I representing interface. The exact jump condition for stress is

$$\left\lfloor \mathbf{n}\cdot\left(-p\mathbf{I}+\mu\left(\nabla\mathbf{u}+\left(\nabla\mathbf{u}\right)^{T}\right)\right)\cdot\mathbf{n}\right\rfloor = \sigma\kappa, \tag{2.6}$$

where **n** is the unit vector normal to the interface, σ is the coefficient of surface tension, and κ is the local curvature of the interface. With a smoothed viscosity and continuous velocity field, the stress jump condition reduces to

$$[p] = p_L^I - p_G^I = -\sigma\kappa, \tag{2.7}$$

2.2.2 Interface Representation and Fluid Properties

The interface is represented by the LS function which is corrected to enforce mass conservation with the aid of the VOF function. The LS function, ϕ, is defined as a distance function which is negative in the air, positive in the liquid, and zero at the interface. The VOF function, *F*, is defined as the liquid volume fraction in a cell with its value in between zero and one in a surface cell and zero and one in air and liquid respectively.

The LS function and the VOF function are advanced by the following equations, respectively,

$$\frac{D\phi}{Dt} = \frac{\partial\phi}{\partial t} + (\mathbf{u}\cdot\nabla)\phi = 0, \tag{2.8}$$

$$\frac{DF}{Dt} = \frac{\partial F}{\partial t} + (\mathbf{u}\cdot\nabla)F = 0. \tag{2.9}$$

The LS advection equation is solved using the third-order TVD Runge-Kutta scheme (Shu and Osher, 1988) for time advancement and the fifth-order HJ-WENO scheme (Jiang and Peng, 1999) for spatial discretization. It should be noted that since the VOF function is not smoothly distributed at the interface, an interface reconstruction procedure is required to evaluate the VOF flux across a surface cell. Finally, in order to achieve mass conservation, the LS functions have to be re-distanced prior to being used. This will be detailed in the next section.

Each phase of constant density and viscosity can be defined using the LS function in the computational domain and sharp jumps of the fluid properties occur at the phase

interface. In this study, the density keeps its sharp jump and the viscosity is smoothed over a transition band across the interface,

$$\begin{aligned} \rho &= \rho_G + (\rho_L - \rho_G) H(\phi), \\ \mu &= \mu_G + (\mu_L - \mu_G) H_\varepsilon(\phi), \end{aligned} \quad (2.10)$$

where the subscripts G and L represent gas and liquid phase, respectively, the stepwise Heaviside function is

$$H(\phi) = \begin{cases} 1 & \text{if} \quad \phi \geq 0 \\ 0 & \text{if} \quad \phi < 0 \end{cases}. \quad (2.11)$$

and the smoothed Heaviside function is

$$H_\varepsilon(\phi) = \begin{cases} 1 & \text{if} \quad \phi > \varepsilon \\ \frac{1}{2}\left[1 + \frac{\phi}{\varepsilon} + \frac{1}{\pi}\sin\left(\frac{\pi\phi}{\varepsilon}\right)\right] & \text{if} \quad |\phi| \leq \varepsilon \\ 0 & \text{if} \quad \phi < -\varepsilon \end{cases}. \quad (2.12)$$

The geometric properties, i.e., the normal vector and curvature, can be estimated readily from the LS function,

$$\mathbf{n} = \frac{\nabla\phi}{|\nabla\phi|}, \quad (2.13)$$

$$\kappa = \nabla \cdot \left(\frac{\nabla\phi}{|\nabla\phi|}\right). \quad (2.14)$$

The flow equations are discretized on a staggered Cartesian grid with the convection terms approximated by a third-order QUICK scheme (Leonard, 1979) and other terms by the standard second-order central difference scheme. A semi-implicit time-advancement scheme is adopted to integrate the momentum equations with the second-order Crank-Nicolson scheme for the diagonal viscous terms and the second-order Adams-Bashforth scheme for the convective terms and other viscous terms. A four-step fractional-step method is employed for velocity-pressure coupling. The resulting

pressure Poisson equation is solved using the PETSc library (Balay et al., 1997). The code is parallelized via a domain decomposition technique using the MPI library.

In the coupled level set volume-of-fluid method (CLVOF), the interface is reconstructed via a PLIC scheme from the VOF function and the interface normal vector is computed from the LS function. Based on the reconstructed interface, the LS functions are re-distanced via a geometric procedure for achieving mass conservation. A flow chart for the CLSVOF algorithm is shown in Fig. 2.1. The coupling of the LS and VOF methods occurs during the interface reconstruction and the LS re-distance processes.

More details of the CLSVOF can be found in Wang et al. (2009).

2.2.3 Turbulence Modeling

In the LES approach, the Navier-Stokes equations are spatially filtered such that the large, energy carrying eddies are resolved and the small scale, dissipative eddies are modeled by a sub-grid scale stress model. After applying the filter operation to Eqs. (2.1) and (2.2), we have

$$\frac{\partial \bar{\mathbf{u}}}{\partial t} + \bar{\mathbf{u}} \cdot \nabla \bar{\mathbf{u}} = -\frac{1}{\rho} \nabla \bar{p} - \nabla \cdot \bar{\tau} + \frac{1}{\rho} \nabla \cdot \left[\mu \left(\nabla \bar{\mathbf{u}} + (\nabla \bar{\mathbf{u}})^T \right) \right] + \mathbf{g} \tag{2.15}$$

$$\nabla \cdot \bar{\mathbf{u}} = 0, \tag{2.16}$$

where $\bar{f}$ denotes the filter operation on a variable f, $\bar{\tau} = \overline{\mathbf{uu}} - \bar{\mathbf{u}}\bar{\mathbf{u}}$ is the subgrid-scale (SGS) stress tensor, whose deviatoric part is parametrized following the Smagorinsky procedure as:

$$\bar{\tau} - \frac{1}{3} \mathrm{trace}(\bar{\tau}) \mathbf{I} = -2\nu_t \bar{\mathbf{S}}, \tag{2.17}$$

and the turbulent eddy viscosity is defined as

$$\nu_t = C\Delta^2 |\bar{\mathbf{S}}|, \quad \text{and} \quad |\bar{\mathbf{S}}| = \sqrt{2\bar{\mathbf{S}} \cdot \bar{\mathbf{S}}}. \tag{2.18}$$

The model parameter C in the eddy viscosity definition has to be determined to close the equations. In this study the Lagrangian dynamic SGS model (Meneveau et al.,

1996) is used as it can handle complex geometries without the requirement of homogeneous direction(s). Therefore, Eq. (2.15) can be rewritten in the following form

$$\frac{\partial \bar{\mathbf{u}}}{\partial t}+\bar{\mathbf{u}}\cdot\nabla\bar{\mathbf{u}}=-\frac{1}{\rho}\nabla\bar{p}+\nabla\cdot\left[\nu_t\left(\nabla\bar{\mathbf{u}}+\left(\nabla\bar{\mathbf{u}}\right)^T\right)\right]+\frac{1}{\rho}\nabla\cdot\left[\mu\left(\nabla\bar{\mathbf{u}}+\left(\nabla\bar{\mathbf{u}}\right)^T\right)\right]+\mathbf{g}, \tag{2.19}$$

with the trace of subgrid-scale stress tensor $\frac{1}{3}\text{trace}(\bar{\tau})$ incorporated into $\bar{p}$.

2.3 Numerical methods of Cartesian grid solver

2.3.1 Governing Equations

A finite difference method is used to discretize the Navier-Stokes equations on a non-uniform staggered Cartesian grid, in which the velocity components *u*, *v*, and *w* are defined at centers of cell faces in the *x*, *y*, and *z* directions, respectively, and all other variables, i.e. p, ϕ, ρ, μ, and ν_t are defined at cell centers, as shown in Fig 2.2. A semi-implicit time-advancement scheme is adopted to integrate the momentum equations with the second-order Crank-Nicolson scheme for the diagonal viscous terms and the second-order Adams-Bashforth scheme for the convective terms and other viscous terms. A four-step fractional-step method is employed for velocity-pressure coupling, in which a pressure Poisson equation is solved to enforce the continuity equation:

1. Predictor:

$$\frac{\hat{u}_i-u_i^n}{\Delta t}=\frac{1}{2}\left(3A_i^n-A_i^{n-1}\right)+\frac{1}{2}\left(C_i^{n+1}+C_i^n\right)-\text{Grad}_i\left(p^n\right) \tag{2.20}$$

2. First Corrector:

$$\frac{u_i^*-\hat{u}_i}{\Delta t}=\text{Grad}_i\left(p^n\right) \tag{2.21}$$

3. Pressure Poisson Equation:

$$\frac{\partial}{\partial x_i}\mathrm{Grad}_i\left(p^{n+1}\right)=\frac{1}{\Delta t}\frac{\partial u_i^*}{\partial x_i} \tag{2.22}$$

4. Second Corrector:

$$\frac{u_i^{n+1}-u_i^*}{\Delta t}=-\mathrm{Grad}_i\left(p^{n+1}\right) \tag{2.23}$$

where superscript n denotes time step, subscript i = 1, 2, 3 represents i-coordinate, A and C denote terms treated by the Adams-Bashforth and Crank-Nicolson schemes, $\hat{u}_i$ and u_i^* are the first and second intermediate velocities, respectively. $\mathrm{Grad}_i(p)$ is a pressure gradient term defined at the center of the cell faces (collocated with velocity components) with the jump conditions incorporated in it. For instance, in the x direction,

$$\mathrm{Grad}_i\left(p\right)_{i+1/2}=\frac{1}{\rho_{i+1/2}}\frac{\left(p_{i+1}-p_i\right)+\sigma\kappa^I}{\Delta x} \tag{2.24}$$

where the cell face density is defined as in the ghost fluid method with the sharp jump condition at the interface considered utilizing the level set function.

In Eq. (2.18) the convective terms are discretized using a third-order QUICK and higher-order WENO schemes are available. All other terms are discretized with the standard second-order central difference scheme. Eq. (2.18) is approximated with the approximate factorization method. A parallel tridiagonal system solver and a multigrid solver are used to inverse the momentum and pressure Poisson equations, respectively.

2.3.2 Interface Tracking

The level set and the reinitialization equations are solved using a third-order TVD Runge-Kutta scheme (Shu and Osher, 1988) for time advancement and the fifth-order HJ-WENO scheme (Jiang and Peng, 2000) for spatial discretization. The solution time of these equations does not pose a significant overhead as they are solved in a narrow band several grid-cells wide.

The coupled level set and volume-of-fluid (CLSVOF) method has been developed in order to improve the mass conservation property of the level set method. The interface is reconstructed via a PLIC scheme and the level set function is re-distanced based on the reconstructed interface. The interface is advected using a Lagrangian method with a second-order Runge-Kutta scheme for time integration. An efficient level set re-distance algorithm is explored, which significantly simplifies the complicated geometric procedure by finding the closest point on the reconstructed interface directly without considering the interface configuration in each computational cell. It is especially efficient for three-dimensional cases where various possibilities of the interface configuration exist. The performance of the CLSVOF method has been evaluated through the numerical benchmark tests and validation and application examples, where mass has been well conserved.

2.3.3 Immersed Boundary Treatment

A sharp interface immersed boundary method is adopted here to treat the immersed boundaries/bodies in a non-uniform Cartesian grid. In this approach, the grid generation for complex geometries is trivial since the requirement that the grid points coincide with the boundary, which is imperative for body-fitted methods, is relaxed; while the solution near the immersed boundary is reconstructed using momentum forcing in a sharp-interface manner. The detailed procedure is given in Yang and Balaras (2006) and summarized here.

The first step is to establish the grid-interface relation with a given immersed boundary description, such as parametrized curve/surface or a triangulation. In this step all Cartesian grid nodes are split into three categories as shown in Fig 2.3: (1): fluid-points, which are points in the fluid phase; (2) forcing points, which are grid points in the fluid phase with one or more neighboring points in the solid phase; (3) solid-points, which are points in the solid phase. The Navier-Stokes solver described in the previous

section is applied on all points of the Eulerian grid as if the fluid/solid interface was not present. The effect of the immersed boundary on the flow is introduced through the discrete forcing function, which is computed only at the forcing points by directly enforcing the boundary conditions. In general, the velocity at the forcing points can be computed by means of linear interpolation that involves the projection of the forcing point on the interface and two points in the fluid phase.

2.3.4 Time Step

The time step Δt is restricted by the CFL condition, gravity, and surface tension. With a CFL restriction of 0.5, the following relationship can be established as discussed in Kang et al. (2000).

$$\Delta t \le 0.5 \left(\frac{C_{cfl} + \sqrt{(C_{cfl})^2 + 4(G_{cfl})^2 + 4(S_{cfl})^2}}{2} \right)^{-1} \tag{2.25}$$

with the convective time step restriction

$$C_{cfl} = \max\left(\frac{|u|}{\Delta x} + \frac{|v|}{\Delta y} + \frac{|w|}{\Delta z} \right) \tag{2.26}$$

the time step restriction due to gravity

$$G_{cfl} = \max\left(\frac{|g_x|}{\Delta x} + \frac{|g_y|}{\Delta y} + \frac{|g_z|}{\Delta z} \right) \tag{2.27}$$

and the time step restriction due to surface tension

$$S_{cfl} = \sqrt{\frac{\sigma|\kappa|}{\rho_G (\min(\Delta x, \Delta y, \Delta z))^2}} \tag{2.28}$$

2.3.5 Software Architecture and HPC

One of the major objectives of the development of CFDShip-Iowa version 6 is to make use of the on-coming petascale computers and provide fast turnaround for

simulation-based design in ship hydrodynamics. Efficiency and sustainable development of the solver are among the major considerations in the software design. Modern programming language Fortran 95 is chosen and a modularized approach is followed for the code development.

The simple topologic structure of Cartesian grids is favorable for coarse-grain parallelization. The parallelization is done via a domain decomposition technique using the MPI library. A simple domain decomposition technique is used in CFDShip-Iowa version 6 where the Cartesian grid is divided into uniform pieces, each of which resides in one processor. Optimal load balance can be achieved except for a small amount of overhead due to interface and immersed boundary treatment, which may be unevenly distributed over processors.

A parallel tri-diagonal system solver is used with the approximate factorization of momentum equations, no iterations are needed for the inversion of the momentum equations. For the pressure Poisson equation, a highly efficient, scalable multigrid-preconditioned Krylov subspace solver from PETSc has been included in the code. Usually, the Poisson solver takes most of the CPU time in a single time step.

Parallel I/O based on MPI 2 is implemented. Instead of the usual approaches that one process collects all data from all processes and write to one file, or, each process write its data to its own file, in the current approach all processes write its data to one single file, which is highly scalable and can greatly simplify the I/O operation and minimize the post-processing overhead.

2.4 Mathematical Methods of Orthogonal Curvilinear Grid Solver

2.4.1 Navier-Stokes Equations

The orthogonal curvilinear coordinate system is adopted for the governing equations, the Navier-Stokes equations for two-phase, immiscible, incompressible flows

and the derivation and notation follows Pope (1978). The continuity equation is written as follows:

$$\nabla(i)[u_i] = 0 \,. \tag{2.29}$$

where u_i is the velocity in the orthogonal coordinate ξ_i direction and $\nabla(i)[\bullet] = \frac{1}{J}\frac{\partial}{\partial \xi_i}\left[\left(\frac{J}{h_i}\right)\bullet\right]$ following Pope (1978). The Jacobian of the coordinate transformation is defined as $J = h_i h_j h_k$, and $h_i = \frac{\partial x_i}{\partial \xi_i}$ with x_i a Cartesian coordinate.

The momentum equations are written as follows:

$$\begin{aligned} &\frac{\partial u_i}{\partial t} + \nabla(j)[u_i u_j] - \frac{1}{\rho}\nabla(j)[\tau_{ij}] = -\frac{1}{\rho}\frac{\partial p}{\partial \xi(i)} + \\ &\quad + H_j(i)\left[u_j u_j - \frac{\tau_{ij}}{\rho}\right] - H_j(i)\left[u_i u_j - \frac{\tau_{ij}}{\rho}\right] + g_i \end{aligned} \,. \tag{2.30}$$

where ρ is the density, p is the pressure, t is the time, and g_i the gravity vector in the ξ_i direction. In addition, $H_i(j) = \frac{1}{h_i h_j}\frac{\partial h_i}{\partial \xi_j}$ and $\partial\xi(i) = h_i \partial\xi_i$ as in Pope (1978). τ_{ij} is defined as follows:

$$\tau_{ij} = (\mu + \nu_t \cdot \rho) S_{ij} \,. \tag{2.31}$$

where μ is the dynamic viscosity, ν_t is the turbulent eddy viscosity, and S_{ij} is the strain rate as defined as below:

$$S_{ij} = \mu\left[\frac{\partial u_i}{\partial \xi(j)} + \frac{\partial u_j}{\partial \xi(j)} - u_i H_i(j) - u_j H_j(i) + 2u_l H_i(l)\delta_{ij}\right]. \tag{2.32}$$

2.4.2 Interface Modeling

The interface is represented by LS function which is corrected using VOF function to enforce mass conservation. The LS function, ϕ, is defined as a distance function which is negative in the air, positive in the liquid, and zero at the interface. The VOF function, F, is defined as the liquid volume fraction in a grid cell that gives zero in

the air, one in the liquid, and a value between zero and one in an interfacial cell, respectively.

The LS function and the VOF function are advanced using

$$\frac{D\varphi}{Dt}=\frac{\partial\varphi}{\partial t}+(\mathbf{u}\cdot\nabla)\varphi=0. \tag{2.33}$$

$$\frac{DF}{Dt}=\frac{\partial F}{\partial t}+(\mathbf{u}\cdot\nabla)F=0. \tag{2.34}$$

respectively.

2.4.3 Turbulence Modeling

In large eddy simulation (LES), the small dissipative eddies are modeled by the SGS model whereas the large, energy carrying eddies are resolved by the spatially filtered Navier-Stokes equations. The Lagrangian dynamic Subgrid-scale (SGS) model based on Sarghini et al. (1999) is adopted in present LES. Eq. (2.30) is rewritten as the following form:

$$\begin{aligned}\frac{\partial\overline{u}_i}{\partial t}+\nabla(j)[\overline{u}_i\overline{u}_j]-\frac{1}{\rho}\nabla(j)[\overline{\tau}_{ij}]&=-\frac{1}{\rho}\frac{\partial\overline{p}}{\partial\xi(i)}+g_i\\&+H_j(i)\left[\overline{u}_j\overline{u}_j-\frac{\overline{\tau}_{ij}}{\rho}-\tilde{\tau}_{ij}\right]-H_j(i)\left[\overline{u}_i\overline{u}_j-\frac{\overline{\tau}_{ij}}{\rho}-\tilde{\tau}_{ij}\right].\end{aligned} \tag{2.35}$$

with $\overline{\tau}_{ij}=\mu\overline{S}_{ij}$ and $\tilde{\tau}_{ij}=\upsilon_t\overline{S}_{ij}$, respectively. Hereafter the filtering sign for LES will be dropped for simplicity.

2.5 Numerical methods of Orthogonal Curvilinear Grid Solver

The finite-difference method is used to discretize the governing equations on a general orthogonal curvilinear grid. A staggered variable arrangement is adopted, i.e., the contravariant velocity components u_i,u_j,u_k are defined at cell faces in the ξ_i,ξ_j,ξ_k directions, respectively, and all other variables are defined at cell centers. A semi-implicit time advancement scheme is used to integrate the momentum equations

with the second-order Crank-Nicolson scheme for the diagonal viscous terms and the second-order Adams-Bashforth scheme for other terms. A four-step fractional-step method is employed for velocity-pressure coupling, in which a pressure Poisson equation is solved to enforce the continuity equation.

The convective terms are discretized using the fifth-order Hamilton-Jacobi Weighted-ENO (HJ-WENO) scheme and other terms are approximated using the second-order central difference scheme. A semi-coarsening multigrid solver from the HYPER library (Falgout et al., 2006) is used for the pressure Poisson equation.

The LS advection equation is solved using the third-order TVD Runge-Kutta scheme (Shu and Osher, 1998) for time advancement and the fifth-order HJ-WENO scheme (Jiang and Shu, 1996) for spatial discretization. To keep the LS function as a signed distance function, it has to be reinitialized after a certain time of evolution. The CLSVOF method (Sussman et al., 2000) is used to re-distance the LS function and improve mass conservation properties of the LS method. In the CLSVOF method, the interface is reconstructed based on the VOF function with the interface normal computed from the LS function. The level set field is then re-distanced to reflect the position of the reconstructed interface, which satisfies the volume conservation constraint. In the present study, the piecewise linear interface construction scheme for the VOF method presented by Gueyffier et al. (1999) is used.

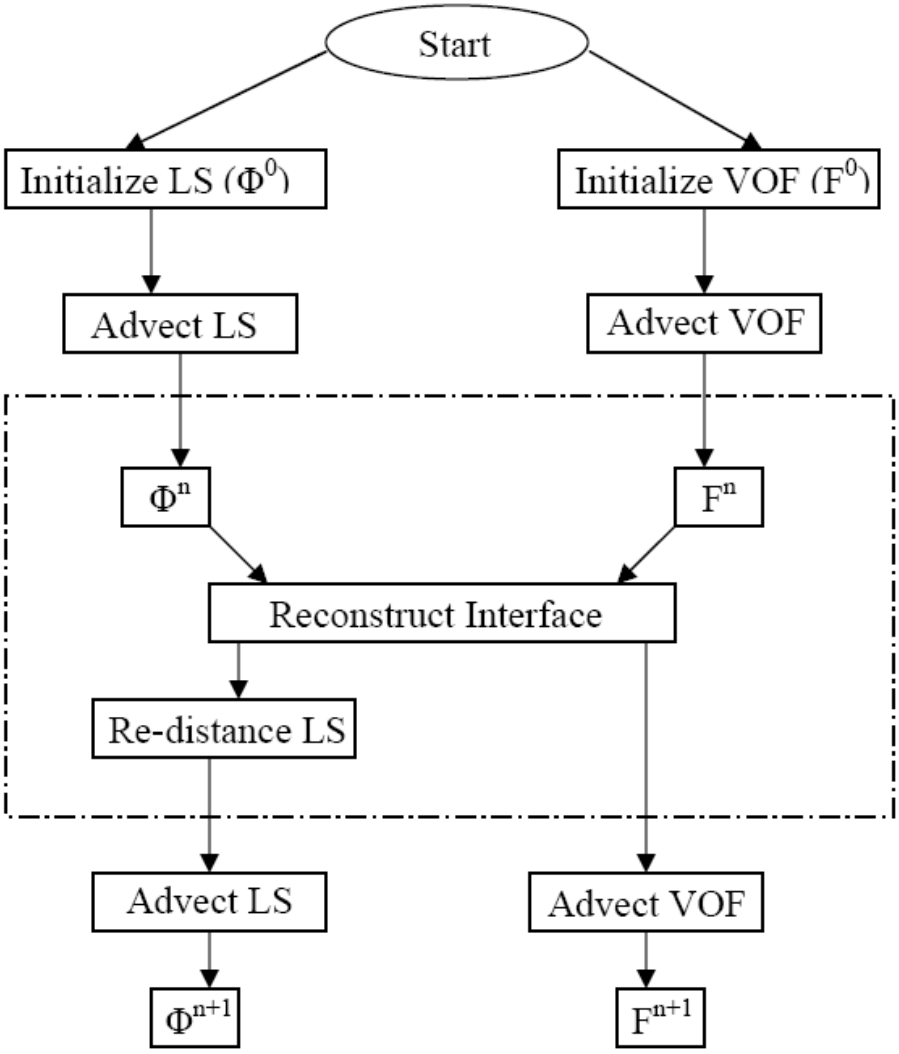

Figure 2.1 Flow chart of the coupled level set and volume-of-fluid method

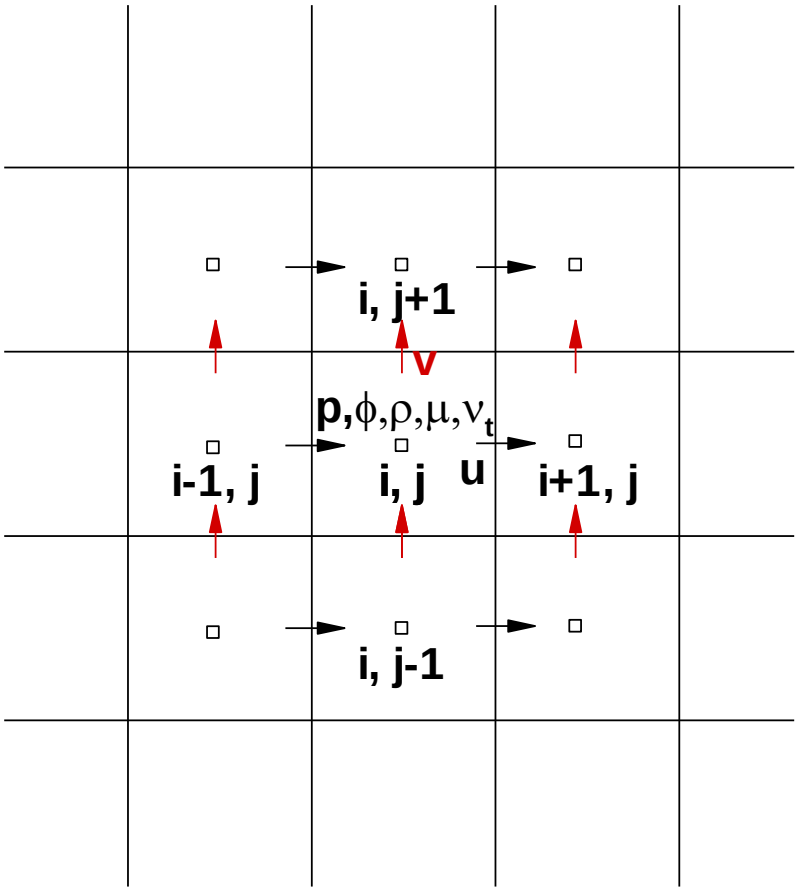

Figure 2.2 Arrangement of variables on staggered Cartesian grid

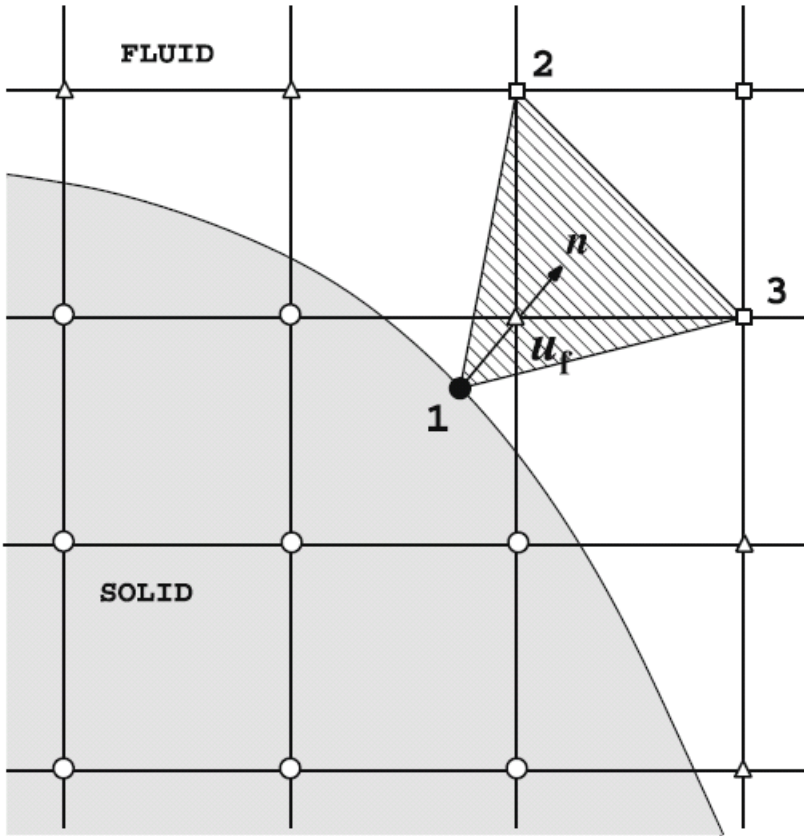

Figure 2.3 Grid-interface relation and the interpolation stencil for u_f (point 1, 2, and 3). O solid points; fluid points; Δ forcing points

CHAPTER 3

NUMERICAL SIMULATION OF PLUNGING WAVE BREAKING DOWNSTREAM OF A BUMP IN A SHALLOW WATER FLUME

3.1 Introduction

Water waves break in both deep and shallow water over a wide range of scales and intensities that range from very gentle spilling breakers to violent plunging breakers. Wave breaking is one of the principal mechanisms for the transfer of momentum from air to surface currents. Breaking waves also play an important role in the near surface turbulence generation and turbulence-wave interactions. Breaking waves impose large and sometimes extreme forces on ships and offshore structures. Due to all the above reasons and several more it is essential to understand the fluid dynamics of wave breaking.

The breaking of surface waves in both deep and shallow water is a very important phenomenon that has a lot of scope for both experimental and computational research. Several researchers have performed field as well as laboratory measurements and studied both qualitative and quantitative aspects of wave breaking. Wave breaking measurements in the field have improved significantly over the last decade but field measurements still cannot match the quality and control which can be achieved in laboratories. Field measurements are difficult and sometimes unable to capture the evolution of wave breaking from pre to post breaking stages and thus laboratory experiments are important in understanding the overall characteristics of the breaking wave. Wave breaking processes especially for plunging wave breaking are not yet well understood, including steep wave formation, jet overturning, splash-up, air entrainment, subsequent events, instabilities and organized vortices, and turbulence structures. Recent experimental and computational studies have focused on qualitative descriptions of the wave breaking

process; energy losses; 2D and 3D vortex and turbulent structures; wave impact and air entrainment.

The current research is part of a larger project funded by the Office of Naval Research. The main goal of this larger project is to improve the understanding of the dynamics of breaking ship waves at the bow, stern and transom including the overall velocity field, and the generation of turbulence and vorticity using complementary CFD approach. Strong breaking waves occur near the bow and stern/transom of naval combatant ships moving in calm seas. In general, ship wave breaking includes both spilling (steady) and plunging (unsteady) breakers. While the theory and modeling of spilling breakers is fairly well developed for both two-dimensional (2D) and three dimensional (3D) models, detailed physical description and accurate modeling are lacking for plunging breakers.

3.1.1 Review of related literature

Plunging wave breaking is one of the most violent phenomena of air-water interface interactions, producing strong turbulence with large amounts of air bubbles, water droplets, jets and sprays. These phenomena commonly occur in ship flows and are one of the main sources of the underwater sounds and white-water wakes, which are of great importance for signature of ships. Many experimental and computational studies for the plunging wave breaking have been done in the past few decades. Early experimental studies are focused on wave geometric properties (Bonmarin, 1989), wave breaking process (Tallent et al., 1990), energy dissipation (Melville, 1994), jet characteristics and air entrainment (Chanson and Fang, 1997), and turbulence (Chang and Liu, 1999). With the Particle Image Velocimetry (PIV) techniques, more detailed velocity field, turbulence, and void fraction data and analysis have been investigated in recent studies (Melville et al., 2002; Deane and Stokes, 2002; Grue and Jensen, 2006; Kimmoun and Branger, 2007; Blenkinsopp and Chaplin, 2007; Drazen and Melville, 2009). Due to the

technical difficulties, the experimental measurements can only be done in the water region, detailed description of the flow field in the energetic wave breaking region is not available. With the development of the computational fluid dynamics (CFD) technology, detailed wave breaking process and velocity profile can be obtained in both water and air phases (Chen et al., 1999; Watanabe and Saeki, 2002). The early CFD studies are usually 2D due to the prohibitive computational cost for the 3D simulations. In the more recent CFD studies (Watanabe et al., 2005; Lubin et al., 2006; Iafrati, 2010), simulations are conducted with the air entrainment, 2D and 3D vortex structures, and energy dissipation discussed.

It should be noted that most previous studies on plunging wave breaking are for deep water or sloping beaches for which wave plunges forward in the same direction of the mean flow. Yao and Wu (2005) experimentally investigated the shear currents effects on unsteady waves but with a focus on incipient breaking. Moreover, the geometry and conditions in most cases of CFD differ from the experiments even though the experiments are usually used to guide the analysis of CFD. Present interest is ship hydrodynamics for which body-wave interactions are important and the direction of wave breaking is opposite or at angle to the mean flow. Previous research used model ships in towing tanks focused on scars, vortices and mean and root mean square (rms) wave elevation induced by ship bow and shoulder wave breaking (Miyata and Inui, 1984; Dong et al., 1997; Olivieri et al., 2007), which suggests the presence of underlying coherent structures. A complementary CFD study to the latter study was carried out by Wilson et al. (2007). However, typical plunging wave breakings can hardly be obtained using model ships in towing tanks, and detailed measurements of the wave breaking processes are difficult. Recently, Shakeri et al. (2009) provide detailed measurements and analysis of divergent bow waves using a unique wave maker for simulating 2D+t flow. For slender bow ships, 2D+t wave breaking process is similar to deep water and sloping beach studies, i.e., plunges with forward splash-ups. In the early experimental studies by

Duncan (1981; 1983), a fully submerged, two-dimensional hydrofoil was towed horizontally to produce breaking waves. These studies are focused on spilling breakers.

In the experimental fluid dynamics (EFD) study by Kang et al. (2011), a quadratic profile bump mounted in a shallow water flume is used to create impulsive sub critical flow conditions where plunging wave breakers are successfully obtained. Phase averaged measurements (relative to the time t_b at which the maximum wave height is reached just before the first plunge) are conducted, including the overall flume flow and 2D PIV center-plane velocities and turbulence inside the plunging breaking wave and bottom pressures under the breaking wave. The plunging wave breaking triggered by the flow over a submerged bump is of relevance to ship hydrodynamics since it includes wave-body interactions and the wave breaking direction is opposite to the mean flow. The idea and approach of creating plunging wave breakers using a submerged bump is obtained collectively from the previous experimental (Cahouet, 1984; Miyata et al., 1985) and CFD studies (Iafrati et al., 2001; Yang and Stern, 2007; Huang et al., 2007). The CFD results were used as a guide for the test design of the experiments (Ghosh, 2008) and the initial experimental data was used for validation. Subsequently, a complementary CFD study was used to aid in the data analysis simultaneously as the experimental data is used to validate a Cartesian grid, immersed boundary, coupled level set and volume-of-fluid CFD method (Wang et al., 2009). Wang et al. (2009) indentified three repeated plunging events each with three sub-events [jet impact (plunge), oblique splash and vertical jet]; however, they used fully impulsive initial conditions and adjusted the initial velocity and water elevation to match Ghosh's (2008) wave breaking position, which precluded detailed spatial and temporal validation.

In the present chapter impulsive plunging wave breakings downstream of a bump in a shallow water flume are numerically simulated with the aim of providing a detailed quantitative description of the overall plunging wave breaking process. The time-dependent velocity and wave elevation boundary conditions are specified at the inlet and

outlet using the exact experimental data provided in Kang et al. (2011). The computational results are compared with the experimental measurements to validate the capability of the code of CFDShip-Iowa Version 6 (Yang and Stern, 2009; Wang et al., 2009) for wave breaking. The simulations are carried out using a Cartesian grid solver with the sharp interface, coupled level set and volume-of-fluid (CLSVOF) and immersed boundary methods.

3.2 Experimental Study by Kang et al. (2011)

The present simulations used initial and boundary conditions from experimental studies by Ghosh (2008), Reins (2008), and Kang et al. (2011). This sub-section briefly describes previous experimental studies, which have been carried out in the IIHR flume.

The Iafrati et al. (2001) quadratic profile bump is mounted in a shallow water flume for impulsive sub critical flow conditions such that a plunging wave breaking occurs downstream of the bump above a region of flow separation. Phase averaged measurements (relative to the time at which the maximum wave height is reached just before the first plunge) are conducted. (1) wave gauge water elevations upstream and downstream; (2) pitot velocities upstream and downstream; (3) venturi meter flow rates; (4) 2D PIV or video wave breaking profiles at maximum height just before the first plunge; (5) 2D PIV center-plane velocities and turbulence upstream and inside the plunging breaking wave; and (6) bottom pressures under the breaking wave.

Each plunging wave breaking experiment consists of J individual tests used for the phase averaging. The experiment was conducted ten times. Initially, Ghosh (2008) conducted seven experiments with J = 22, but with limited documentation of the overall flume flow. Experiments L1-L3 are for PIV with large field of view. Experiments S1-S3 are for PIV with small field of view. Experiment V1 is for upstream PIV and limited overall flume flow. Subsequently, Reins (2008) conducted three more experiments L4,

S4, V2 with J = 24 and improved individual test repeatability and extensive documentation of the overall flume flow.

The experiments were conducted in the IIHR 30.0 m long, 0.91 m wide and 0.45 m deep re-circulating flume. The flume has glass-sided walls with leveled steel rails and instrument carriage. Water is re-circulated by two 7.5 horsepower (maximum frequency 60 Hz), variable speed, pumps located beneath the tailbox. The flow is returned to the headbox via two 0.25 m diameter pipes each having a venturi meter.

The bump is mounted to the flume floor 17.29 m from the headbox. A Cartesian coordinate system is used for the measurements with x = 0 at the bump maximum height H with x > 0 pointed downstream, y = 0 at the flume/bump centerplane, and z = 0 at the flume/bump bottom with z > 0 pointed upwards. The coordinates (x,y,z) and water elevations ζ are non-dimensional using H. The bump profile z_B is

$$z_B(x) = 1 - 2x^2 / L^2 + x^4 / L^4 \tag{3.1}$$

where L=2.5 is the bump half-length.

A bump height H = 0.1143 m, initial water depth ζ/H = 2 (aspect ratio = 5.0), and pump frequency of 55 Hz in 7 s for Ghosh (2008) and 40 Hz in 7 s for Reins (2008) are used, which generates an impulsive plunging wave breaking with maximum wave height of about 12 cm and relatively small side disturbances. The wave breaking time t_b, i.e., the time at which the maximum height is reached just before the first plunge is used for phase averaging. An individual test is considered acceptable if the maximum height (x_b, z_b) is within a box of $\pm 6\%(x_b, z_b)$ where $(x_b, z_b) = (3.12, 1.98)$ for Ghosh (2008) and $(x_b, z_b) = (3.14, 2.15)$ for Reins (2008). Reins (2008) reduced the pump frequency from 55 Hz to 40 Hz for improved repeatability of individual tests, which is the reason for the differences in x_b and especially z_b values. In general, one in three individual tests was deemed acceptable. Unacceptable tests were due to side disturbances. Overhead video images were used to document the two-dimensionality of the plunging wave breaking. At

maximum wave height just before the first plunge, the region $y = \pm 2.1$(54%W where W is the flume width) is approximately 2D, whereas close to the walls the wave profile is disturbed/broken. At the first plunge, the center 2D region increases to 60%W. Water temperature varied from 11˚C to 19.9˚C during the experiments. The repeatability and side disturbances did not depend on the water temperature. Average water temperatures were 15.7˚C and 18.5˚C for L4 and S4, respectively. Density ρ = 1000 kg/m^3, viscosity μ = .001 kg/ms and gravity g=9.8 m/s^2 values were used for data reduction. Fig. 3.1 shows the experimental setup and measurement locations.

Data reductions equations are derived for the ith time of the jth test t_{ij} referenced to the breaking time t_{bj} and phase averaged water elevations, upstream and downstream axial velocity, 2D PIV axial and vertical velocities and Reynolds stresses under the breaking wave, and bottom pressures under the plunging breaking wave. Water elevations were measured using four Kenek servo-type needlepoint wave gauges. United Sensor pitot probes were used. Two venturi meters located within the re-circulation pipes are used to calculate the instantaneous flow rate. PIV measurements were made using a LaVision 2D system. Pressure taps are connected to pressure transducers. Data acquisition uses two synchronized PCs. PC1 uses a data acquisition board with LabView for acquisition of analog data for water elevations, pitot axial velocities, ventrui flow rates, and bottom pressures. PC1 triggers PC2 using the wave elevation at x = -7.5. When the water elevation drops by a specified amount $\Delta\zeta$ the LabView program sends a 5 Volt square sine wave to PC2. The initial condition for all tests was ζ = 2. The pumps were primed and the water elevation was calm, which required 30 minutes between individual tests. The tests were initiated by turning on the pumps and starting the PC1 LabView data acquisition. Ghosh (2008) triggered PC1 using the criteria $\Delta\zeta$=-0.0175 at x=-62; however, this did not provide as accurate estimate of the time difference between the start of the pumps and PC1 data acquisition. Reins (2008) manually started PC1 just after turning on the pumps with a difference of less than 0.1 s, which was corrected using the

ventrui meter flow rate measurements. Convergence studies were conducted to determine the number of individual tests required for the phase averaging. Kang et al. (2011) provides a detailed description of the experimental methods and overall results.

3.3 Plunging Wave Breaking Simulation Using Cartesian Grid Solver

3.3.1 Computational Setup

The simulations are conducted on a 2D computational domain of x/H= [-52, 44] and z/H = [0, 5], where H = 0.1143 m is the maximum bump height. The coordinates (x, y, z) are normalized by H as discussed in Kang et al. (2011). Three different grids are used in the simulations, as shown in Table 3.1. Grids (CG1, CG2, CG3) are systematic with consecutively reduced (by a factor of 2) sizes from 3072×832 (2.5M) to 1536×416 (0.63M) and 768×208 (0.16M) and used for a grid convergence study. The fine grid results are mainly presented in this study and details of other solutions can be found in the appendix. The computational domain and boundary conditions are given in Fig. 3.2. The time-dependent velocity and wave elevation boundary conditions are specified at the inlet and outlet using the exact experimental data (Reins, 2008) as shown in Fig. 3.3. The computation is started with both water and air at rest. In the present simulation, a constant CFL number of 0.2 is used where the magnitude of the time step varies from 1×10^{-2} to 1×10^{-5} depending on the flow conditions.

3.3.2 Verificationa and Validation

Figure 3.4 shows the wave profiles at t_b for all three grids and the experiments. It is clear that the computational results approach the experimental measurement as the grid is refined. It should be noted that the wave profile is averaged for the experiments, whereas the instantaneous values of the wave elevation are plotted for the CFD. Water droplets and air bubbles generated by the small wave breakings can be observed on the

fine grid. For the coarse grid, there are also some droplets and bubbles further downstream of the flume, which are out of the view window in the figure.

Wave breaking time (t_b), position (x_b, z_b), and distance to the experimentally measured position (d_b) on the three different grids are shown in Table 3.1 along with the experimental results of case L4 of Kang et al. (2011). Verification study is conducted following the factor of safety (FS) method (Stern et al., 2001; Xing and Stern, 2010). The convergence ratio (R_G), the order of accuracy (P_G), and the grid uncertainty (U_G) for t_b, x_b, z_b, and d_b are shown in Table 3.2. Monotonic convergence is observed for t_b, x_b, z_b, and d_b with R_G of 0.11, 0.67, 0.66, and 0.045, respectively. High order of accuracy and small grid uncertainty are achieved for both t_b and d_b, whereas relatively low order of accuracy and large grid uncertainty are shown for both x_b and z_b. As the grid is refined, t_b and x_b are closer to the experimental results and errors are reduced to 1.26% and 0.3%, respectively, as shown in Table 1. Although z_b from the fine grid has the largest error compared to the other two grids, the wave breaking position (x_b, z_b) on the fine grid is the closest to the experimental results.

3.3.3 Overview of Computational Results

The wave breaking time and maximum height are accurately predicted for the fine grid case but the axial distances are 26%x_b, 55%x_b downstream for medium and coarse grid cases, respectively, as shown in Fig. 3.4a. This discrepancy is attributed to the use of medium/coarse grids that under resolve the bump boundary layer and region of separation. Thus, to facilitate the comparisons the simulation results on medium and coarse girds were translated axially for the same x_b at t_b, as also shown in Fig 3.4b. For illustration purposes, the small droplets and bubbles are not shown in this figure. The shape of the predicted wave profile is similar to the experiments. In the following, the results computed on the fine grid are presented. Four time phases are defined in the experiments: startup (Δt_S); steep wave formation (Δt_{SWF}); plunging wave breaking (Δt_{PWB}); and chaotic

wave breaking swept downstream (Δt_{CWB}). The plunging wave breaking process consists of four repeated plunging events each with three sub-events: jet impact (plunge), oblique splash and vertical jet as shown in Fig. 3.5. The simulations predict the same four time phases and four repeated plunging events as the experiments.

Tables 3.3-3.6 provide the percentage of the plunging wave breaking time phases for the experiments and simulations, respectively, truncated at the end of the plunging wave breaking phase to facilitate the comparisons such that Δt_T = 14.8 s for the experiments and 15.59 s, 15.76 s, and 16.01 for fine grid, medium grid, and coarse grid simulations, respectively. The combination of the startup and steep wave formation phases are 90.5 and 87%Δt_T(CG1), 87.3%Δt_T (CG2), 90.7%Δt_T (CG3), respectively for the experiments and simulations. The differences in t_b between the experiments and simulations are 0.17 s, 0.37 s, and 1.12 s for CG1, CG2, and CG3, respectively. However, the plunging wave breaking phase is 0.62 s (CG1), 0.59 s (CG2), and 0.09 s (CG3) longer for the simulations than the experiments such that Δt_{PWB} = 9.5 and 13%Δt_T (CG1), 12.6%Δt_T (CG2), and 9.3%Δt_T (CG3), respectively for the experiments and simulations. This is likely due to the 3D instability in the experiments where the entrapped air tube collapses faster than the simulations after the plunge. The 3D instability contributes to the short lifetime of the air tube (Peregrine, 1983) that does not exist in the 2D simulations. The average plunging event time interval is 0.35 s for the experiments and 0.5 s (CG1), 0.5 s (CG2), and 0.37 s (CG3) for the simulations. The second plunge takes the longest followed by the third/last and the first for CG1, as shown Table 3.7 and oblique splashes and vertical jets account for 11.9%Δt_{PWB} and 52.5%Δt_{PWB}, respectively, i.e., more time is spent in plunging than splashing, which is opposite to the experiment. Table 3.7 shows time interval of each plunging phase. Grid CG1 and CG2 spend longer time on the second plunge than other plunging phases, while EFD and CG3 show the first plunge takes longer than other phases.

Figure 3.6 compares the wave breaking profiles at the maximum height just before the first plunge (i.e., at t_b) with experiments by Kang et al. (2011) and other studies using wave height H_w and length λ for scaling of z and x, respectively. The average H_w for the other experimental studies is 0.13 m, which is similar to L4/S4 H_w = 0.12/0.13 m values. The λ values were estimated using the zero crossing method either twice trough to crest or trough to trough depending on the available data. Some data are extracted from the figures in the references. For the other experimental studies, the λ values vary considerably $0.3 \le \lambda \le 0.8\,\text{m}$ such that wave steepness $0.45 \le ak \le 1.15$. For L4/S4 λ = 0.28/0.23 m such that *ak* = 1.35/1.79. For all studies the *ak* values are consistent with geometric breaking criteria for deep (Tian et al., 2008) and shallow (Chanson and Fang, 1997) water. The wave faces for all studies have similar shapes albeit with spreading, whereas the wave back shapes correlate with *ak*. The smaller *ak* values the more symmetric wave shapes and the larger *ak* values the wave backs approach more to the horizontal similar to a tidal bore. The wave faces for all studies are much steeper than the limiting Stokes wave and nearly vertical near the crest. The wave backs for all studies are also much less steeper than the limiting Stokes wave and approach the horizontal for large *ak* such that the wave asymmetry is largest for the steepest waves. Note that the average wave speed C for the other experimental studies is 1.5 m/s in the direction of wave breaking, whereas the average axial velocity at t_b, $\langle \bar{U}_b \rangle$, for L4/S4 is 0.6 m/s in the opposite direction to the wave breaking. It should be noted that the gross features of the flow as shown by the comparison given in the figure compare well for all of these cases. This indicates that for these flows the mechanism by which the wave breaks is not as important, but post-breaking, sub-surface flows are more affected by these differences.

Figures 3.7a, b and c show the time history of the bump vortex, n=1−4 entrapped air tube (x_{An},z_{An}) trajectories, and the cross-sectional diameters of the entrapped air tube (D_{An}), respectively, as compared with experiments. The simulations predict the bump

vortex trajectories well, but with some differences. The average penetration depth of entrapped air tubes is $0.165\zeta_0/H$ for experiments and $0.155\zeta_0/H$ for simulations which is similar to the previous studies. The mean entrapped air tube diameter is 0.185 H_w for experiments and 0.578 H_w for the simulations.

3.3.4 Flume Flow

The simulations accurately predict the water elevations including the flume acceleration wave, as shown in Figs. 3.8 and 3.9. Figure 3.8 shows the time history of the water elevation at various axial locations. The upstream water elevation increase is due to the flume acceleration wave η that travels down the flume which is also observed in the experiments. The wave is visible in the time histories of the water elevations. The downstream wave elevation initially decreases and then increases to reach the maximum wave height. The downstream wave heights are smaller than the upstream. The water elevations at the inlet (x/H = -52) and outlet (x/H = 44) are very close to the experimental results since experimental boundary conditions are enforced at these two locations. It is interesting to see that the water elevation over the bump at x/H = 0 is also very close to the experimental value, this is likely because the flow is relatively stable at this location due to the bump effect. Moreover, before the first plunge (t < 0 s), the water elevations in most locations match the experimental measurements very well. Large discrepancies can be found after the first plunge. This is because the flow becomes very violent after the plunge and the instantaneous water elevation in the simulations demonstrates large fluctuations.

Figure 3.9 shows the time history of the location, amplitude and speed of the flume-acceleration wave η. The location was defined as the time when half the wave height passes the measurement location. As shown in the figure, the wave location is very accurately predicted and the wave amplitude is under-predicted. The wave speed is

approximately constant with an average value of 1.93 m/s for the experiments and approximately 2.0 m/s for all the three simulations, respectively.

3.3.5 Plunging Wave Breaking

The major events of the plunging wave breaking process are shown in Fig. 3.10, including the video images, PIV image with overlaid CFD wave profile, *U* and *W* velocity contours from both experiments and CFD. The grid resolution for the simulations in the view window is 760×735 with Δx_{min}=0.3 mm and Δz_{min}=0.2 mm. For illustration purposes, the PIV velocity vectors are plotted every 32 grid points. The resolution in the PIV domain is 89×67 with the space interval 3.49 mm. The simulations qualitatively predict the same four time phases as the experiments, but with different percentages of the total time, as already discussed. The experimental trends are exhibited by the simulations, but generally with reduced axial and vertical velocity magnitudes, as shown in Fig. 3.10. The predicted wave profile is close to the experiment which similarly scales with the other studies as discussed in Kang et al. (2011).

Figure 3.10a is for t_b when the wave crest becomes steepest and reaches its maximum height ζ_{max}/H=1.97 at x/H=3.39 (row 2). The maximum height position is very close to the experimental measurement (ζ_{max}/H=2.04 at x/H=3.38). Small wave breakings occur prior to the maximum height (clearly shown in Fig. 3.4). This can also be seen from the experimental video image which shows a broken wave face. The average wave height H_w for the experiments L4/S4 are 0.12/0.13 m, which is similar to the computational value H_w = 0.1 m. For the simulations, the wave length λ = 0.26 m and *ak* = 1.2, which are close to the the experiments L4/S4 λ= 0.28/0.23 m and *ak*=1.35/1.79.

Figure 3.10b is for the first plunge. The plunging jet shoots out from the wave face, falls, and touches the wave trough entraining air tube A1. The jet angle is 50º and 48º for the simulations and experiments, respectively, which is close to the average (51º) of the other experimental and computational studies. The jet velocity is -0.4 m/s and

experimental value is -0.2 m/s. The jet thickness is 0.14 H_w for the simulations and $0.2H_w$ for the experiment. The shape of the first entrained air tube is an ellipse with aspect ratio $\sqrt{3}$ for the experiment and 1.67 for the simulations as reported in most other studies. The air tube diameter is $0.45H_w$ for the simulations and $0.18H_w$ for the experiments. The air tube penetrates to $0.2\zeta_0/H$ for the simulations and $0.375\zeta_0/H$ for the experiments.

Figures 3.10c is for the first oblique splash. The plunging jet rebounds off the wave trough forming the oblique splash, which subsequently grows and fans out. The angle of the oblique splash is 35º for both the experiments and simulations, which is similar to the other experimental values 32º-40º with 35º average value. The region of bubbly flow increases, as the wave crest plunges into the wave trough as shown in both the video image and computational wave profile. Figure 6d is for the first vertical jet. The video image shows a large region of splashing and bubbly flow above the free surface, but the organized structure of the vertical jet at $(x_{VJ1}/H, z_{VJ1}/H)=(3.5, 2)$ and the first air tube A1 at $(x_{A1}/H, z_{A1}/H)=(4.2, 1)$ can still clearly be seen. The axial location and height of the vertical jet in the simulations is at $(x_{VJ1}/H, z_{VJ1}/H)=(2.7, 2.0)$. As the first vertical jet decreases in height, another jet is formed which starts to initiate the second plunge as shown in Fig. 3.10e. The first air tube A1 is swept downstream. Figures 3.10e to 3.10i show the 3 repeated plunging events each with jet impact, oblique splash and vertical jet. The air tube diameters and trajectories are evident, as summarized in Fig. 3.6. In the experiments, the air tube diameters and trajectories are estimated using the video images by tracking the size of the two-phase region of entrapped air corresponding to each plunging event. After the repeated plunging events, chaotic wave breakings and splash ups are swept downstream leaving a trail of aerated region.

3.3.6 Velocity, Vortices, Energy and Flume Bottom Pressure

Both the experiments and simulations show a high axial velocity region over the bump and under the wave trough when the wave reaches the maximum height (Figure 3.10a, rows 3 and 4). This high axial velocity region extends under the wave crest and pushes the separation region downstream. A high axial velocity region on the backside of the wave crest can also be observed. The high axial velocity region over the bump further extends and pushes the separation region downstream with the wave breaking process, whereas the high axial velocity region on the backside of the wave crest soon disappears after the first plunging event. The simulations show the similar flow trend, with more detailed resolutions of plunging, oblique splashing, vertical jet and air entrainment. As shown in Figure 3.10a (rows 5 and 6), a high vertical velocity region downward behind the bump and a high vertical velocity region upward towards the wave crest are formed. The vertical velocity in these two regions intensifies and reaches the maximum in magnitude before the first plunging. The vertical velocities decreases in magnitude after the first wave plunging events as wave crest falls in height. During the whole wave breaking process, the axial velocity increases and upward vertical velocity decreases in magnitudes. The turbulence is high in the breaking region.

Figure 3.11 shows wave breaking energies compared with the experimental measurements averaged over the PIV field of view. Prior to t_b the potential energy is much larger than the kinetic energy with maximum value at maximum height. Subsequently, the potential energy drops rapidly to about 40% of its maximum value with oscillations, whereas the kinetic energy continuously increases. The potential energy decays as $t^{-0.3}$. After the second plunge, the kinetic energy is larger than the potential energy. Thus, the total energy continuously increases reaching its maximum at t_b after which it drops with oscillations until the third plunge followed by oscillatory and continuous increase. The simulation results have the similar trend as the experimental

measurements. The kinetic energy is over predicted for $t_b<0$, the potential energy is over predicted for $t_b>0$ such that the total energy is over predicted. Note that the present simulations used the exact experimental upstream and downstream velocity and water elevation as initial and boundary conditions; however, for laminar flow, i.e., a turbulence model was not used.

Bottom pressure variations with time are given in Figs. 3.12 and 3.13. The simulations show similar bottom pressure magnitudes to the experiments, but with fairly large oscillations, which correlate with the plunging wave breaking events and sub-events. Figure 12 shows pressure distribution (red line) with wave profile and vector field colored using U velocity component. As shown in Fig. 3.13, pressure peaks are corresponding to the locations where water height increases. When the first plunge occurs, pressure increases at the plunge point and decreases at the points downstream. After the first plunge, pressure decreases at most points; and the oblique splash occurs as the pressure drops. The vertical jet is formed at the location where the pressure increases again. As the vertical jet decreases in height, the overall pressure at most positions drops. Same pressure patterns are shown in the repeated processes.

3.4 Conclusions

The plunging wave-breaking process for impulsive flow over a bump in a shallow water flume is numerically simulated using the exact experimental initial and boundary conditions, which allows more detailed spatial and temporal validations. The grid sensitivity study shows a monotonic convergence based on the results computed using three systematically refined grids. The results computed on the fine grid are compared with the experimental measurements. The wave profile and location at the maximum height is very close to the experiment results. The simulations qualitatively predict all four time phases, all four plunging events and their sub-events. Detailed wave breaking processes, including wave profile at maximum height, first plunge, entrapped air bubble

trajectories and diameters, kinetic, potential, and total energy, and bottom pressures are discussed along with the experimental results. The flume flow and velocity demonstrate the same flow trend as the experiments but with reduced velocity magnitudes. The simulations show similar bottom pressure to the experiments but with large oscillations, which correlate with the plunging wave breaking events and sub-events. The post-breaking water elevations is larger as compared to the experimental results.

The present results show differences and similarities with other experimental and computational studies for deep water and sloping beaches. In particular, the breaking processes show differences due to the differences in mean flow direction. In the present study where the breaking is opposite to the mean flow, the breaking events involve repeated plunge, oblique splash, vertical jet, air-bubble entrainment sub events near the first plunge. In the other studies, the breaking is in the direction of the mean flow such that the breaking events involve repeated plunge/forward splashups and air-bubble entrainment sub events. Both show smaller scales as the plunging wave breaking repeated sub events dissipate into chaotic wave breaking. The present wave breaking profile is similar to those for very steep waves. The present results involve wave-body interactions due to the separated flow and bump vortex downstream of the bump. Nonetheless, many variables are similar for the present and other studies, including wave height, length, and steepness; jet angle, speed, and thickness; air bubble shape and size; splash angle and height; wave breaking vortex size and strength; potential energy dissipation; and turbulence intensity.

The experiment provides benchmark validation data for two-phase flow CFD for ship hydrodynamics building block geometry. The initial CFD used fully impulsive initial conditions, which precluded temporal validation. Present CFD is using experimental upstream and downstream conditions for more detailed and temporal validation. Three different grids for each grid solver are used in the present simulations. Solutions are sensitive to the grids; however, all the grids show all the plunging wave

breaking features. In the present study, the fine grid results from Cartesian grid solver are presented and other solutions are discussed in Appendix A and B.

Table 3.1 Plunging wave breaking with EFD for Cartesian grid solver

	EFD (L4)	Fine (CG1)	E (%)	Medium (CG2)	E (%)	Coarse (CG3)	E (%)
t_b	13.4 s	13.57 s	1.26	13.77 s	2.7	14.52 s	8.3
x_b/H	3.38	3.39	0.3	4.26	26	5.24	55
z_b/H	2.14	1.97	7.9	2.03	5.1	2.09	2.3
d_b/H	0	0.17	-	0.88	-	1.86	-

Table 3.2 Verification study

Parameter	R_G	P_G	U_G (%)
t_b	0.11	3.08	0.18
x_b/H	0.67	0.57	118
z_b/H	0.66	0.58	9.4
d_b/H	0.045	1.8	2.0

Table 3.3 Percentage of the plunging breaking wave time phase for each of the sub-events for experiment

Time	$\Delta t_T'$ = 14.8 s		$\%\Delta t_T'$					
-13.4 s	-		-					Startup
-0.9 s	Δt_S =12.5 s		84.5					
-	Δt_{SWF} = 0.9 s	-	6					Steep wave formation
0.0 s		0.9 s						
-	Δt_{PWB} = 1.4 s	Δt		$\%\Delta t_{PWB}$	Δt			1st plunge
0.067 s		0.067 s	P1 38.1%	4.8	0.533			
0.133 s		0.066 s		4.7				1st oblique splash
0.533 s		0.4 s		28.6				1st vertical jet
0.6 s		0.067 s	P2 23.9%	4.8	0.334	9.5	Plunging wave breaking	2nd plunge
0.667 s		0.067 s		4.8				2nd oblique splash
0.867 s		0.2 s		14.3				2nd vertical jet & 3rd plunge
0.933 s		0.066 s	P3 19%	4.7	0.266			3rd oblique splash
1.133 s		0.2 s		14.3				3rd vertical jet & 4th plunge
1.267 s		0.134 s	P4 19.1%	9.6	0.267			4th oblique splash
1.4 s		0.133 s		9.5				4th vertical jet

Table 3.4 Percentage of the plunging breaking wave time phase for each of the sub-events for CG1

Time	$\Delta t_T'$ =15.59 s		$\%\Delta t_T'$					
-13.57 s	-		-				Startup	
-1.05 s	Δt_S =12.52 s		80.3					
-	Δt_{SWF} = 1.05 s	-	6.7				Steep wave formation	
0.0 s		1.05 s						
-	Δt_{PWB} = 2.02 s	Δt	P1 16.4%	$\%\Delta t_{PWB}$	Δt	13	Plunging wave breaking	1st plunge
0.19 s		0.19 s		9.4	0.33			
0.24 s		0.05 s		2.5				1st oblique splash
0.33 s		0.09 s		4.5				1st vertical jet
0.7 s		0.37 s	P2 32.2%	18.3	0.65			2nd plunge
0.79 s		0.09 s		4.5				2nd oblique splash
0.98 s		0.19 s		9.4				2nd vertical jet
1.02 s		0.04 s	P3 25.7%	2	0.52			3rd plunge
1.07 s		0.05 s		2.4				3rd oblique splash
1.5 s		0.43 s		21.3				3rd vertical jet
1.62 s		0.12 s	P4 25.7%	5.9	0.52			4th plunge
1.67 s		0.05 s		2.5				4th oblique splash
2.02 s		0.35 s		17.3				4th vertical jet

Table 3.5 Percentage of the plunging breaking wave time phase for each of the sub-events for CG2

Time	$\Delta t_T'$ =15.76 s		$\%\Delta t_T'$					
-13.77 s	-		-				Startup	
-0.95 s	Δt_S =12.82 s		81.3					
-	Δt_{SWF} = 0.95 s	-	6				Steep wave formation	
0.0 s		0.95 s						
-	Δt_{PWB} = 1.99 s	Δt	P1 19.1%	$\%\Delta t_{PWB}$	Δt	12.6	Plunging wave breaking	1st plunge
0.16 s		0.16 s		8	0.38			
0.19 s		0.03 s		1.5				1st oblique splash
0.38 s		0.19 s		9.5				1st vertical jet
0.91 s		0.53 s	P2 33.2%	26.6	0.66			2nd plunge
0.98 s		0.07 s		3.5				2nd oblique splash
1.04 s		0.06 s		3				2nd vertical jet
1.55 s		0.51 s	P3 27.1%	25.7	0.54			3rd plunge
1.58 s		0.03 s		1.5				3rd oblique splash
1.83 s		0.25 s	P4 20.6%	12.7	0.41			4th plunge
1.89 s		0.06 s		3				4th oblique splash
1.99 s		0.1		5				4th vertical jet

Table 3.6 Percentage of the plunging breaking wave time phase for each of the sub-events for CG3

Time	$\Delta t_T'$ =16.01 s		$\%\Delta t_T'$					
-14.52 s	-		-				Startup	
-1.35 s	Δt_S =13.17 s		82.3					
-	Δt_{SWF} = 1.35 s	-	8.4				Steep wave formation	
0.0 s		1.35 s						
-	Δt_{PWB} = 1.49 s	Δt	P1 36.24%	$\%\Delta t_{PWB}$	Δt	9.3	Plunging wave breaking	1st plunge
0.31 s		0.31 s		20.8	0.54			
0.35 s		0.04 s		2.7				1st oblique splash
0.54 s		0.19 s		12.8				1st vertical jet
0.67 s		0.13 s	P2 20.8%	8.7	0.31			2nd plunge
0.72 s		0.05 s		3.4				2nd oblique splash
0.85 s		0.13 s		8.7				2nd vertical jet
0.95 s		0.1 s	P3 20.8%	6.7	0.31			3rd plunge
0.99 s		0.04 s		2.7				3rd oblique splash
1.16 s		0.17 s		11.4				3rd vertical jet
1.3 s		0.14 s	P4 22.16%	9.4	0.33			4th plunge
1.31 s		0.01 s		0.6				4th oblique splash
1.49 s		0.18 s		12.1				4th vertical jet

Table 3.7 Time interval of for each plunging phase

Plunging phase	EFD (L4)	CG1	CG2	CG3
P1	0.533	0.33	0.38	0.54
P2	0.334	0.65	0.66	0.31
P3	0.266	0.52	0.54	0.31
P4	0.267	0.52	0.41	0.33

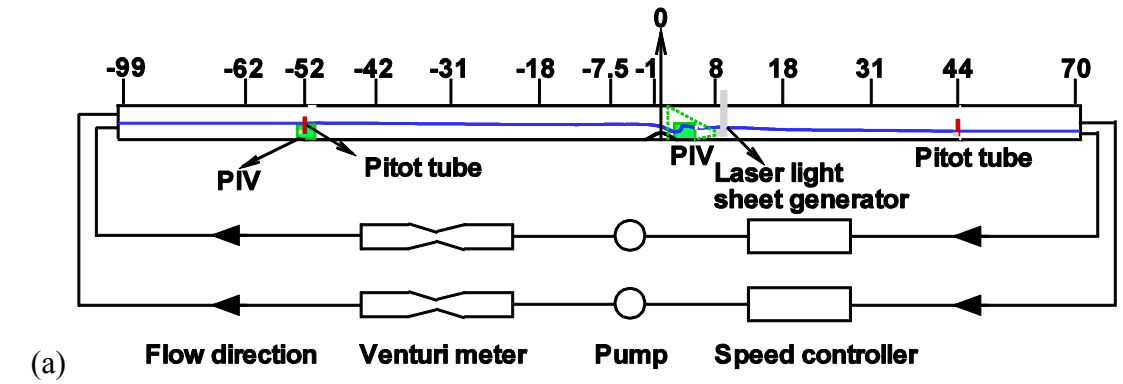

(a)

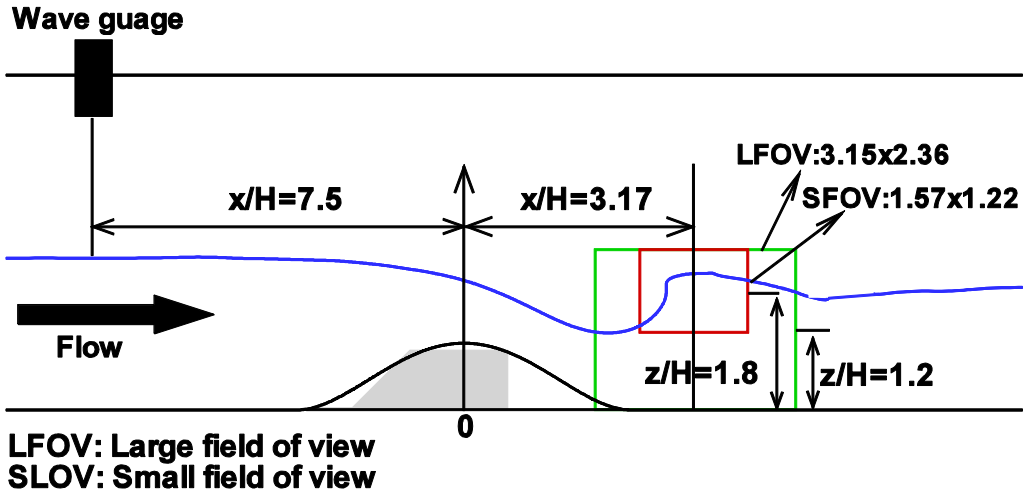

(b)

Figure 3.1 Plunging wave breaking experimental setup and measurement locations: (a) side view; (b) breaking region

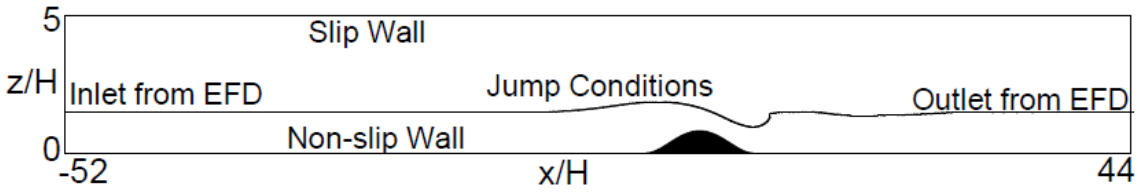

Figure 3.2 Computational domain and IC/BC

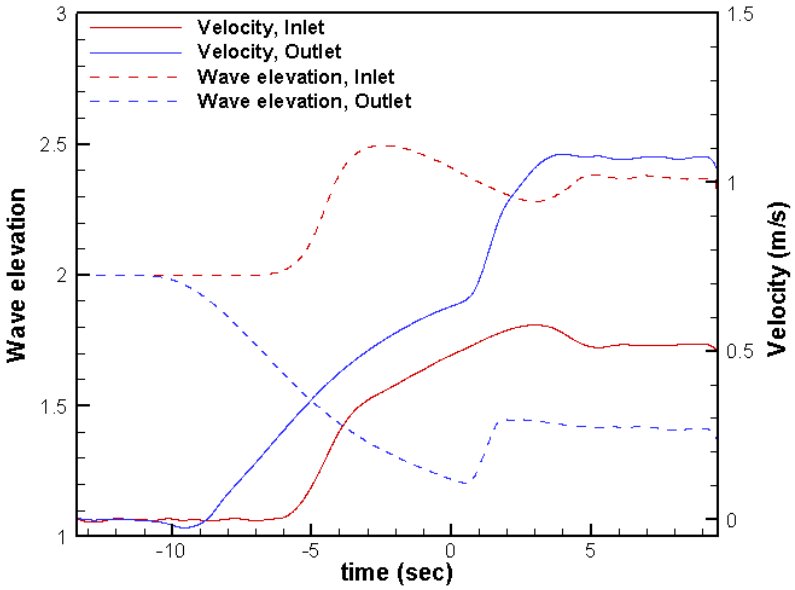

Figure 3.3 EFD data used for CFD simulation

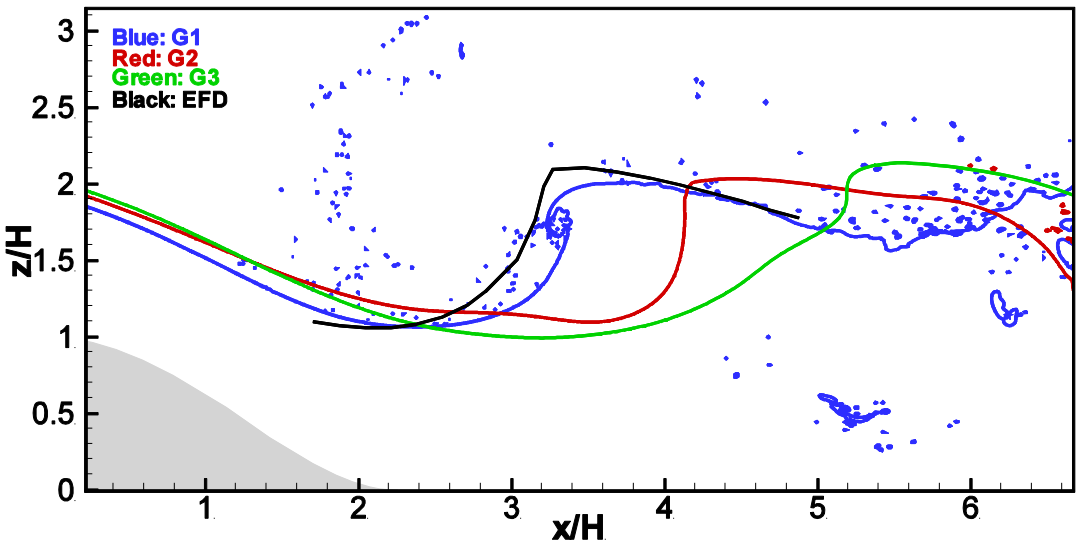

(a)

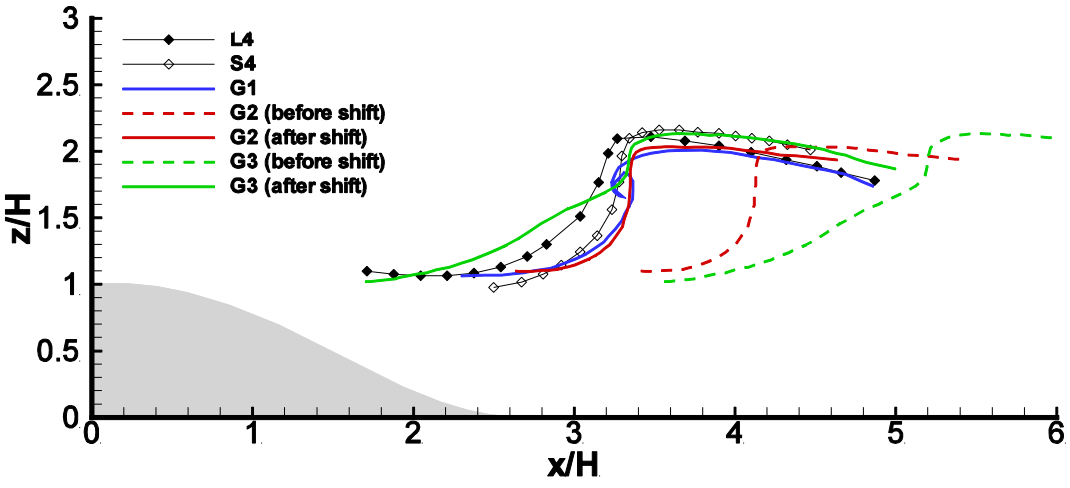

(b)

Figure 3.4 Wave profiles at t_b for different grids and compared with experiements. (a) Wave profile without shift; (b) wave profile with shift

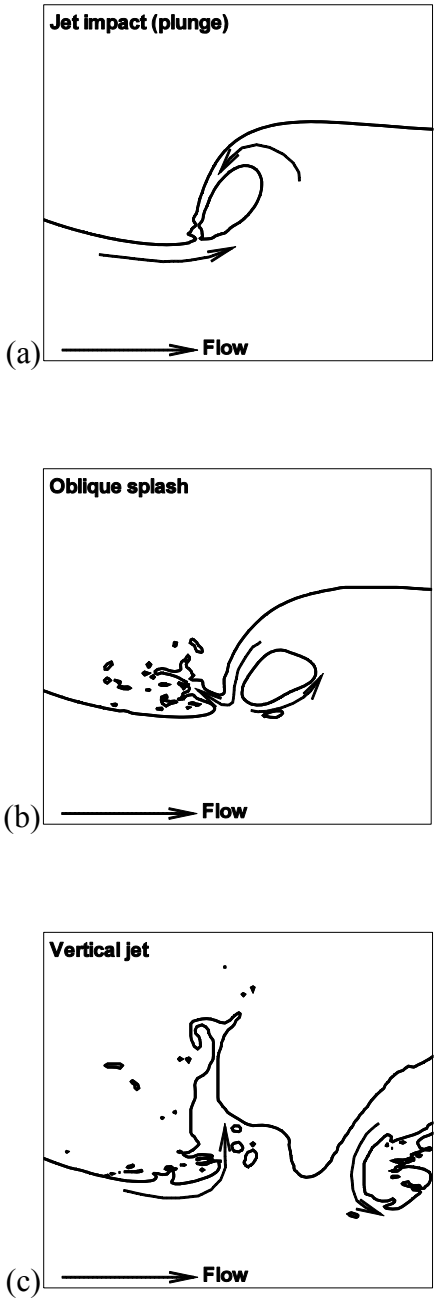

Figure 3.5 Major events of the plunging wave breaking over a submerged bump. (a). Jet impact (plunge); (b); Oblique splash; (c) Vertical jet

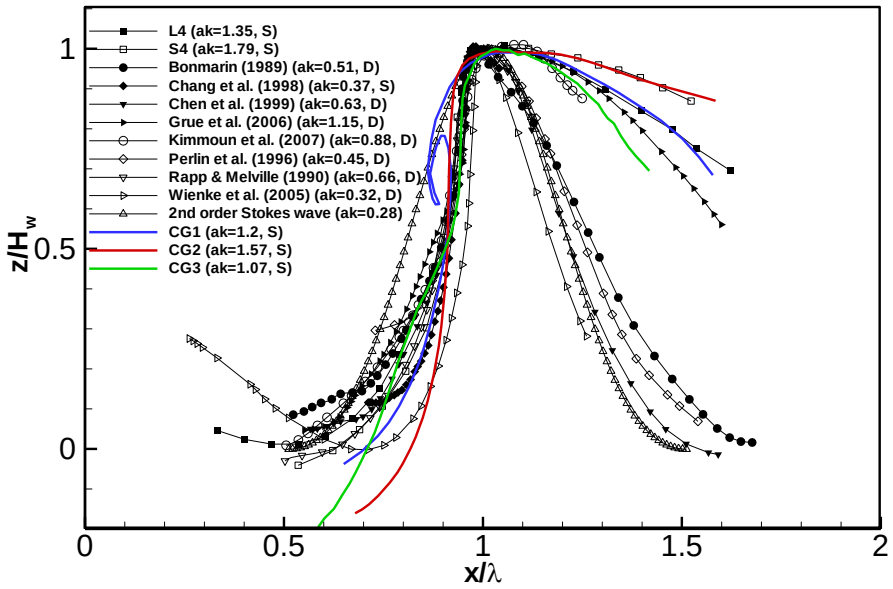

Figure 3.6 Wave profile comparison with EFD; non-dimensional with wave length (λ) and wave height (H_w) at t_b in X, Z, respectively

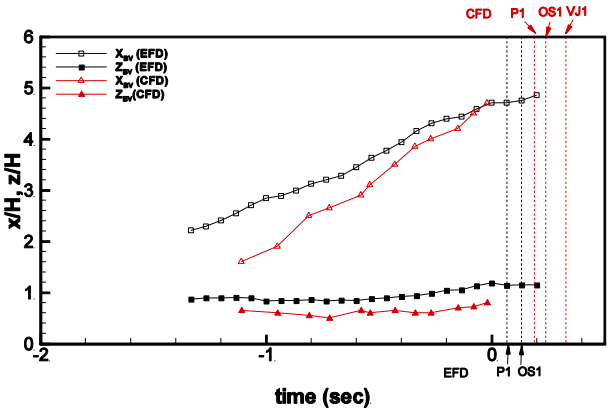

(a)

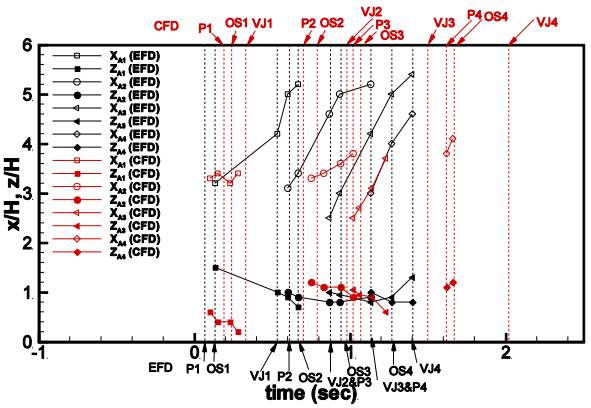

(b)

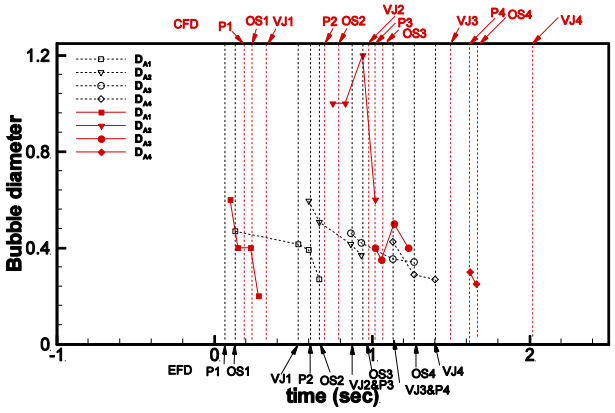

(c)

Figure 3.7 Time history of vortex and air entrainment paths, and air bubble size. Red: CFD; black: EFD

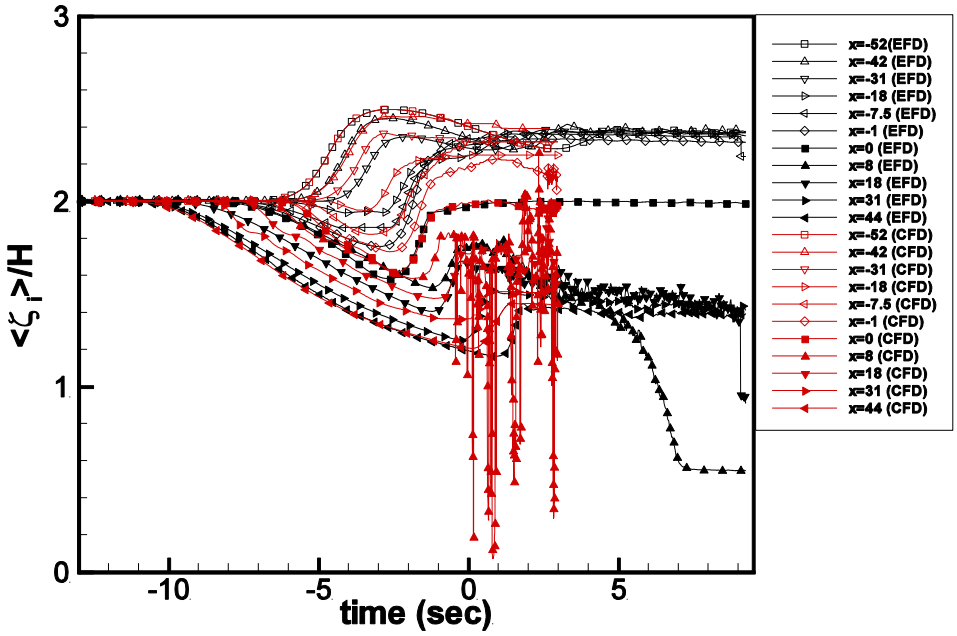

(a)

Figure 3.8 Time history of water elevations

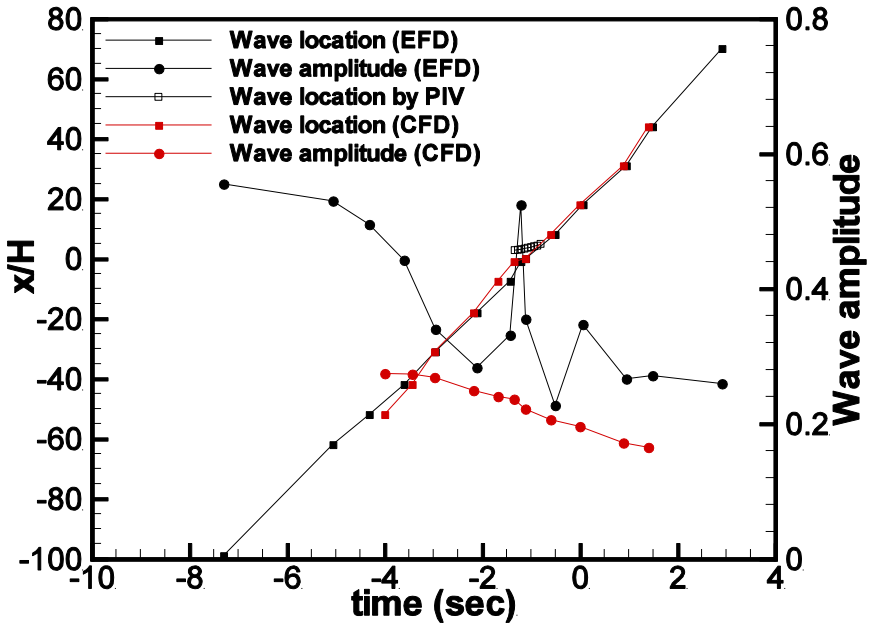

(a)

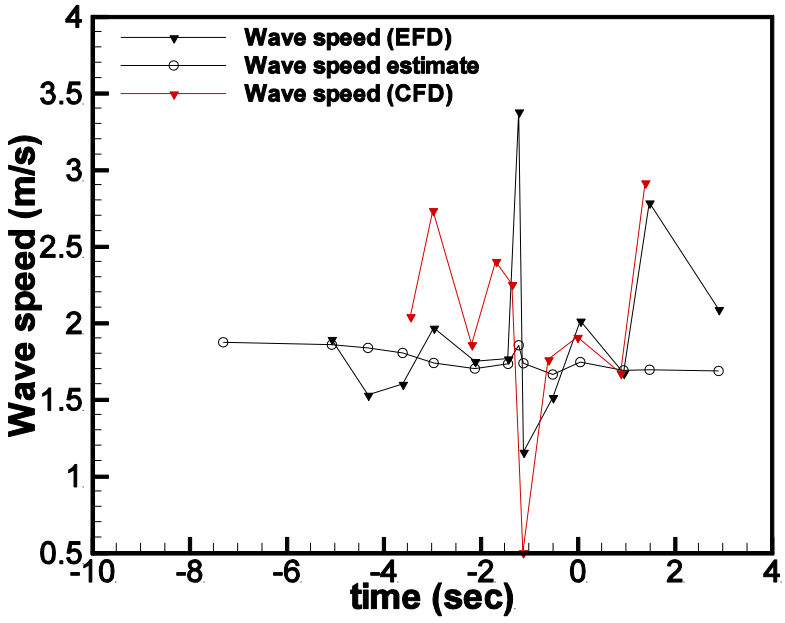

(b)

Figure 3.9 Time history: (a) acceleration wave location and amplitude; (b) wave speed

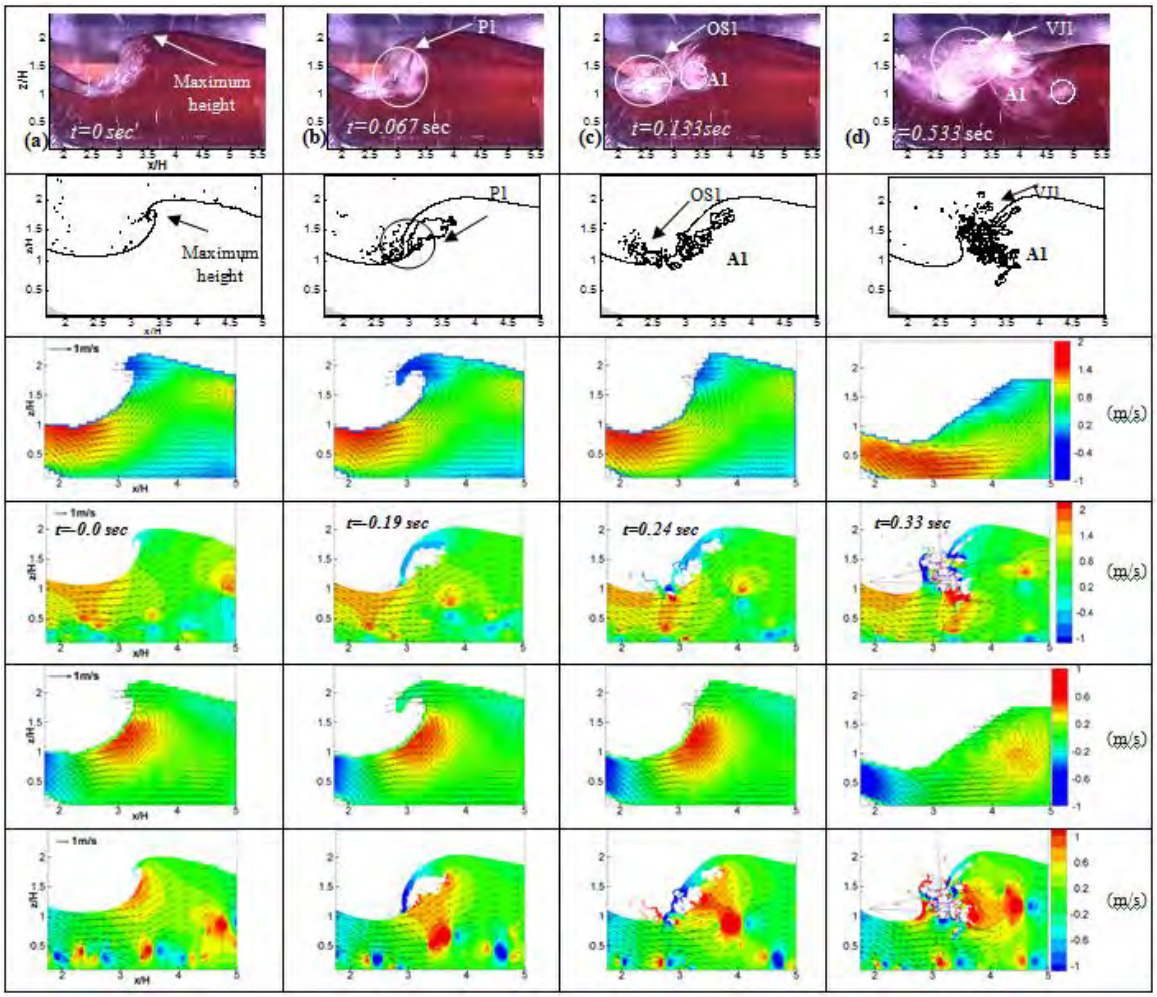

Figure 3.10 Video images (Reins, 2008); PIV image with CFD; EFD U velocity contours; CFD U velocity contours; EFD W velocity contours; CFD W velocity contours

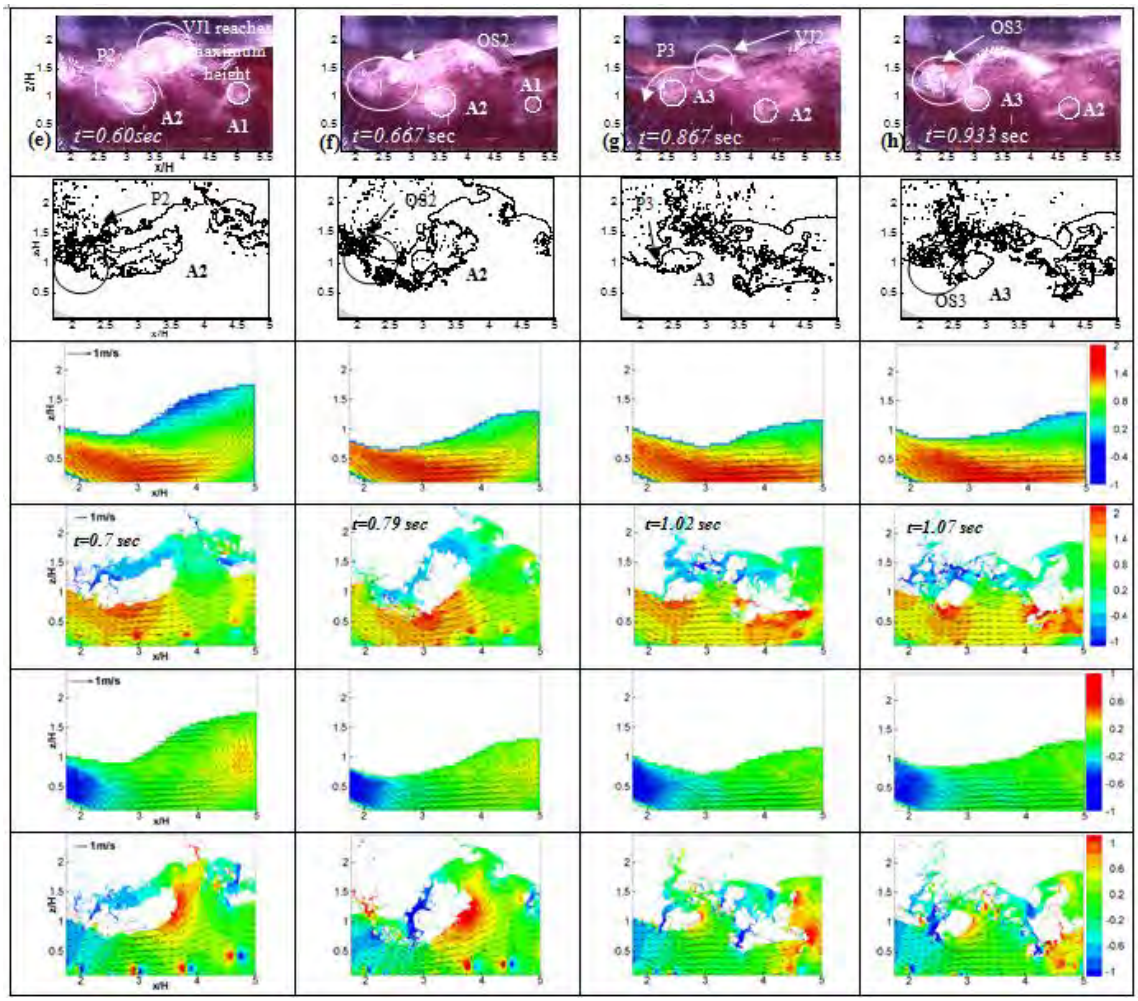

Figure 3.10 (continued)

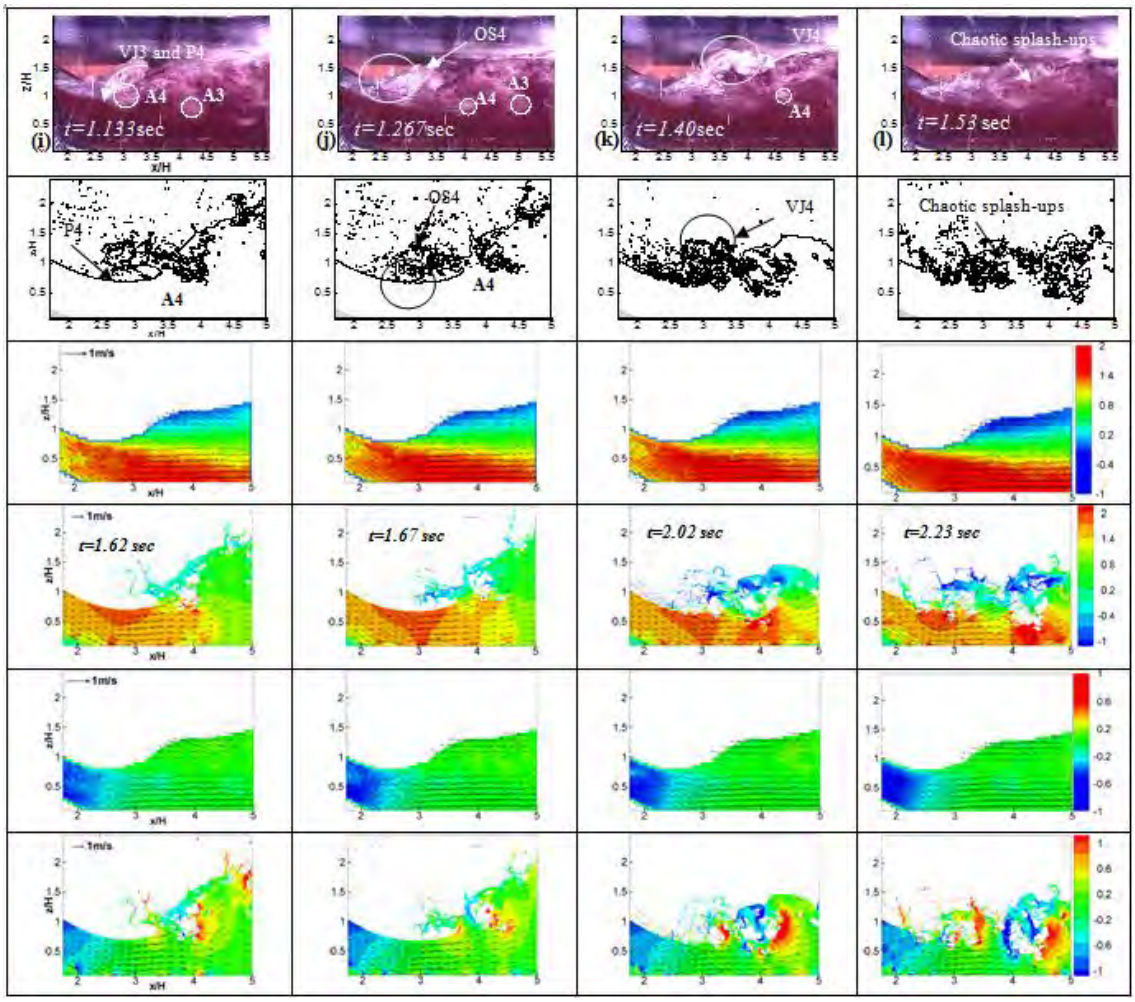

Figure 3.10 (continued)

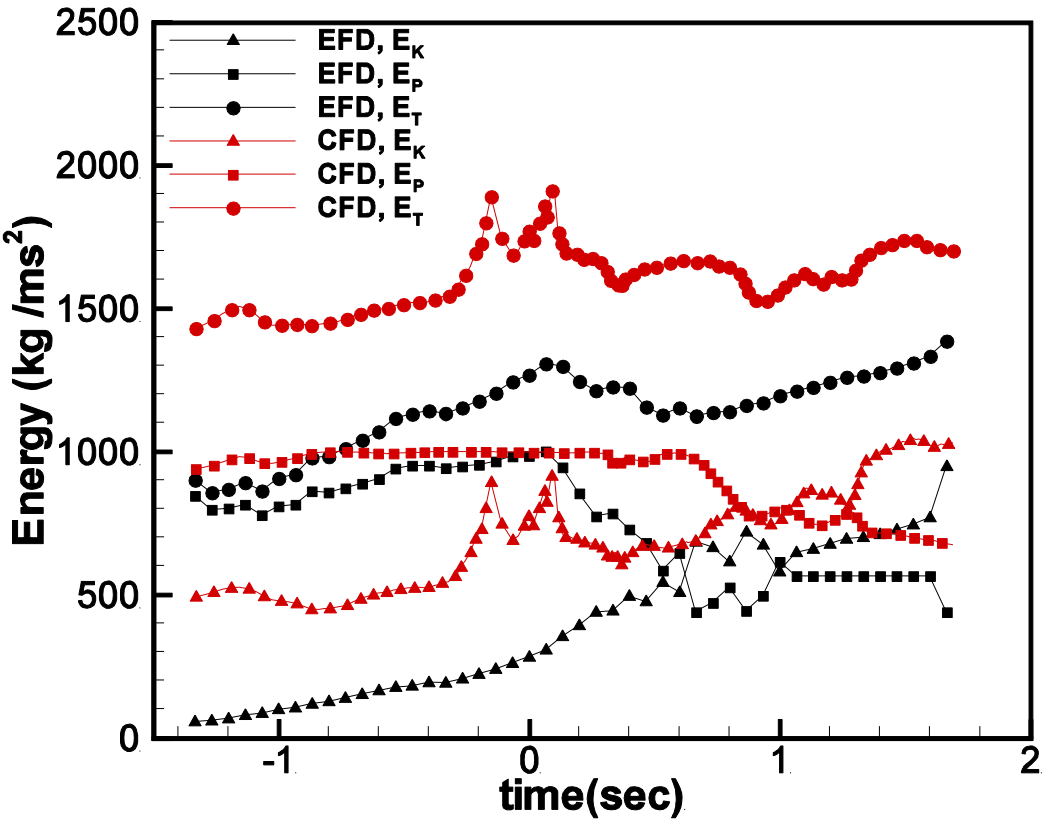

Figure 3.11 Time evolutions of the total energy, the wave kinetic energy, the wave potential energy

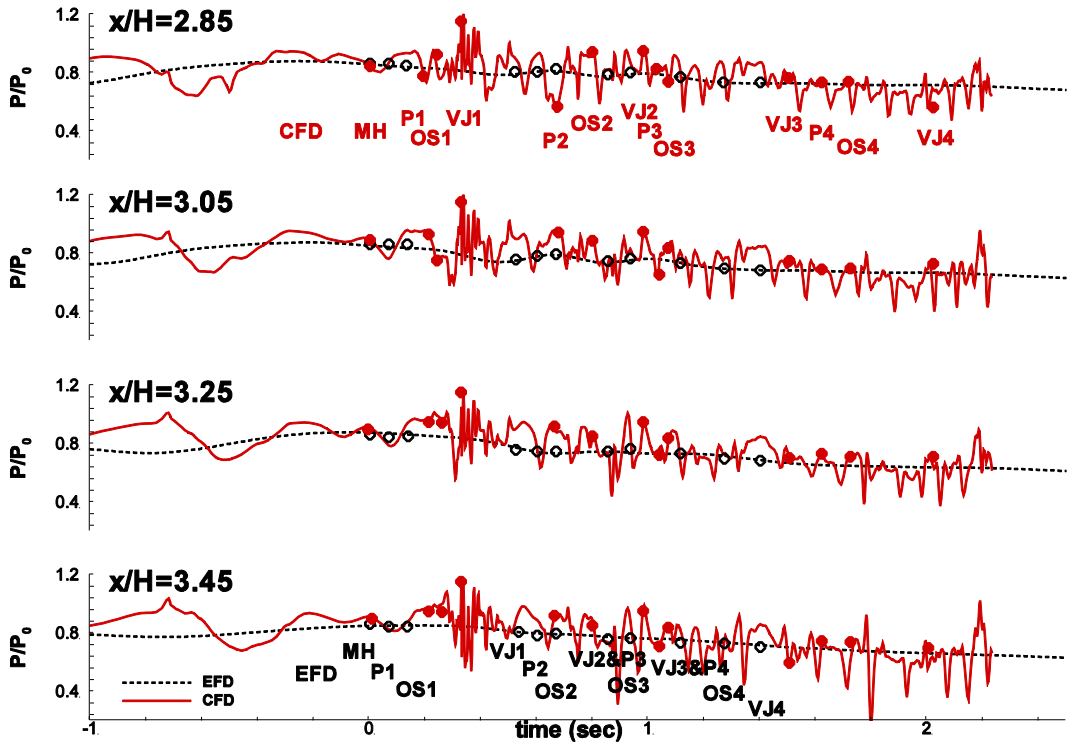

Figure 3.12 Average pressure time series for EFD and CFD at various stream-wise positions

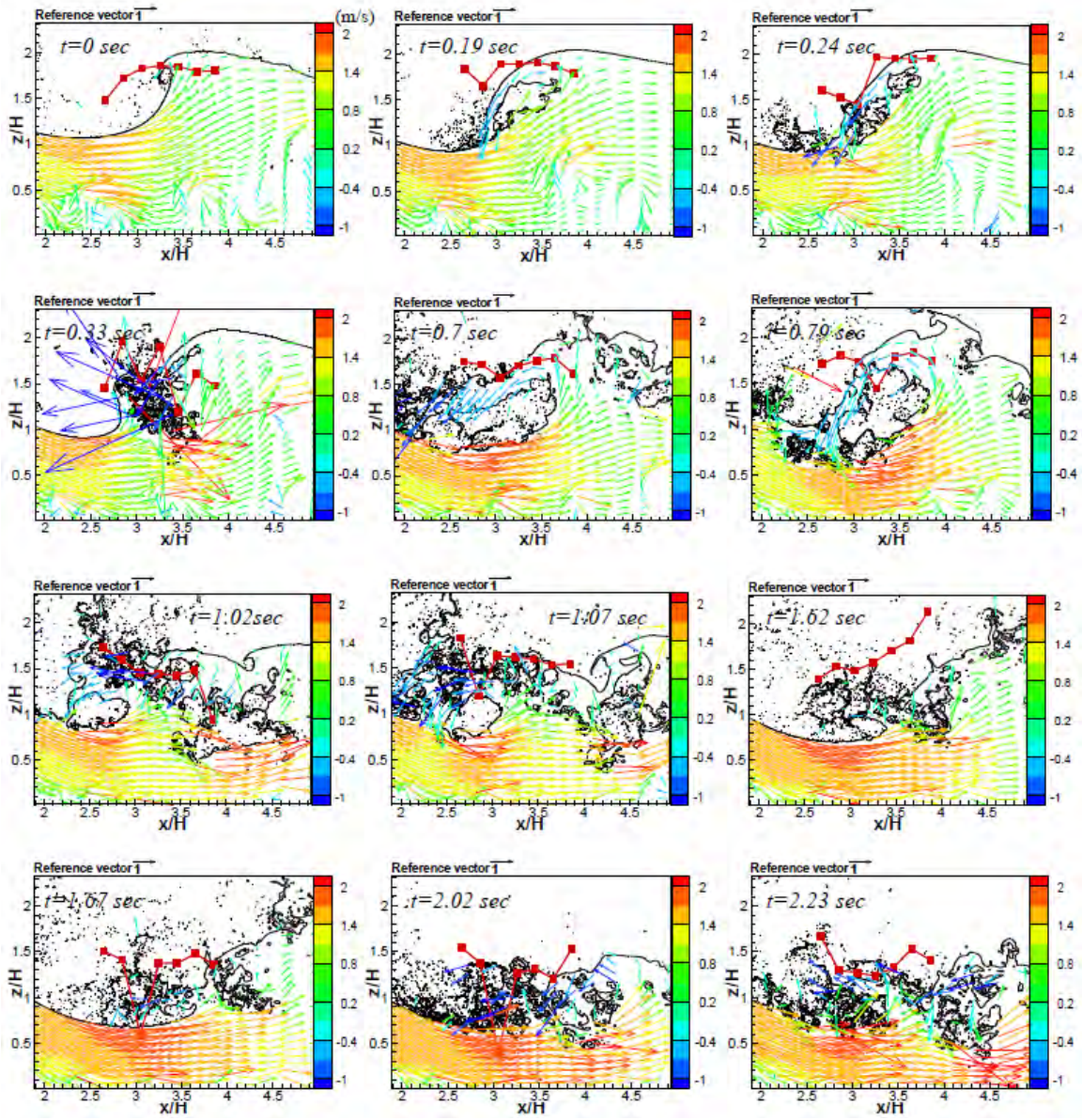

Figure 3.13 CFD with overlaid vector field and water height normalized by bump height describing breaking events

CHAPTER 4
THE EFFECT OF REYNOLDS AND FROUDE NUMBER ON THE FLOW PAST A SURFACE-PIERCING CIRCULAR CYLINDER

4.1 Introduction

Turbulent flows past bluff bodies have been investigated extensively for a long time due to their importance in many engineering applications. The flow past a circular cylinder shows different features at different Reynolds numbers (Re), based on the free-stream velocity, cylinder diameter, and kinematic viscosity. There are three states of the flow with different Re; sub-critical flow ($Re = 1000 \sim 2\times10^5$), critical flow ($Re = 2\times10^5 \sim 3.5\times10^6$), and super-critical flow ($Re > 3.5\times10^6$). In the sub-critical range the boundary layer along the cylinder is laminar and transition to turbulence happens in the free shear layer downstream of the cylinder. With an increase of Re, the location of the transition moves upstream (Wissink and Rodi, 2008). In the critical range the base suction and the drag decrease dramatically and this is associated with a revitalized boundary layer characterized by events in order of a laminar separation, a transition to turbulence, a reattachment, and another separation further downstream with much reduced downstream wake width. In the super-critical regime, the boundary layer along the cylinder becomes turbulent before separation. The base suction and drag of this regime is low due to the later separation of the turbulent boundary layer (Kravchenko and Moin, 2000).

The flow around a surface-piercing bluff body is much more complicated than the single-phase flow due to the interaction between the viscous effects near the body and air-water interface phenomena, including breaking waves, thin liquid sheet formation, and air entrainment. It also exists in many engineering applications such as ship, ocean, coastal, and hydraulic engineering. The effects of the interface on the force distributions on the body, vortex generation and turbulent structures, and air-water inerface structures, especially, their changes with the Reynolds and Froude (Fr) numbers are not well

understood. A better understanding of these effects is also important for the cases when vortex- and wave-induced vibrations of the cylinder are to be considered.

4.1.1 Review of related literature

There were some studies of free-surface flows past blunt bodies such as NACA0024 airfoil, wedge-shaped bow, and circular cylinder, in the literature. Experimental measurements (Metcalf et al., 2001; Metcalf et al., 2006) of flow around a surface-piercing NACA 0024 foil were conducted in a towing tank with Fr (0.19, 0.37, and 0.55) and Re (0.822, 1.52, and 2.26 × 10^6). No separation and the expected Kelvin waves are observed for low Fr while a wedge-shaped separation is presented on the interface for medium and high Fr. A large bow wave resembles a spilling breaker with low root mean square (rms) for medium Fr. Mean wave elevations in the separation region is relatively constant with intense interface oscillations, turbulence and breaking and the Kelvin wave are evident outside of the separation and wake region. For high Fr, the bow wave increases remarkably. The separation region is shifted towards the trailing edge with increased splashes and bubbles. The Kelvin waves are no longer distinguishable due to increased interface turbulence. Zhang and Stern (1996) performed numerical simulations for the flow of a surface-piercing NACA 0024 foil with same range of Fr and Re as Metcalf et al. (2001 and 2006). The drag coefficients, interface waves, and the separation patterns are all Fr dependent. The bow-wave peak increases with Fr and the separation region increases as Fr increases from small (0.2) to medium (0.37) and then decreases as Fr increases further to high (0.55). Recently, numerical studies were conducted to investigate the unsteady interface wave-induced separation with the same geometry from Metcalf et al. (2006) at Fr = 0.37 and Re = 1.52 × 10^6 (Xing et al., 2007; Kandasamy et al., 2009) using detached-eddy simulation (DES) and unsteady Reynolds-averaged Navier-Stokes (URANS), respectively. Xing et al. (2007) found that the interface attenuated velocity and pressure fluctuations and moved the

maximum values of turbulence quantities from the high-speed to low-speed side of the free shear layer. Kandasamy et al. (2009) were focused on vortical structures. Both numerical studies (Kandasamy et al., 2009; Xing et al., 2007) have limitations due to a single-phase level set method for the interface tracking and they are unable to resolve complicated interface structures including splashing, breaking waves, bubble entrainment, and interface turbulence which are observed in experimental study (Metcalf et al., 2006).

The bow wave structures including thin water sheet formation, overturning sheet with surface disturbance, fingering and breaking up into spray, plunging and splashing, and air entrainments are explained with experimental measurements around a bow-shaped wedge by Waniewski et al. (2002). Waniewski et al. (2002) generated the bow waves by a deflecting plate in flumes and two different wedge models are also used to create the waves in the towing tank. It is shown that a thin liquid sheet is created at the leading edge of the wedge and it continues to ride up on the side wall for typical bow wave profile generated in the towing tank. The thin sheet starts to separate from the side wall as it reaches its maximum height. After it gets its maximum height, the jet overturns and plunges into the undisturbed water. A large area of splash is created at the wake of the wedge due to the plunge and air entrainment. Broglia et al. (2004) conducted numerical simulation of the flow around a sharp wedge using a single phase level set approach for interface tracking. They showed good agreements with the experimental results from Waniewski (1999) and Waniewski et al. (2002) on bow wave structures (formation of water jet; contact lines; plunging jet shape, angle, and velocity) whereas the small scale interface structures were not obtained due to the single-phase level set interface tracking method. Recently, Wang et al. (2010) have performed numerical simulation of wave breakings around a wedge-shaped bow to investigate the wave breaking mechanism and small scale interface structures of bow waves. The bow wave profile (thin liquid sheet at the leading edge, overturning jet and plunging, and splashes at

the wake), plunging jet shape, and surface disturbances are observed, which are also discussed in the experimental study (Waniewski et al., 2002).

There are several experimental and numerical studies on the flow past a surface-piercing circular cylinder. Inoue et al. (1993) conducted a towing tank experiment to investigate the characteristics of free surface turbulence. They found that the periodic vortex shedding occurs in deep flow, while this periodic vortex shedding is attenuated and higher frequency fluctuations are more prominent near the interface. Chaplin and Teigen (2003) carried out experimental study at a constant ratio of Reynolds number to Froude number of 2.79×10^5. They found that the total resistance coefficient reached a maximum at a Froude number of about 1. They also measured the run-up on the front of the cylinder and the depth of depression at the back and the run-up at a given Fr has a strong dependence on the Re. Kawamura et al. (2002) investigated the wave-wake interaction about a surface-piercing circular cylinder using large-eddy simulation (LES) based on a Smagorinsky sub-grid scale (SGS) model at Re = 27,000 with three different Fr = 0.2, 0.5 and 0.8. At a low Fr, surface deformations were small and the influence on the wake was negligible. On the contrary, the generated surface wave was very steep and strongly unsteady at a high Fr. They also predicted significant surface fluctuations inside the recirculation zone immediately after the surface wave crest. In addition, they were able to visualize the attenuation of vortex shedding near the interface. Flows past an interface piercing cylinder at various Reynolds and Froude numbers simulated using LES based on a Smagorinsky SGS model and a volume of fluid (VOF) method by Yu et al. (2008). They also showed that the free-surface attenuates the organized vortex shedding at the interface. At a higher Re, the free surface effect was reduced whereas this effect was enhanced at a higher Fr. As the Re increases, the mean drag coefficient increases; however, it decreased along with the Fr. They also showed that the dominant Strouhal number of the lift force decreased along with the Re. Recently, Suh et al. (2011) studied the effects of air-water interface on the vortex shedding from a vertical circular cylinder

for Re = 27,000 and Fr = 0.2, 0.8 using a high-fidelity orthogonal curvilinear grid solver. They showed that the organized periodic vortex shedding was observed in the deep flow whereas it was attenuated and replaced by small-scale vortices at the interface. The attenuation of the organized vortex shedding at the interface is caused by the streamwise vorticity and the outward transverse velocity generated near the edge of the separated region. The anisotropy between the vertical and transverse Reynolds normal stresses is the primary source of the streamwise vorticity and the outward transverse velocity at the interface.

Previous studies have not yet fully explained the nature of unsteady free-surface at different Re and Fr, which is the aim of the present numerical study. The present study extends and supports the conclusions of the precursory work for medium Re and Fr numbers (Suh et al. 2011). Simulations are performed for two-phase turbulent flow past a circular cylinder in a free stream with conditions mainly based on the experiments of Chaplin and Teigen (2003). Air-water interface structures (Kelvin waves and angle, wave elevations, run-up height on the front face of the cylinder and depression depth behind cylinder), vortical structures, wave breaking phenomena are discussed at different Re and Fr.

4.2 Computational Setup

4.2.1 Grid, Computational Domain, and Geometry

Body-fitted cylindrical grids were used for all cases and Table 1 shows the number of grid points and distance of the first grid point from the cylinder wall (y^+) for each case. Case 5 shows large y^+ and this case has been re-run with smaller y^+ value to resolve the boundary layer. Note that three different grids (coarse, medium, and fine) for Re = 458,000 and Fr = 1.64 were used for a grid convergence study. The clustered grid points are used near the cylinder wall to resolve the boundary layer and flow separation. Near the interface the grid was also refined to capture the interface deformation. The

computational domain was set up such that the portions of cylinder in the water and air are of length 4D and 2D with D the cylinder diameter, respectively. The distance from the center of the cylinder to the outer boundary is 20D including a buffer zone to damp wave reflections as shown in Fig. 4.1.

4.2.2 Flow conditions, boundary conditions, and initial conditions

The diameter of cylinder, D and the freestream velocity, U_∞ were used for normalization of all variables and the two non-dimensional parameters, Froude number and Reynolds number, are defined as follows:

$$Fr = \frac{U_\infty}{\sqrt{gD}} \tag{4.1}$$

$$\mathrm{Re} = \frac{U_\infty D}{\nu} \tag{4.2}$$

As shown in Table 4.1, different Re and Fr cases were investigated and a constant ratio of Re and Fr of 2.79×10^5 was used, following Chaplin et al. (2003).

As shown in Fig. 4.1 (a), the outer boundary was divided into inflow and outflow boundaries at $\theta = 90°$ and $\theta = 270°$, in which θ is the tangential angle starting from the downstream direction and a uniform inflow and a convective outflow boundary conditions (Breuer, 1998) were used. No-slip boundary conditions were applied on the cylinder wall, while the slip boundary condition was adopted at the bottom and the top of the computational domain as shown in Fig. 4.1 (b). A uniform velocity field as the upstream velocity is prescribed to the entire computational domain at rest. In the present simulation, a constant Courant–Friedrichs–Lewy (CFL) number of 0.3 was used where the magnitude of the time step varied from 1×10^{-2} to 1×10^{-4} D/U_∞ depending on the flow conditions.

4.3 Verification and Validation of Integral Variables

The time histories of the drag coefficient (C_D) and lift coefficient (C_L) with the running mean of C_D and C_L are shown in Fig. 4.2. The drag and lift coefficients are defined as

$$C_D = \frac{Drag}{\frac{1}{2}\rho_L U_\infty^2 DH} \tag{4.3}$$

$$C_L = \frac{Lift}{\frac{1}{2}\rho_L U_\infty^2 DH} \tag{4.4}$$

It should be noted that the still water depth H and the water density ρ_L are used for these coefficients (Kawamura et al., 2002; Yu et al., 2008; Suh et al., 2011).

The statistically stationary state is defined using the convergence of the running mean from the time history of C_D. When the fluctuations of the running mean are smaller than 1% of the mean value, the flow is considered statistically stationary. After the flow reached steady state, 16 vortex shedding cycles, 80 non-dimensional time, were used for statistics as shown Fig. 4.2.

The grid verification study is performed following the methodology and procedures proposed by Stern et al. (2006) and Xing and Stern (2010) with three different grids (coarse, medium, and fine) for Re = 458,000 and Fr = 1.64 using four parameters (total drag coefficient C_D, friction drag coefficient C_{Df}, pressure drag coefficient C_{Dp}, and rms of lift coefficient C_L^{rms}). Verification is a process for assessing the simulation numerical uncertainty U_{SN}, defined as followed, $U^2_{SN} = U^2_I + U^2_T + U^2_G$, where U_I is the iterative uncertainty, U_T is the time-step uncertainty, and U_G is the grid uncertainty. It should be noted that U_T was not considered in the present study due to the use of a constant CFL number, i.e. varied time steps.

Iterative convergence is assessed by examining iterative history of drag forces and the iterative uncertainty U_I is estimated as half the range of the maximum and minimum values as shown below;

$$U_I = \left| \frac{1}{2}(S_U - S_L) \right| \tag{4.5}$$

where S_U is the maximum solution and S_L is the minimum solution. In Table 4.2, U_I/ε_{12} for three different grids are shown and its magnitude is one order smaller than that of the grid error.

For all three grids, the iteration uncertainties are considered to be negligible in comparison to the grid uncertainties. Table 4.3 shows the iterative uncertainties for all the cases and it is less than 1% of the mean value of S, which also implies that the simulations are not contaminated by the iterative errors. $U_I \ll U_G$ so that simulation numerical uncertainty $U_{SN} = \sqrt{(U_I^2 + U_G^2)} \sim U_G$.

In Table 4.2, all the parameters show monotonic convergence using the grid refinement ratio $r_G = 1.41$ and the order of accuracy p_G for C_D, C_{Df}, C_{Dp}, and C_L^{rms} is 1.13, 1.71, 1.14, and 0.67 respectively and the grid uncertainty U_G for C_D, C_{Df}, C_{Dp}, and C_L^{rms} is 1.1%S_1, 0.13%S_1, 1.1% S_1, and 0.79% S_1, respectively.

Validation is a process for assessing the simulation modeling uncertainty by comaparing with experimental data D. The comparison error E is defined as the difference between D and the simulation S. If the absolute value of E is less than the validation uncertainty U_V, given by $U_V^2 = U_D^2 + U_{SN}^2$, where U_D is the uncertainty in the data, the combination of the all the errors in D and S is smaller than U_V and validation is achieved at the U_V level. As presented in Table 4.4, U_V of all the variables is greater than E although U_D is not available, which shows the present simulation has achieved the U_V level of validation.

The drag coefficients with different Re and Fr are shown in Fig. 4.3, comparing with previous studies. The numerical studies (Kawamura et al., 2002; Yu et al., 2008;

Suh et al., 2011) used Re = 27,000 and Fr = 0.8 while the present simulation and experimental measurements by Chaplin et al. (2003) used a constant ratio of Re to Fr of 2.79×10^5. The results from present simulations have good agreement with experimental study (Chaplin et al., 2003) from the subcritical Re ($1000 \sim 2 \times 10^5$) to critical Re. However, there are differences of C_D among the present study and computational studies due to different Re. Kawamura et al. (2002) and Suh et al. (2011) showed higher C_D than the present simulation and this is because their Re is almost 9 times smaller than the current calculation whereas smaller C_D was reported by Yu et al. (2008).

Figure 4.4 shows the Fast Fourier Transform (FFT) of the C_D and C_L for Re = 458,000 and Fr = 1.64. The dominant Strouhal number (St) for C_L is presented while the FFT of C_L shows a large range of frequencies. Figure 4.5 presents St with different Re and Fr. In this figure, 2-D experimental measurements by UTIA (1955) and Roshko (1953) are compared with the current simulations at the deep flow. There are differences between two experiments. It is noted that St may vary by up to ± 10% (Zdravkovich, 1997). The results have good agreement with previous studies and the dominant St of the C_L increases with Re and Fr increase. The dominant St from three different grids for Fr =1.64 are also shown in Fig. 4.5 and the fine grid simulation predicts closest with experiments by Roshko (1953).

Figure 4.6 shows the run-up height and depression depth with different Re and Fr numbers. The run-up height is the maximum bow wave height in front of the cylinder and the depression depth is the largest cavity depth behind the cylinder. Both run-up height and depression depth increase as Fr increases. The run-up heights of the present simulations have good agreement with the Bernoulli's equation ($Fr^2/2$) and the results from the previous studies by Chaplin et al. (2003) and Yu et al. (2008). Figure 4.6 also shows the run-up height from three grids for Re = 458,000 and Fr = 1.64 and the fine grid has the closest to that from the Bernoulli's equation and previous experiments (Chaplin et al., 2003). A ratio between run-up height and depression depth for Fr = 0.84, 1.24, and

1.64 is 1.375, 0.97, and 1.23, respectively. It should be noted that there is no available experimental data to compare with depression depth.

4. 4 Validation of Re = 234,000 and Fr = 0.84, Comparing with Previous Studies

4.4.1 Flow near the Interface

In this section, the flow near the interface is compared with previous studies (Suh et al., 2011; Kawamura et al., 2002; Yu et al., 2008; Inoue et al., 1993). Note that similar flow patterns are expected among the present simulation and the previous work since same Fr was used for all the studies.

Contours of the mean interface elevation and the rms of the interface fluctuations for Re = 234,000 and Fr = 0.84 are shown in Fig. 4.7 and compared with measurements by Inoue et al. (1993) using Re = 27,000 and Fr = 0.80. Overall, the present results of the mean interface elevation are in good agreement with the previous study (Inoue et al., 1993) including the magnitude, location of interface waves, and the expansion angle of Kelvin wave, although lower interface elevations are observed near the rear parts of the cylinder and this might be due to higher Re. The rms of the interface fluctuations from the current simulation also shows a good agreement with the experimental work (Inoue et al., 1993) including the location of the peak fluctuations.

Figure 4.8 presents the mean interface elevation and the rms of the interface fluctuations at two transverse planes for Fr = 0.84, comparing with previous studies (Kawamura et al., 2002; Suh et al., 2011) with Re = 27,000 and Fr = 0.8. The results of the current simulation with larger Re (= 234,000) are in good agreement with previous studies except for the under-prediction of the depression, which is also reported in Suh et al. (2011). And this indicates that Re has little effect to the mean interface elevation behind the cylinder.

Figure 4.9 shows the vertical profiles of the mean streamwise velocity at x = 4.5 and y = 0 for Fr = 0.84. The previous studies from Inoue et al. (1993), Kawamura et al. (2002), and Suh et al. (2011) of Re = 2.7×10^4 and Fr = 0.8 were compared. Note that the fine grid solutions were compared for Suh et al. (2011). The present results for Fr = 0.84 agree with ones from Inoue et al. (1993), Kawamura et al. (2002), and Suh et al. (2011) near the air-water interface and it is clearly shown that the mean streamwise velocity decreases as the interface approaches. However, slightly larger streamwise velocity profile is shown than previous studies in the deep flow due to the higher Re.

4.4.2 Deep Flow

In this section, the flow in the deep water was compared with previous experiments on the single-phase flow past a cylinder at a similar Reynolds numbers as the present Re (=234,000) which is in the subcritical Re regime (Raghavan and Bernitsas, 2010). Figure 4.10 shows the mean streamwise velocity on the centerline at y = 0.0 along with the single-phase experimental measurements (Cantwell and Coles, 1983). Overall the profile of the present simulation has a good agreement with experiement. The recirculation region is shown immediately after the cylinder (x=0.5 to x=1.4) in the present simulation.

Figure 4.11 shows the mean streamwise and transverse velocity in the wake at x=1. For comparison the data of the experiments at Re = 140,000 (Cantwell and Coles, 1983) are also used. They agree fairly well with experimental data; however, larger streamwise velocity is observed and smaller transverse velocity is shown at y=0.5 and y=-0.5 due to higher Re.

Figure 4.12 presents the pressure and friction coefficients, defined as follows;

$$C_p = \frac{\bar{p} - p_\infty}{\frac{1}{2}\rho_L U_\infty^2} \tag{4.6}$$

$$C_f = \frac{\tau_w}{\frac{1}{2}\rho_L U_\infty^2} \tag{4.7}$$

where τ_w is the wall shear stress.

The pressure distributions in the deep flow have good agreement with the experiments of Re = 210,000 by Norberg (1992) up to the cylinder shoulder; however, the present simulation over-predicts the pressure coefficients than the experiment at the rear part of the cylinder. The friction coefficients in the deep flow are compared with the single-phase experimental studies of Re = 210,000 (Fage and Falkner, 1931; Achenbach, 1968). The present results have good agreement with those from the experiments. The separation point where C_f becomes negative value occurs at about 0.5π which is similar to that of Fage and Falkner (1931) and Achenbach (1968). There is a jump at about 0.6 π in Fage and Falkner (1931) due to the beginning of the separation bubble while Achenbach (1968) measured a pronounced laminar separation. This fact seems to be due to the turbulence level (Achenbach, 1968).

4.5 Results

4.5.1 Reynolds number effect with Fr = 0.84

Three different Reynolds numbers from sub-crtical to critical (27,000, 234,000, and 458,000) with Fr = 0.84 are used to investigate Reynolds number effect on flow structures near the interface.

4.5.1.1 Mean separation pattern

The separation pattern of the mean flow with vortex core lines is shown in Fig. 4.13, obtained from the approach discussed in Kandasamy et al. (2009) and Sujudi and

Haimes (2005). The separated shear layer was visualized approximately using the iso-surfaces of the stagnation C_p near the interface immediately before separation, assuming that the flow outside the separation is inviscid. Inside the separated region, the mean vortex core lines are extracted using the vortex core identification technique. The separated region at the interface decreases as Re increases from sub-critical to critical since the separation point is delayed, which is also shown in single-phase flow past a circular cylinder (Achenbach, 1968). Immediately below the interface, the separation region is reduced for all Re and "neck" shape is observed. The thickness of the neck is remarkably smaller with the critical Re at about z=-1 and it recovers 80% of that of the interface at the deep flow while its size has almost 90% of that of the interface. At Re=458,000, it is interesting that the separated region is detached from the cylinder wall in deep water probably due to the separation bubble. Three different types of vortices (V1, V2, and V3) were defined in Suh et al. (2011) as the mean vertical vortices, the mean streamwise vortices, and the V-shaped mean vortices and these vortices are observed in all Re. The vertical vortices (V1) are generated from the vortex shedding behind the cylinder and these vortices are inclined and connected to the cylinder wall as the interface is approached. The other two vortices (V2, V3) are observed inside the separation region near the interface as discussed in Suh et al. (2011).

4.5.1.2 Vorticity

It is well known that for low Re the regular Karman vortex street and very organized wake patterns are observed whereas the separated shear layer becomes unstable and smaller vortices are generated at higher Re. Instantaneous vertical vorticity contours with streamlines for different Re at various depths are shown in Fig. 4.14. Near the interface at z=-0.5 the attenuated vortex shedding. i.e. no organized periodic vortex is observed for all Re regimes due to the streamwise vorticity generated near the separated region. However, the separation point is much delayed with an increase in Re. Suh et al.

(2011) also showed that the delayed separation occurs near the interface. At z=-1 where the "neck" shape is formed, the narrowing of the wake is observed for the critical Re (234,000, 458,000). In addition, the separation point moves downstream as with Re increase. The narrow wake region becomes wider at the z=-2 which is correlated to the recovery of the separation region as shown in the mean separation patterns.

Figure 4.15 shows the mean streamwise vorticity contours for various Re at three different depths. Near the interface small vortices are dominant instead of the organized vortices and more small vortical structures are observed as Re increases. In addition, the width of wake is significantly large for all Re. The maximum streamwise vortices are observed in the edge of the separation region. As discussed in Suh et al. (2011), three pairs of counter-rotating vortices are observed at z=-1 for Re=27,000 while only two pairs of counter-rotating vortices are shown with much reduced wake region for critical Re due to the delayed separation point and smaller recirculation region. The increased wake region and strong transverse velocity near the interface are generated from these vorticity pairs (Suh et al., 2011). Relatively smaller vortices are shown at z=-2 for all Re.

The contours of the mean transverse vorticity are presented in Fig. 4.16. The mean transverse vorticity is significantly large as the interface approaches. High vorticity magnitudes are observed in the place where the separated region is located and it is related to high interface fluctuations inside separation region. At z=-1 two positive vortices are detached from the cylinder wall and negative vortices are observed near the cylinder for Re=27,000 while a pair of the symmetric positive vortices forms from the cylinder surrounding the negative vortices for critical Re, which is the recirculation region. Since the transverse vorticity is responsible for the interface fluctuations, much smaller values are observed at z=-2.

Figure 4.17 shows the mean vertical vorticity contours. The vertical vorticity is inclined outward in transverse direction from the interface to z=-1 as shown Fig. 4.17. Similar patterns are observed for critical Re with steeper inclined angle. It is also shown

that in deep flow the vertical vorticity is created by Karman vortex shedding and the unstable shear-layers behind the cylinder.

4.5.1.3 Reynolds stresses

The streamwise Reynolds stress ($\overline{u'u'}$) is shown in Fig. 4.18. Sub-critical Re (27,000) shows much higher magnitude of $\overline{u'u'}$ than critical Re (234,000, 458,000) at all three depths. It is also shown in Singh and Mittal (2005) that sub-critical Re has larger $\overline{u'u'}$ than critical and super-critical Re. The peak $\overline{u'u'}$ values are concentrated on the separated region where very high mean velocity gradients are observed. They are inclined into transverse direction from the interface to about z=-1 as shown Fig. 4.22 for sub-critical Re and critical Re, respectively. The size of wake decreases with Re increase at z=-1 due to the delayed separation point and it gets recovery at z=-2, which is also shown in the mean separation pattern.

Figure 4.19 presents the mean transverse Reynolds stress ($\overline{v'v'}$). Near the interface high values of $\overline{v'v'}$ are observed at near separation point and its magnitude shows stronger as Re increases. It is shown that from z=-1 to deep flow $\overline{v'v'}$ achieves a peak along the center axis while the peaks in other Reynolds stresses are located off the flow axis. At z=-1 the peak moves toward into the cylinder as Re increases. However, the peak moves downstream with increase in Re at z=-2. Increased magnitude is observed close to the cylinder especially in the region of separated shear layer as Re increases, indicating an increased unsteady activity in that region of the flow, particularly for critical Re.

The vertical Reynolds stress ($\overline{w'w'}$) is shown in Fig. 4.20. Three peaks in $\overline{w'w'}$ are observed from the interface to the deep flow as shown in Fig. 4.22. The maximum magnitudes are observed near the interface for all Re due to the fluctuations of the interface which matches with the first peak from sub-critical Re and critical Re (Fig. 4.22). The second one is at around z=-1 and this is also seen in Fig. 4.20 with smaller

wake region as Re increases into the critical regime. The features of $\overline{w'w'}$ near the interface are similar with that of $\overline{u'u'}$.

The mean Reynolds shear stress ($\overline{u'v'}$) is shown in Fig. 4.21. It is shown that the interface reduces the shear stress remarkably in the wake region (Yu et al., 2008; Suh et al., 2011). For critical Re, much smaller wake region is observed at z=-1 and it recovers at z=-2.

4.5.1.4 Vorticity transport

Suh et al. (2011) studied the mechanism of the vorticity generation at sub-critical Re (27,000) using the Reynolds-averaged vorticity transport equations which can be obtained by taking curl of the time-averaged Navier-Stokes equation (eqn. 4.8). It is noted that the effect of the air-water interface including the density discontinuity across the interface was neglected.

$$\underbrace{\left(U\frac{\partial\Omega_x}{\partial x}+V\frac{\partial\Omega_x}{\partial y}+W\frac{\partial\Omega_x}{\partial z}\right)}_{(A)}=\underbrace{\left(\Omega_x\frac{\partial U}{\partial x}+\Omega_y\frac{\partial U}{\partial y}+\Omega_z\frac{\partial U}{\partial z}\right)}_{(B)}+\underbrace{\nu\left(\frac{\partial^2\Omega_x}{\partial x^2}+\frac{\partial^2\Omega_x}{\partial y^2}+\frac{\partial^2\Omega_x}{\partial z^2}\right)}_{(C)}+\underbrace{\frac{\partial}{\partial x}\left(\frac{\partial\overline{u'v'}}{\partial z}-\frac{\partial\overline{u'w'}}{\partial y}\right)}_{(D)}+\underbrace{\frac{\partial}{\partial y\partial z}\left(\overline{v'v'}-\overline{w'w'}\right)}_{(E)}+\underbrace{\left(\frac{\partial^2}{\partial z^2}-\frac{\partial^2}{\partial y^2}\right)\overline{v'w'}}_{(F)} \tag{4.8}$$

where Ω_x, Ω_y, and Ω_z are the streamwise, transverse, and vertical components of the mean vorticity, respectively. Details of each term can be found in Suh et al. (2011).

Dominant source terms for the mean vorticity for Re=27,000, Re=234,000, and Re=458,000 are shown in Fig. 4.23, Fig. 4.24 and Fig. 4.25, respectively. In the streamwise vorticity equation, the dominant terms are y and z components of term B and term E. The y and z components of term B create the vortex bending whose have a similar magnitude but with opposite signs so they have little effect. The remaining E

term, anisotropy term between transverse and vertical Reynolds stress, is mainly responsible for the generation of the mean streamwise vorticity near the interface. This behavior is observed in all Re from sub-critical to critical Re regime.

In the transverse vorticity equation, the dominant terms are z component of term B, E term, and F term. Due to the vortex shedding and shear layer instability, the bending of the vertical vorticity is generated which is the z component of term B.

In deep water, the term F is a dominant for the vertical vorticity equations.The z component of the term B is the vortex stretching of the vertical vorticity. The anisotropy term between the streamwise and transverse Reynolds stresses is responsible for the term E.

4.5.2 Overall Froude Number Effect with Different Re

As mentioned previously, there is relatively small influence of Reynolds number at the air-water interface. The instantaneous air-water interface elevations for all different Fr with different Re are shown in Fig. 4.26. For the lowest Fr (= 0.2), it is hard to see the bow wave in front of the cylinder and small interface deformation is observed in the wake region. For smaller Fr (= 0.44, 0.84), relatively smaller bow wave are observed in front of the cylinder with Kelvin waves behind the cylinder. There are some free-surface roughness and turbulence in the wake region behind the cylinder. For Fr = 1.24, much increased bow wave is observed and it breaks and wraps around the bow. A lot of splashes and bubbles are intense immediately behind the cylinder. The Kelvin waves are less visible just behind the cylinder due to stronger free-surface oscillations and turbulence. For Fr = 1.64, the bow wave increases remarkably with the largest wake region among four Fr and it also breaks with similar patterns of plunging breakers. Much more small air-water interface structures including splashes and bubbles are observed behind the cylinder. It is also hard to distinguish the Kelvin waves behind the cylinder due to much larger free-surface oscillations and turbulence.

The mean air-water interface elevations (top) are presented in Fig. 4.27. The time-averaged free surface shows the bow wave in front of the cylinder, depression region or cavity region behind the cylinder, and the diverging Kevin wave. It is also confirmed that the height of the bow wave and the depression depth increases as Fr increases. Except for Fr = 0.2, the diverging Kelvin wave is evident but it is not shown for high Fr (1.24, 1.64) since it is in the far downstream. More details of the diverging Kelvin wave will be discussed later. Figure 4.27 also shows the rms of the interface fluctuations (bottom) for different Fr and Re. The fluctuation of the interface starts near the end of the slope from the crest to the surface cavity for low Fr (0.2-0.84), while it is observed from the cylinder front to the depression region for high Fr (1.24, 1.64). For low Fr (0.2-0.84), the peak value is observed near the edge of the bottom of the depression region, whereas it is shown in further downstream and detached from the cylinder wall for high Fr (1.24, 1.64). In addition, small structures of the interface fluctuation are observed for high Fr due to high Re.

4.5.3 Froude Number Effect on Flow Structures with Re = 458,000

Three different Froude numbers (0.84, 1.24, and 1.64) with Re = 458,000 are investigated to have better understanding of how the free-surface affects on the flow structures in the near wake at different Froude numbers. Different Reynolds numbers with above Fr are also compared to examine the Reynolds number dependency. The fine grid solutions will be used for Fr = 1.64 with Re = 458,000 in this study unless otherwise mentioned.

4.5.3.1 Air-water interface structures at different Fr

The mean air-water interface elevation contours for all three Fr in Fig. 4.28 shows diverging and transverse wave patterns. The diverging waves are more dominant than the transverse waves with wave lengths that roughly correspond to the theoretical transverse

wave length in a Kelvin wave pattern, i.e. $\lambda_t = 2\pi Fr^2$. The diverging wave lengths for all three Fr match well with theoretical values as shown in Fig. 4.29 (a). In addition, different Reynolds numbers other than Re = 458,000 at Fr = 0.84 and Fr = 1.24 are compared and they show almost similar wave length with ones of Re = 458,000 and this indicates that the free-surface flow is independent with Re.

The diverging angles for all three Fr are also shown in Fig. 4.28 and they are all larger than that of the Kelvin wave value (19˚) which is typically observed in ship flows. It decreases linearly with Fr as shown in Fig. 4.29 (b), which implies that a body becomes more slender as Fr increases due to a cavity region immediately behind the cylinder. Bhushan et al. (2010) studied the flow around the air-cushion vehicle (ACV) numerically with different Froude numbers and they showed similar Froude number effects that the diverging wave angle of the ACV decreases almost linearly up to Fr = 1.0 and is almost constant thereafter which is within 10% of the Kelvin waves. The flow patterns at high Fr show similar flow features with a slender body whereas the body acts like a blunt object at low Fr. In Fig. 4.29 (b), different Reynolds numbers than Re = 458,000 are also added to investigate Re dependency on the free-surface flow and there is no dependency of Re on the diverging wave angle.

Figure 4.30 presents the close-up view of the mean air-water interface elevation contours with iso-surface near the cylinder. Contour levels for high Fr (1.64) is 2 and about 5 times greater than those for medium (1.24) and low Fr (0.84), respectively. For Fr = 0.84, the Kelvin waves propagate with a wide angle and relatively small depression depth behind the cylinder. For Fr = 1.24, the depression region immediately behind the cylinder is narrow and deep, which makes the cylinder act like a slender body and this causes smaller diverging angle than that of low Fr. For Fr = 1.64, much larger depression depth is observed and it is even narrower and longer than that of both low and medium Fr, implying that the flow past the cylinder at Fr =1.64 shows features with more slender body.

Figure 4.31 shows the mean wave profiles at different streamwise locations for three Fr. There is a small and wide depression region behind the cylinder and its recovery is fast for Fr = 0.84. In contrast, it is clearly seen that there is a deep and narrow cavity behind the cylinder for Fr = 1.24 and Fr = 1.64 which is also shown in Fig. 4.30 (b) and (c). The mean wave profile for Fr = 1.24 recovers faster than that for Fr = 1.64, as shown in Fig. 4.31 (d), (e), and (f). A small bump is shown on the centerline y = 0.0 at x = 1.0 for both Fr = 1.24 and Fr = 1.64 and it grows in the streamwise direction up to x = 3.0 and then it starts spreading out to the transverse direction with reduced wave elevation.

4.5.3.2 Vorticity and velocity at the interface

Three-dimensional instantaneous coherent vortical structures identified by the second invariant of the velocity gradient tensor (Hunt et al., 1998) for three Fr are shown in Fig. 4.32. At a Fr of 0.84, the organized shed vortex tubes are present in the deep flow and they are attenuated as the air-water interface approaches. This is consistent with previous work (Suh et al., 2011; Yu et al., 2008). Due to the interface deformations, smaller scale of vortical structures are observed at the air-water interface for all three Fr. At medium and high Fr (1.24, 1.64) small vortical structures near the air-water interface are disappeared due to the cavity region behind the cylinder and there are only large structures in the deep flow.

Figure 4.33 presents contours of the mean vertical vorticity magnitude at different depths for three Fr. At the air-water interface, the shear layer stretches out with a smaller angle and smaller vertical vortices are observed behind the cylinder as Fr increases. The shear layer is separated from the cylinder wall for Fr = 0.84 at z = -0.5, whereas the separation point is not from the cylinder wall for medium and high Fr (1.24, 1.64) at z = -0.5. It is clearly shown that a cavity behind the cylinder for high Fr makes the cylinder a slender body such that the separation of the shear layer occurs away from the cylinder

wall. There is no significant difference in the shear layer pattern and regular vortex streets are observed in the deep flow (z = -3.5) for all the Fr cases.

Contours of the mean streamwise velocity with the streamlines are shown in Fig. 4. 34. No remarkable difference in the streamline pattern is observed in the deep flow for all the Fr cases. For low Fr, the recirculation length at the air-water interface is approximately two times of the cylinder diameter while it has much reduced length for high Fr and it has similar size of the cavity behind the cylinder. For both medium and high Fr, count-rotating vortices are shown immediately behind the cylinder at the interface which is also observed in the deep flow. The streamline patterns for high Fr also confirm that the depression region behind the cylinder acts as a cavity resulting in flow around a slender body.

4.5.3.3 Wave breaking at different Fr

Figure 4.35 shows the iso-surface of the air-water interface with the slices of the wave profile cut orthogonal to the cylinder wall for three Fr. For Fr = 0.84, small disturbances are shown on the interface; however, no breaking waves are observed. For medium and high Fr (1.24, 1.64), the flow becomes unsteady such that small interface structures including splashes and air bubbles are present especially for Fr =1.64 which is also shown in Chaplin et al. (2003). The waves arise and break down to the cylinder shoulder as shown Fig. 4.35 (b) and (c), which corresponds to a spilling breaker and a plunging breaker, respectively according to the analysis of Galvin (1968). Similar wave breaking patterns are observed in experimental study of the divergent ship bow waves using eight different Froude numbers by Shakeri et al. (2009) and they showed that for Fr < 1.0 non-breaking waves were generated; spilling breaking waves occurred at between Fr = 1.0 and Fr = 1.3; and plunging breakers were generated at 1.4 < Fr < 1.8.

The slices of the wave profile cut for Fr = 1.24 at different circumferential planes, which are presented by the tangential angle θ starting from the downstream direction, are

given in Fig. 4.36 and it demonstrates the spilling wave breaking. In this figure, the flow direction is into the paper which is perpendicular to the cylinder. A small jet grows and starts overturning as shown in Fig. 4.36 (a). It falls into the undisturbed water surface and then a small air entrainment is shown in Fig. 4.36 (b) and (c), respectively. The repeated spilling breaking events including overturning and entrapping air are presented in Fig. 4.36 (d) – (f).

The plunging wave breaking is described in Fig. 4.37 using the slices of the wave profile cut for Fr =1.64. The wave propagates from the center of cylinder to the cylinder shoulder as shown in Fig. 4.35 (c). When the wave crest grows and starts overturning (Fig. 4.37 (a) and (b)), a jet is stretched and breaks up into droplets before it plunges on the undisturbed water surface (Fig. 4.37 (c) and (d)). After the jet touches the water surface, an oblique splash is created (Fig. 4.37 (e)). These plunging wave breaking events are very similar to those observed in the previous plunging wave breaking literatures (Bonmarin, 1989; Peregrine, 1983; Tallent et al., 1990). However, the direction of the plunging wave breaking is different from the mean flow, which is similar to the numerical simulation of the plunging wave breaking over a submerged bump (Koo et al., 2011) and the numerical study of wave breaking around a wedge-shaped bow (Wang et al. 2010). It should be mentioned that the wave plunges forward in the same direction of the mean flow for most previous studies on plunging wave breaking. The shape of the plunging jet is an ellipse with aspect ratio 1.8 which is close to the findings from most previous studies ($\sqrt{3}$). The thickness of the jet is approximately 0.012 and the similar jet thickness is reported in the experimental studies (Bonmarin, 1989; Grue and Jensen, 2006; Kimmoun and Branger, 2007). The jet angle relative to the undisturbed water surface is about 67˚ which is larger than that from previous experimental and computational studies on the plunging wave breaking.

The velocity vectors of the plunging jet are given in Fig. 4.38 with the colored vectors by the vertical velocity component. Strong air flows are induced by the

overturning motion of the jet as shown in Fig. 4.38 (a) and (b), resulting in a pair of vortices immediately before the overturning jet. After the jet touches the free-surface, a strong vortex is created as a result of the entrained air and small vortices are also produced due to splashes as shown in Fig. 4.38 (c).

4.6 Conclusions

Flow past a surface-piercing circular cylinder at different Reynolds and Froude numbers is studied numerically using large-eddy simulation with a Lagrangian dynamic subgrid-scale model. Verification and validation studies are performed to show the accuracy of the simulation in this work and available experimental data are compared with the present results.

The flow features near the air-water interface show significant changes with different Reynolds numbers from sub-critical to critical regime at Fr = 0.84. The present simulations show that the interface makes the separation point more delayed for all regime of Re. Remarkably reduced separated region below the interface at z=-1 is observed for critical Re regime and it is responsible for much reduced wake and recirculation region behind the cylinder and it recovers in the deep flow.

The present study shows that the air-water interface structures are remarkably changed with different Froude numbers. For sub-critical Fr, relatively smaller bow waves are observed in front of the cylinder with Kelvin waves behind the cylinder and small amount of free-surface roughness and turbulence are also seen in the wake region. For Fr = 1.24, much increased bow wave is observed and it breaks and wraps around the bow. A lot of splashes and bubbles are presented immediately behind the cylinder. Stronger free-surface oscillations and turbulence makes Kelvin waves less visible. For Fr = 1.64, the bow wave increases remarkably with the largest wake region and deepest depression and it also breaks with similar features of plunging breakers which are also shown in previous plunging wave breaking literatures. Much more small air-water interface structures

including splashes and bubbles are observed behind the cylinder. It is also hard to distinguish the Kelvin waves behind the cylinder due to much larger free-surface oscillations and turbulence. As Fr increases, the Kelvin wave angle decreases and deeper and narrower depression region behind the cylinder are observed. This cavity region behind the cylinder makes the cylinder more slender body so that the flow features are significantly different that around the cylinder.

Table 4.1 Simulation conditions

Case	Grid ($N_r \times N_\theta \times N_z$)	Re	Fr	y^+
1	4.2M, 256×128×128	55,800	0.2	0.96
2	4.2M, 256×128×128	123,000	0.44	0.96
3	4.2M, 256×128×128	27,000	0.84	0.96
4	4.2M, 256×128×128	234,000		0.96
5	4.7M, 272×136×128	346,000	1.24	20
6	2.3M, 192×96×128 (C)	458,000	1.64	1.38
7	4.7M, 272×136×128 (M)			0.96
8	9.4M, 384×192×128 (F)			0.54
9	4.2M, 256×128×128		0.84	0.96
10	4.2M, 256×128×128		1.24	0.96

Table 4.2 Verification study with Re/Fr=458,000/1.64

Parameter	ε_{21}	ε_{32}	R_G	P_G	U_G %S_1	U_I/ε_{12}		
						C	M	F
C_D	0.01	0.07	0.14	1.13	0.476	0.034	0.031	0.029
$C_{D,f}$	-0.0001	-0.0019	0.05	1.71	0.13	0.028	0.026	0.025
$C_{D,p}$	0.01	0.04	0.24	0.79	1.1	0.034	0.032	0.029
C_L^{rms}	-0.004	-0.015	0.26	0.67	0.79	0.021	0.024	0.022

Table 4.3 Iterative uncertainty using drag coefficient (C_D)

Re_D	27,000	55,800	123,000	234,000	346,000	458,000		
Fr_D	0.0	0.2	0.44	0.84	1.24	1.64		
						C	M	F
U_I %S	0.06	0.02	0.05	0.03	0.05	0.058	0.06	0.057

Table 4.4 Validation study with Re/Fr=458,000/1.64

	C_D	S_t	Run-up height
E	0.005	0.001	0.02
U_{SN}	0.0074	0.005	0.03

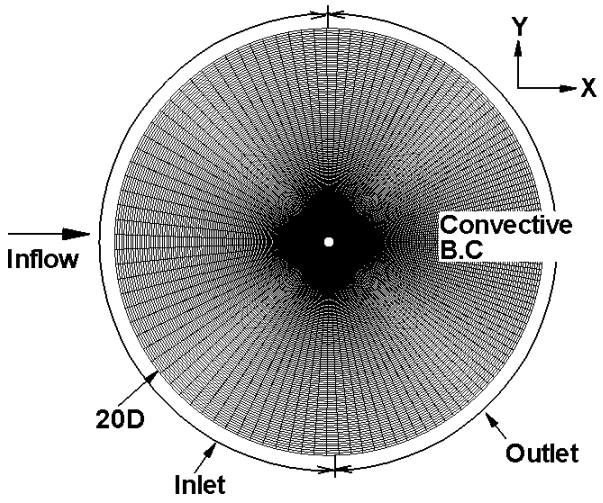

(a)

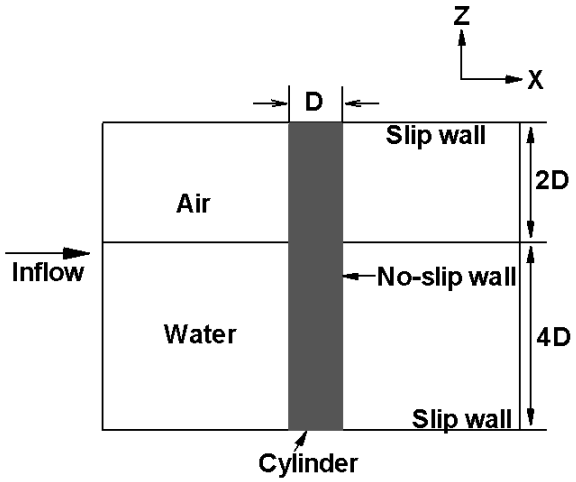

(b)

Figure 4.1 Computational domain with grid and boundary conditions: (a) plan view; (b) side view

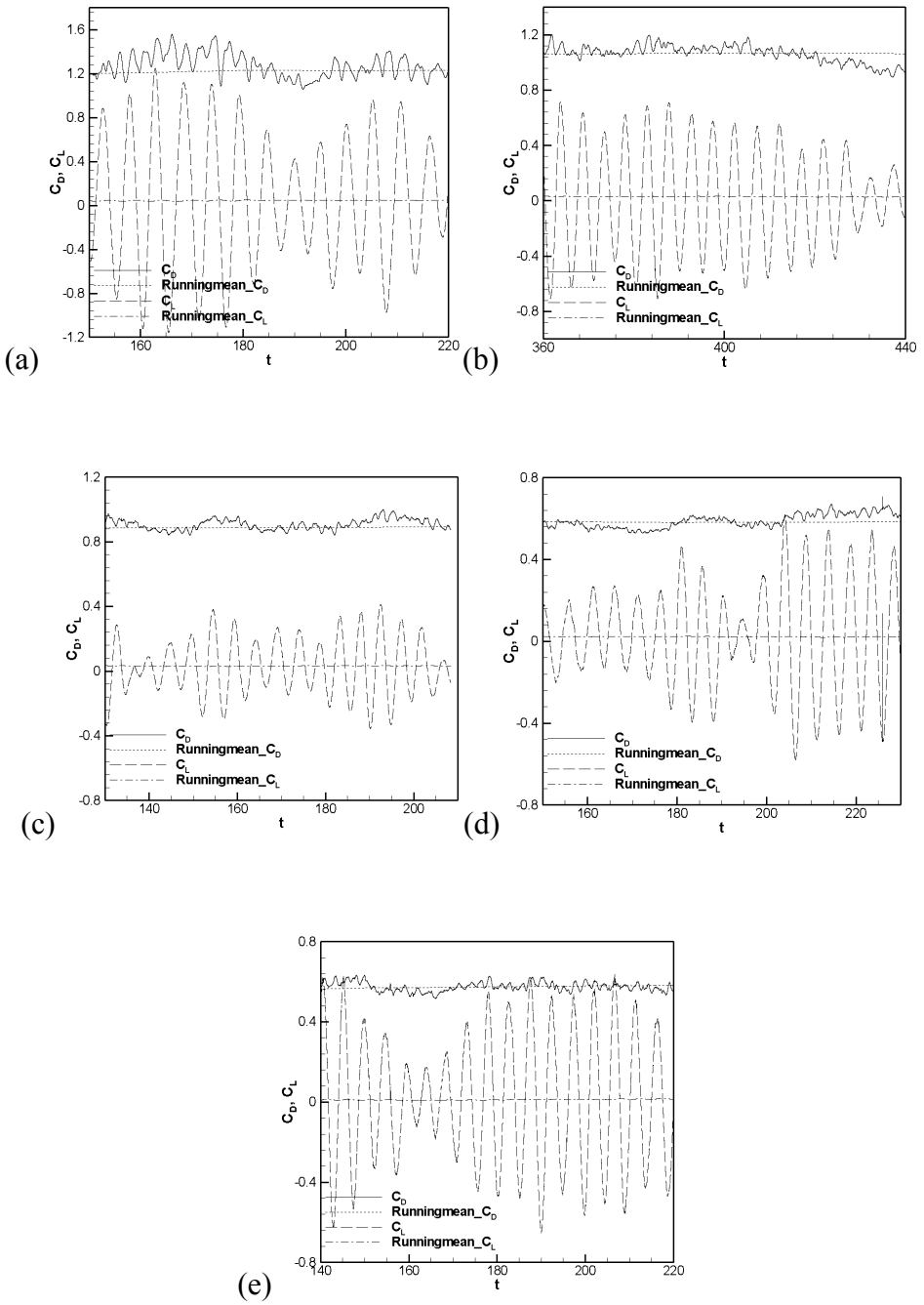

Figure 4.2 Time history and running mean for drag coefficient and time history for lift coefficient. (a) Fr = 0.2; (b) Fr = 0.44; (c) Fr = 0.84; (d) Fr =1.24; (e) Fr = 1.64

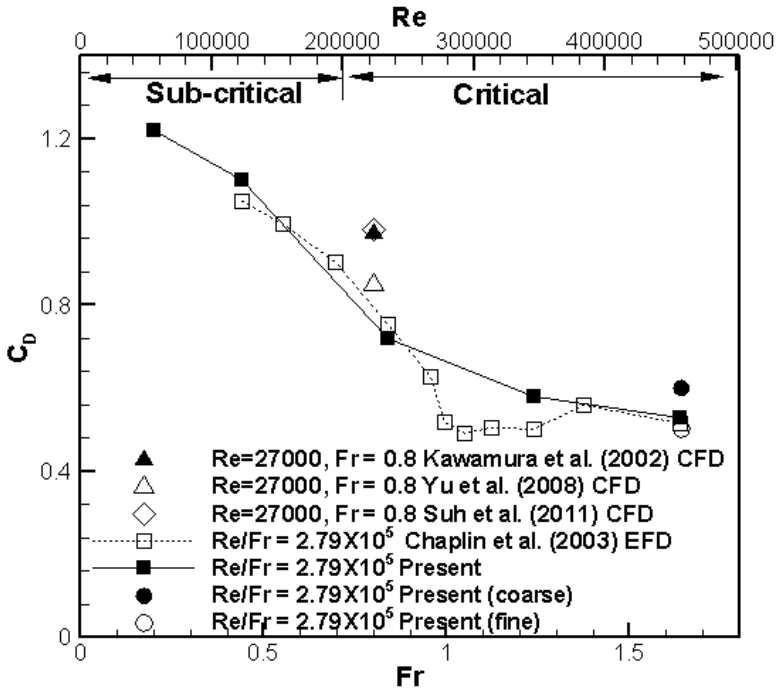

Figure 4.3 Drag coefficient (C_D) vs. Fr and Re

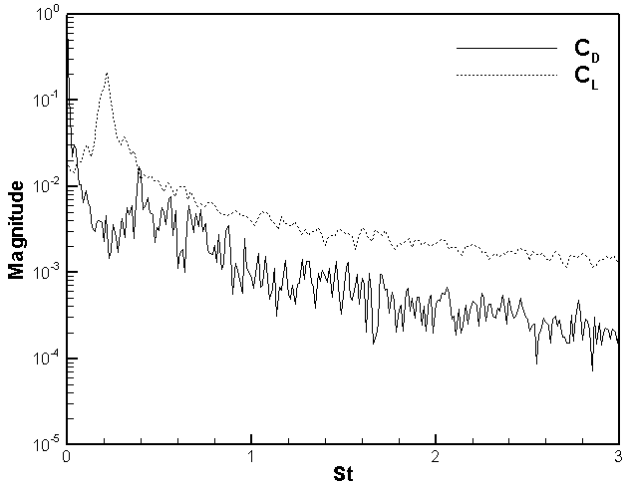

Figure 4.4 FFT of the drag and lift coefficients for Re = 458,000 and Fr = 1.64 with fine grid

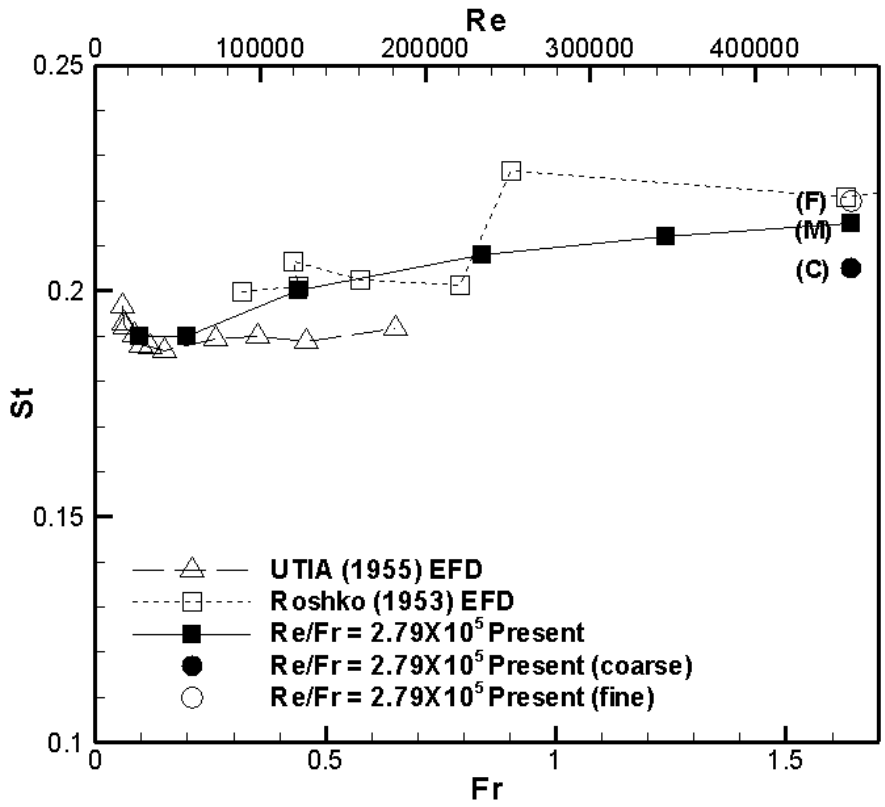

Figure 4.5 Strouhal number with different Re and Fr. Note UTIA (1955) and Roshko (1953): 2D EFD, and present simulations: deep flow

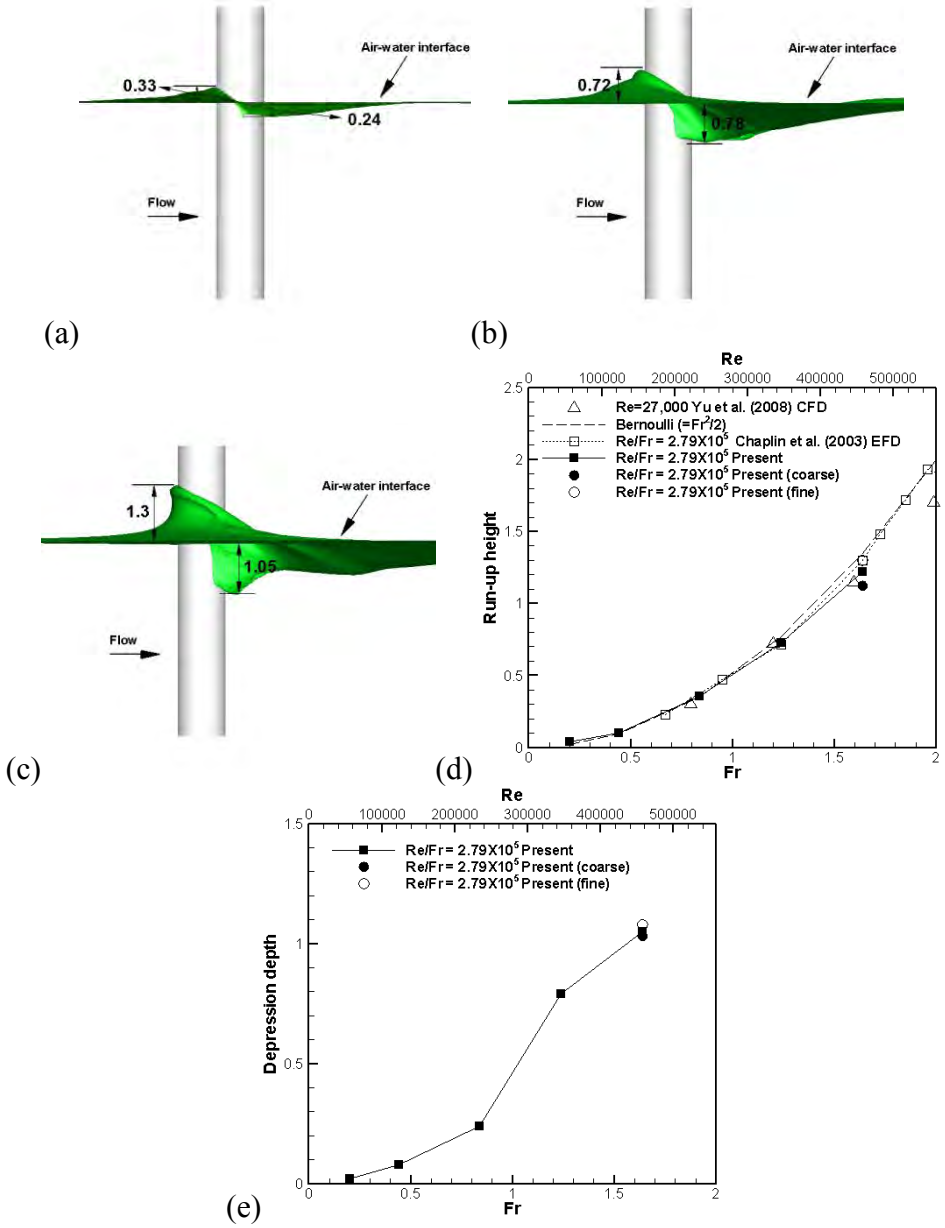

Figure 4.6 Run-up height and depression depth with various Re and Fr: (a) Fr = 0.84; (b) Fr = 1.24; (c) Fr = 1.64; (d) run-up height comparison with other studies; (e) depression depth

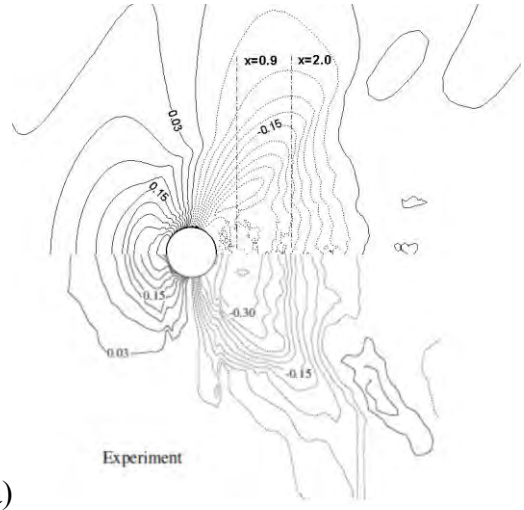

(a)

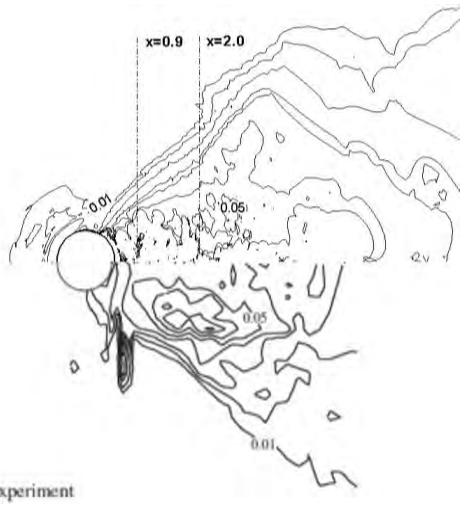

(b)

Figure 4.7 Comparisons of interface strucutres: (a) Mean interface elevation and (b) the rms of the interface fluctuations for Re = 234,000 and Fr = 0.84. Bottom: measurement by Inoue et al. (1993), Re = 27,000, Fr = 0.8

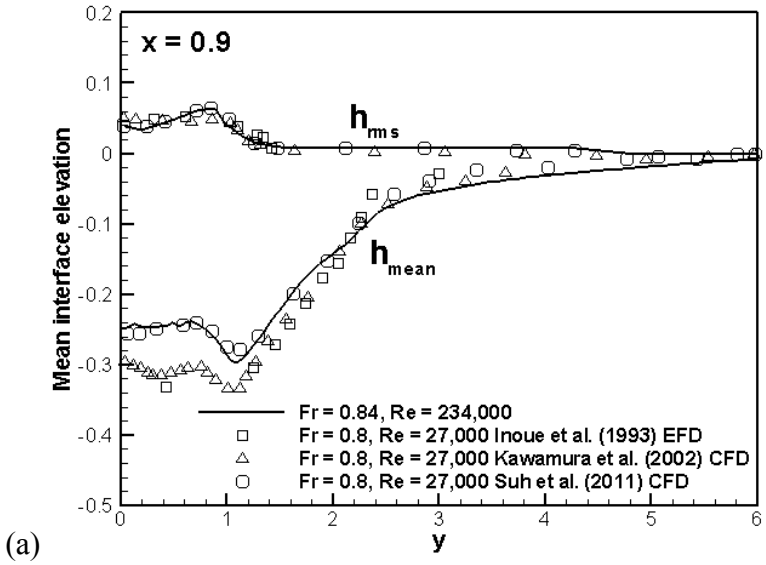

(a)

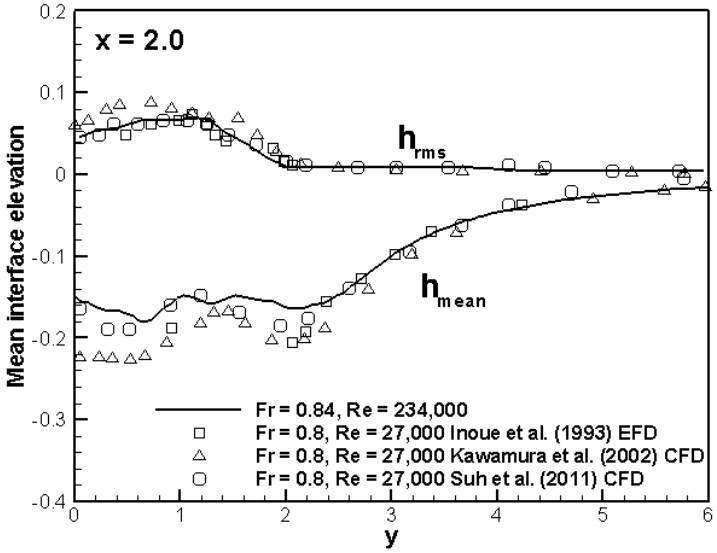

(b)

Figure 4.8 Profiles of mean interface elevation at x = 0.9 and x = 2.0

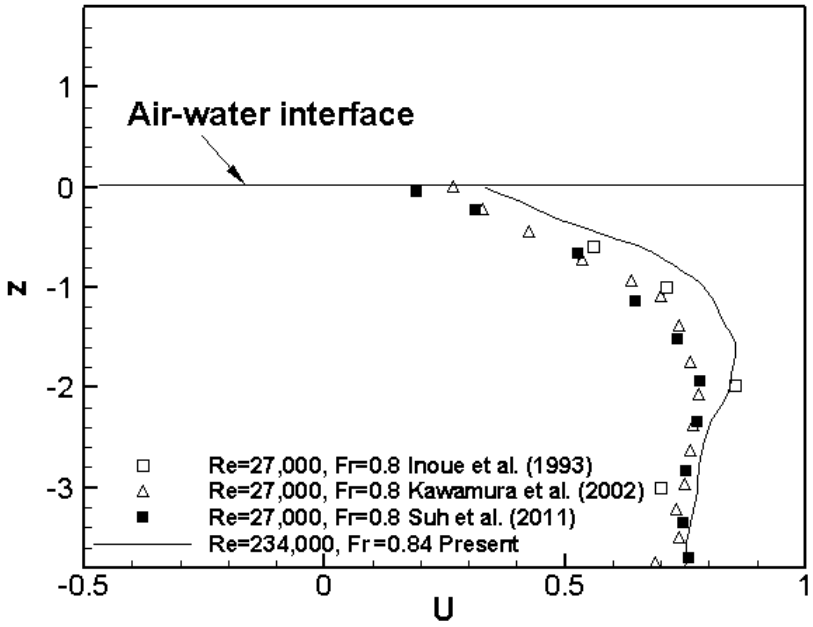

Figure 4.9 The vertical profiles of the mean streamwise velocity at x = 4.5, y = 0.0 for Re = 234,000 and Fr = 0.84

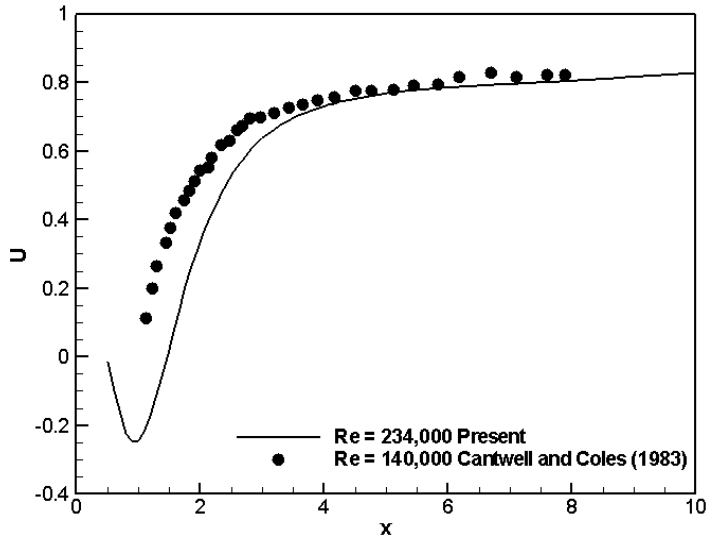

Figure 4.10 Mean streamwise velocity on the centerline y=0.0 (deep flow)

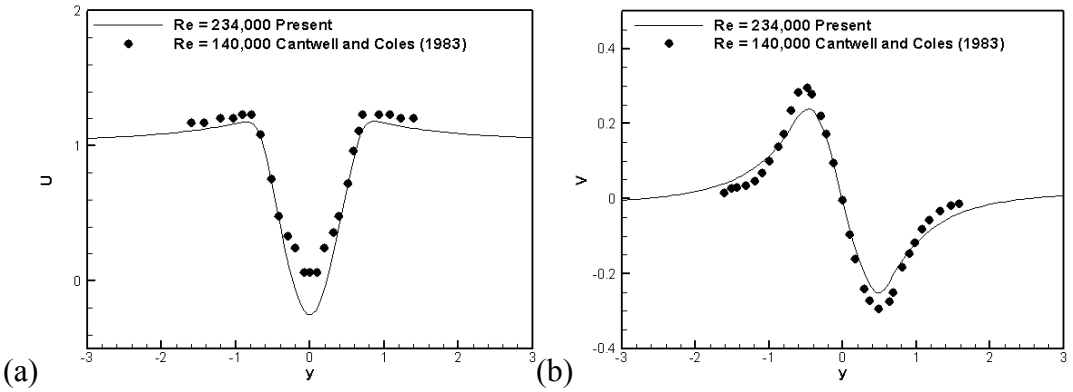

Figure 4.11 Mean streamwise and transverse velocity at x=1 (deep flow): (a) streamwise velocity; (b) transverse velocity

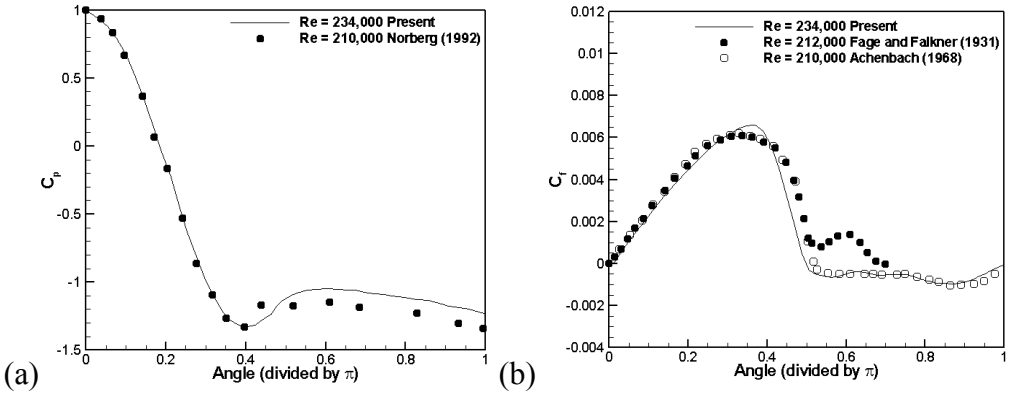

Figure 4.12 Force coefficients on the cylinder surface (deep flow): (a) pressure coefficient; (b) friction coefficient

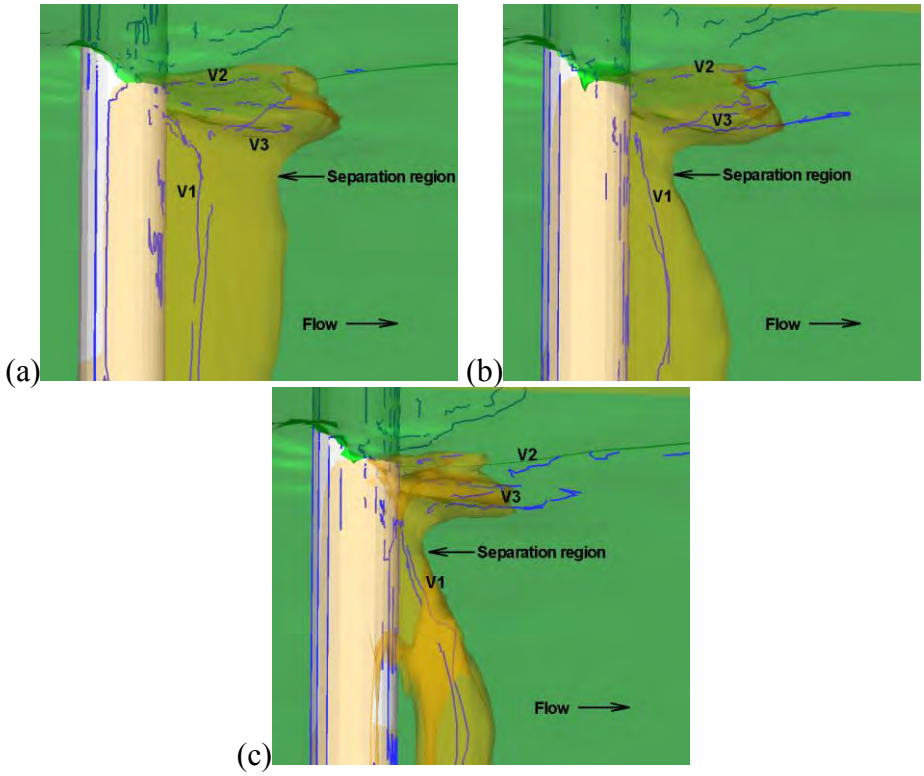

Figure 4.13 Mean separation pattern with vortex core lines: (a) Re = 27,000; (b) Re = 234,000; (c) Re = 458,000

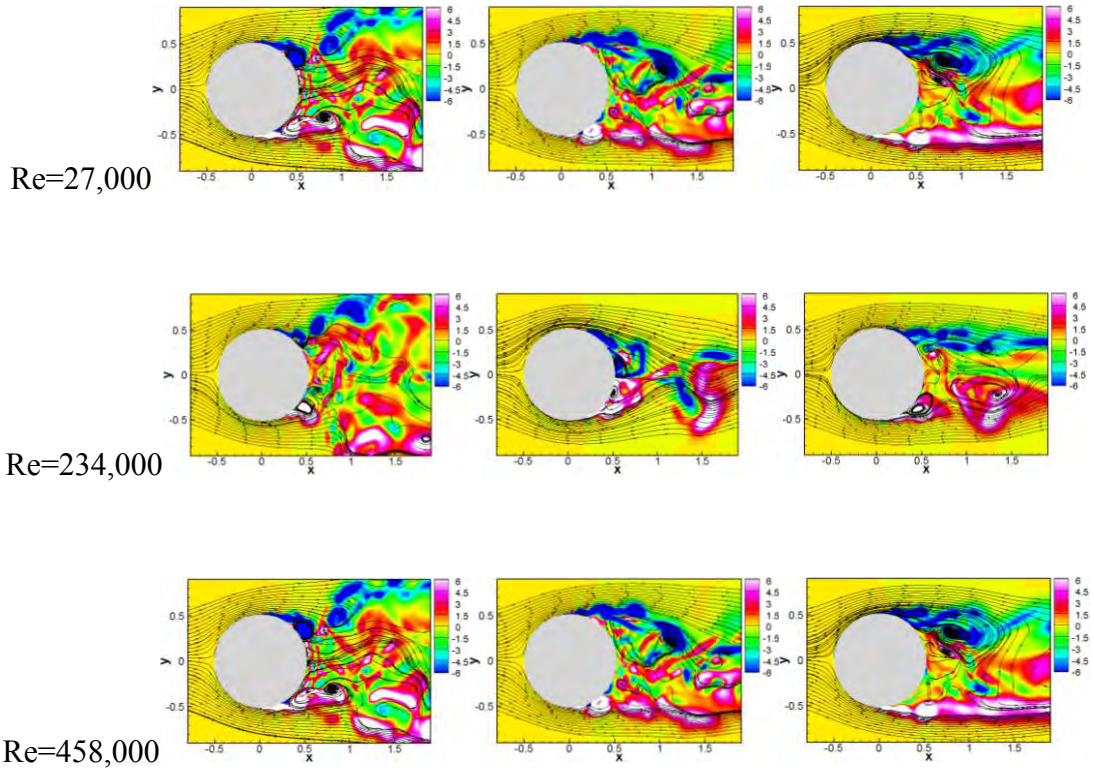

Figure 4.14 Instantaneous vertical vorticity contours with streamlines

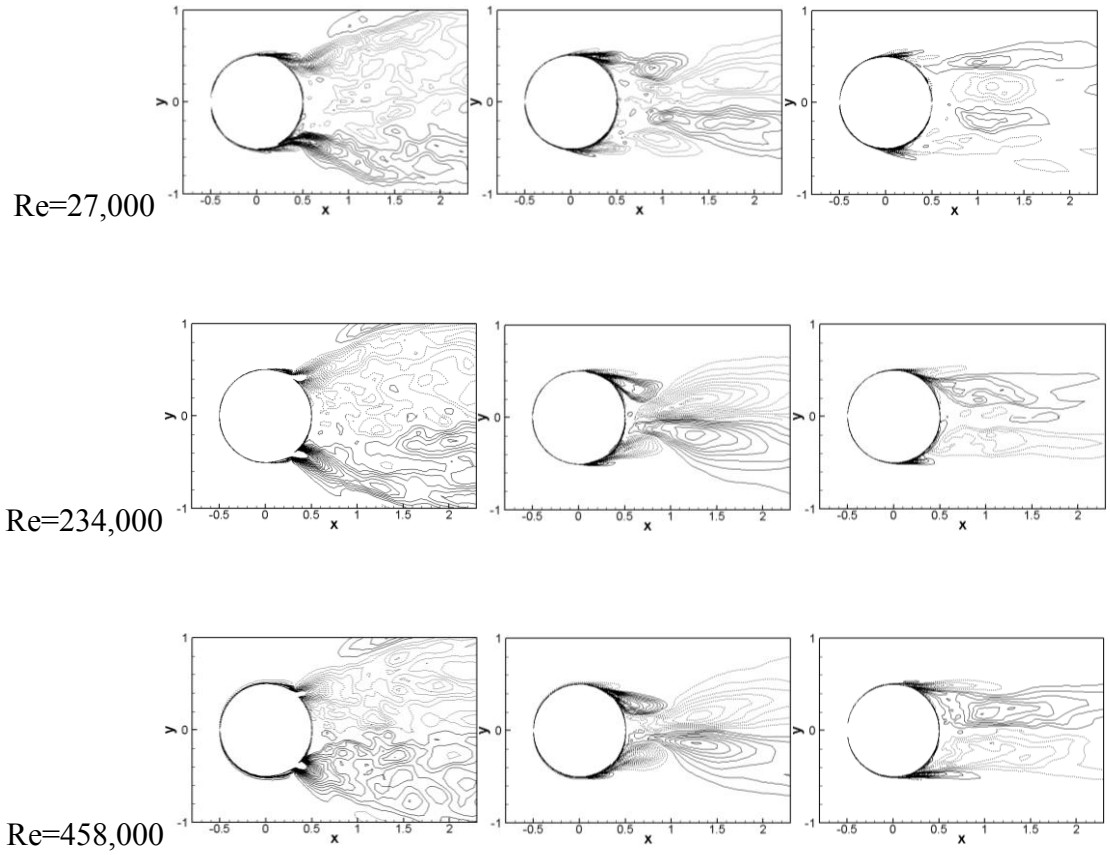

Figure 4.15 Mean streamwise vorticity contours. Contour levels: -5 to 5 with interval 0.25

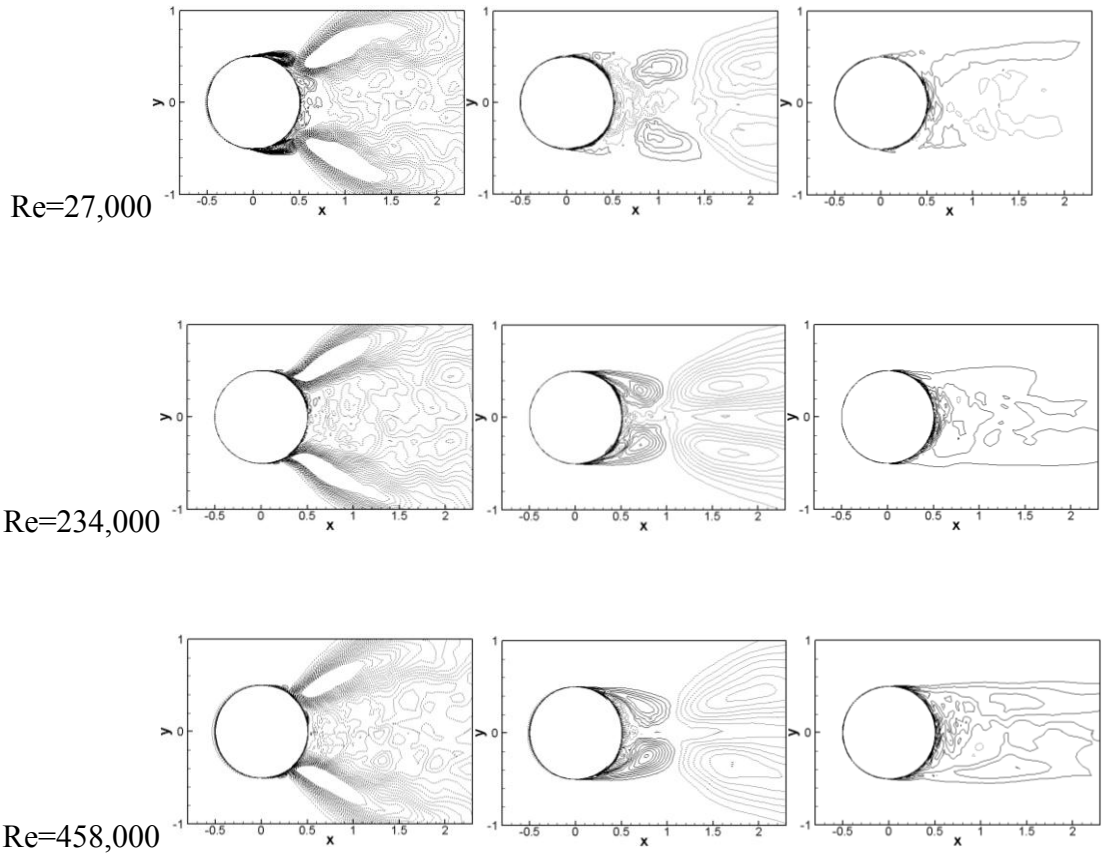

Figure 4.16 Mean transverse vorticity contours. Contour levels: -5 to 5 with interval 0.25

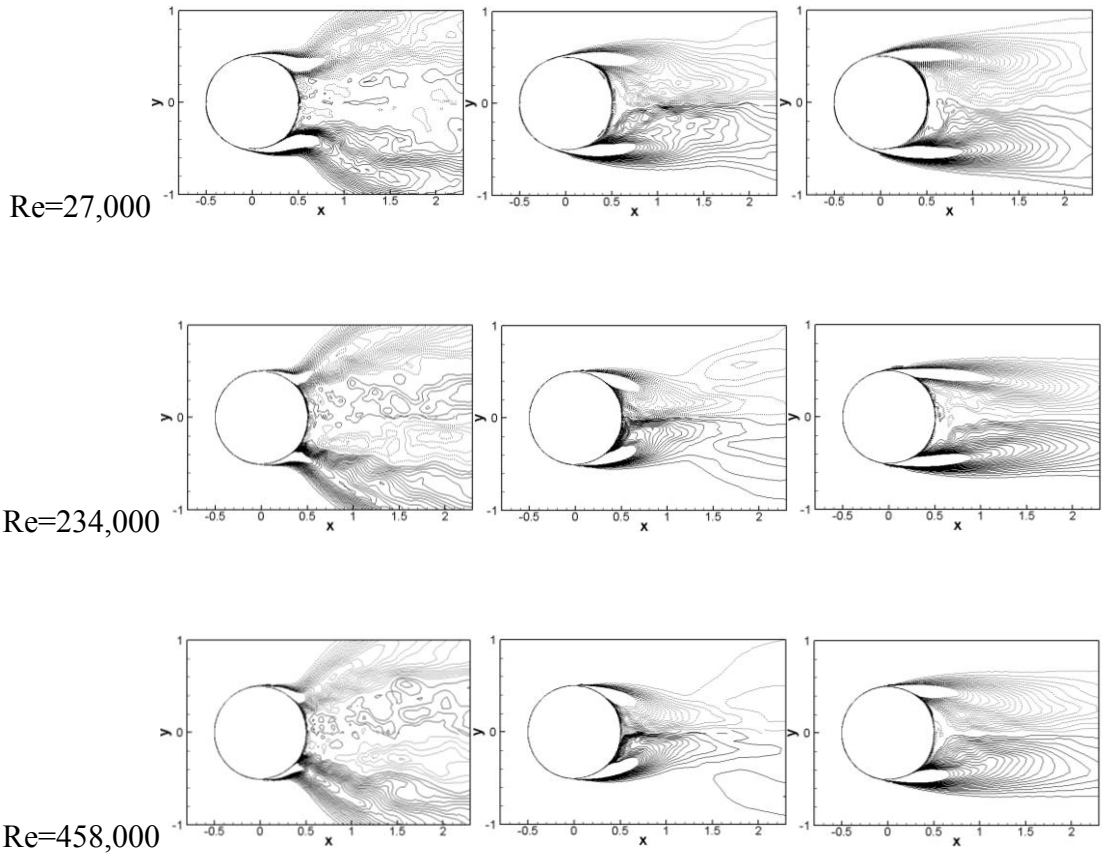

Figure 4.17 Mean vertical vorticity contours. Contour levels: -5 to 5 with interval 0.25

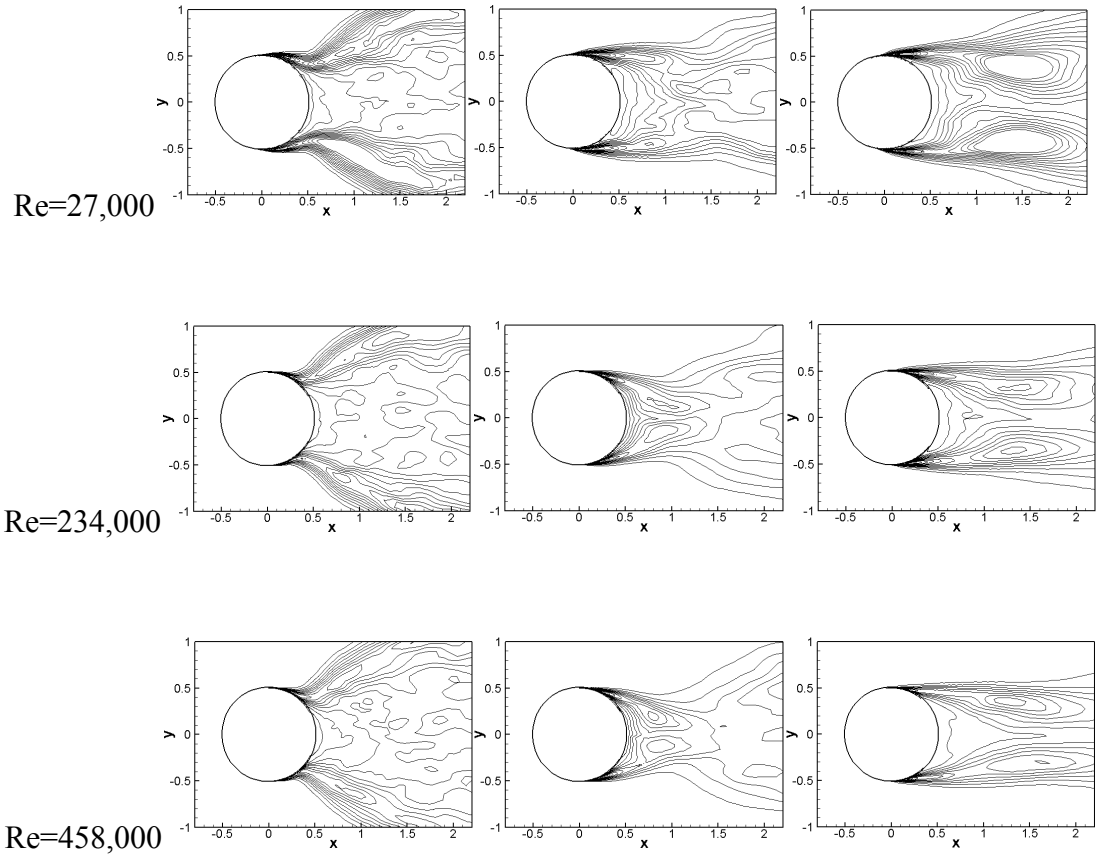

Figure 4.18 Contours of streamwise Reynolds stress ($\overline{u'u'}$)

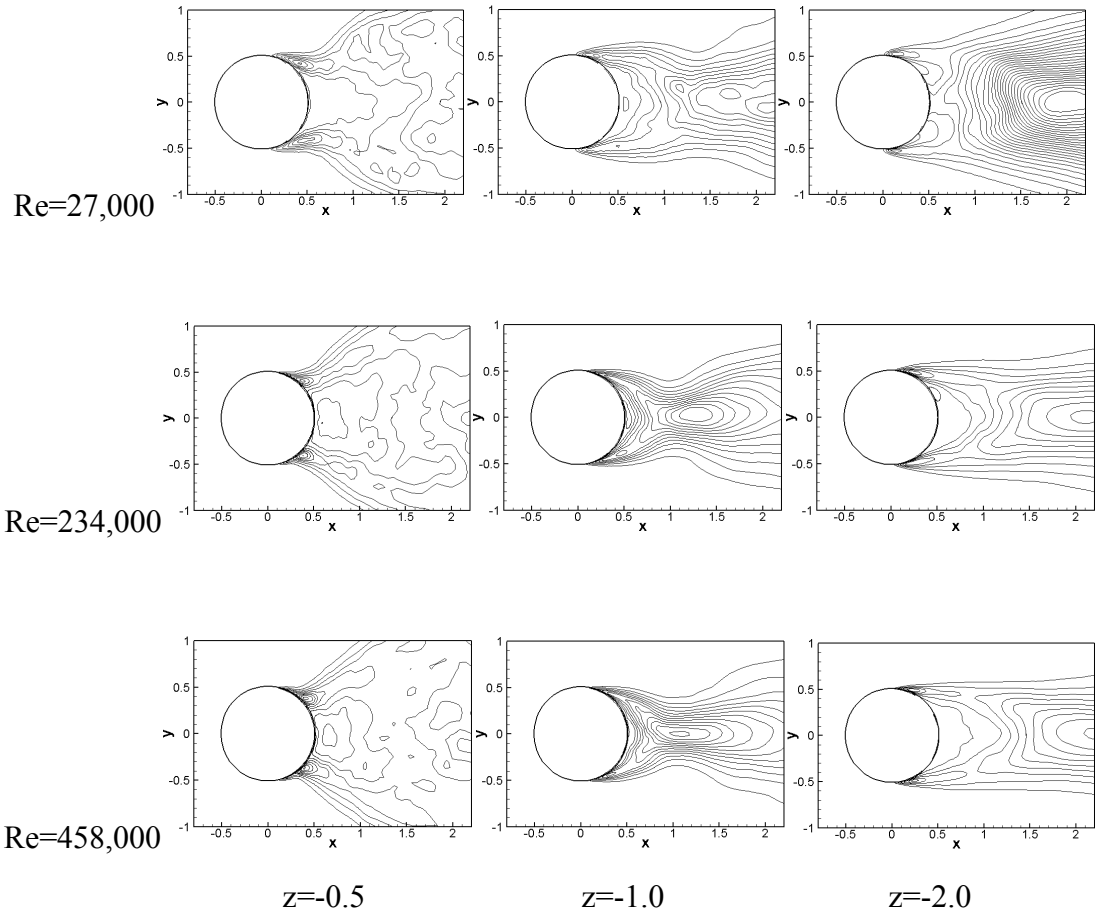

Figure 4.19 Contours of transverse Reynolds stress ($\overline{v'v'}$)

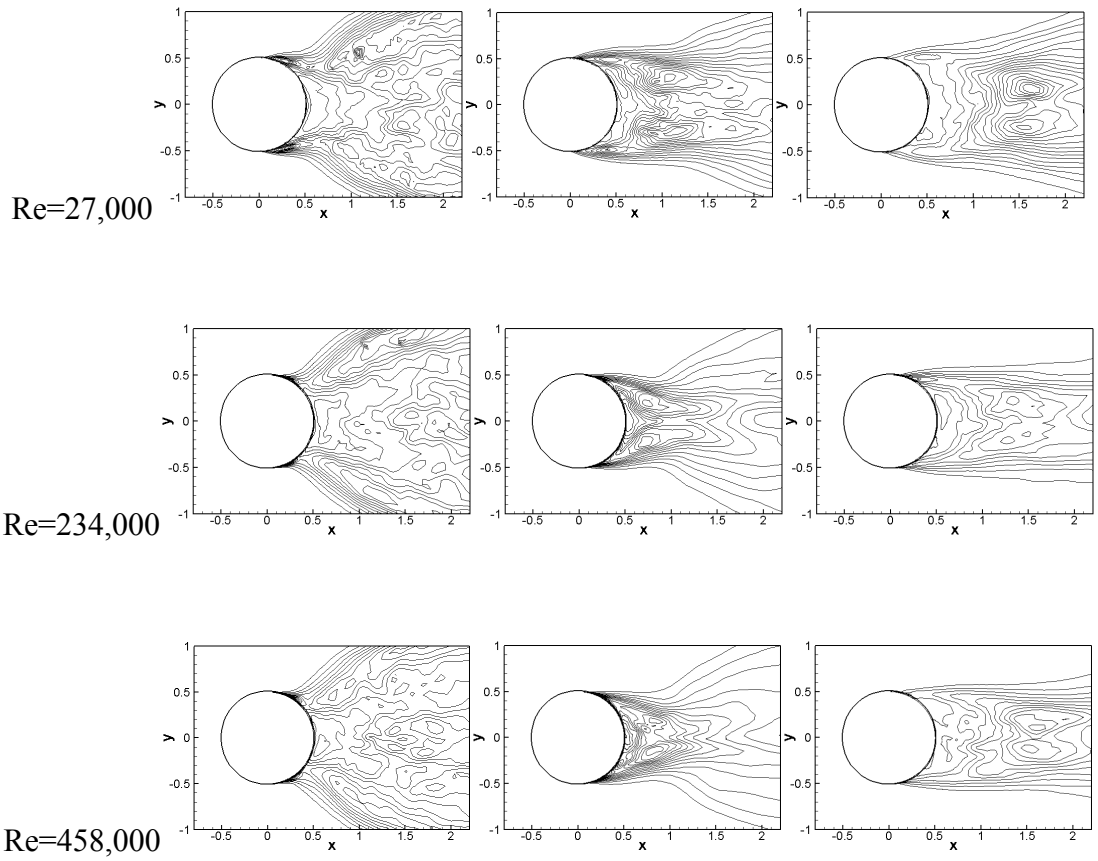

Figure 4.20 Contours of vertical Reynolds stress ($\overline{w'w'}$)

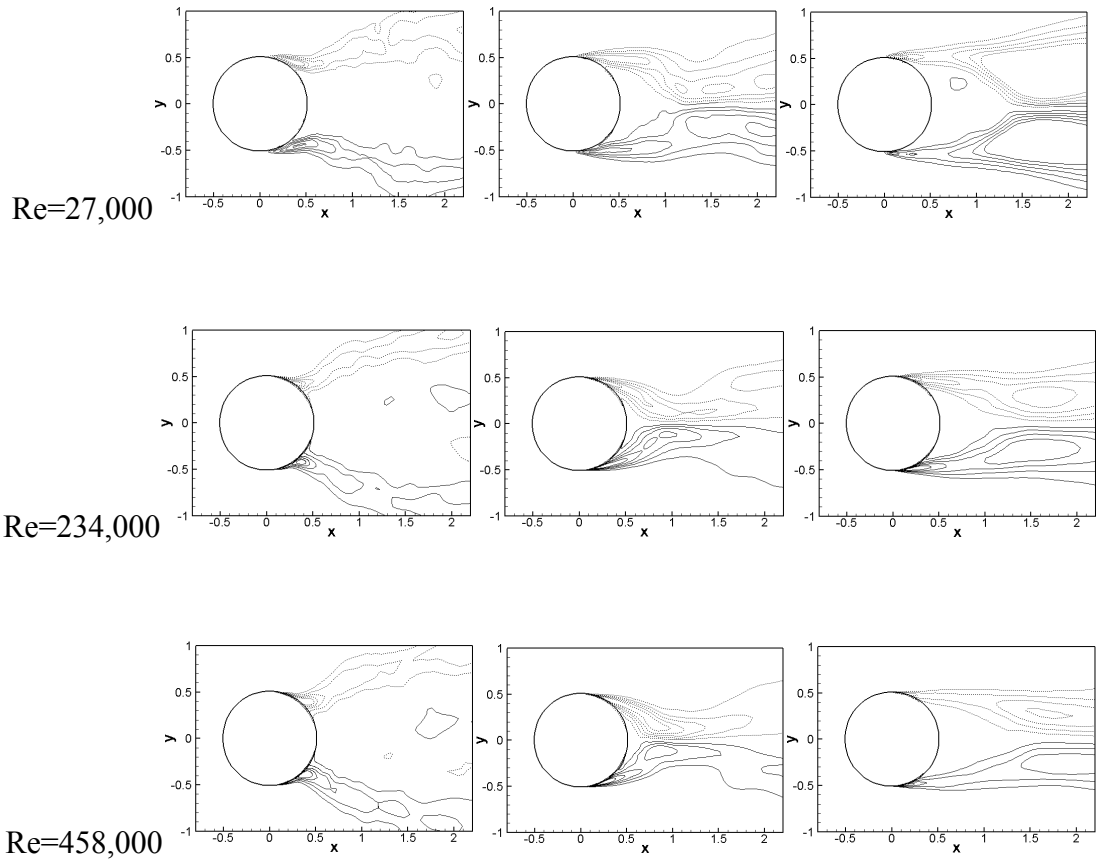

Figure 4.21 Contours of Reynolds shear stress ($\overline{u'v'}$)

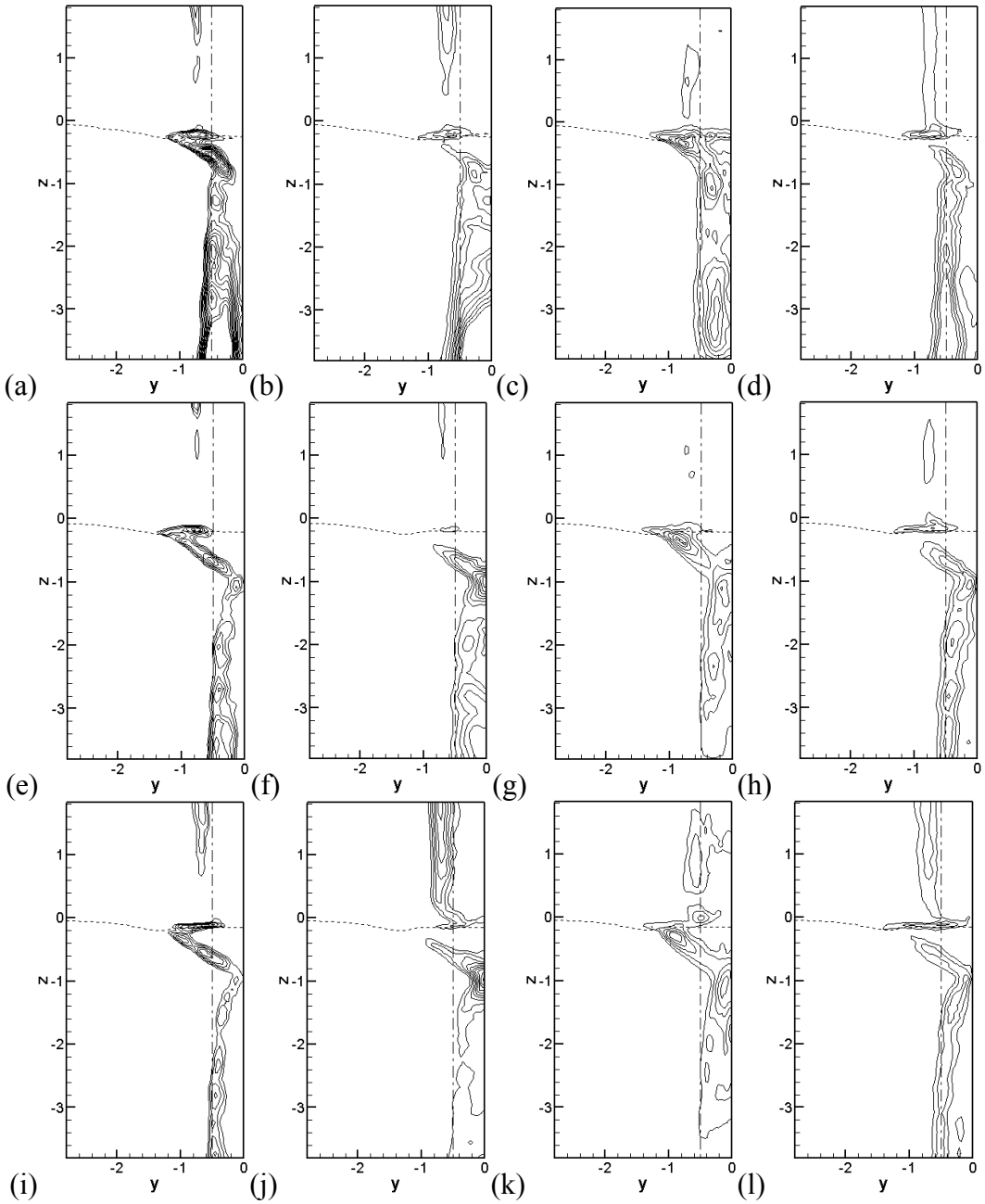

Figure 4.22 Reynolds stress at x = 1.0: (a) $\overline{u'u'}$; (b) $\overline{v'v'}$; (c) $\overline{w'w'}$; (d) $\overline{u'v'}$ for Re = 27,000; (e) $\overline{u'u'}$; (f) $\overline{v'v'}$; (g) $\overline{w'w'}$; (h) $\overline{u'v'}$ for Re = 234,000; (i) $\overline{u'u'}$; (j) $\overline{v'v'}$; (k) $\overline{w'w'}$; (l) $\overline{u'v'}$ for Re = 458,000

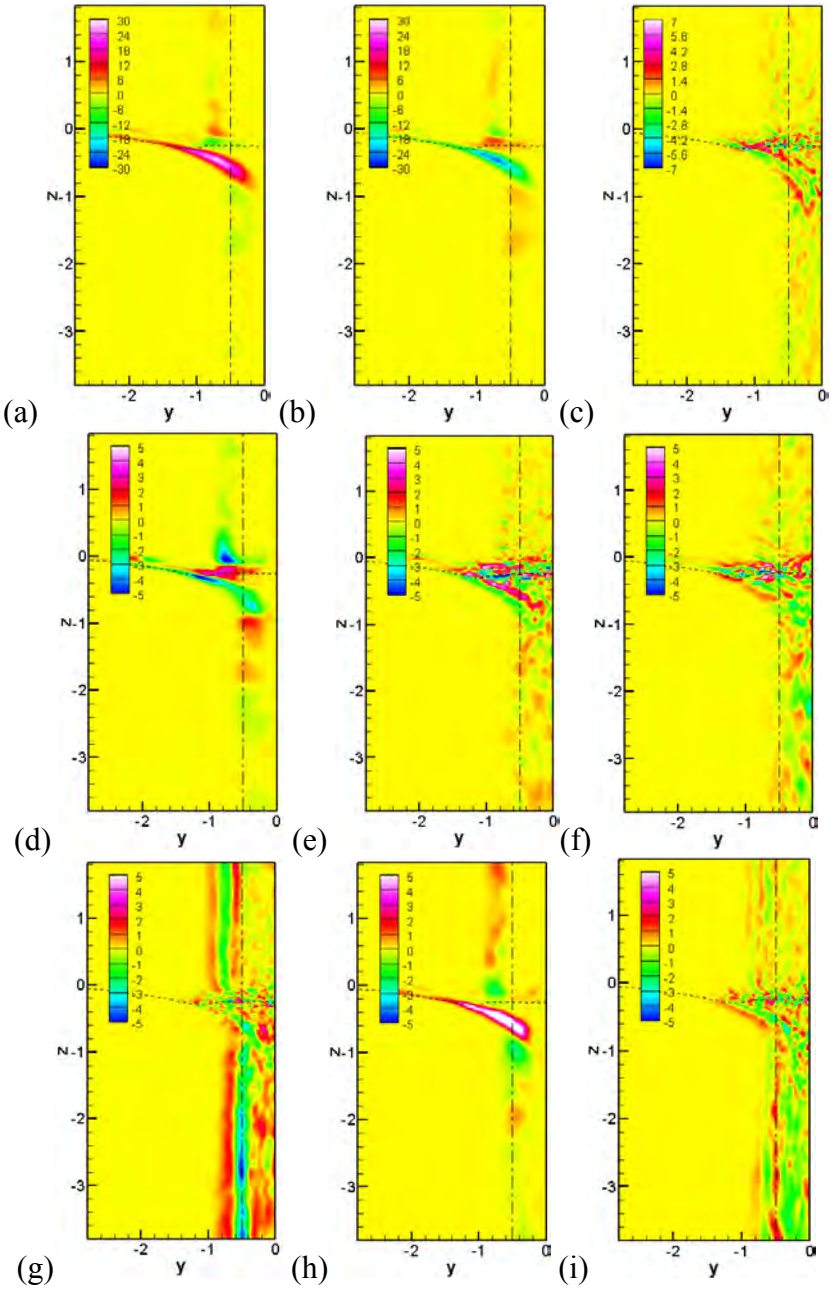

Figure 4.23 Dominant source terms for the mean vorticity at the cross-stream plane for Re = 27,000: (a) y component of term (B) for streamwise vortocity; (b) z component of term (B) for streamwise vortocity; (c) term (E) for streamwise vorticity; (d) z component of term (B) for transverse vorticity; (e) term (E) for transverse vorticity; (f) term (F) for transverse vorticity; (g) term (F) for vertical vorticity; (h) z component of term (B) for vertical vorticity; (i) term (E) for vertical vorticity

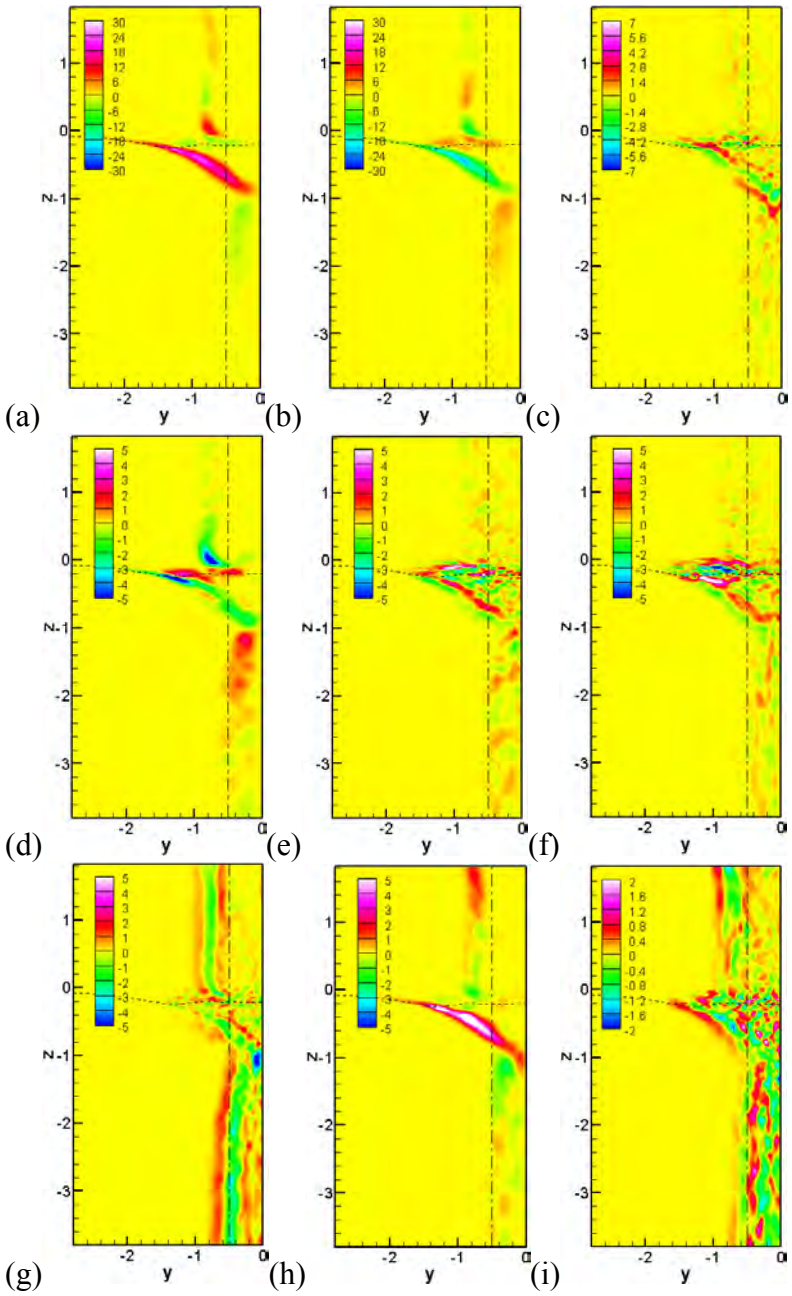

Figure 4.24 Dominant source terms for the mean vorticity at the cross-stream plane for Re = 234,000: (a) y component of term (B) for streamwise vortocity; (b) z component of term (B) for streamwise vortocity; (c) term (E) for streamwise vorticity; (d) z component of term (B) for transverse vorticity; (e) term (E) for transverse vorticity; (f) term (F) for transverse vorticity; (g) term (F) for vertical vorticity; (h) z component of term (B) for vertical vorticity; (i) term (E) for vertical vorticity

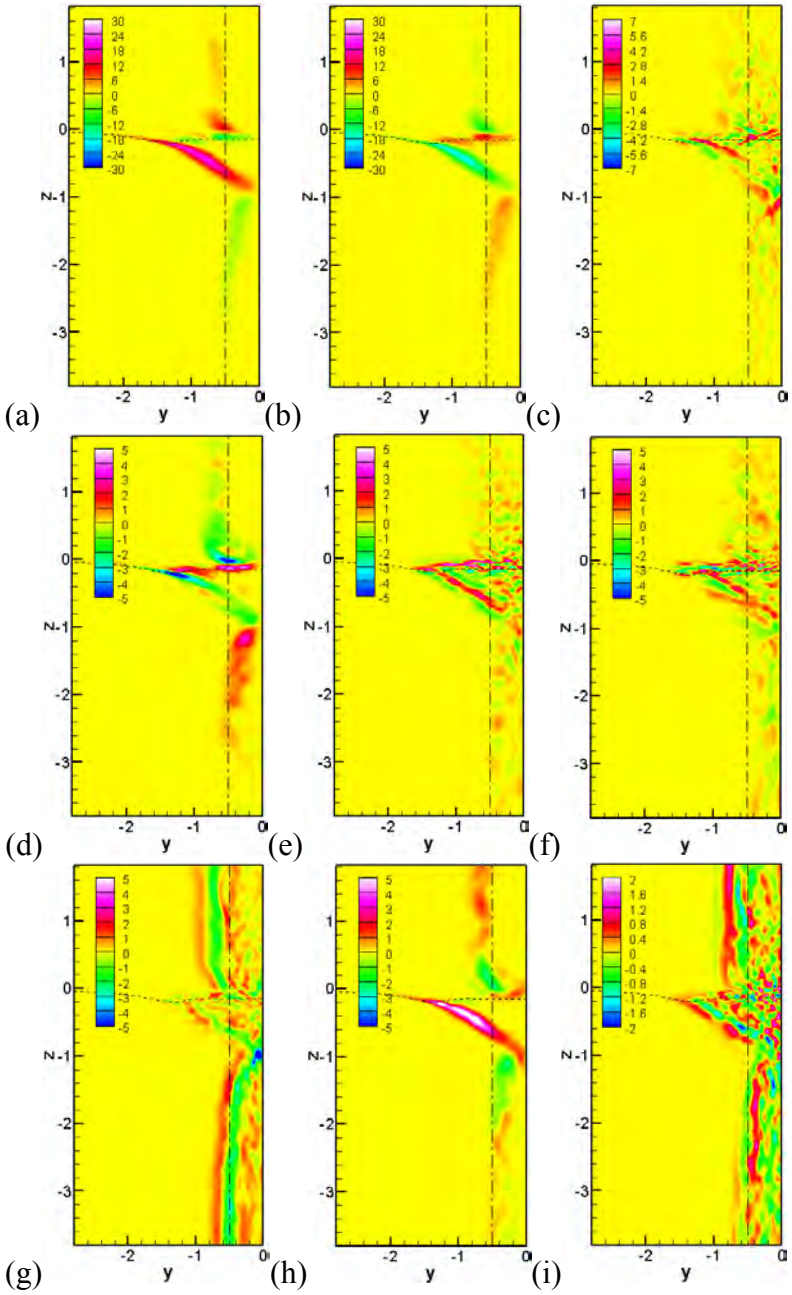

Figure 4.25 Dominant source terms for the mean vorticity at the cross-stream plane for Re = 458,000: (a) y component of term (B) for streamwise vortocity; (b) z component of term (B) for streamwise vortocity; (c) term (E) for streamwise vorticity; (d) z component of term (B) for transverse vorticity; (e) term (E) for transverse vorticity; (f) term (F) for transverse vorticity; (g) term (F) for vertical vorticity; (h) z component of term (B) for vertical vorticity; (i) term (E) for vertical vorticity

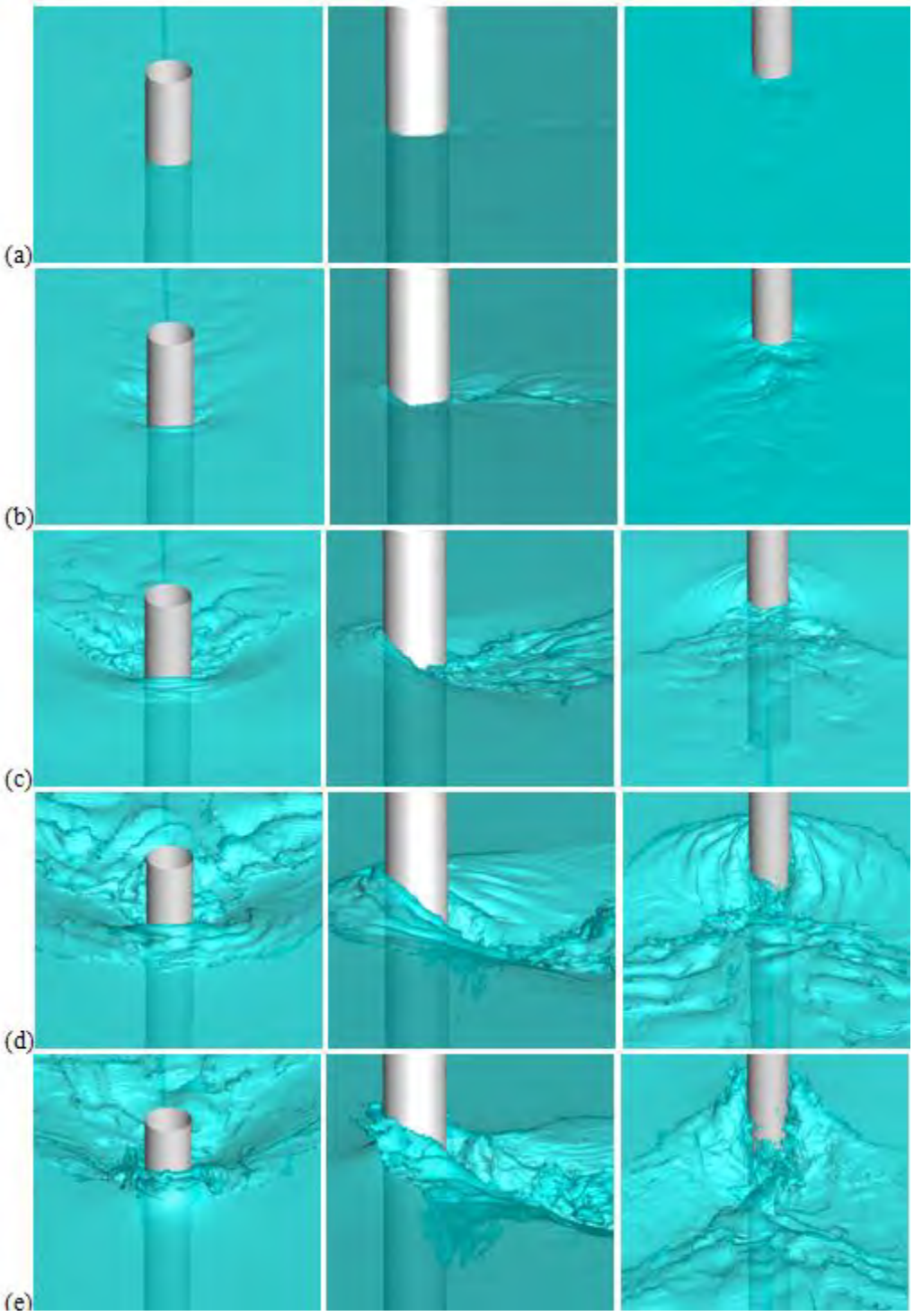

Figure 4.26 Wave field: 1st column, front view; 2nd column, side view; 3rd column, wake region: (a) Fr=0.2; (b) Fr=0.44; (c) Fr=0.84; (d) Fr=1.24; (e) Fr=1.64

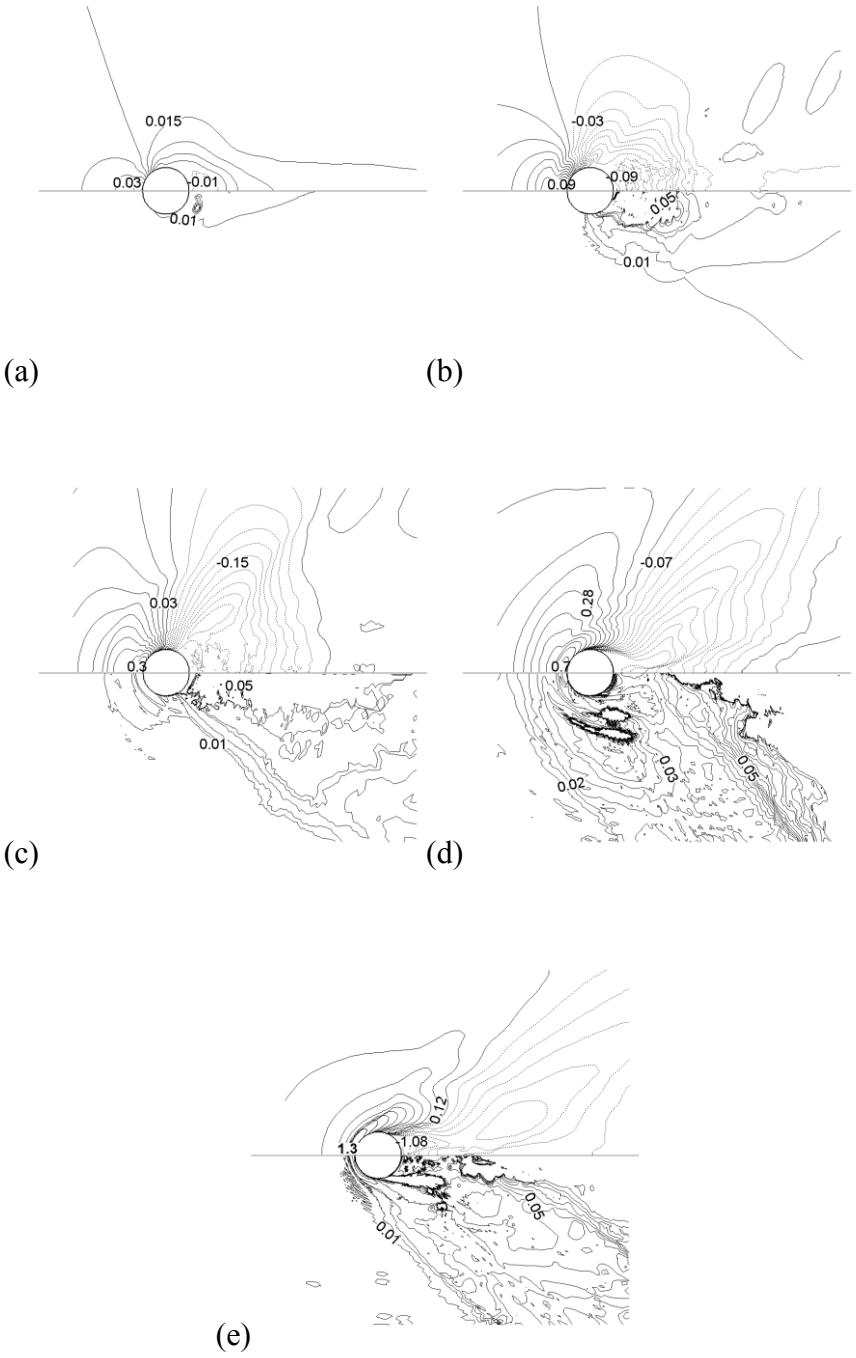

Figure 4.27 Mean interface elevation (top) and the rms of the interface fluctuations (bottom) around the cylinder: (a) Fr=0.2; (b) Fr=0.44; (c) Fr=0.84; (d) Fr=1.24; (e) Fr=1.64

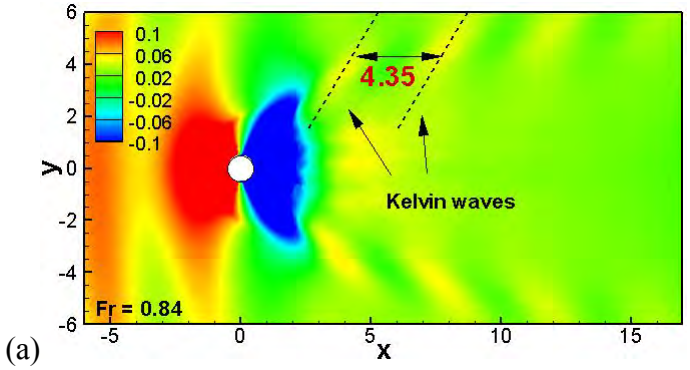

(a)

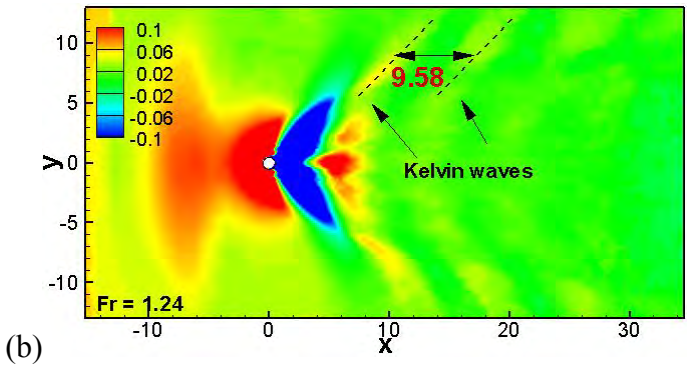

(b)

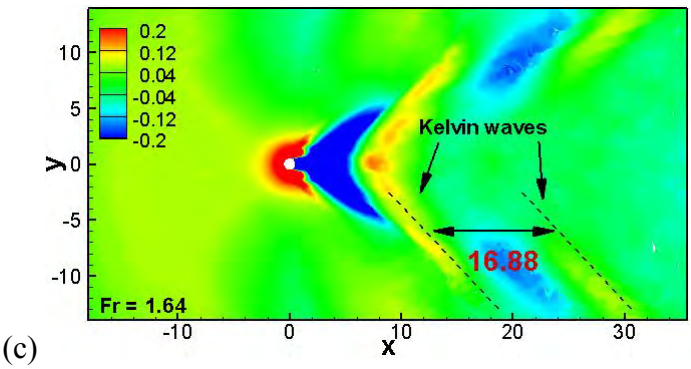

(c)

Figure 4.28 Mean air-water interface elevation contours: (a) Fr=0.84; (b) Fr=1.24; (c) Fr=1.64

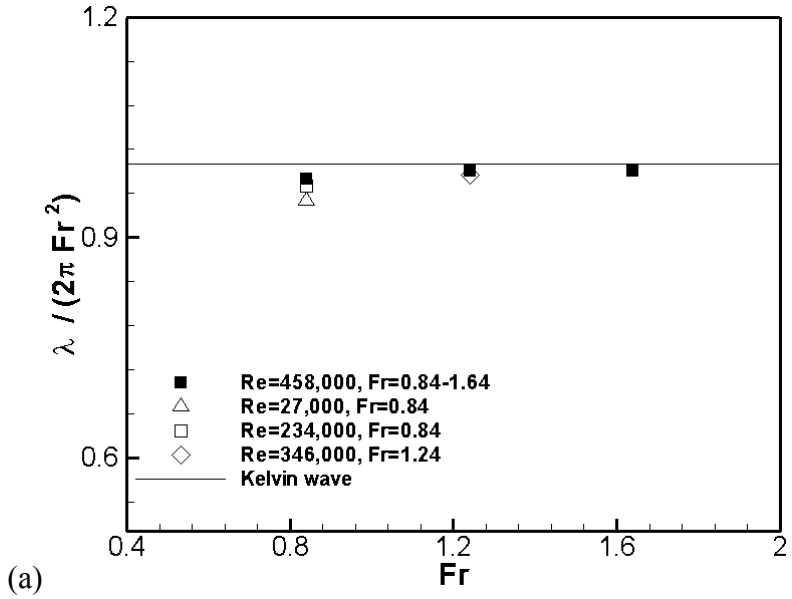

(a)

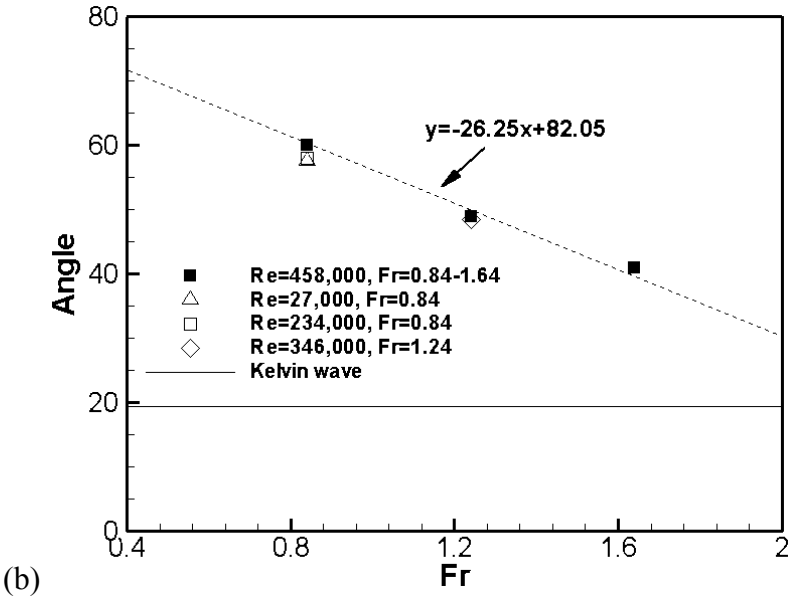

(b)

Figure 4.29 (a) Wave lengths normalized with that of Kelvin waves and (b) diverging wave angle

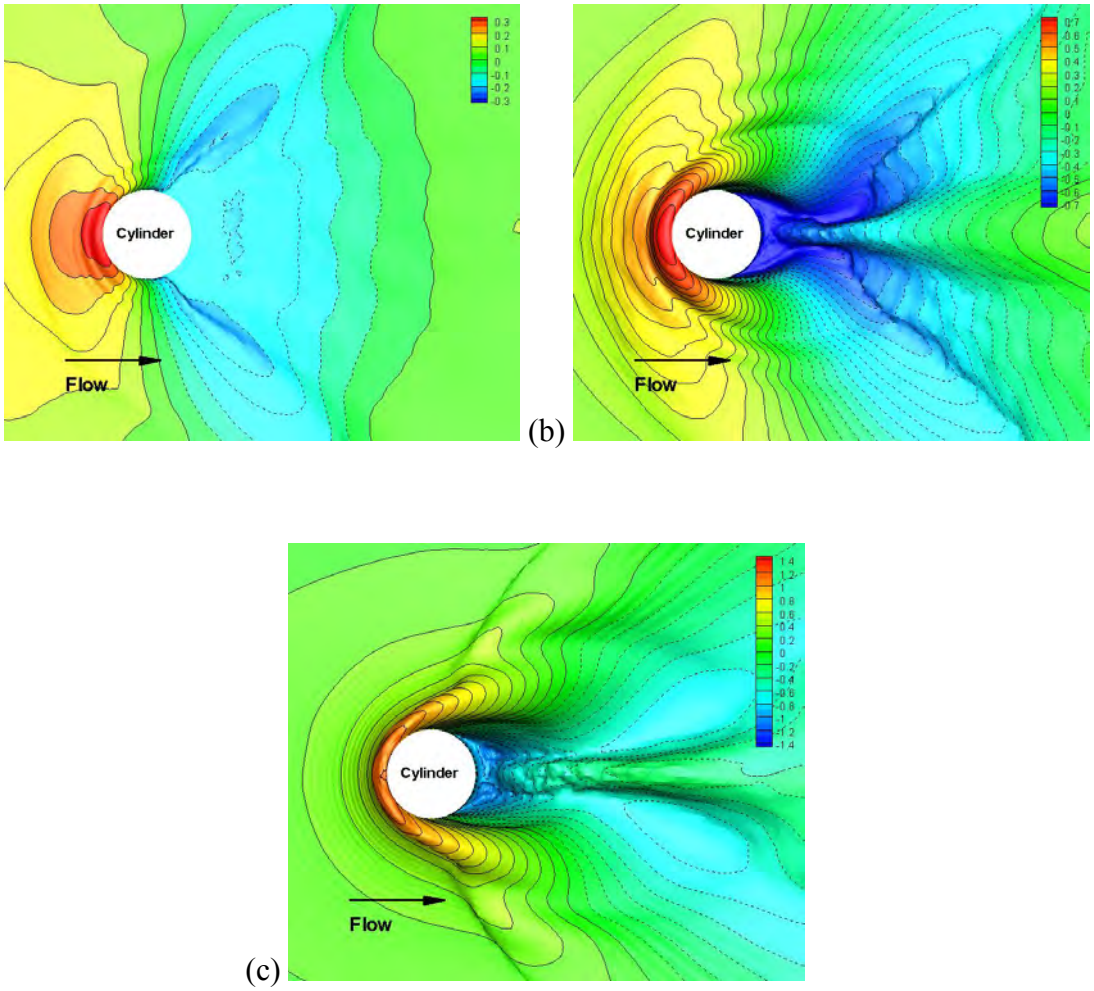

Figure 4.30 Close-up of mean air-water interface elevation contours: (a) Fr=0.84; (b) Fr=1.24; (c) Fr=1.64

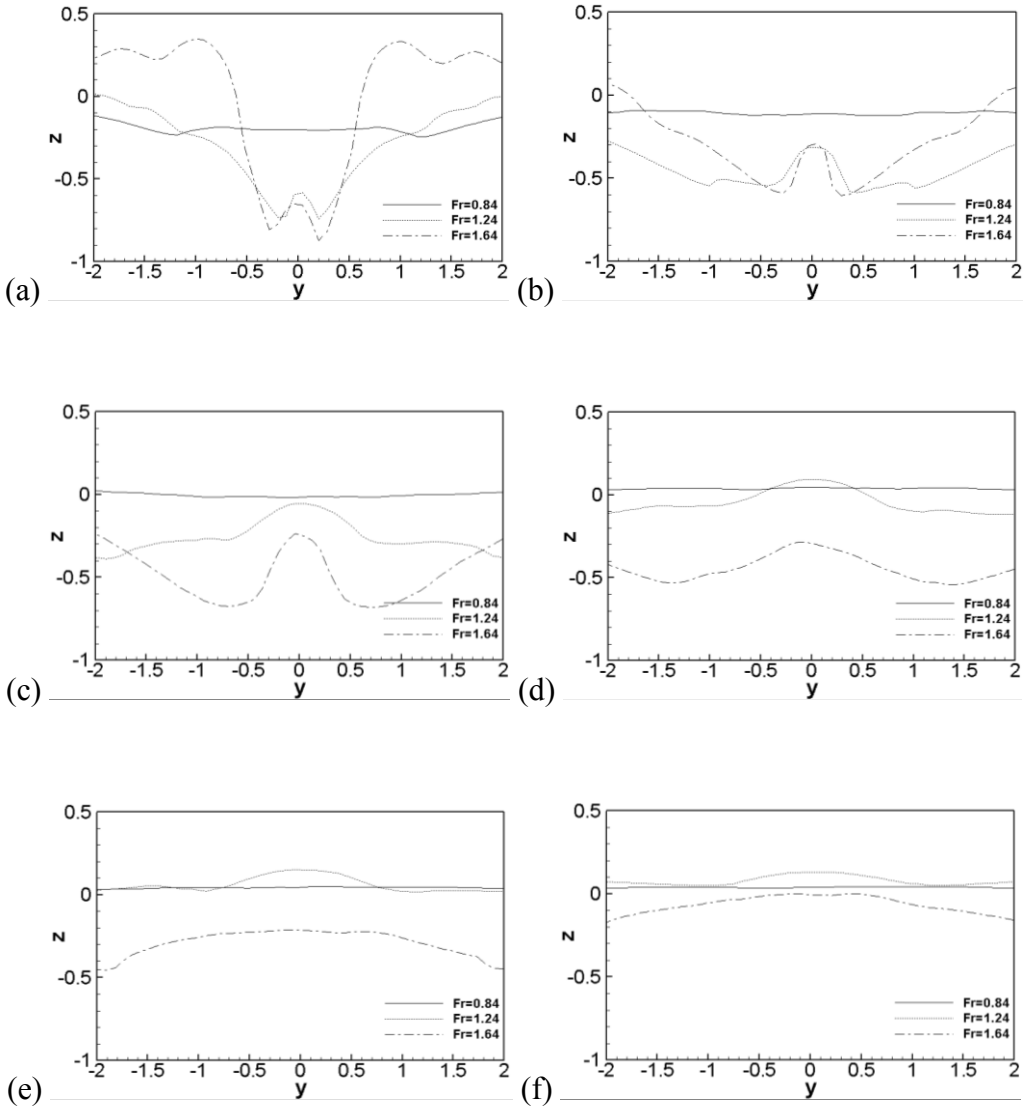

Figure 4.31 Wave profiles at different streamwise locations for three Fr: (a) x=1.0; (b) x=2.0; (c) x=3.0; (d) x=4.0; (e) x=5.0; (f) x=6.0

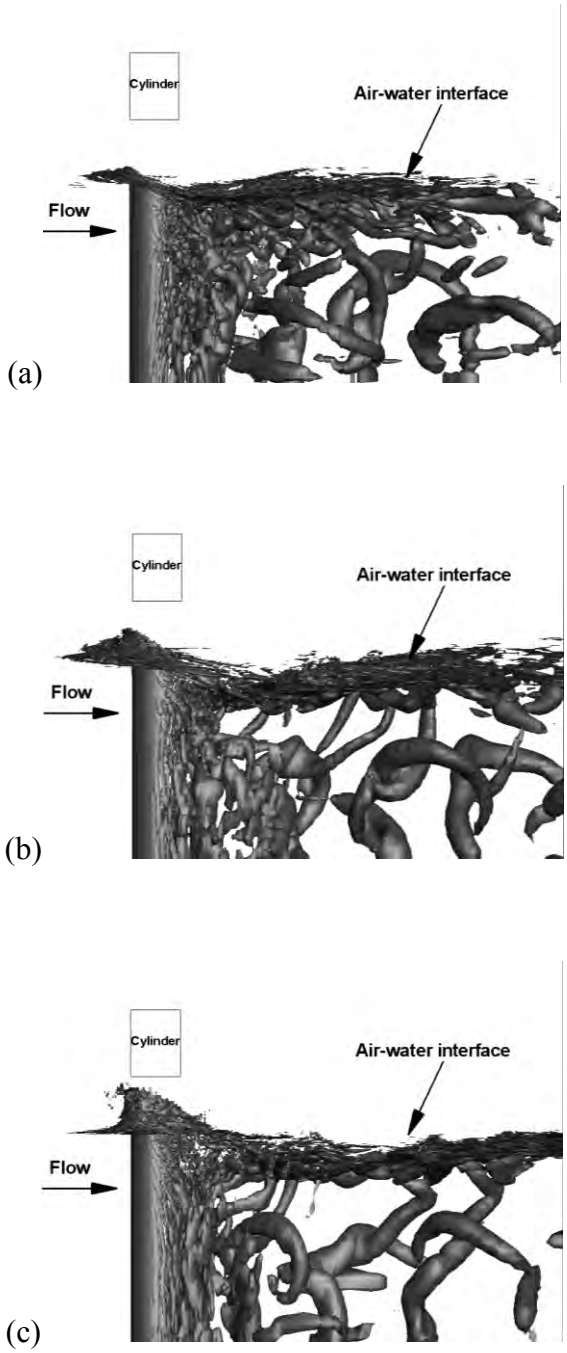

Figure 4.32 Instantaneous vortical structures identified by the second invariant of the velocity gradient tensor Q = 1.0 for three Fr : (a) Fr=0.84; (b) Fr=1.24; (c) Fr=1.64

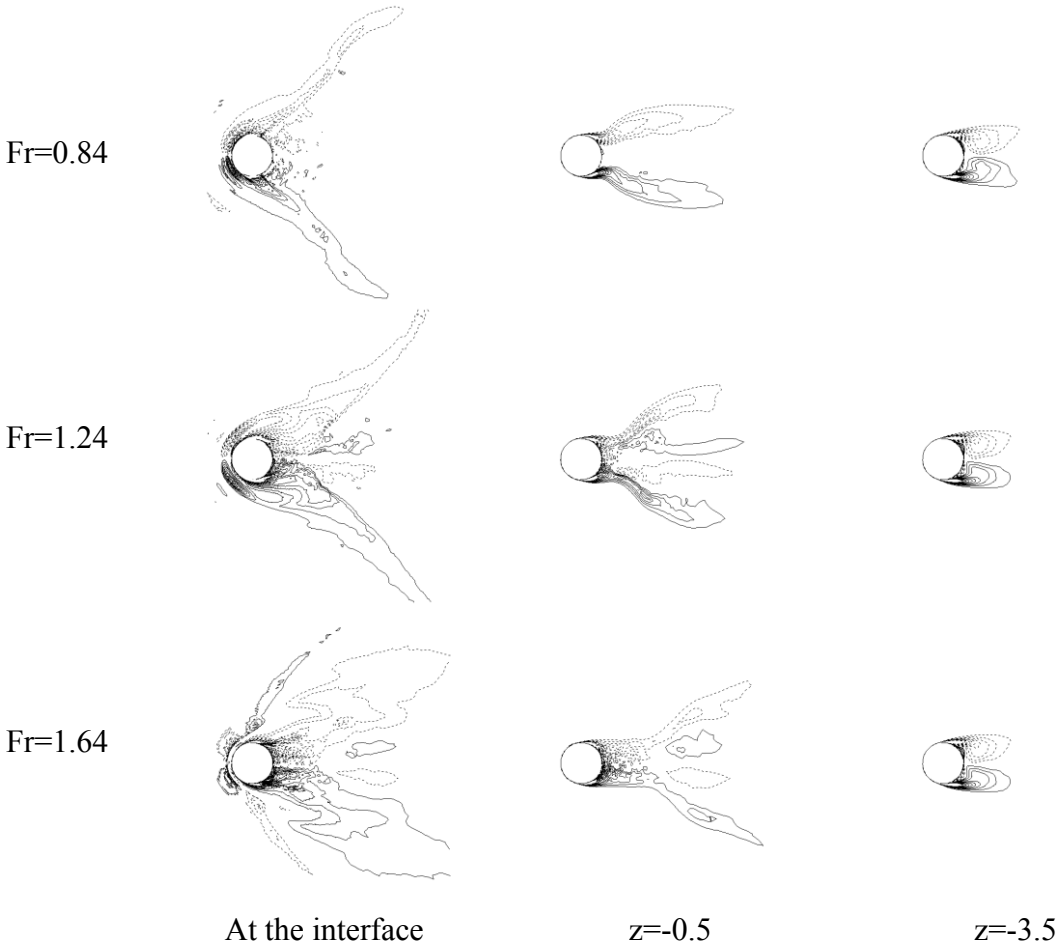

Figure 4.33 Mean vertical vorticity contours at different depths

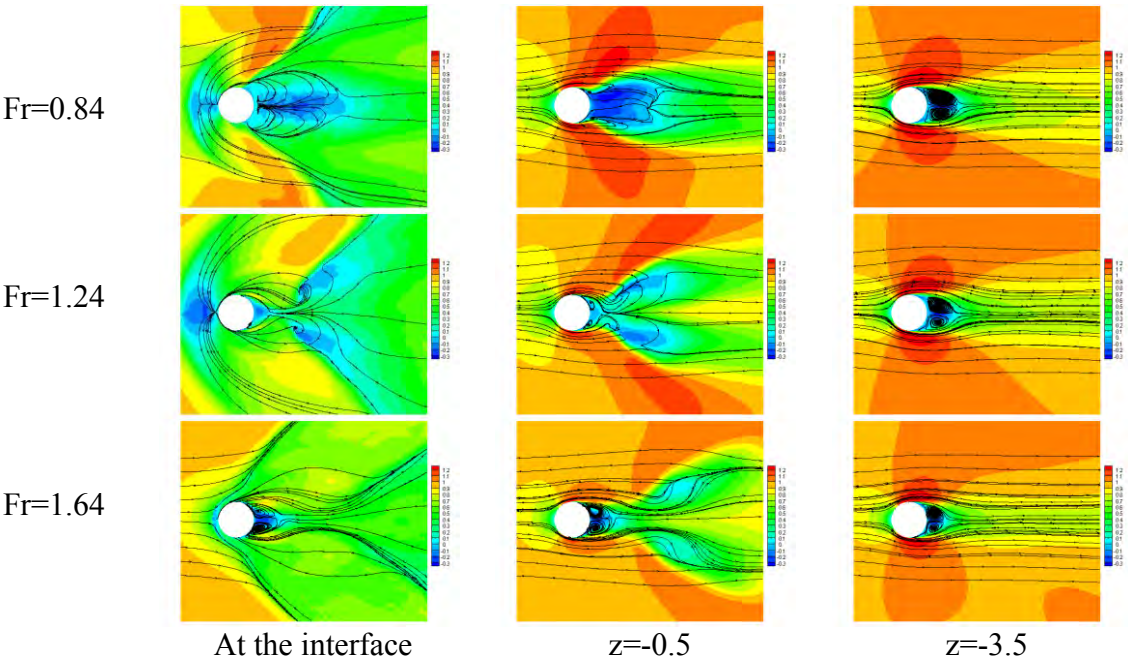

Figure 4.34 Mean streamwise velocity contours with streamlines at different depths

(a)

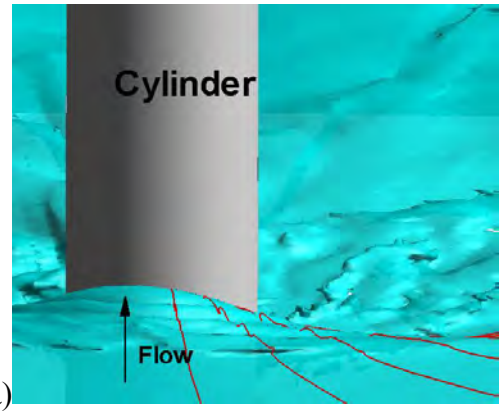

(b)

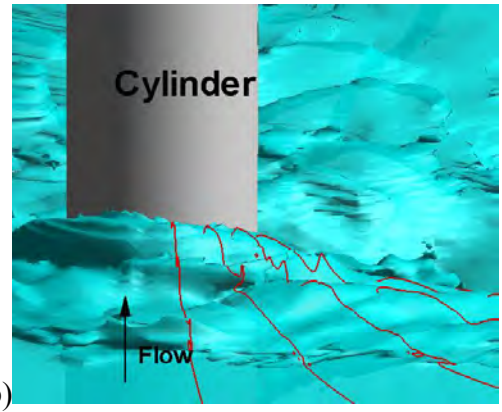

(c)

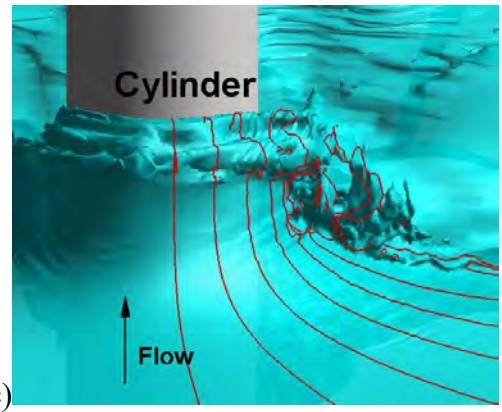

Figure 4.35 Iso-surface of air-water interface with the slices of the wave profile cut: (a) Fr = 0.84; (b) Fr = 1.24; (c) Fr = 1.64

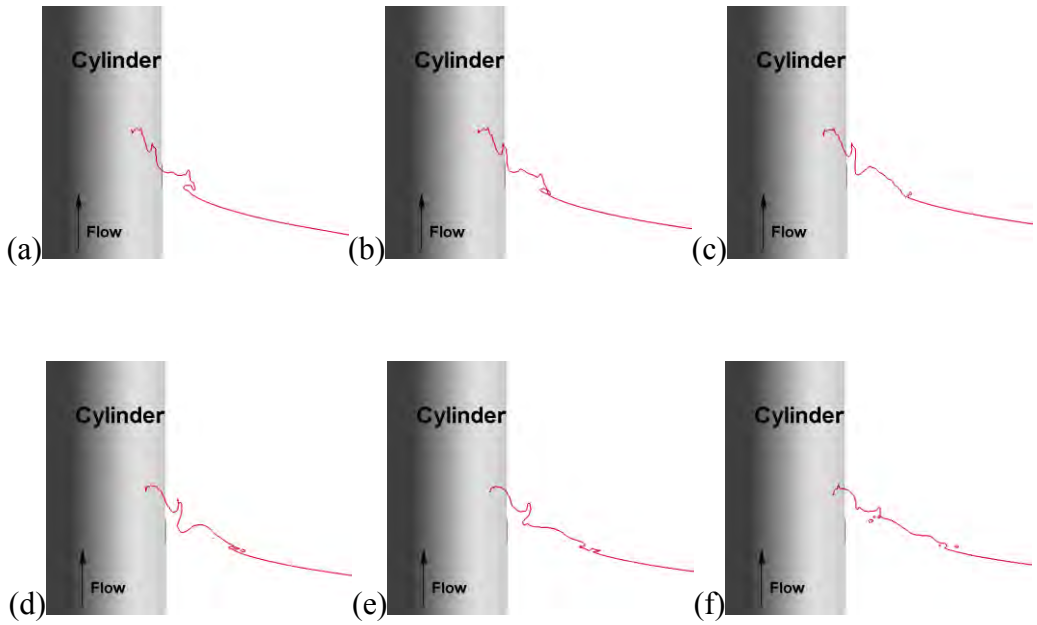

Figure 4.36 Slices of the wave profile cut for Fr = 1.24: (a) θ=198˚; (b) θ=202˚; (c) θ=207˚; (d) θ=210˚; (e) θ=215˚; (f) θ=222˚

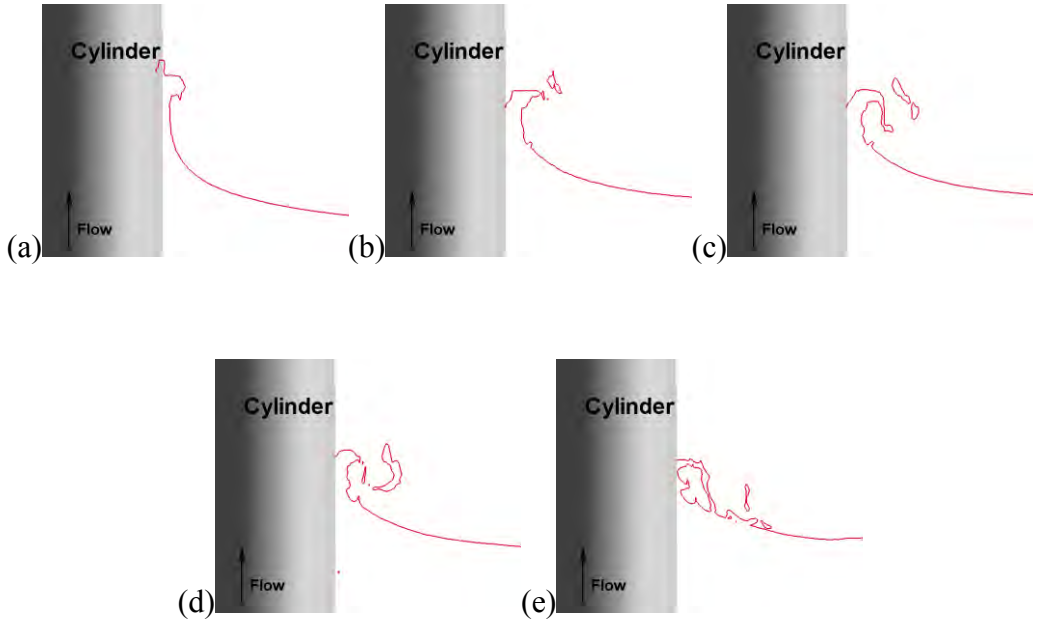

Figure 4.37 Slices of the wave profile cut for Fr = 1.64: (a) θ=212˚; (b) θ=267˚; (c) θ=280˚; (d) θ=288˚; (e) θ=300˚

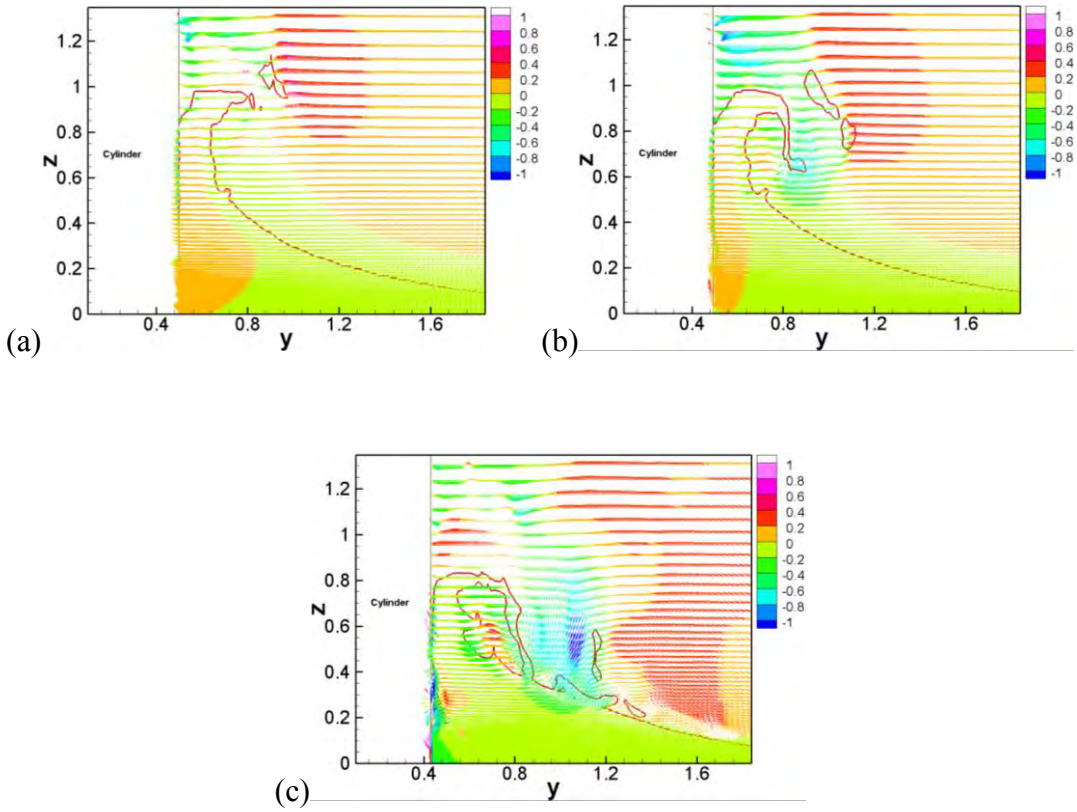

Figure 4.38 Velocity vector fields of plunging jet for Fr = 1.64: (a) θ=267˚; (b) θ=280˚; (c) θ=300˚

CHAPTER 5

CONCLUSIONS

Air-water interfacial flows have been numerically investigated using complementary CFDShip-Iowa version 6 including Cartesian grid solver and orthogonal curvilinear grid solver. Two different flows, i.e. plunging wave breaking and flow past a vertical surface-piercing circular cylinder are studied in this thesis.

The plunging wave-breaking process for impulsive flow over a bump in a shallow water flume has been simulated using the exact experimental initial and boundary conditions, which allows more detailed spatial and temporal validations. The results computed on the fine grid are compared with the experimental measurements. The wave profile and location at the maximum height is very close to the experiment results. The simulations qualitatively predict all four time phases (startup, steep wave formation, plunging wave, and chaotic wave breaking swept downstream), all four plunging events and their sub-events. Detailed wave breaking processes, including wave profile at maximum height, first plunge, entrapped air bubble trajectories and diameters, kinetic, potential, and total energy, and bottom pressures are discussed along with the experimental results. The flume flow and velocity demonstrate the same flow trend as the experiments but with reduced velocity magnitudes. The simulations show similar bottom pressure to the experiments but with large oscillations, which correlate with the plunging wave breaking events and sub-events. The post-breaking water elevation is larger as compared to the experimental results.

The present results show differences and similarities with other experimental and computational studies for deep water and sloping beaches. In particular, the breaking processes show differences due to the differences in mean flow direction. The geometry and conditions in the present study are relevant to ship hydrodynamics since it includes

effects of wave-body interactions and wave breaking direction is opposite to the mean flow.

The flow past a surface-piercing circular cylinder has been studied for Re and Fr effects using large-eddy simulation with the Lagrangian dynamic subgrid-scale model. To systematically study the origin of the surface current, i.e., the outward transverse velocity at the interface, a series of cases at different Re/Fr (from 5.58×10^4/0.2 to 3.46×10^5/1.24 and 4.58×10^5/1.64) reported in Chaplin et al. (2003), were simulated and the effects of Re/Fr on the flow have been investigated.

The flow features near the air-water interface show significant changes with different Reynolds numbers from sub-critical to critical regime at Fr = 0.84. The present simulations show that the interface makes the separation point more delayed for all regime of Re. Remarkably reduced separated region below the interface at z=-1 is observed for critical Re regime and it is responsible for much reduced wake and recirculation region behind the cylinder and it recovers in the deep flow.

The present study shows that the air-water interface structures are remarkably changed with different Froude numbers. For sub-critical Fr, relatively smaller bow waves are observed in front of the cylinder with Kelvin waves behind the cylinder and small amount of free-surface roughness and turbulence are also seen in the wake region. For Fr = 1.24, much increased bow wave is observed and it breaks and wraps around the bow. A lot of splashes and bubbles are presented immediately behind the cylinder. Stronger free-surface oscillations and turbulence makes Kelvin waves less visible. For Fr = 1.64, the bow wave increases remarkably with the largest wake region and deepest depression and it also breaks with similar features of plunging breakers which are also shown in previous plunging wave breaking literatures. Much more small air-water interface structures including splashes and bubbles are observed behind the cylinder. It is also hard to distinguish the Kelvin waves behind the cylinder due to much larger free-surface oscillations and turbulence. As Fr increases, the Kelvin wave angle decreases and deeper

and narrower depression region behind the cylinder are observed. This cavity region behind the cylinder makes the cylinder more slender body so that the flow features are significantly different that around the cylinder.

In the future work for the flow over the submerged bump, the 3D simulations will be conducted and used to guide future 3D experiments to document span-wise instabilities and vortex and turbulent structures. The orthogonality correction term will be added to overcome non-orthogonality from the orthogonal curvilinear grid generations. In addition turbulent modeling for interface will be implemented to predict more accurate air-water two-phase turbulent flows.

Much more grid points (upto 0.6 billion grid points) will be used to understand more details of interface flows around cylinder and to resolve air entrainments in the cylinder wake regions at higher Froude number. The effect of the interface density jump on vorticity transport will be investigated. Further investigations will be performed to study the origin of the mean streamwise vorticity and the outward transverse velocity near the interface using the mean streamwise vorticity transport equations. To obtain better understanding of vortex- and wave- induced vibrations, forced pure sway motion simulations will be conducted.

REFERENCES

Achenbach, E., 1968. Distribution of local pressure and skin friction around a circular cylinder in cross-flow up to Re = 5×10^6. Journal of Fluid Mechanics 34, 625-639.

Balay, S., Gropp, W., McInnes, L., Smith, B., 1997. Efficient management of parallelism in object-oriented numerical software libraries. In Modern Software Tools in Scientific Computing, E. Arge, A. Bruaset, and H. Langtangen, Eds., Birkhauser Press, Cambridge, Massachusetts 163-202.

Bhushan, S., Stern, F., and Doctors, L. J., 2010, Verification and validation of URANS wave resistance for air cushion vehicles, and comparison with linear theory. submitted to the Journal of Ship Research.

Blenkinsopp, C. E., and Chaplin, J. R., 2007. Void fraction measurements in breaking waves. Proceedings of the Royal Society A 463, 3151-3170.

Bonmarin, P., 1989. Geometric properties of deep-water breaking waves. Journal of Fluid Mechanics 209, 405-433.

Breuer, M., 1998. Large eddy simulation of the subcritical flow past a circular cylinder: numerical and modeling aspect. International Journal for Numerical Methods in Fluids 28, 1281-1302.

Broglia, R., Di Mascio, A., and Muscari, R. 2004. Numerical simulation of breaking wave around a wedge. Proceedings of 25th symposium on naval hydrodynamics, St. John's Newfoundland and Labrador, Canada.

Cahouet, J., 1984. Etude numerique er experimentale du problem bidimensionnel de la resistance de vaques non-lineaire. Ph.D. Thesis, ENSTA, Paris, (in French).

Cantwell, B. J., and Coles, D., 1983. An experimental study of entrainment and transport in turbulent near wake of a circular cylinder. Journal of Fluid Mechanics 136, 321-374.

Chanson, H., Fang L., 1997. Plunging jet characteristics of plunging breakers. Coastal Engineering 31, 125-141.

Chang, K. A. and Liu, P. L. F., 1999. Experimental investigation of turbulence generated by breaking waves in water of intermediate depth. Physics of Fluids 11, 3390-3400.

Chaplin, J. R., and Teigen, P., 2003. Steady flow past a vertical surface-piercing circular cylinder. Journal of Fluids and Structures 18, 271-285.

Chen, G., Kharif, C., Zaleski, S., Li J., 1999. Two-dimensional Navier-Stokes simulation of breaking waves. Physics of Fluids 11, 121-133.

Choi, H., and Moin, P., 1994. Effects of the computational time step on numerical solutions of turbulent flow. Journal of Computational Physics 113, 1-4.

Deane, G. B. and Stokes, M. D., 2002. Scale dependence of bubble creation mechanisms in breaking waves. Nature 418, 839– 844.

Drazen, D. A. and Melville, W. K., 2009. Turbulence and mixing in unsteady breaking surface waves. Journal of Fluid Mechanics 628, 85-119.

Dong, R. R., Katz, J. and Huang, T. T., 1997. On the structure of bow waves on a ship model. Journal of Fluid Mechanics 346, 77-115.

Ducan, J.H., 1981. An experimental investigation of breaking waves produced by a towed hydrofoil. Proc. R. Soc. London Ser. A, 377, 331-348.

Ducan, J.H., 1983. The breaking and nonbreaking wave resistance of a two-dimensional hydrofoil. Journal of Fluid Mechanics, 126, 507-520.

Fage, A., and Falkner, V. M., 1931. Future experiments on the flow around circular cylinder. (British) Aeronautical Research Council, Rep. and Memo. 1369.

Falgout, R. D., Jones, J. E., Yang, U. M., 2006. Numerical solution of partial differential equations on parallel computers. Vol. 51. Springer-Verlag, Ch. The design and implementation of HYPRE, a library of parallel high performance preconditions, pp. 267-208.

Galvin, C. J., 1968. Breaker type classification on three laboratory beaches. Journal of Geophysical Research 73, 3651-3659.

Ghosh, S., 2008. Free surface instabilities and plunging breaking wave downstream of a bump in shallow water open channel flume. Ph.D. Thesis, The University of Iowa, USA.

Grue, J., Jensen, A., 2006. Experimental velocities and accelerations in very steep wave events in deep water. European Journal of Mechanics B/Fluids 25, 554-564.

Guyeffier, D., Li, J., Nadim, A., Scardovelli, S., Zaleski, S., 1999. Volume of fluid interface tracking with smoothed surface stress methods for three-dimensional flows. Journal of Computational Physics 152, 423-456.

Huang, J., Carrica, P. M., and Stern, F., 2007. Coupled ghost fluid/two-phase level set method for curvilinear body-fitted grids. International Journal for Numerical Method and Fluids 55, 867-897.

Hunt, J., Wray, A., Moin, P., 1988. Eddies, stream, and convergence zones in turbulent flows. In: Proc. CTR Summer Program. Center for Turbulence Research, Stanford, CA, 193-208.

Iafrati, A., Di Mascio, A., Campana, E. F., 2001. A level set technique applied to unsteady free surface flows. International Journal for Numerical Method and Fluids 35, 281-297.

Iafrati, A., 2010. Air-water interaction in breaking wave events: quantitative estimates of drops and bubbles. In: Proceedings of 28th Symposium on Naval Hydrodynamics, Pasadena, California, 12-17 September 2010.

Inoue, M., Bara, N., Himeno, Y., 1993. Experimental and numerical study of viscous flow field around an advancing vertical circular cylinder piercing a free-surface. Journal of Kansai Society Naval Architecture 220, 57-64.

Jiang, G. and Peng, D., 1999. Weighted ENO schemes for Hamilton-Jacobi equations. SIAM Journal on Scientific Computing 21, 2126-2143.

Jiang, G. and Shu, C. W., 1996. Efficient implementation of weighted ENO schemes. Journal of Computational Physics 126, 202-228.

Kang, D., Ghosh, S., Reins, G., Koo, B., Wang, Z., and Stern, F., 2011. Impulsive plunging wave breaking downstream of a bump in a shallow water flume—Part I: Experimental observations. Journal of Fluids and Structures (to appear) .

Kandasamy, M., Xing, T., Stern, F., 2009. Unsteady free surface wave-induced separation: Vortical structures and instabilities. Journal of Fluids and Structures 25, 343-363.

Kawamura, T., Mayer, S., Garapon, A., Sørensen, L., 2002. Large eddy simulation of a flow past free surface piercing circular cylinder. Journal of Fluids Engineering 124, 91-101.

Kimmoun, O. and Branger, H., 2007. A particle image velocimetry investigation on laboratory surf-zone breaking waves over a sloping beach. Journal of Fluid Mechanics 588, 353-397.

Koo, B., Wang, Z., Yang, J., and Stern, F., 2011. Impulsive plunging wave breaking downstream of a bump in a shallow water flume—Part II: Numerical simulations. Journal of Fluids and Structures (to appear).

Kravchenko, A. G., and Moin, P., 2000. Numerical studies of flow over a circular cylinder at Re_D=3900, Physics of Fluids 12, 403-417.

Leonard, B.P., 1979. A stable and accurate convective modeling procedure based on quadratic upstream interpolation. Computer Methods in Applied Mechanics and Engineering 19, 59-98.

Lubin, P., Vincent, S., Abadie, S., Caltagirone, J. P., 2006. Three-dimensional large eddy simulation of air entrainment under plunging breaking waves. Coastal Engineering, 53, 631-655.

Melville, W. K., 1994. Energy dissipation by breaking waves. Journal of Physical Oceanography 24, 2041-2049.

Melville, W. K., Veron, F. and White, C. J., 2002. The velocity field under breaking waves: coherent structures and turbulence. Journal of Fluid Mechanics 454, 203-233.

Metcalf, B., Longo, J., Ghosh, S., Stern, F., 2006. Unsteady free-surface wave-induced boundary-layer separation for a surface-piercing NACA 0024 foil: towing tank experiments. Journal of Fluids and Structures 22, 77-98.

Metcalf, B., Longo, J., Stern, F., 2001. Experimental investigation of wave-induced separation around a surface-piercing NCA 0024 hydrofoil. 26th American Towing Tank Conference 23-24 July, 2001, Webb Institute, Glen Cove, New York.

Miyata, H. and Inui, T., 1984. Nonlinear ship waves. Advances in Applied Mechanics 24, 215-288.

Miyata, H., Matsukawa, C., and Kajitani, H., 1985. Shallow water flow with separation and breaking wave. Autumn meeting of Naval Architecture, Japan.

Norberg, C., 1992. Pressure forces on a circular cylinder in cross Flow. In: IUTAM Symposium Bluff-Body Wakes, Dynamics and Instabilities. Göttingen, Germany, pp. 275-278.

Olivieri, A., Pistani, F., Wilson, R., Campana, E. F., and Stern, F., 2007. Scars and vortices induced by ship bow and shoulder wave breaking. Journal of Fluids Engineering 129, 1445-1459.

Peregrine, D. H., 1983. Breaking waves on beaches. Annual Review of Fluid Mechanics 15, 147-178.

Pope, S. B., 1978. The calculation of turbulent recirculating flows in general orthogonal coordinates. Journal of Computational Physics 26, 197-217.

Raghavan, K., Bernitsas, M. M., 2010. Experimental investigation of Reynolds number effect on vortex induced vibration of rigid circular cylinder on elastic supports. in press in Ocean Engineering.

Reins, G., 2008. Experimental study of an impulsive plunging breaker downstream of a bump in a shallow water open channel flume. Master's Thesis, The University of Iowa, USA.

Roshko, A., 1953, On the drag and shedding frequency of two-dimensional bluff bodies. National Advisory Committee for Aeronautics, NACA TN 3169. (Th. Exp. Notch hodograph theory). 3,5.

Sarghini, F., Piomelli, U., Balaras, E., 1999. Scale-similar models for large-eddy simulations. Physics of Fluids 11(6), 1596-1607.

Shakeri, M., Tavakolinejad, M., and Duncan, J. H., 2009. An experimental investigation of divergent bow waves simulated by a two-dimensional plus temporal wave marker technique. Journal of Fluid Mechanics 634, 217-243.

Shu, C.W. and Osher, S., 1988. Efficient implementation of essentially non oscillatory shock-capturing schemes. Journal of Computational Physics 77, 439-471.

Stern, F., Wilson, R. V., Coleman, H. W., and Paterson, E. G., 2001. Comprehensive approach to verification and validation of CFD simulations-part 1: methodology and procedures. ASME Journal of Fluids Engineering 123, 793-802.

Stern, F., Wilson, R., and Shao, J., 2006. Quantitative V&V of CFD simulations and certification of CFD codes. International Journal for Numerical Methods in Fluids 50, 1335-1355.

Suh, J., Yang, J., and Stern, F., 2011. The effect of air-water interface on the vortex shedding from a vertical circular cylinder. Journal of Fluids and Structure 27, 1-22.

Sujudi, D., Haimes, R., 1975. Identification of swirling flow in 3-D vector fields. AIAA 95-1715.

Sussman, M., Smereka, P., Osher, S., 1994. A level set approach for computing solutions to incompressible two-phase flow. Journal of Computational Physics 114, 146-159.

Tallent, J.R., Yamashita, T., Tsuchiya, Y., 1990. Transformation characteristics of breaking water waves. Water Wave Kinematics 178, 509-523.

Tian, Z., Perlin, M., and Choi, W., 2008. Evaluation of a deep-water wave breaking criterion. Physics of Fluids 20, 1-13.

Wang, Z., Yang, J., Koo, B. G., and Stern, F., 2009. A coupled level set and volume-of-fluid method for sharp interface simulation of plunging breaking waves. International Journal of Multiphase Flow 35, 227-246.

Wang, Z., Yang, J., and Stern, F., 2010. Numerical simulations of wave breakings around a wedge-shaped bow. Proceedings of 28th Symposium on Naval Hydrodynamics, Pasadena, California, September 12-17, 2010.

Waniewski, T. A., 1999. Air entrainment by bow waves. Ph.D. Thesis, California Institute of Technology, Pasadena, California, USA.

Waniewski, T. A., Brennen, C. E., and Raichlen, F., 2002. Bow wave dynamics. Journal of Ship Research 46, 1-15.

Watanabe, Y. and Saeki, H., 2002. Velocity field after wave breaking. International Journal for Numerical Method and Fluids 39, 607-637.

Watanabe, Y., Saeki, H., Hosking, R., 2005. Three-dimensional vortex structures under breaking waves. Journal of Fluid Mechanics 545, 291-328.

Wilson, R. V., Carrica, P. M., Stern, F., 2007. Simulation of a ship breaking bow wave and induced vortices and scars. International Journal for Numerical Method and Fluids 54, 419-451.

Wissink, J. G., Rodi, W., 2008. Numerical study of the near wake of a circular cylinder. International Journal of Heat and Fluid Flow 29, 1060-1070.

Xing, T., Kandasamy, M., Stern, F., 2007. Unsteady free surface wave-induced separation: analysis of turbulent structures using detached eddy simulation and single phase level-set. Journal of Turbulence 8, 1-35.

Xing, T. and Stern, F., 2010. Factors of safety for Richardson extrapolation. ASME Journal of Fluids Engineering 132, 061403.1-13.

Yang, J., Balaras, E., 2006. An embedded-boundary formulation for large-eddy simulation of turbulent flows interacting with moving boundaries. Journal of Computational Physics 215, 12-40.

Yang, J. and Stern, F., 2007. Large-eddy simulation of breaking waves using embedded-boundary/level-set method. In: 45th AIAA Aerospace Sciences Meeting and Exhibit, Reno, Nevada, USA, AIAA Paper 2007-1455.

Yang, J. and Stern, F., 2009. Sharp interface immersed-boundary/level-set method for wave-body interactions. Journal of Computational Physics 228, 6590-6616.

Yao, A. F. and Wu, C. H., 2005. Incipient breaking on unsteady waves on sheared currents. Physics of Fluids 17, 082104-1–082104-10.

Yu, G., Avital, E. J., Williams, J. J. R., 2008. Large eddy simulation of flow past free surface piercing circular cylinders. Journal of Fluids Engineering 130, 10134.1-9.

Zhang, Z. J., Stern, F., 1996. Free-surface wave-induced separation. ASME Journal of Fluids Engineering 118, 546-554.

Zdravkovich, M. M., 1997. Flow around circular cylinders: a comprehensive guide through flow phenomena, experiments, applications, mathematical models, and computer simulations, Fundamentals, vol. 1. Oxford University Press, New York, NY.

APPENDIX A

PLUNGING WAVE BREAKING SIMULATION USING CARTESIAN GRID SOLVER (CG0, CG2, AND CG3)

Initially, the grid CG0 was used to guide systematic grid generations and it has 48 more points in the z direction than the coarse grid (CG3) and has similar plunging wave breaking positions as the medium grid (CG2). This chapter discusses the plunging wave breaking simulations with other grids (CG0, CG2, and CG3). The general trends are similar to simulations with the fine grid, which is shown in the previous chapter 3. The results are also compared with previous experimental and computational studies.

Table A.1 Percentage of the plunging breaking wave time phase for each of the sub-events for CG0

Time	**$\Delta t_T'$ =15.9 s**		**$\%\Delta t_T'$**				
-13.53 s	-		-			Startup	
-1.76 s	Δt_S =11.77 s		74				
-	Δt_{SWF} =	-	11			Steep wave formation	
0.0 s	1.76 s	1.76 s					
-	Δt_{PWB} = 2.37 s	Δt		$\%\Delta t_{PWB}$	Δt	Plunging wave breaking	
0.25 s		0.25 s	P1 16.9%	10.6	0.4		1st plunge
0.29 s		0.1 s		1.7			1st oblique splash
0.4 s		0.11 s		4.6			1st vertical jet
0.99 s		0.59 s	P2 57%	24.9	1.35		2nd plunge
1.04 s		0.05 s		2.1			2nd oblique splash
1.07 s		0.03 s		1.2			2nd vertical jet
1.75 s		0.68 s		28.7			3rd plunge
1.79 s		0.04 s	P3 8%	1.7	0.19		3rd oblique splash
1.94 s		0.15 s		6.3			3rd vertical jet and 4th plunge
2.27 s		0.33 s	P4 18.1%	14	0.43		4th oblique splash
2.37 s		0.1 s		4.2			4th vertical jet

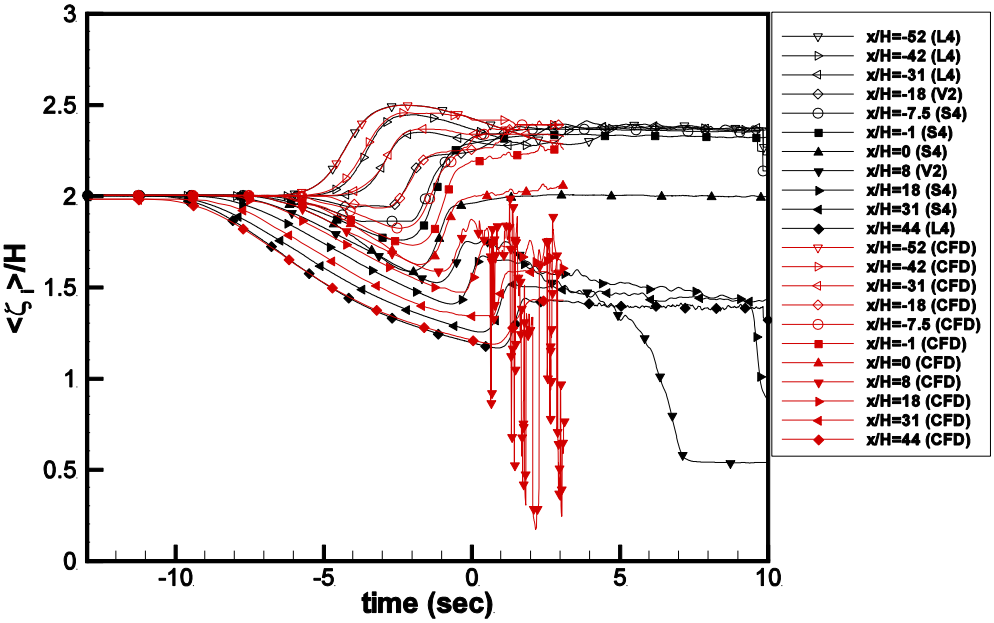

(a)

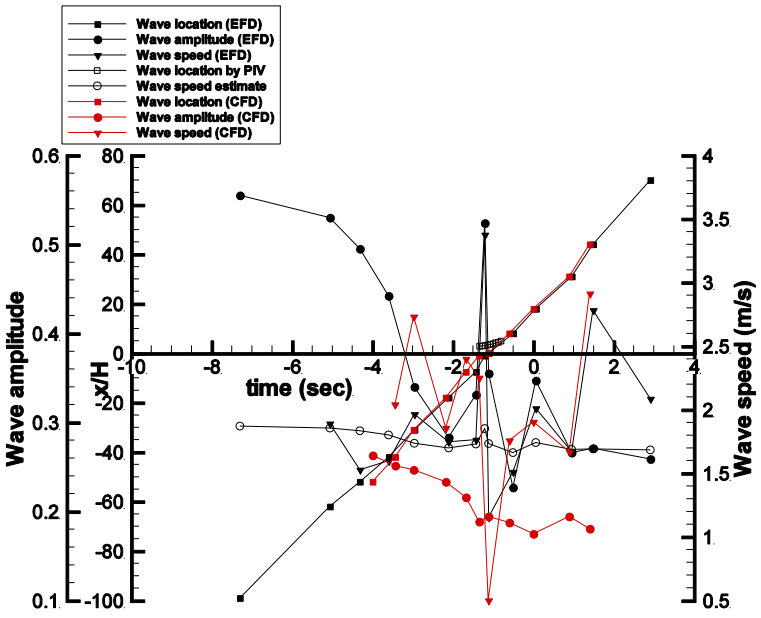

(b)

Figure A.1 Time history: (a) water elevations; (b) acceleration wave location, speed, and amplitude (CG0)

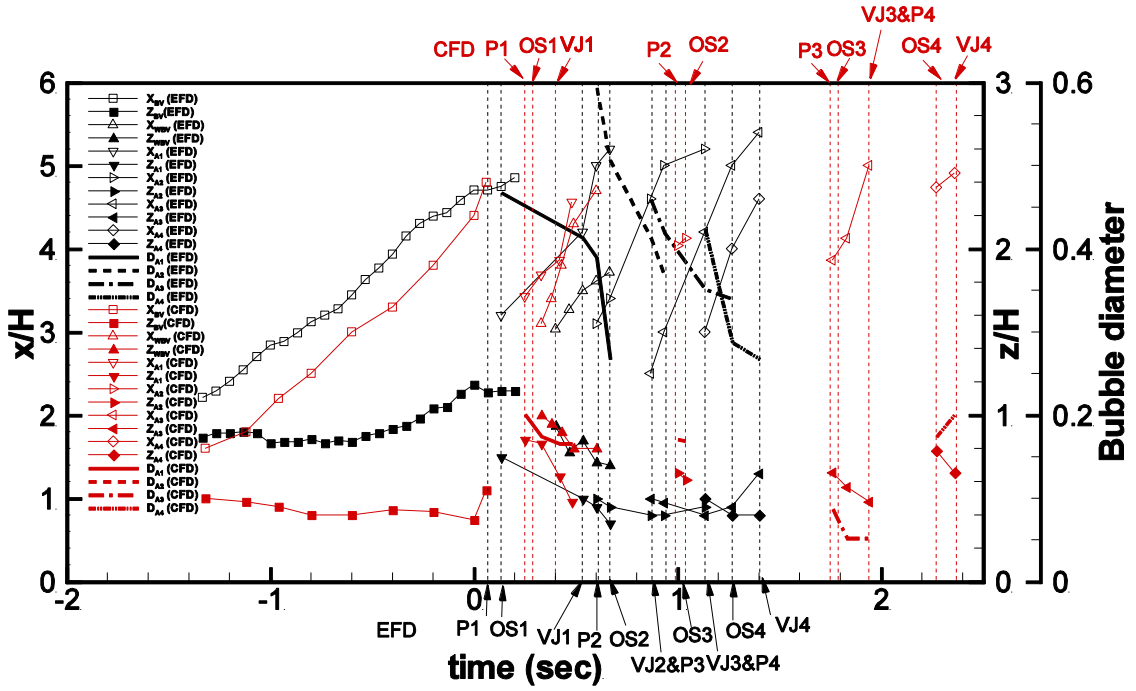

Figure A. 2 Time history of vortex and air entrainment paths, and air bubble size. Red: CFD; black: EFD (CG0)

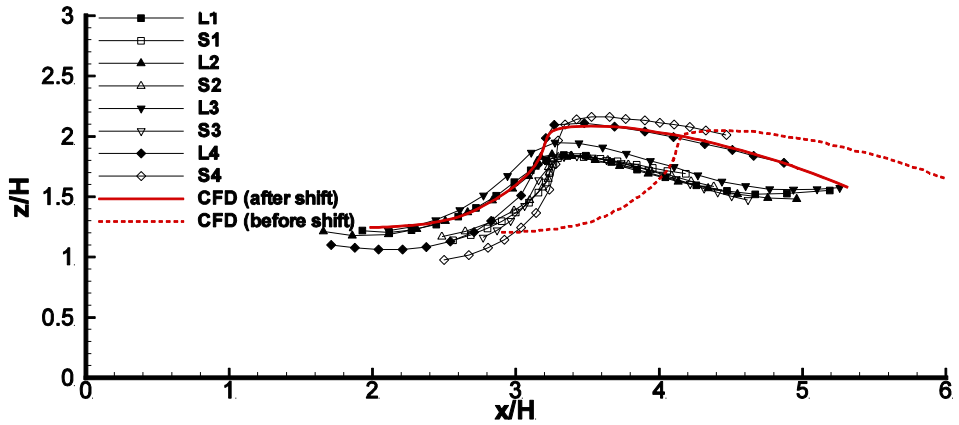

(a)

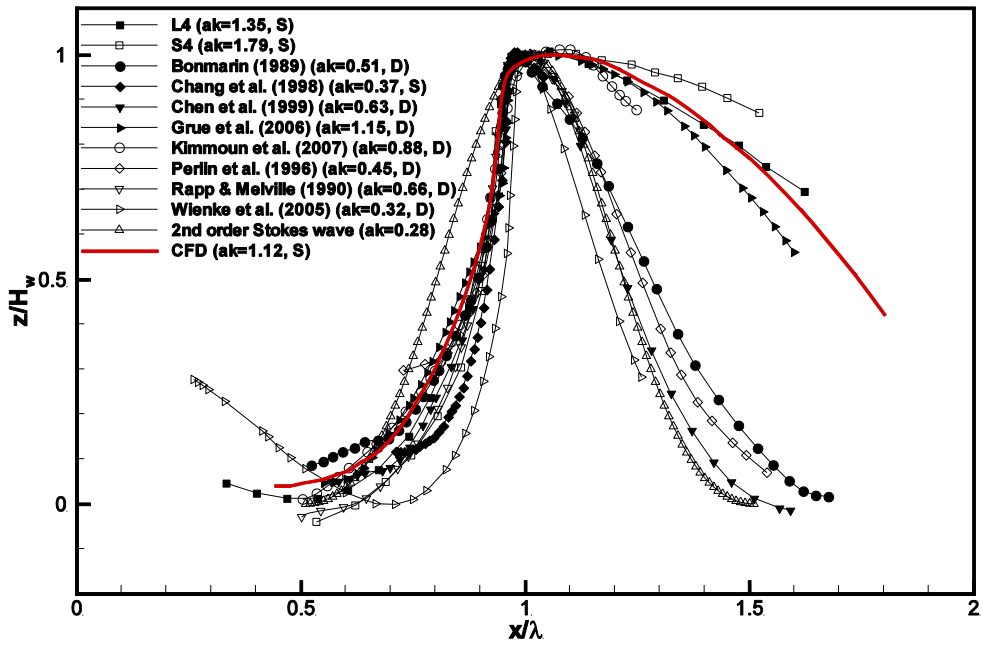

(b)

Figure A.3 Wave profile comparison with EFD. (a) CFD profile; (b) non-dimensional with wave length (λ) and wave height (H_w) at t_b in X, Z, respectively (CG0)

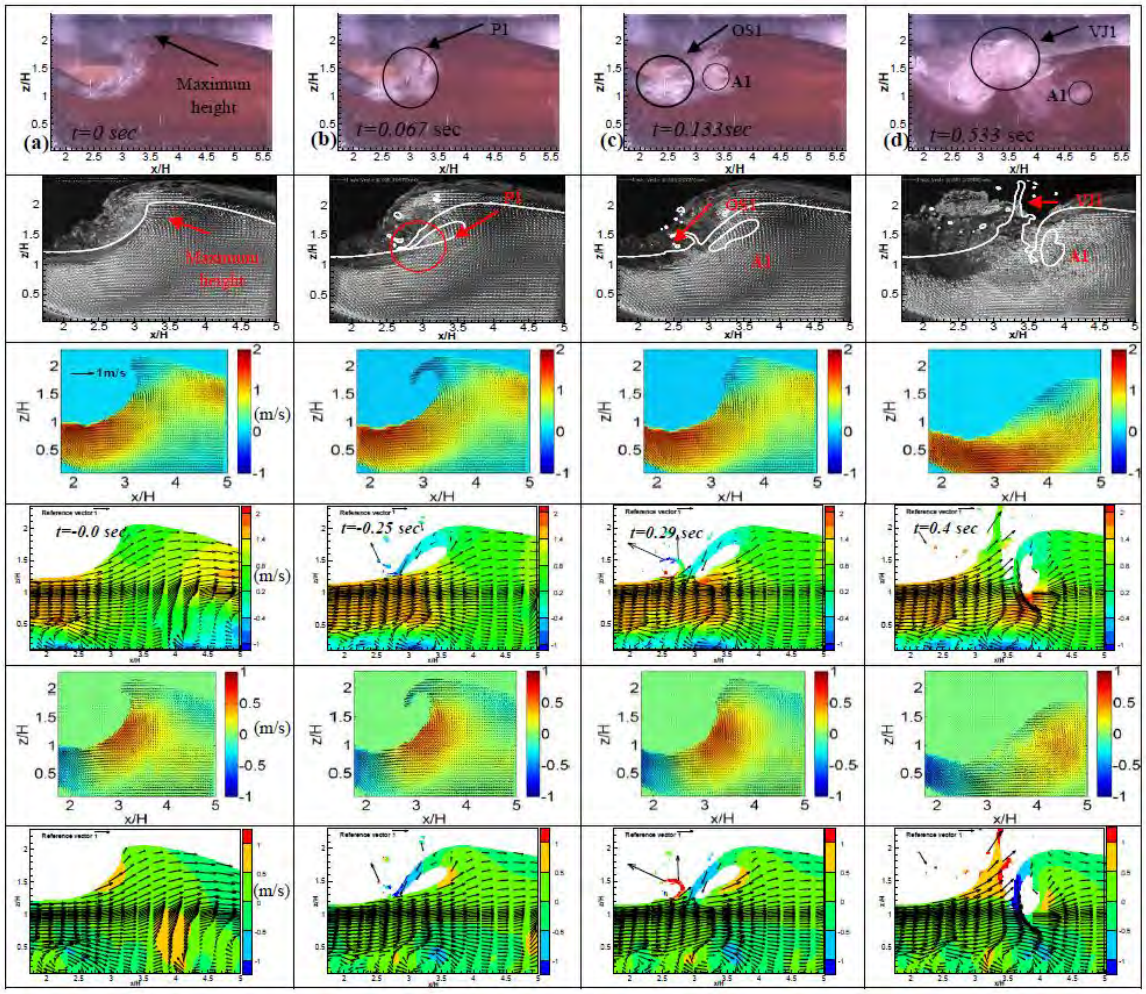

Figure A.4 Video images (Reins, 2008); PIV image with CFD; EFD U velocity contours; CFD U velocity contours; EFD W velocity contours; CFD W velocity contours (CG0)

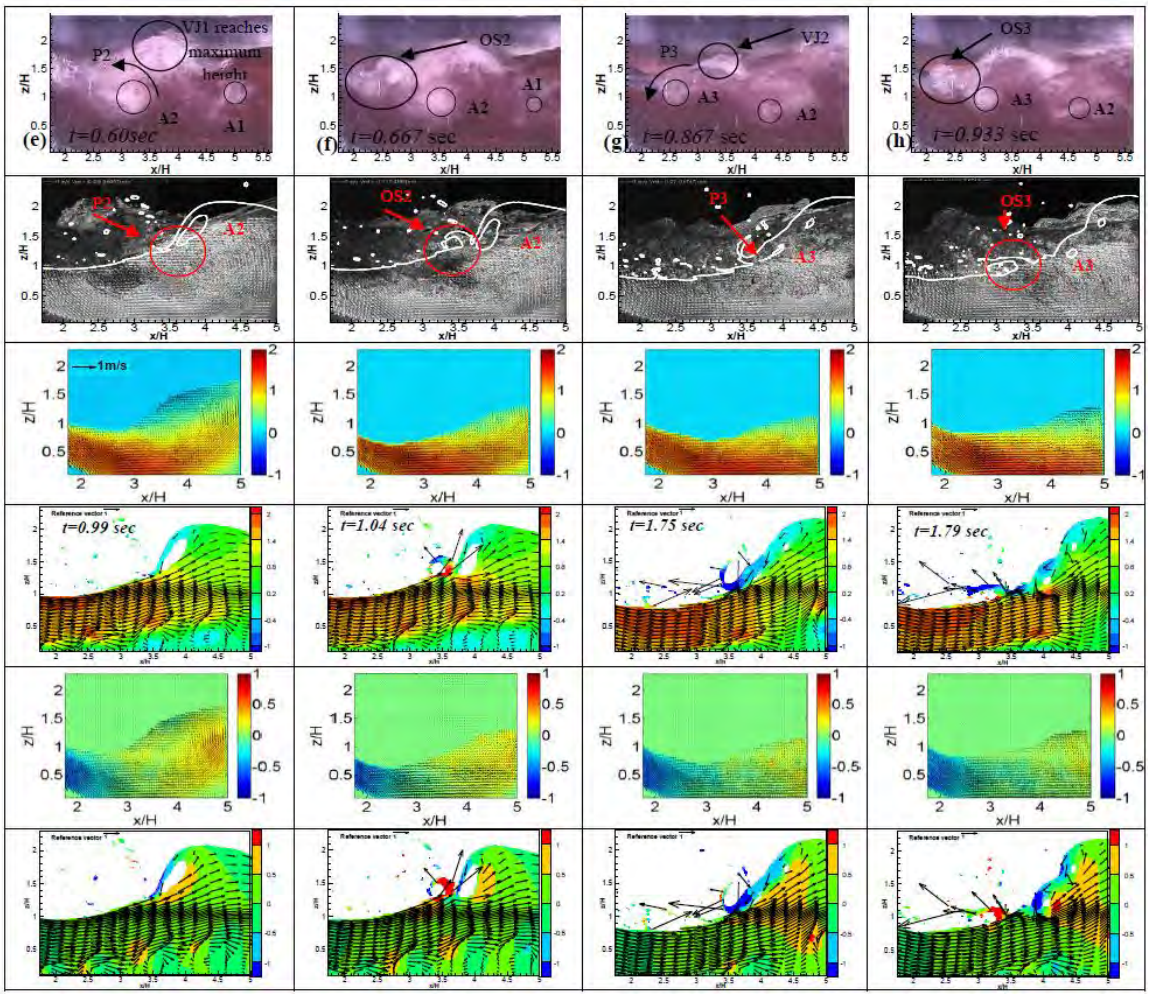

Figure A.4 (continued)

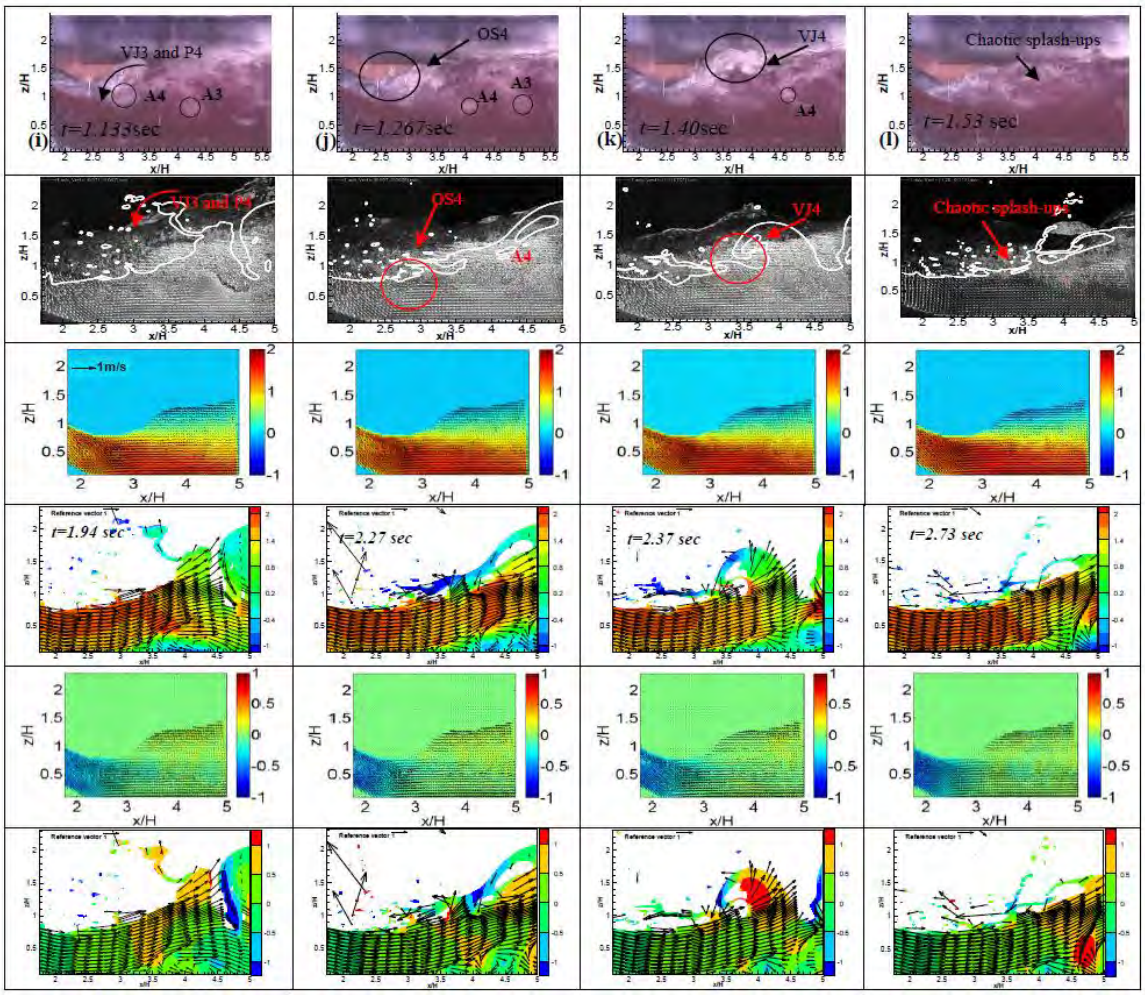

Figure A.4 (continued)

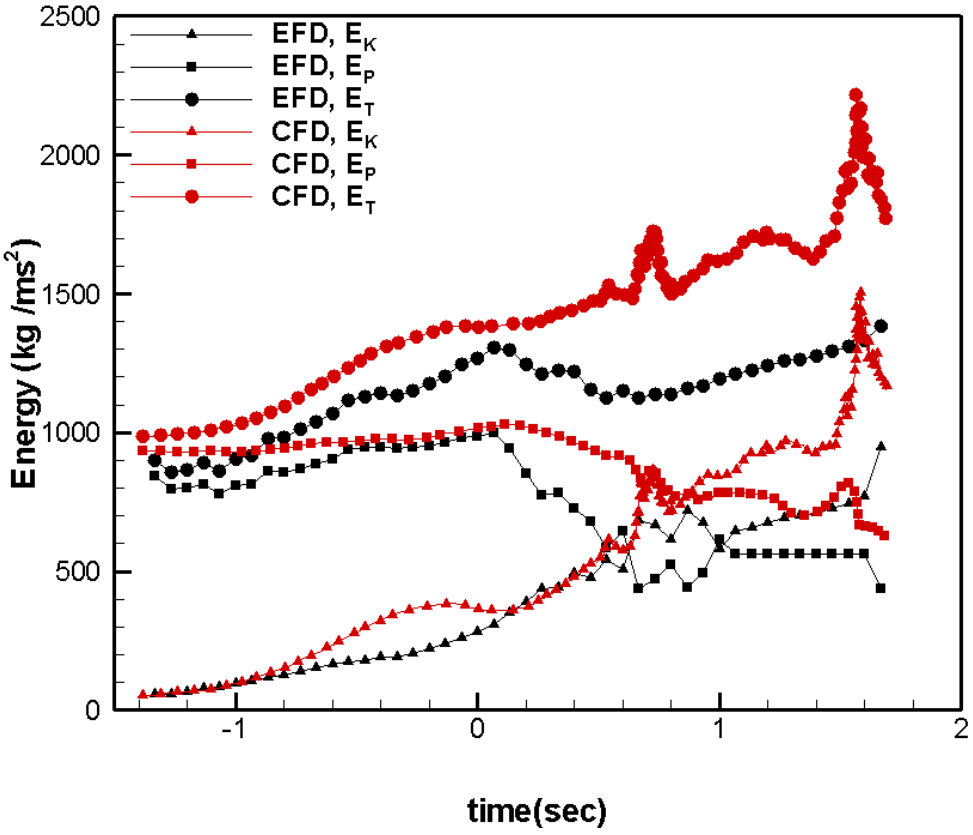

Figure A.5 Time evolutions of the total energy, the wave kinetic energy, the wave potential energy (CG0)

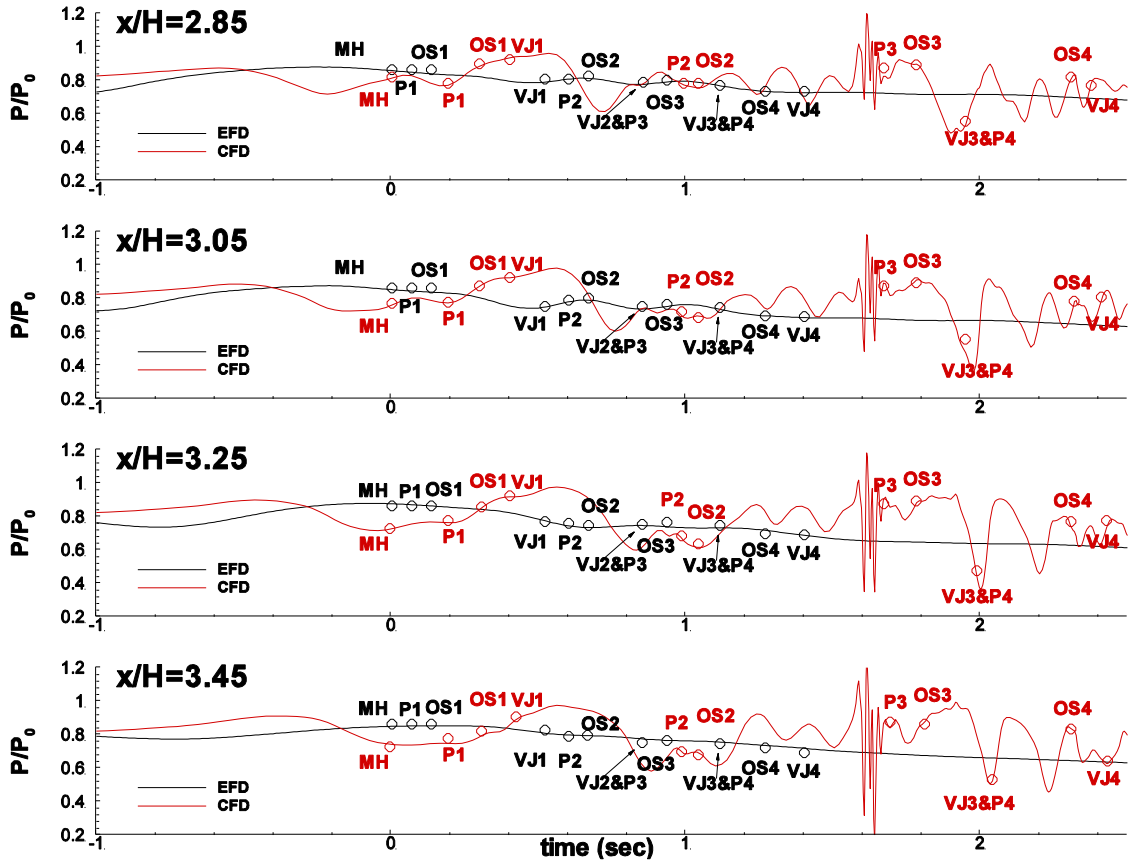

Figure A.6 Average pressure time series for EFD and CFD at various stream-wise positions (CG0)

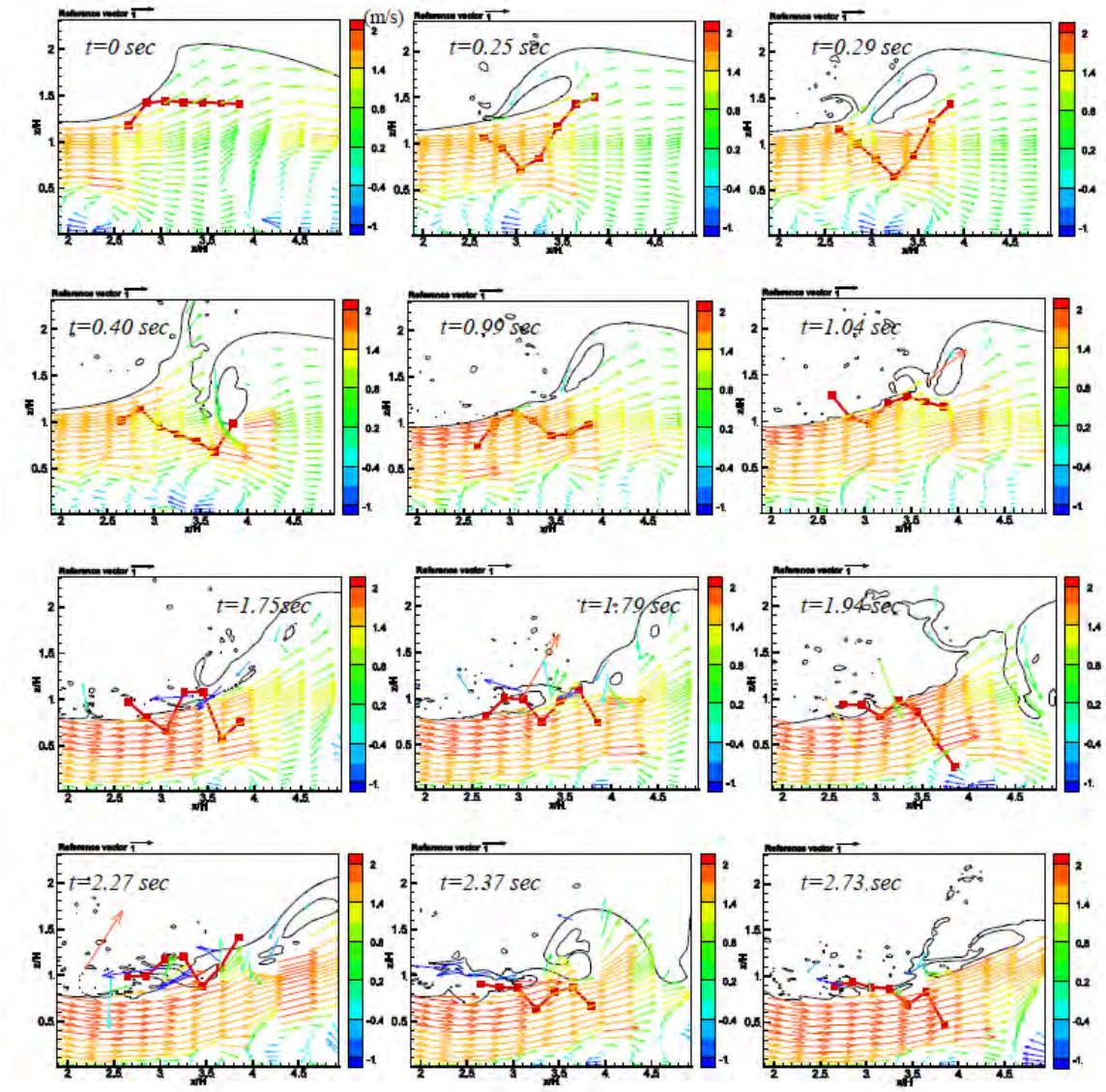

Figure A.7 CFD with overlaid vector field and water height normalized by bump height describing breaking events (CG0)

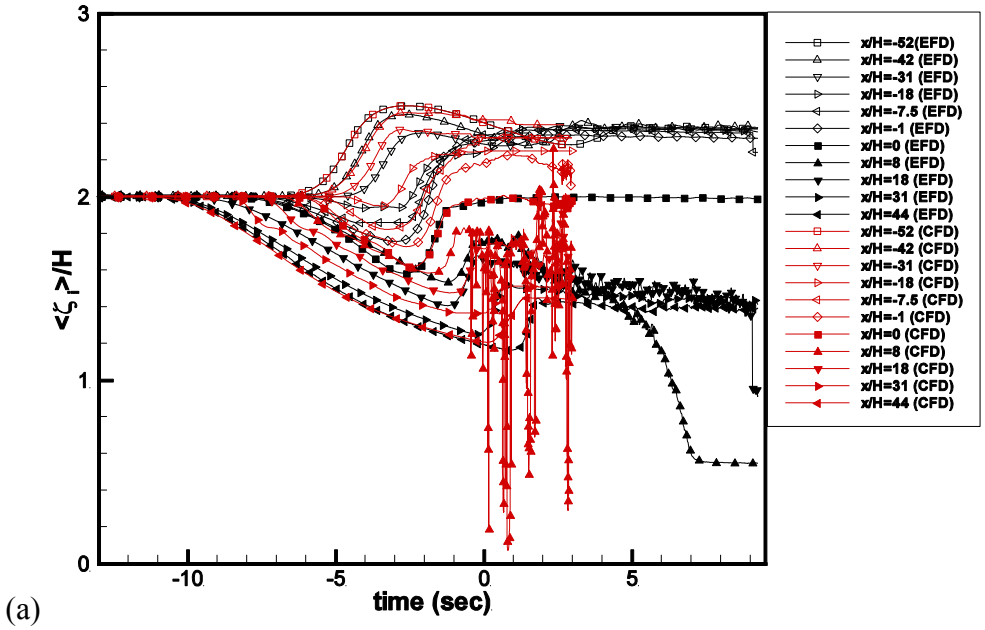

(a)

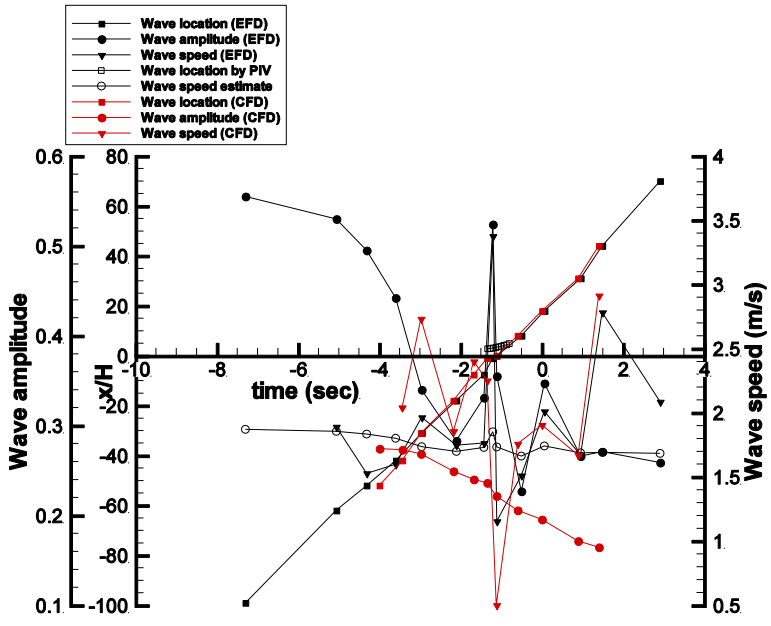

(b)

Figure A.8 Time history: (a) water elevations; (b) acceleration wave location, speed, and amplitude (CG2)

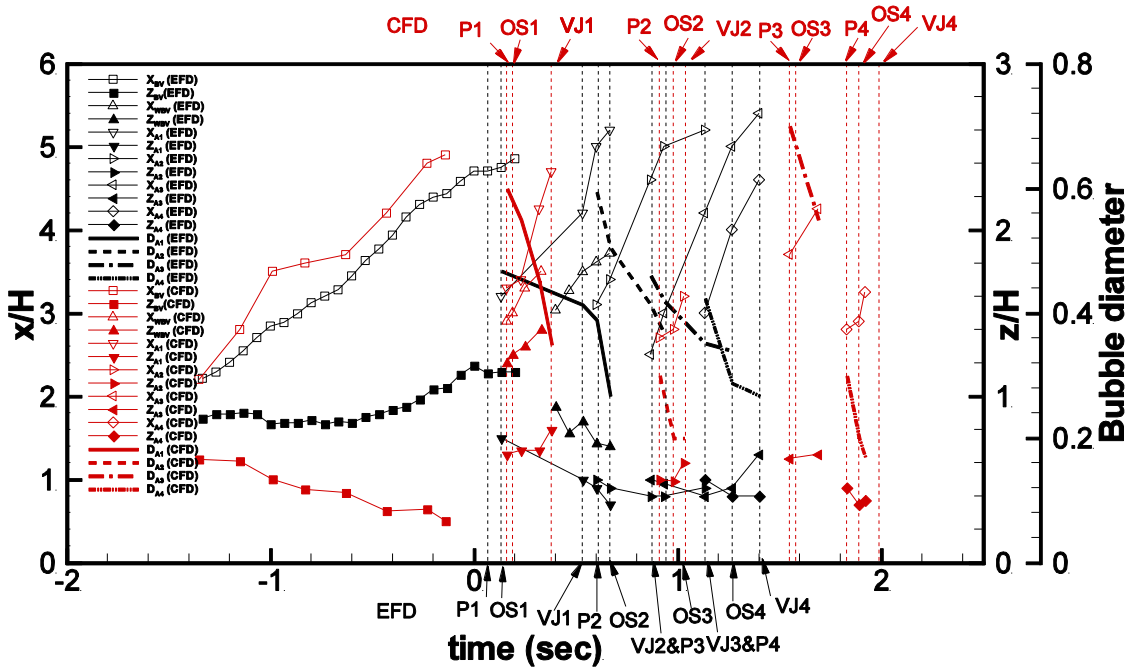

Figure A.9 Time history of vortex and air entrainment paths, and air bubble size. Red: CFD; black: EFD (CG2)

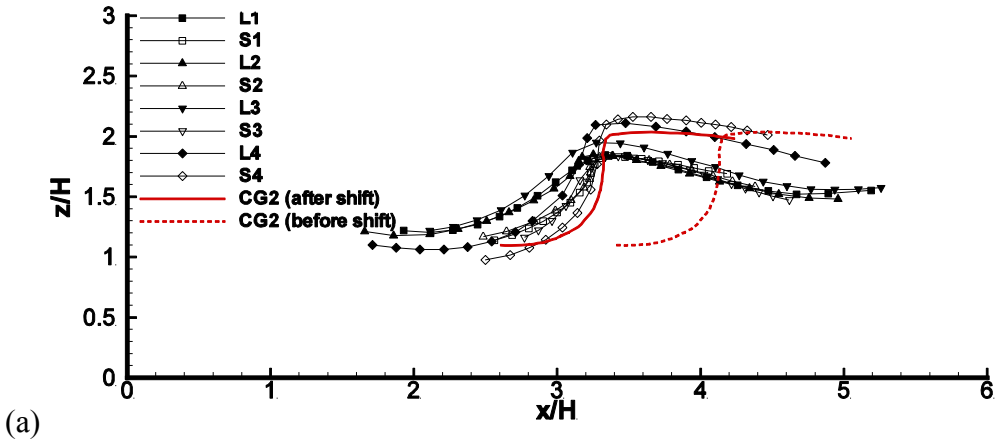

(a)

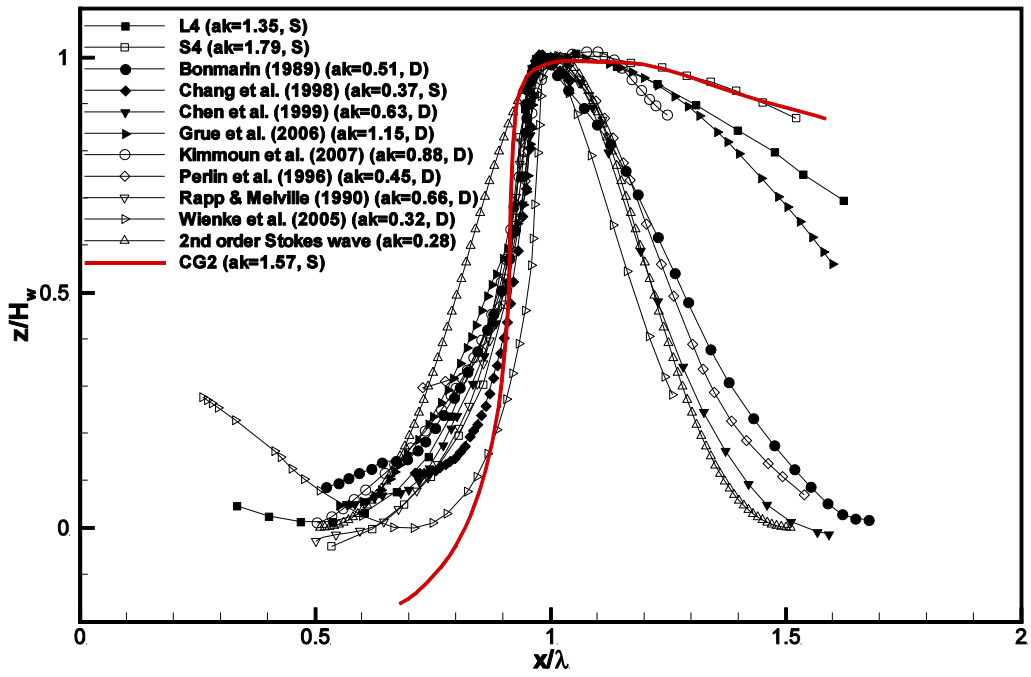

(b)

Figure A.10 Wave profile comparison with EFD. (a) CFD profile; (b) non-dimensional with wave length (λ) and wave height (H_w) at t_b in X, Z, respectively (CG2).

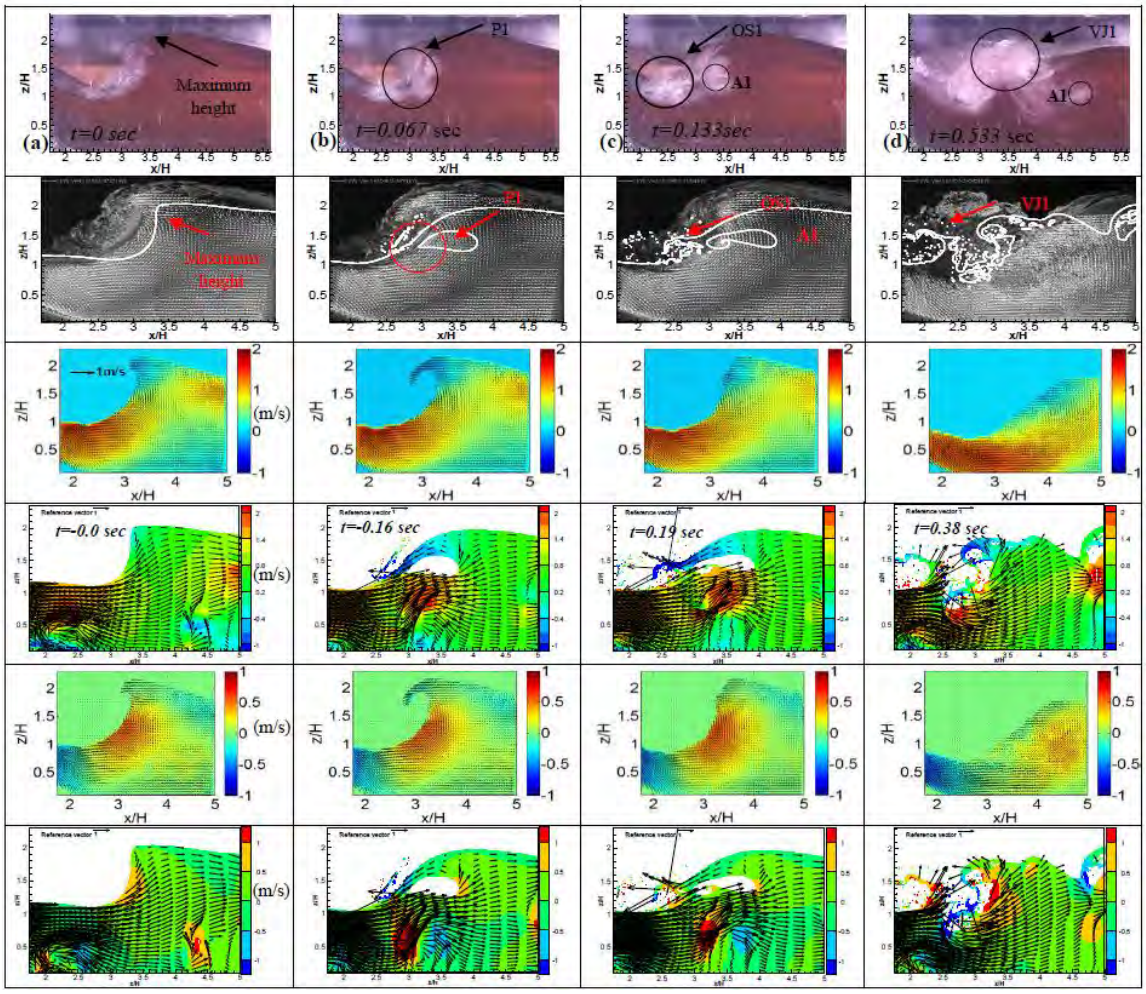

Figure A.11 Video images (Reins, 2008); PIV image with CFD; EFD U velocity contours; CFD U velocity contours; EFD W velocity contours; CFD W velocity contours (CG2)

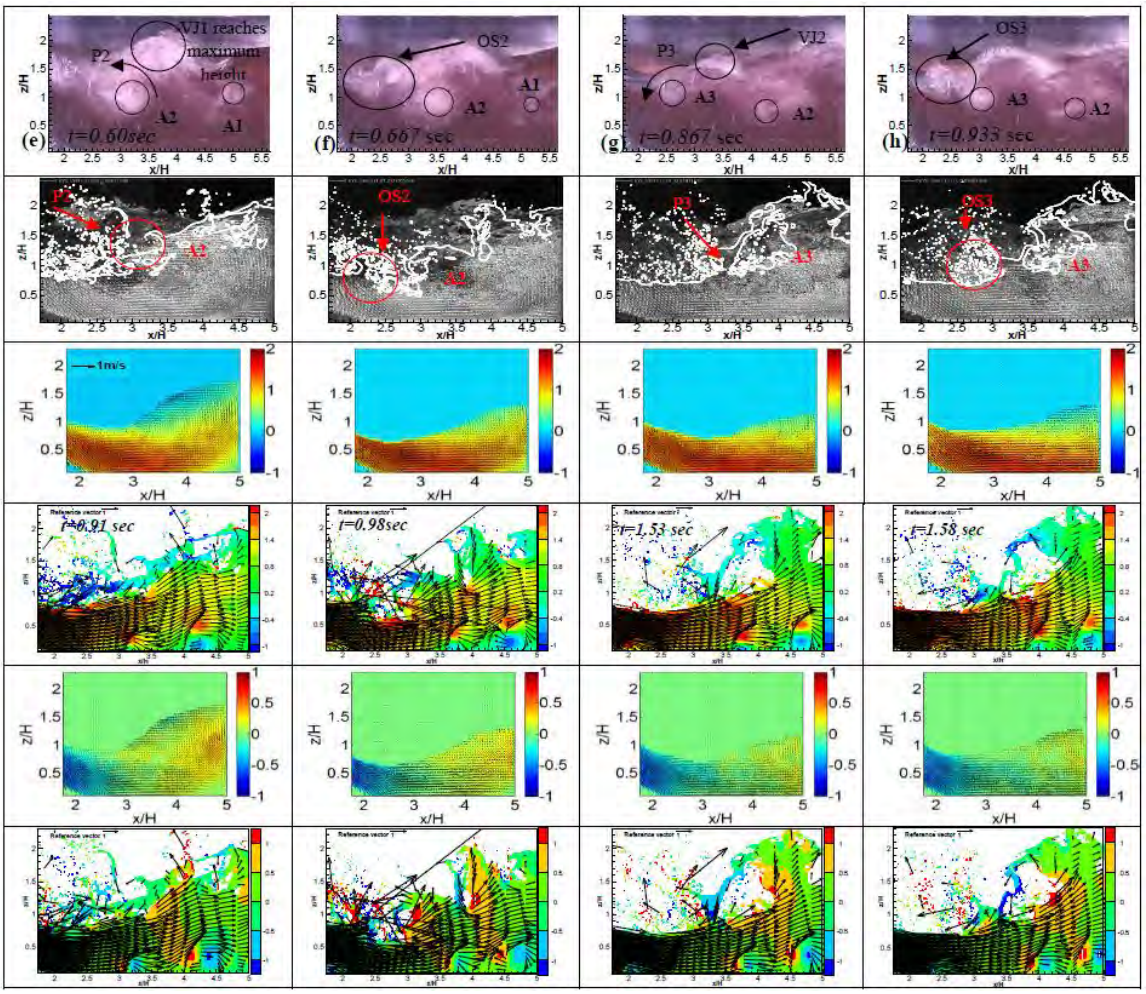

Figure A.11 (continued)

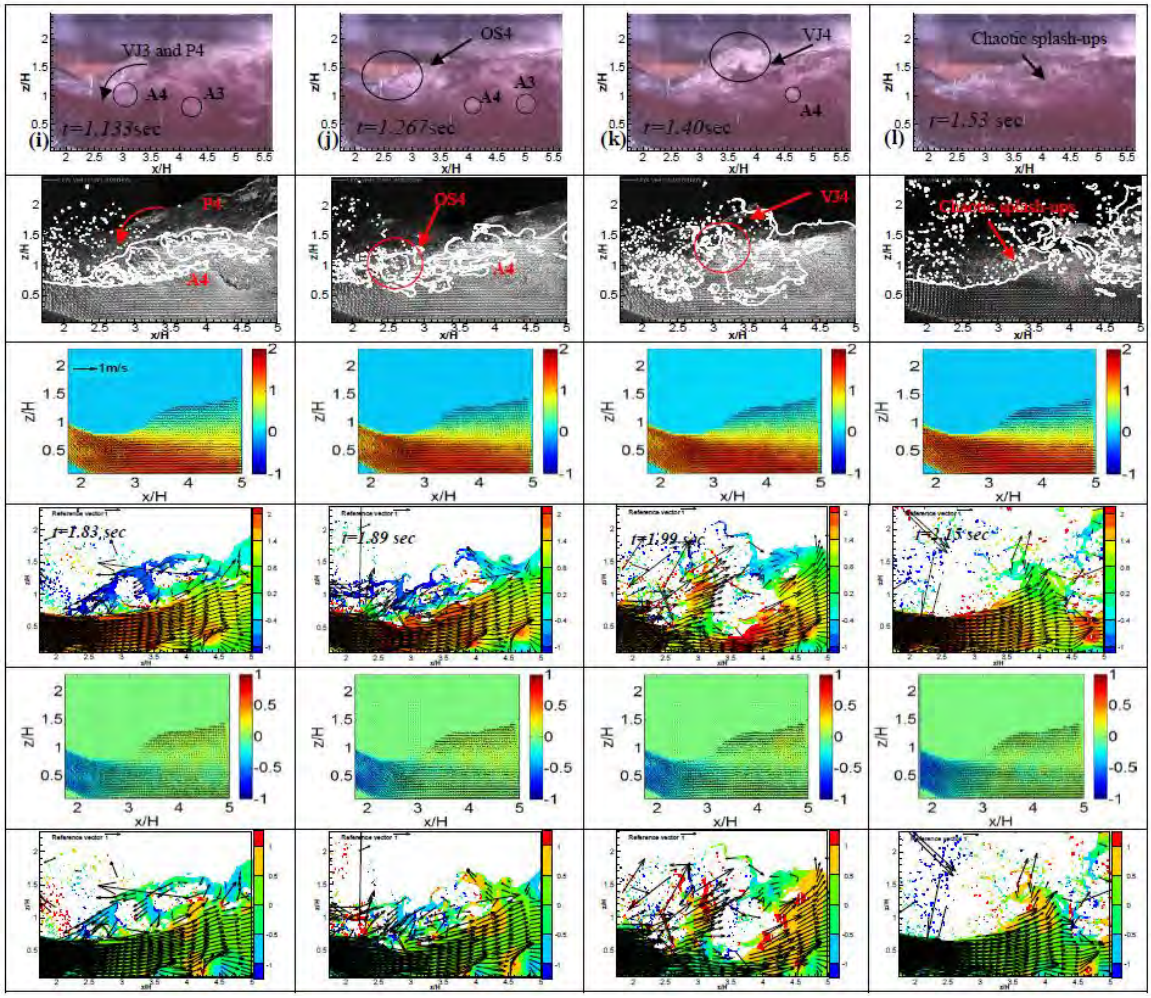

Figure A.11 (continued)

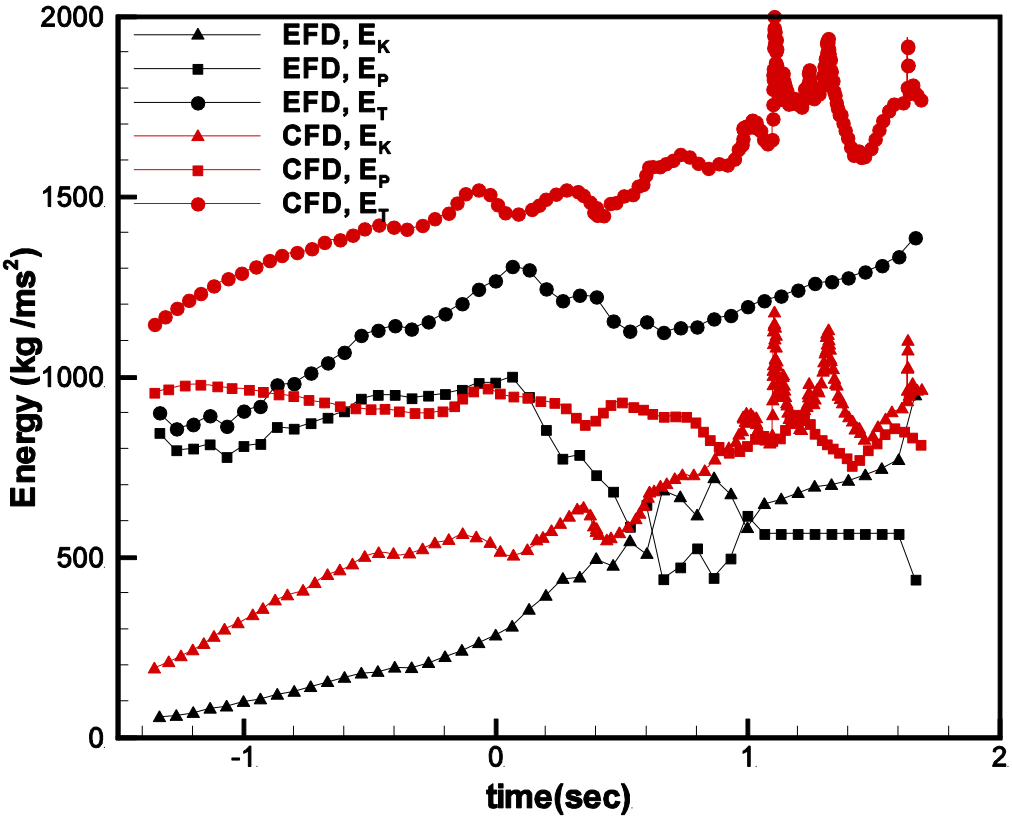

Figure A.12 Time evolutions of the total energy, the wave kinetic energy, the wave potential energy (CG2)

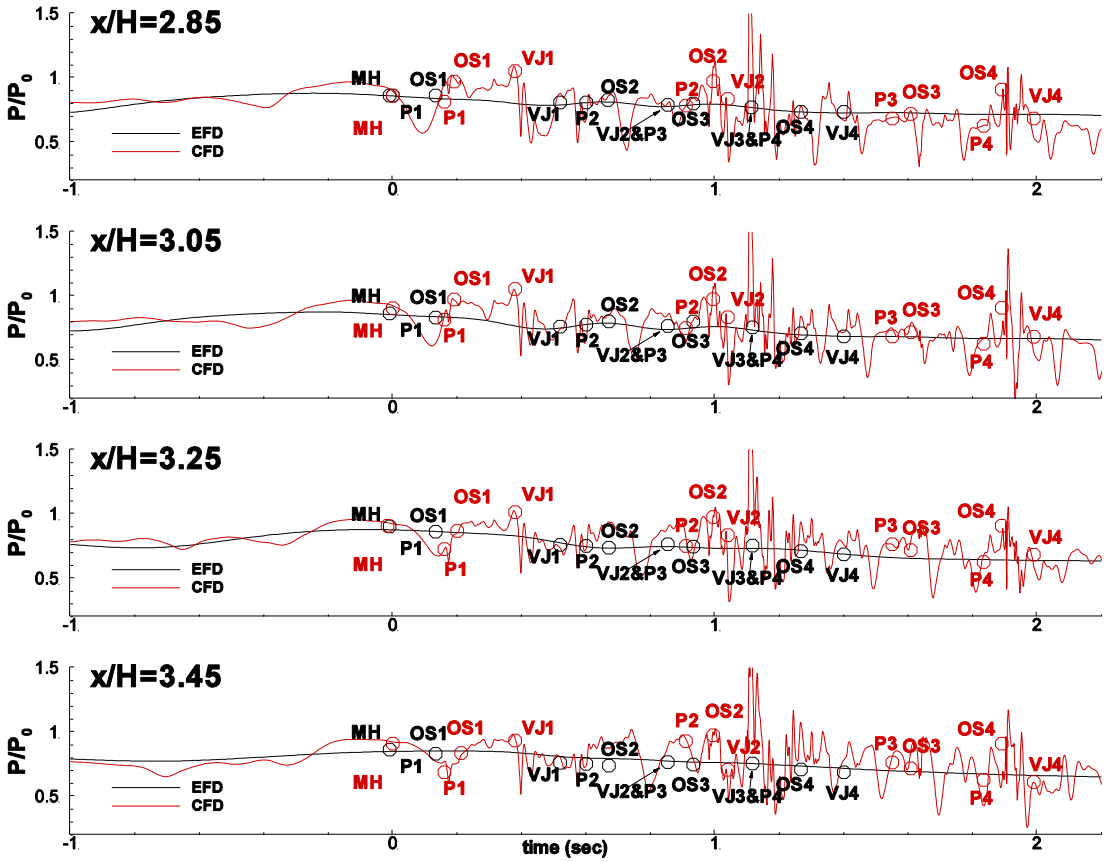

Figure A.13 Average pressure time series for EFD and CFD at various stream-wise positions (CG2).

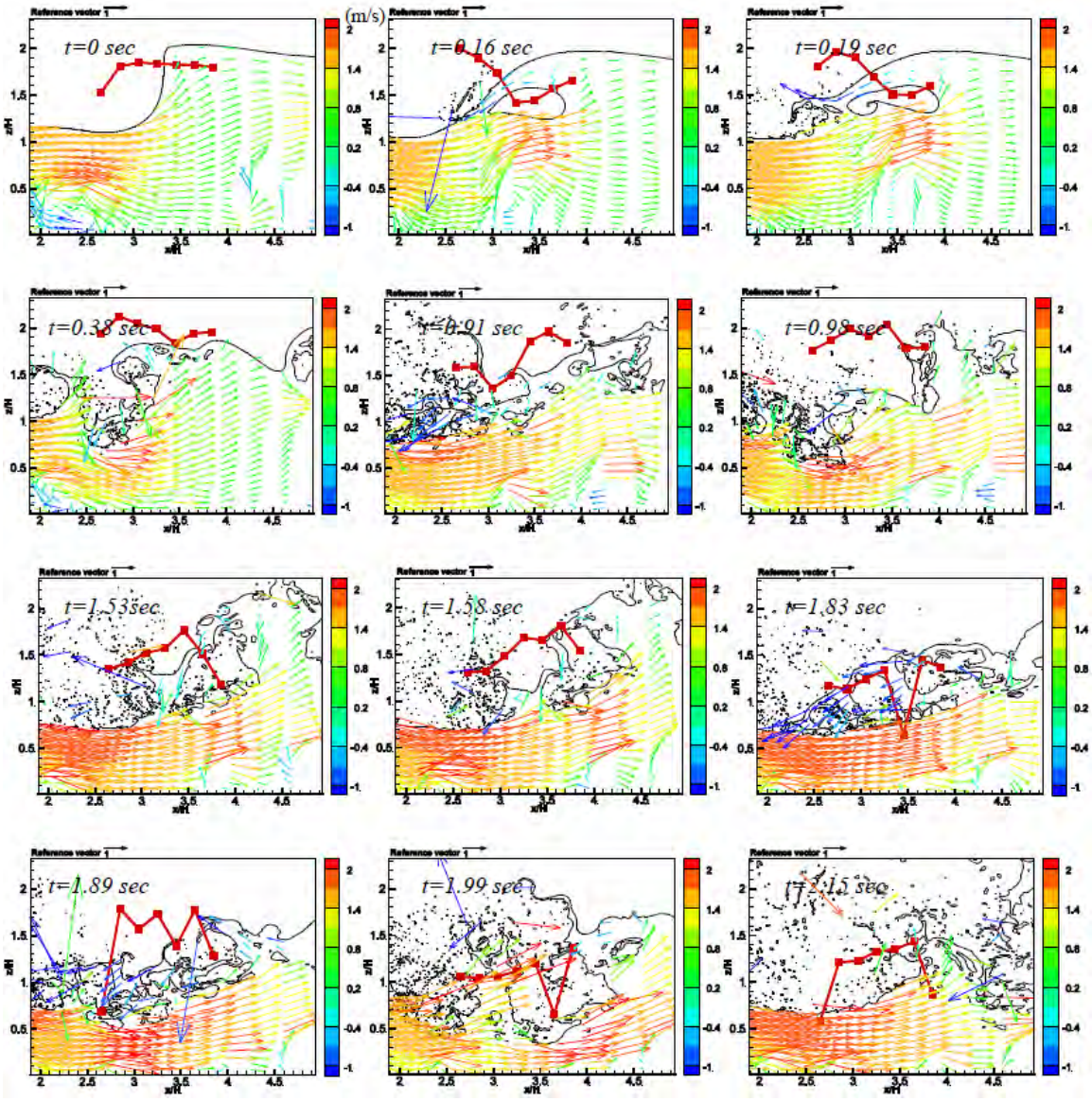

Figure A.14 CFD with overlaid vector field and water height normalized by bump height describing breaking events (CG2)

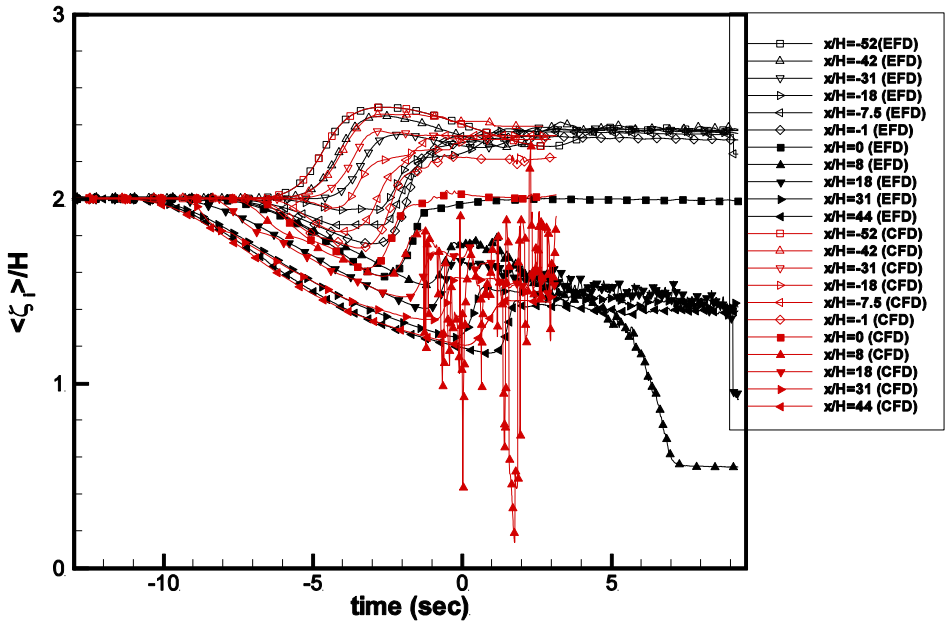

(a)

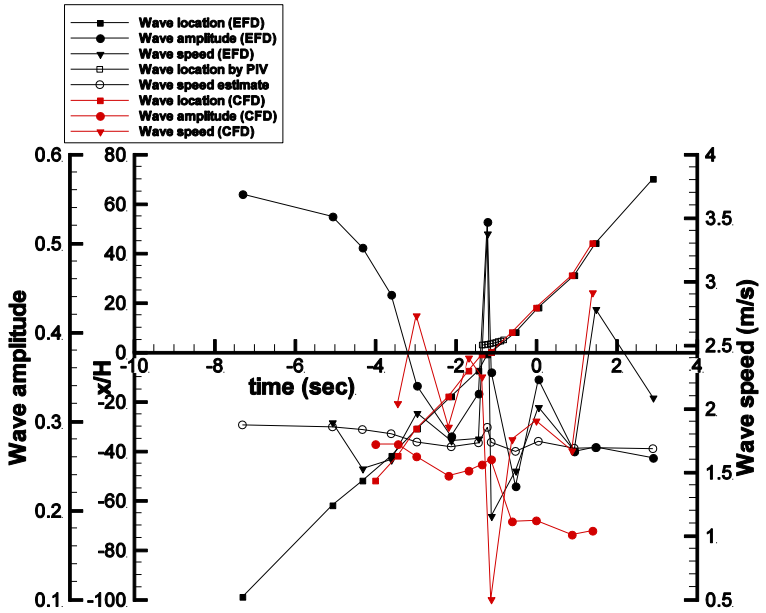

(b)

Figure A.15 Time history: (a) water elevations; (b) acceleration wave location, speed, and amplitude (CG3)

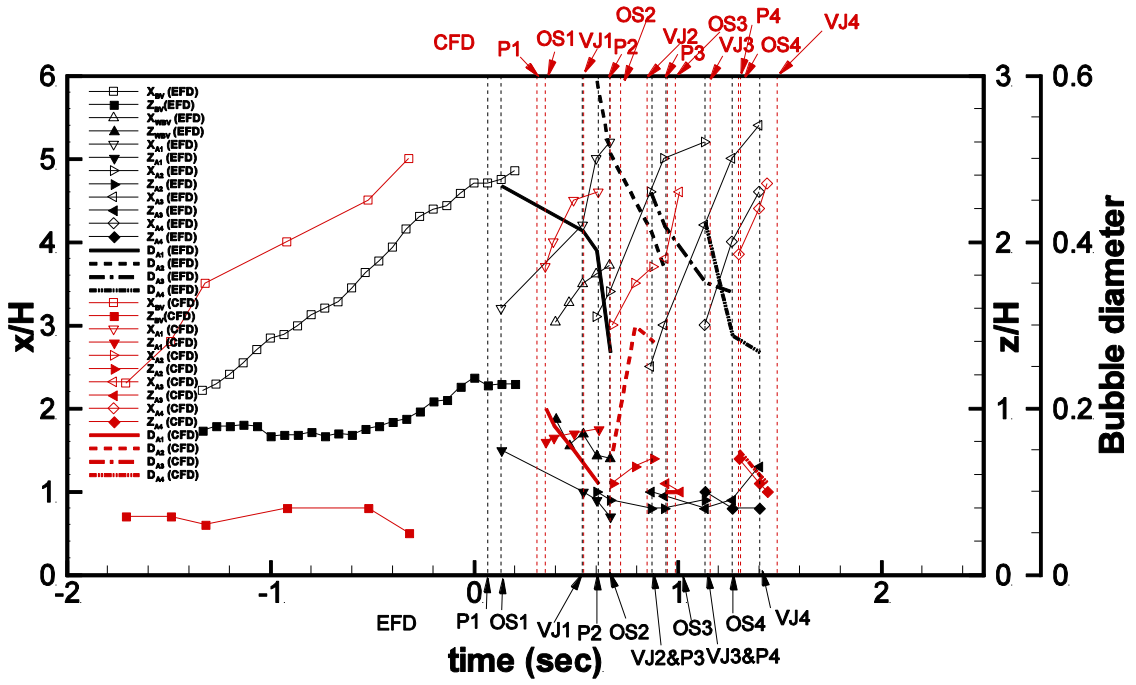

Figure A.16 Time history of vortex and air entrainment paths, and air bubble size. Red: CFD; black: EFD (CG3)

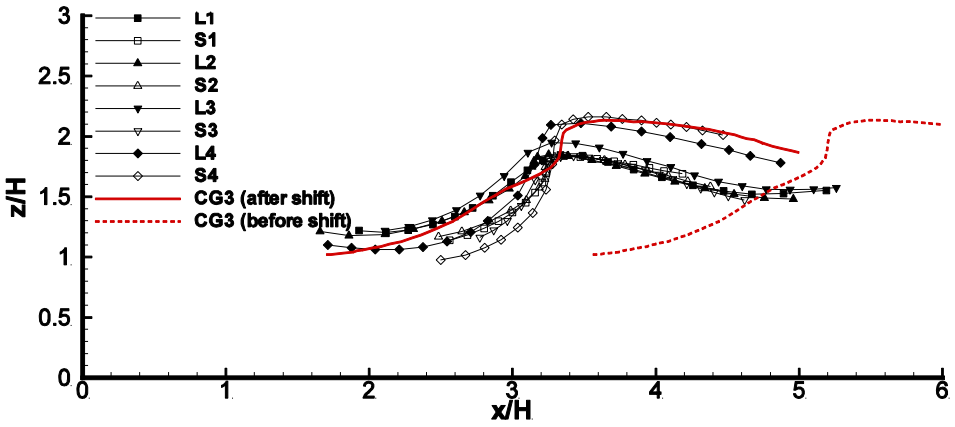

(a)

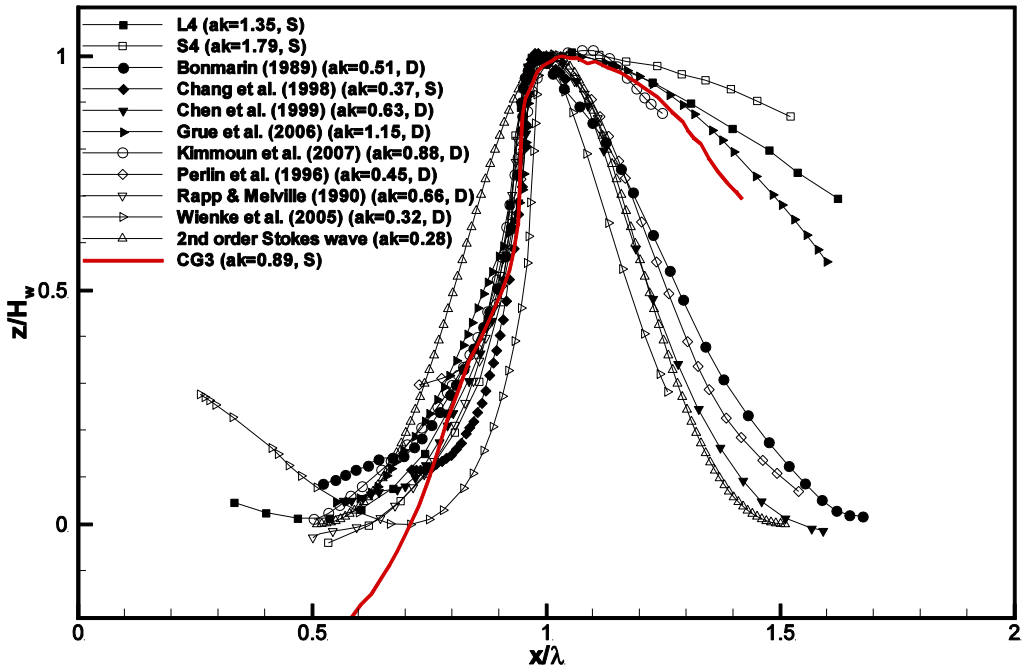

(b)

Figure A.17 Wave profile comparison with EFD. (a) CFD profile; (b) non-dimensional with wave length (λ) and wave height (H_w) at t_b in X, Z, respectively (CG3)

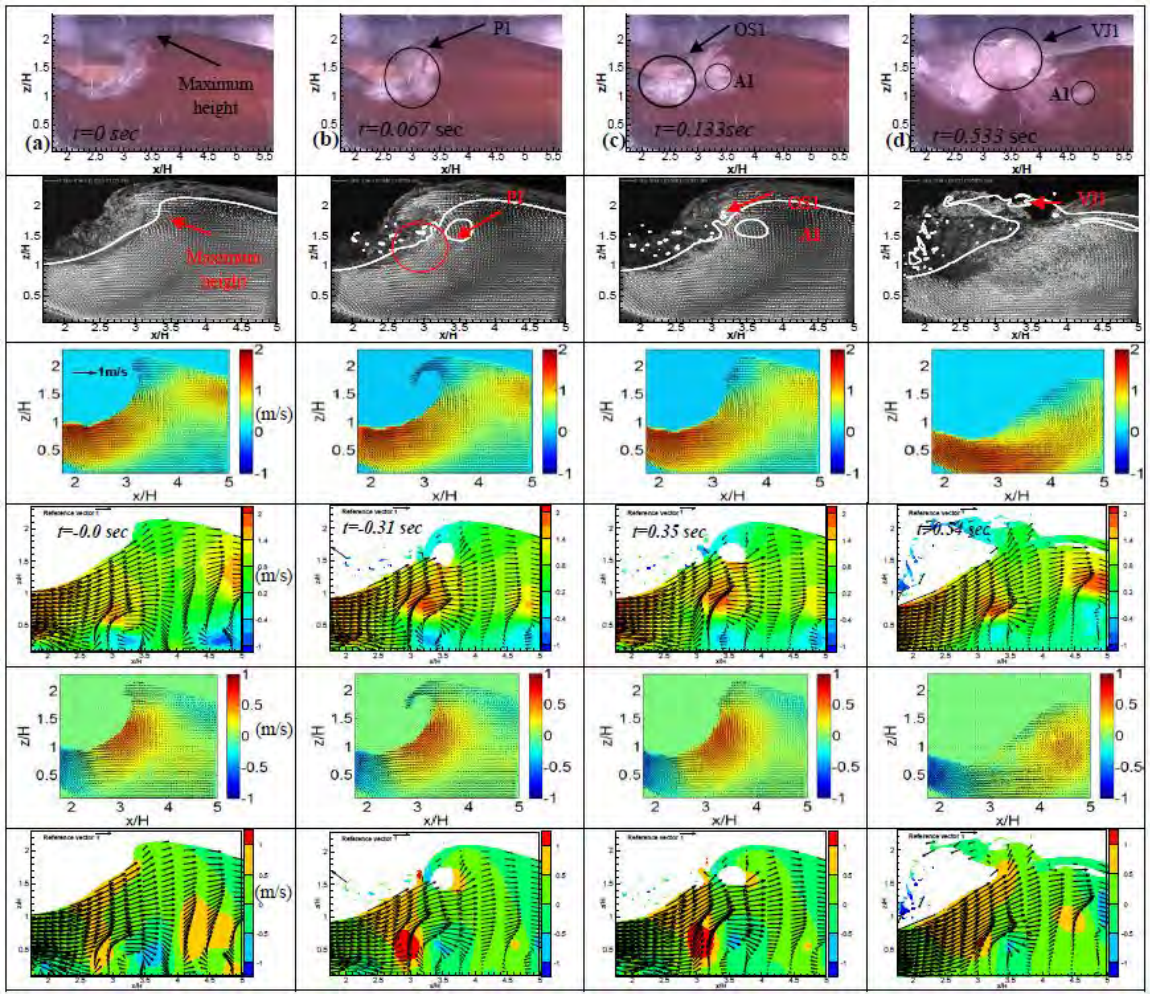

Figure A.18 Video images (Reins, 2008); PIV image with CFD; EFD U velocity contours; CFD U velocity contours; EFD W velocity contours; CFD W velocity contours (CG3)

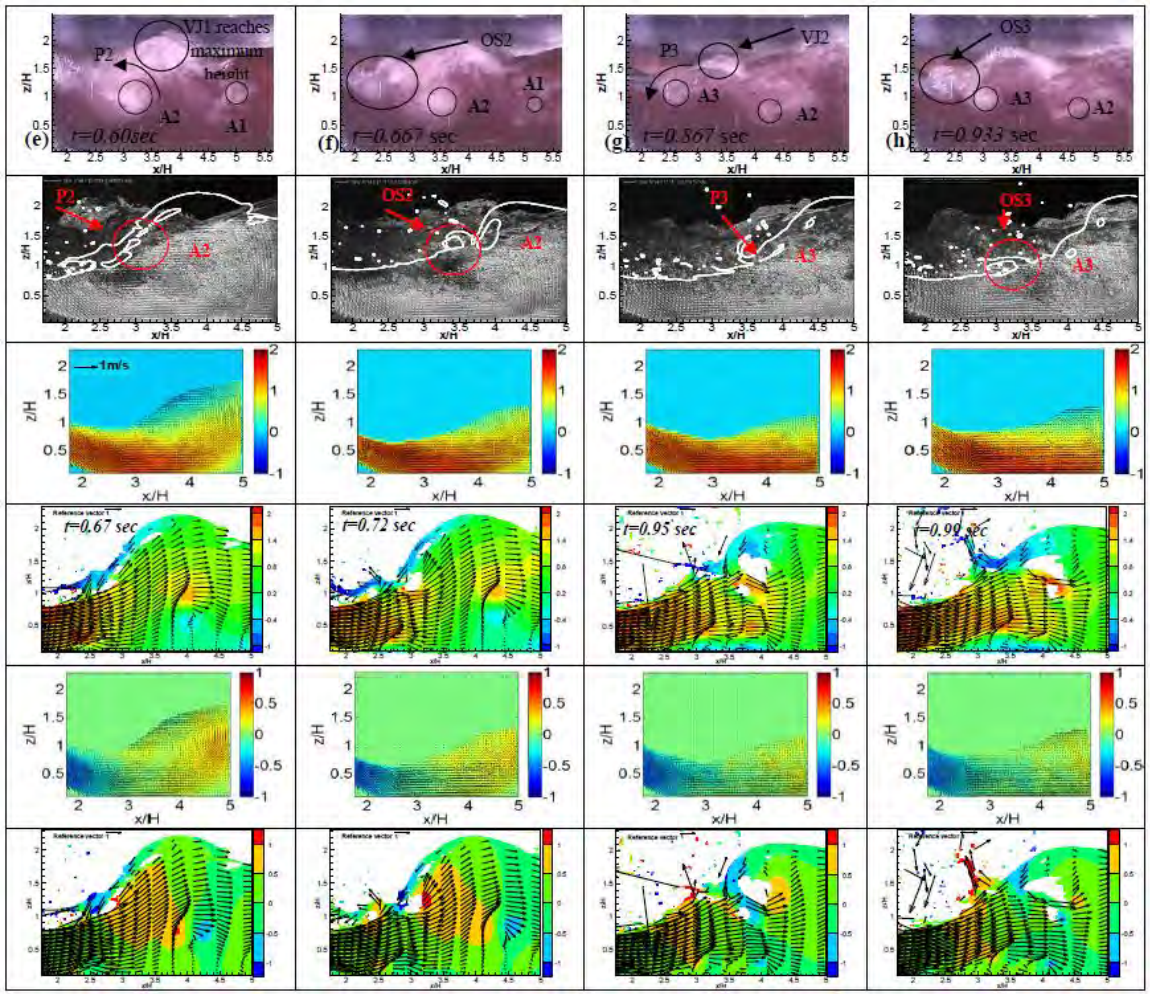

Figure A.18 (continued)

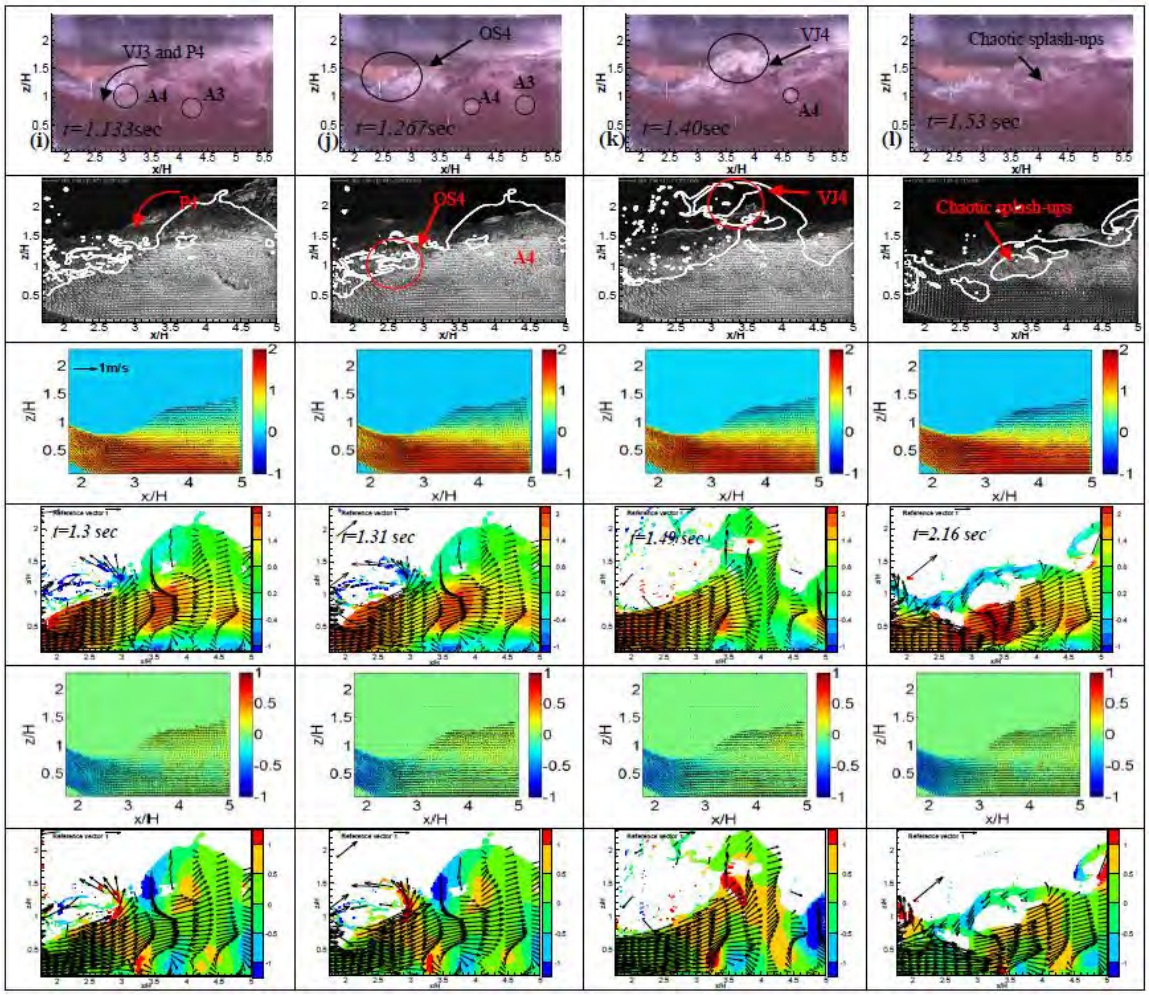

Figure A.18 (continued)

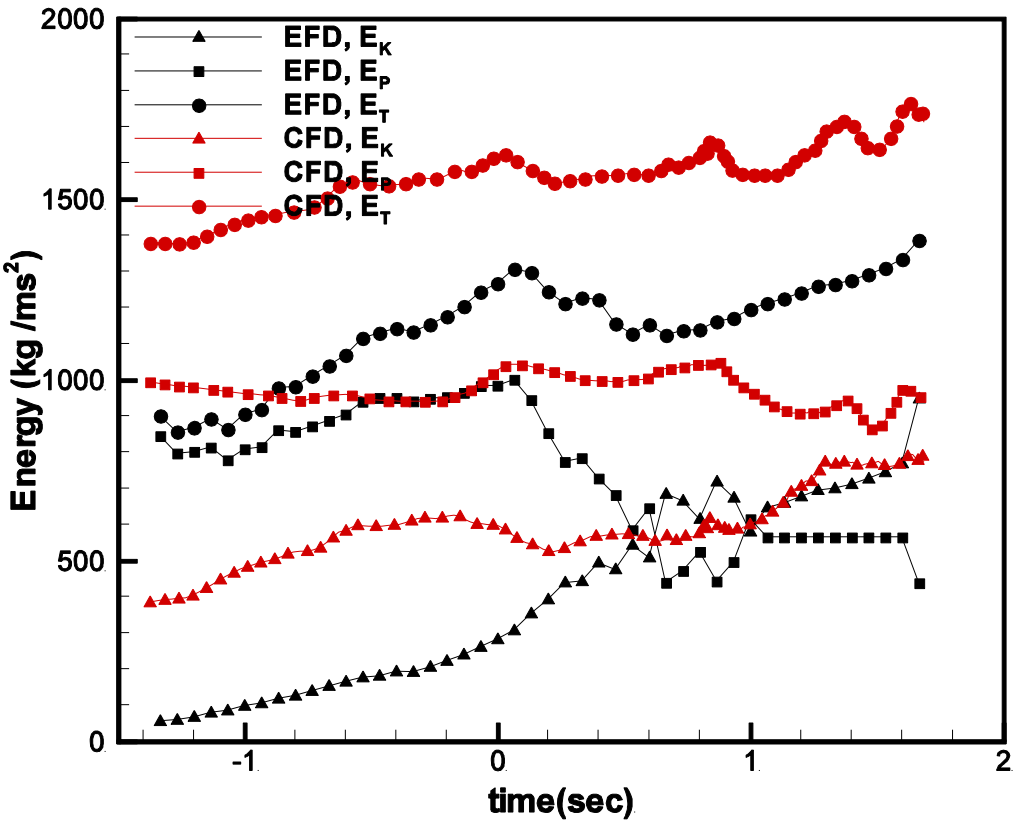

Figure A.19 Time evolutions of the total energy, the wave kinetic energy, the wave potential energy (CG3)

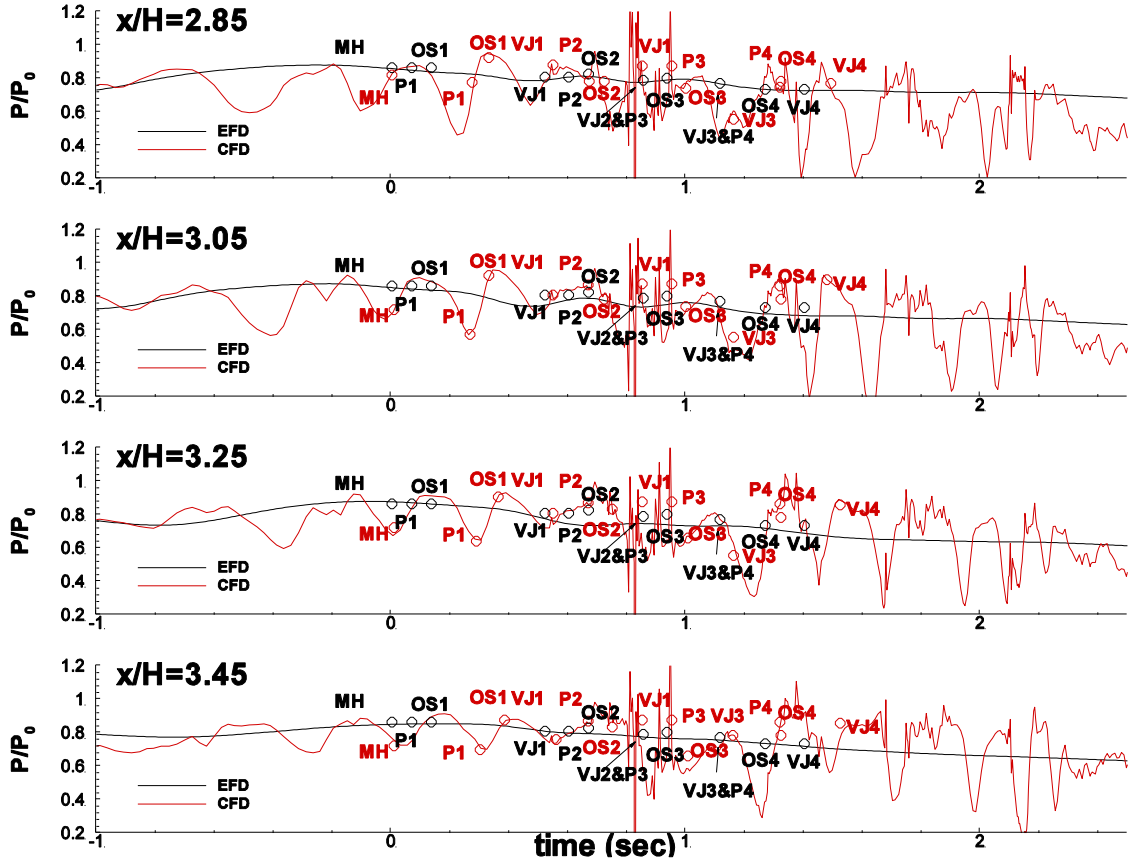

Figure A.20 Average pressure time series for EFD and CFD at various stream-wise positions (CG3)

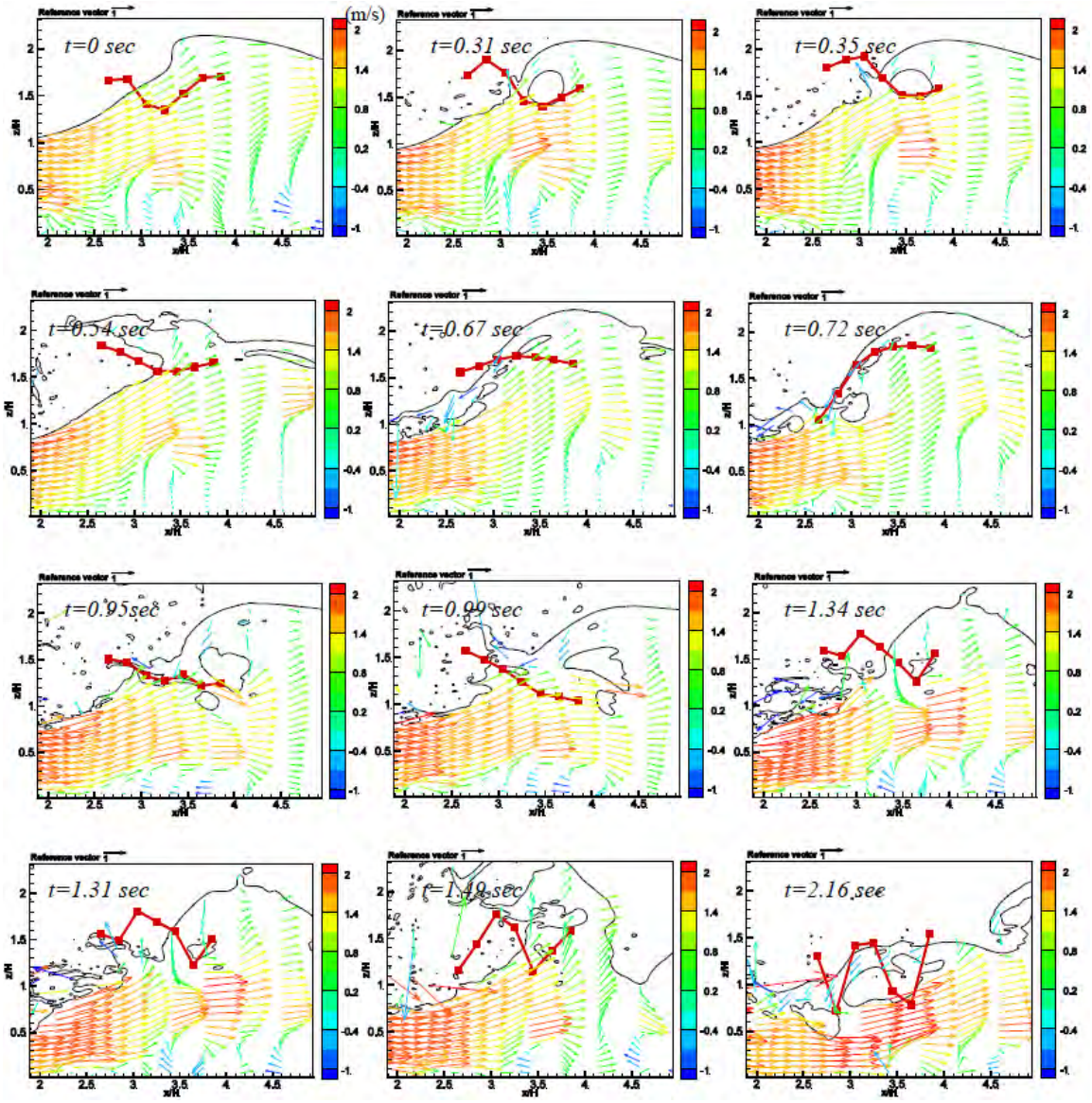

Figure A.21 CFD with overlaid vector field and water height normalized by bump height describing breaking events (CG3)

APPENDIX B
PLUNGING WAVE BREAKING SIMULATION USING ORTHOGONAL CURVILINEAR GRID SOLVER

B.1 Introduction

This chapter discusses the plunging wave breaking simulations using orthogonal curvilinear grid solver (Suh et al., 2011). The general trends are similar to simulations using Cartesian grid solver with the immersed boundary method which is shown in the previous chapter 3. The results are also compared with previous experimental and computational studies.

B.2 Computational Setup

The 2D simulations are conducted on a computational domain of x = [-52, 44] and z = [0, 5]. Three different orthogonal grids are used in the simulations, as shown in Table B.1. Grids (OG1, OG2, OG3) are systematic with consecutively reduced (by a factor of 2) sizes from 1536×512 to 768×256 and 384×128. Note that since Orthogonal curvilinear grid solver can resolve flow features near the bump, the number of grid for orthogonal curvilinear grid solver is much smaller than ones for Cartesian grid solver. The computational domain and boundary conditions are same as ones for Cartesian grid solver as discussed in previous section.

B.3 Computational Results and Comparisons

As same as with Cartesian grid solver simulations, orthogonal curvilinear grid solver simulations use the exact experimental initial and boundary conditions (Kang et al, 2011). The simulations predict the same four time phases and four repeated plunging events as the experiments. The wave breaking time, positions, and maximum height are accurately predicted. The shape of the predicted wave profile is similar to the

experiments. All the solutions from different grids show differences and similarities with experimental studies and Cartesian grids.

Table B.1 Plunging wave breaking with EFD for orthogonal curvilinear grid solver

	EFD (L4)	Fine (OG1)	E (%)	Medium (OG2)	E (%)	Coarse (OG3)	E (%)
t_b	13.4 s	13.50 s	0.7	13.08 s	2.3	13.67 s	2
x_b/H	3.38	3.44	1.7	3.08	8.8	3.13	7.4
z_b/H	2.14	2.10	1.8	2.01	6	1.88	12
d_b/H	0	0.07	-	0.32	-	0.36	-

Table B.2 Percentage of the plunging breaking wave time phase for each of the sub-events for OG1

Time	$\Delta t_T'$ =15.75 s		$\%\Delta t_T'$				
-13.80 s	-		-			Startup	
-1.1 s	Δt_S =12.7 s		80.6				
-	Δt_{SWF} = 1.1 s	-	7			Steep wave formation	
0.0 s		1.1 s					
-	Δt_{PWB} = 1.46 s	Δt	P1 28.7%	$\%\Delta t_{PWB}$	Δt	Plunging wave breaking	1st plunge
0.12 s		0.12 s		6.2	0.56		
0.16 s		0.04 s		2.1			1st oblique splash
0.56 s		0.4 s		20.5			1st vertical jet
1.02 s		0.46 s	P2 34.35%	23.6	0.67		2nd plunge
1.03 s		0.01 s		0.5			2nd oblique splash
1.23 s		0.2 s		10.3			2nd vertical jet
1.42 s		0.19 s	P3 22.6%	9.7	0.44		3rd plunge
1.44 s		0.02 s		1			3rd oblique splash
1.67 s		0.23 s		11.8			3rd vertical jet
1.78 s		0.11 s	P4 14.35%	5.6	0.28		4th plunge
1.81 s		0.03 s		1.5			4th oblique splash
1.95 s		0.14 s		7.2			4th vertical jet

Table B.3 Percentage of the plunging breaking wave time phase for each of the sub-events for OG2

<table>
<tr><td>Time</td><td colspan="2">$\Delta t_T{}' = 14.54$ s</td><td colspan="4">$\%\Delta t_T{}'$</td><td colspan="2"></td></tr>
<tr><td>-13.08 s</td><td colspan="2">-</td><td colspan="4">-</td><td colspan="2" rowspan="2">Startup</td></tr>
<tr><td>-0.83 s</td><td colspan="2">$\Delta t_S = 12.25$ s</td><td colspan="4">84.3</td></tr>
<tr><td>-</td><td rowspan="2">Δt_{SWF} = 0.83 s</td><td>-</td><td colspan="4" rowspan="2">6</td><td colspan="2" rowspan="2">Steep wave formation</td></tr>
<tr><td>0.0 s</td><td>0.83 s</td></tr>
<tr><td>-</td><td rowspan="12">Δt_{PWB} = 1.46 s</td><td>Δt</td><td rowspan="3">P1
37%</td><td>$\%\Delta t_{PWB}$</td><td>Δt</td><td rowspan="12">9.7</td><td rowspan="12">Plunging wave breaking</td><td>1st plunge</td></tr>
<tr><td>0.22 s</td><td>0.22 s</td><td>15</td><td rowspan="3">0.54</td></tr>
<tr><td>0.28 s</td><td>0.06 s</td><td>4.1</td><td>1st oblique splash</td></tr>
<tr><td>0.54 s</td><td>0.26 s</td><td>17.8</td><td>1st vertical jet</td></tr>
<tr><td>0.62 s</td><td>0.08 s</td><td rowspan="3">P2
11%</td><td>5.5</td><td rowspan="3">0.16</td><td>2nd plunge</td></tr>
<tr><td>0.66 s</td><td>0.04 s</td><td>2.7</td><td>2nd oblique splash</td></tr>
<tr><td>0.7 s</td><td>0.04 s</td><td>2.7</td><td>2nd vertical jet</td></tr>
<tr><td>1.26 s</td><td>0.56 s</td><td rowspan="3">P3
45.2 %</td><td>38.4</td><td rowspan="3">0.66</td><td>3rd plunge</td></tr>
<tr><td>1.28 s</td><td>0.02 s</td><td>1.4</td><td>3rd oblique splash</td></tr>
<tr><td>1.36 s</td><td>0.08 s</td><td>5.5</td><td>3rd vertical jet</td></tr>
<tr><td>1.37 s</td><td>0.01 s</td><td rowspan="2">P4
6.8%</td><td>0.7</td><td rowspan="2">0.1</td><td>4th plunge</td></tr>
<tr><td>1.46 s</td><td>0.09 s</td><td>6.2</td><td>4th vertical jet</td></tr>
</table>

Table B.4 Percentage of the plunging breaking wave time phase for each of the sub-events for OG3

Time	$\Delta t_T'$ =14.78 s		$\%\Delta t_T'$				
-13.67 s	-		-			Startup	
-1.07 s	Δt_S =12.6 s		85.2				
-	Δt_{SWF} = 1.07 s	-	7.2			Steep wave formation	
0.0 s		1.07 s					
-	Δt_{PWB} = 1.11 s	Δt	$\%\Delta t_{PWB}$		Δt	Plunging wave breaking	1st plunge
0.15 s		0.15 s	P1 23.42%	13.6	0.26		
0.2 s		0.05 s		4.5			1st oblique splash
0.26 s		0.06 s		5.4			1st vertical jet
0.52 s		0.26 s	P2 32.43%	23.4	0.36		2nd plunge
0.55 s		0.03 s		2.7			2nd oblique splash
0.62 s		0.07 s		6.3			2nd vertical jet
0.65 s		0.03 s	P3 33.33%	2.7	0.37		3rd plunge
0.99 s		0.34 s		30.6			3rd vertical jet
1.06 s		0.07 s	P4 10.82%	6.3	0.12		4th plunge
1.08 s		0.02 s		1.8			4th oblique splash
1.11 s		0.03 s		2.7			4th vertical jet

Table B.5 Time interval of for each plunging phase

Plunging phase	EFD (L4)	OG1	OG2	OG3
P1	0.533	0.55	0.54	0.26
P2	0.334	0.3	0.16	0.36
P3	0.266	0.6	0.66	0.37
P4	0.267	0.77	0.1	0.12

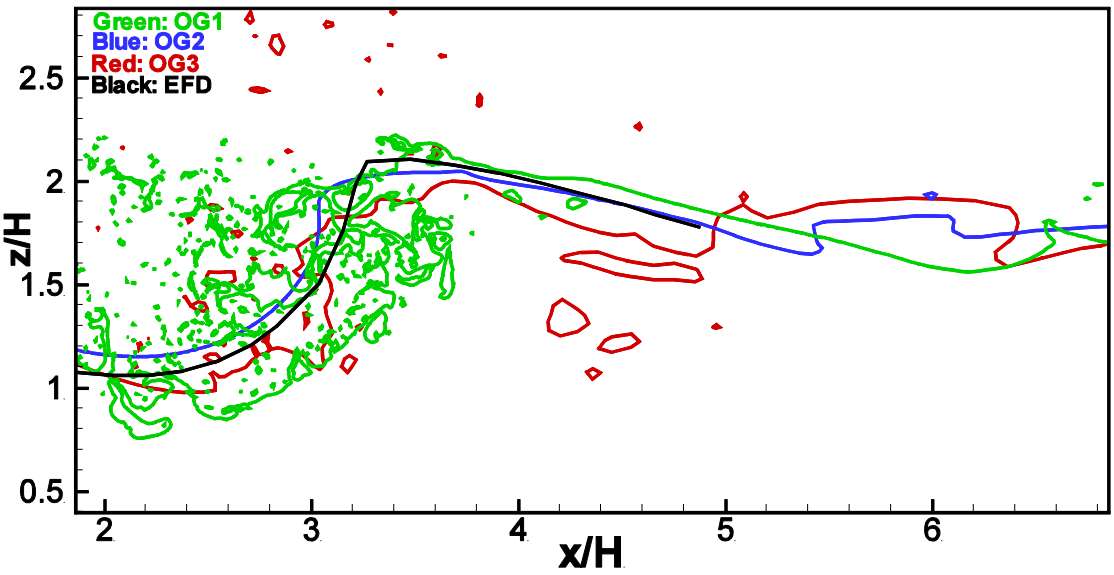

Figure B.1 Wave profiles at t_b for orthogonal curvilinear grid solver

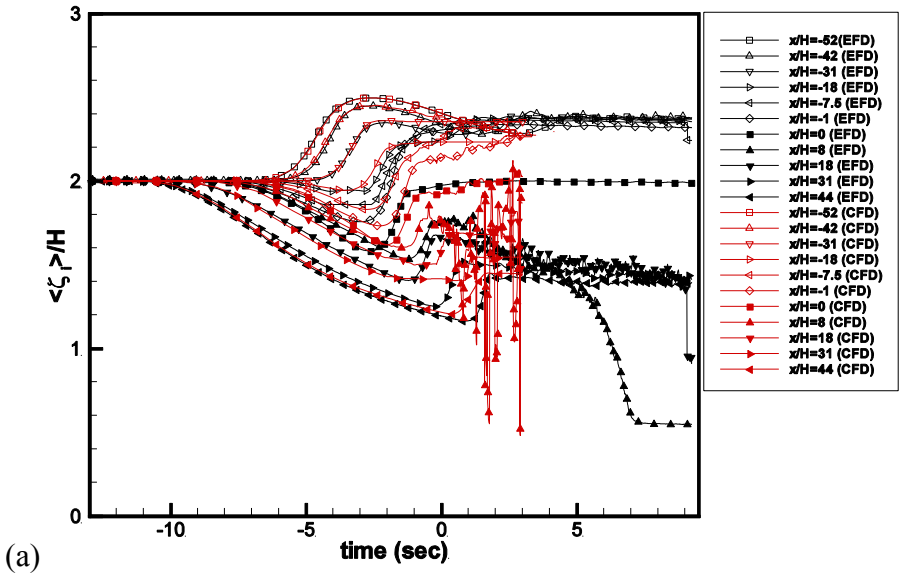

(a)

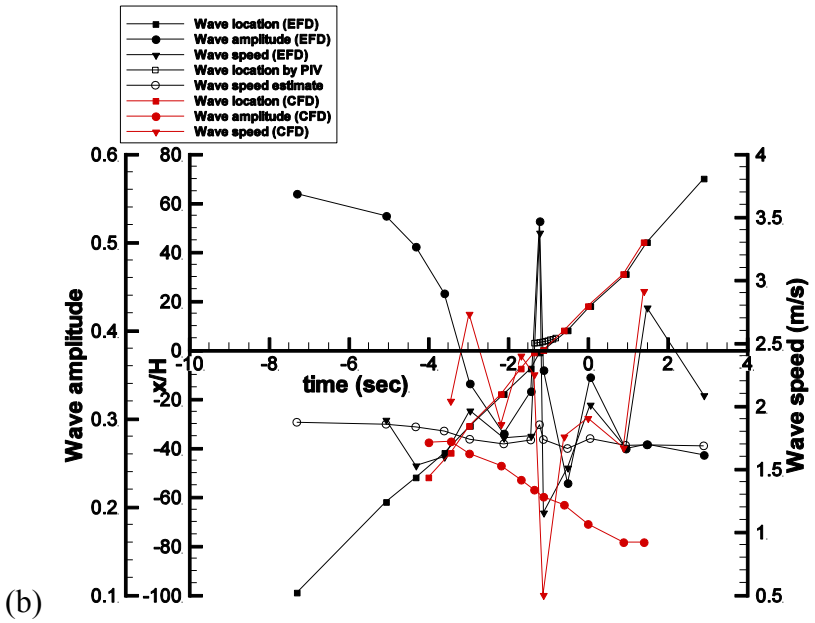

(b)

Figure B.2 Time history: (a) water elevations; (b) acceleration wave location, speed, and amplitude (OG1)

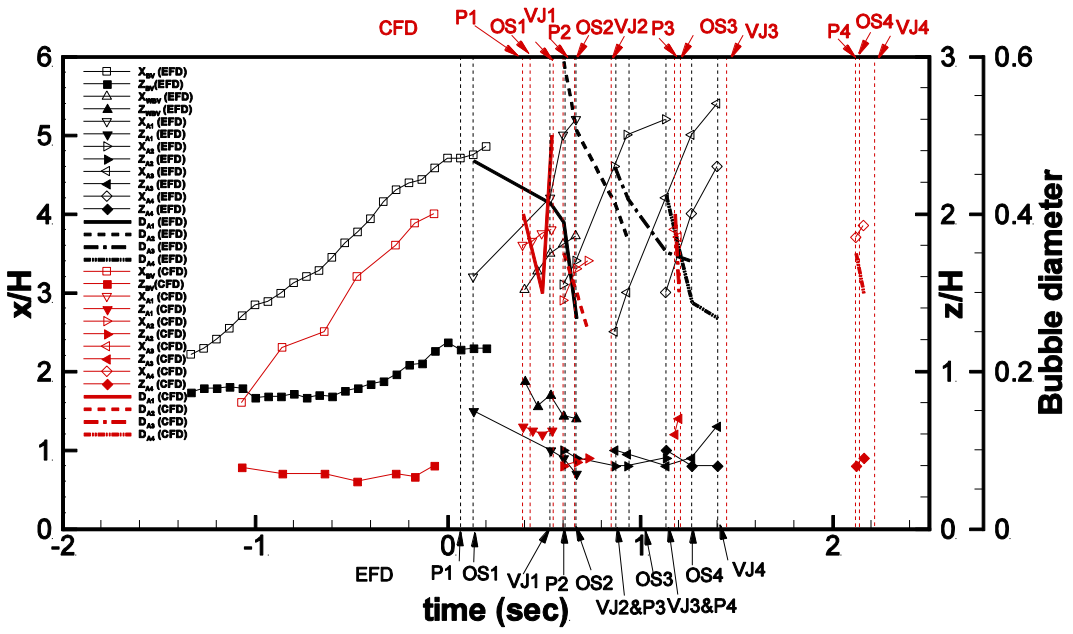

Figure B.3 Time history of vortex and air entrainment paths, and air bubble size. Red: CFD; black: EFD (OG1)

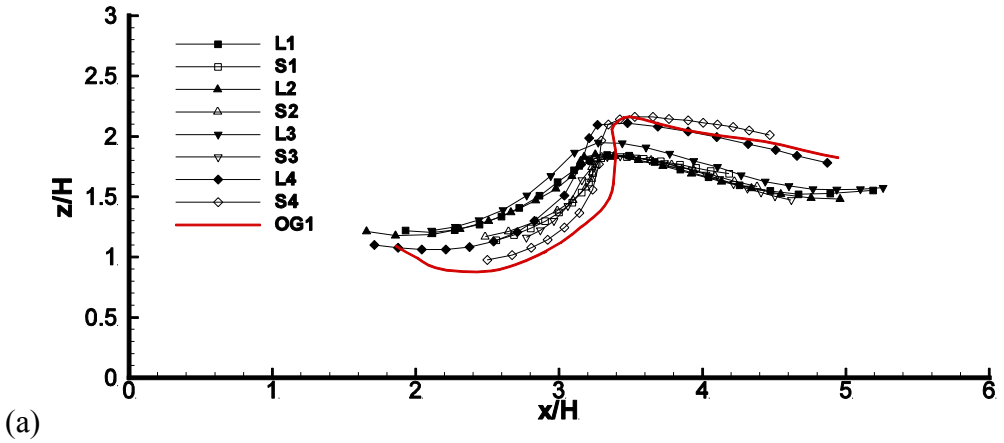

(a)

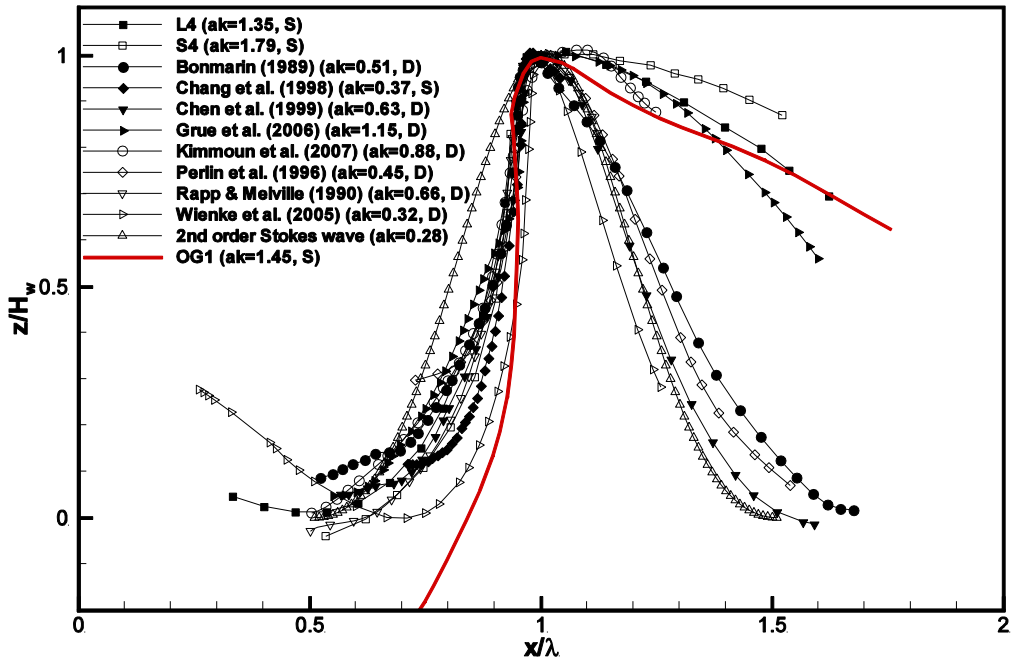

(b)

Figure B.4 Wave profile comparison with EFD. (a) CFD profile; (b) non-dimensional with wave length (λ) and wave height (H_w) at t_b in X, Z, respectively (OG1)

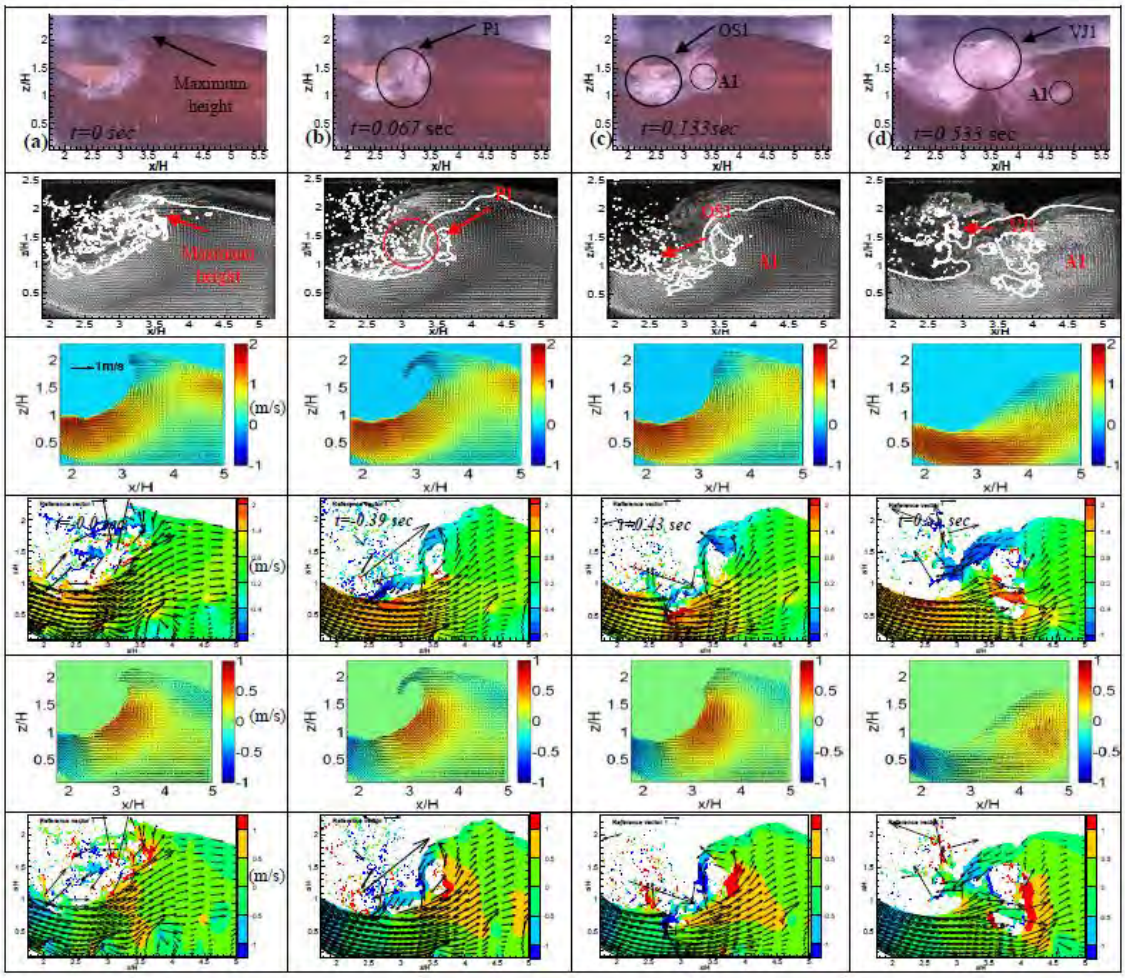

Figure B.5 Video images (Reins, 2008); PIV image with CFD; EFD U velocity contours; CFD U velocity contours; EFD W velocity contours; CFD W velocity contours (OG1)

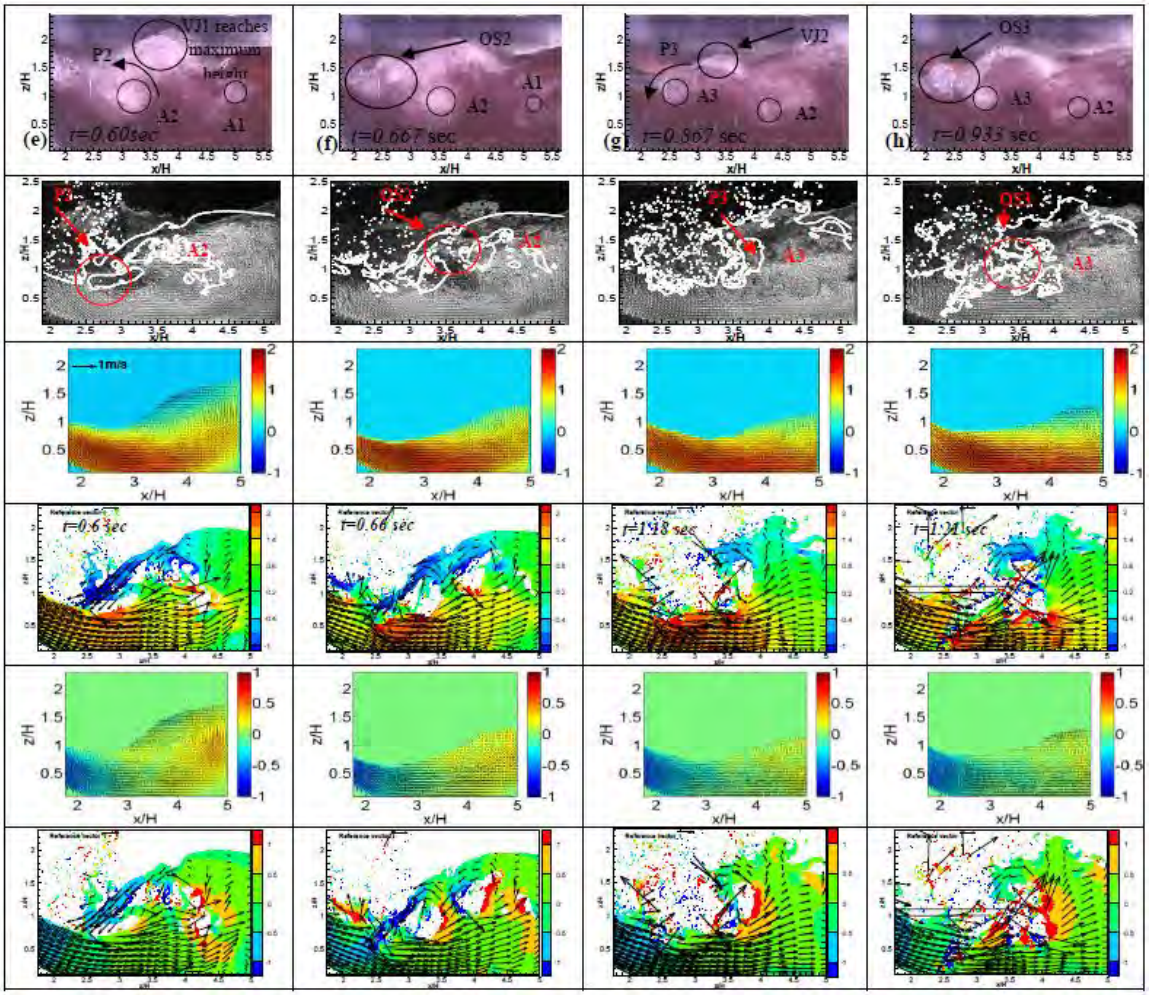

Figure B.5 (continued)

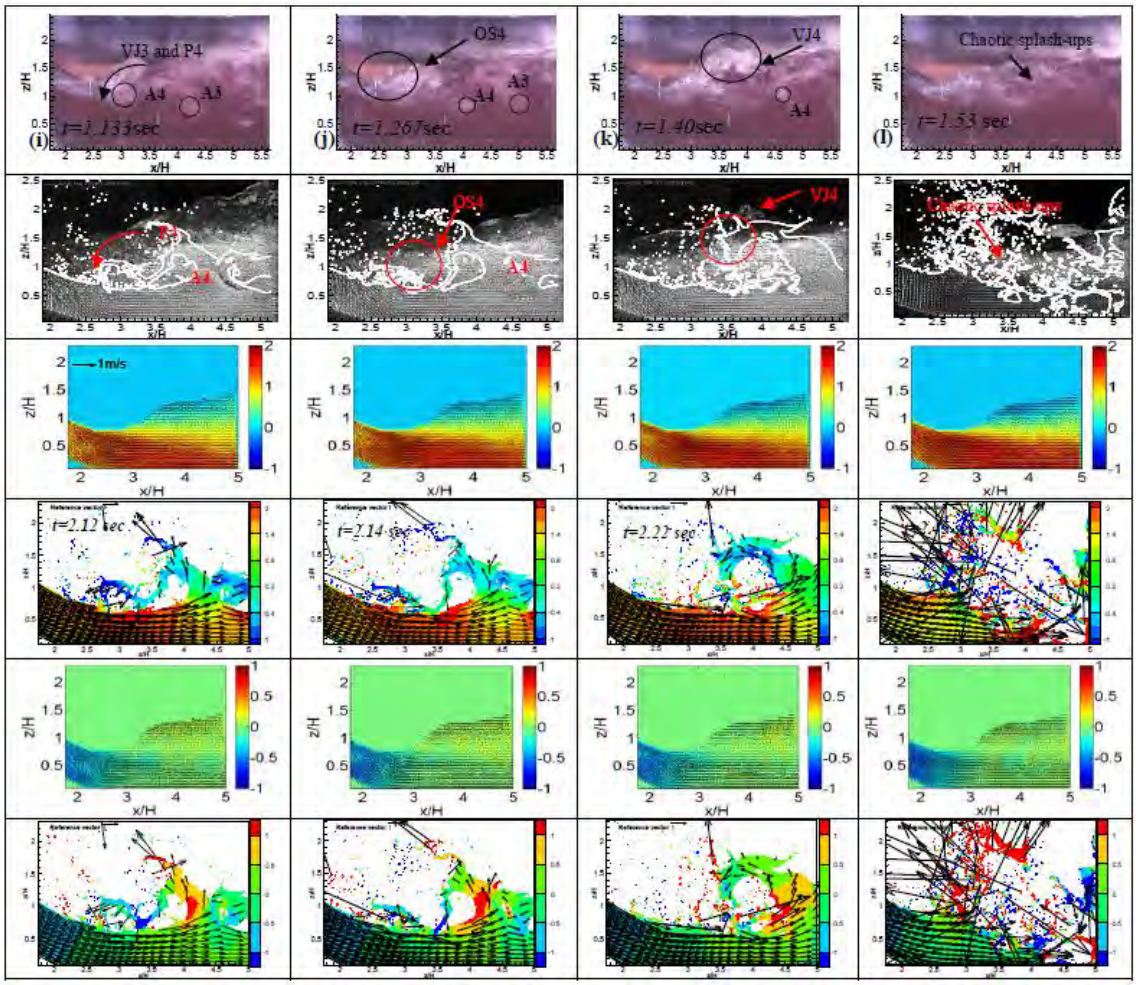

Figure B.5 (continued)

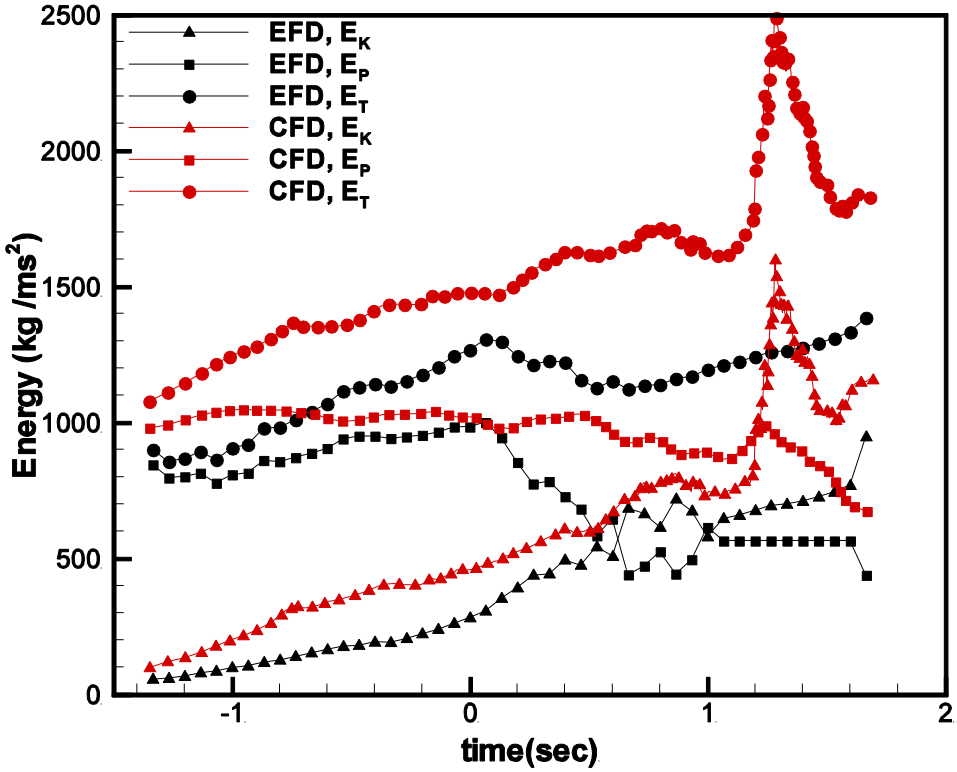

Figure B.6 Time evolutions of the total energy, the wave kinetic energy, the wave potential energy (OG1)

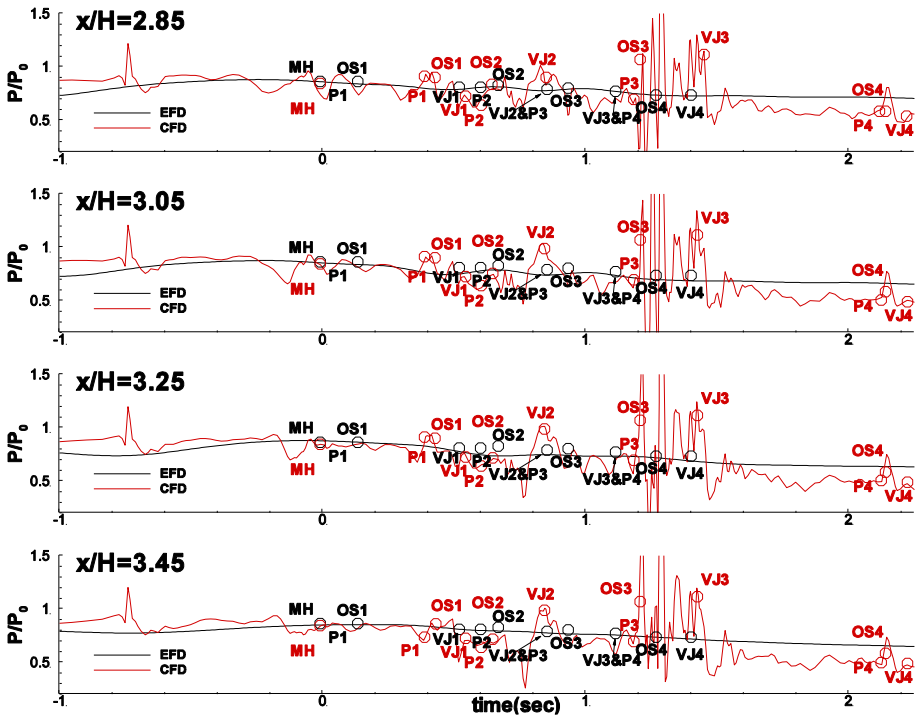

Figure B.7 Average pressure time series for EFD and CFD at various stream-wise positions (OG1)

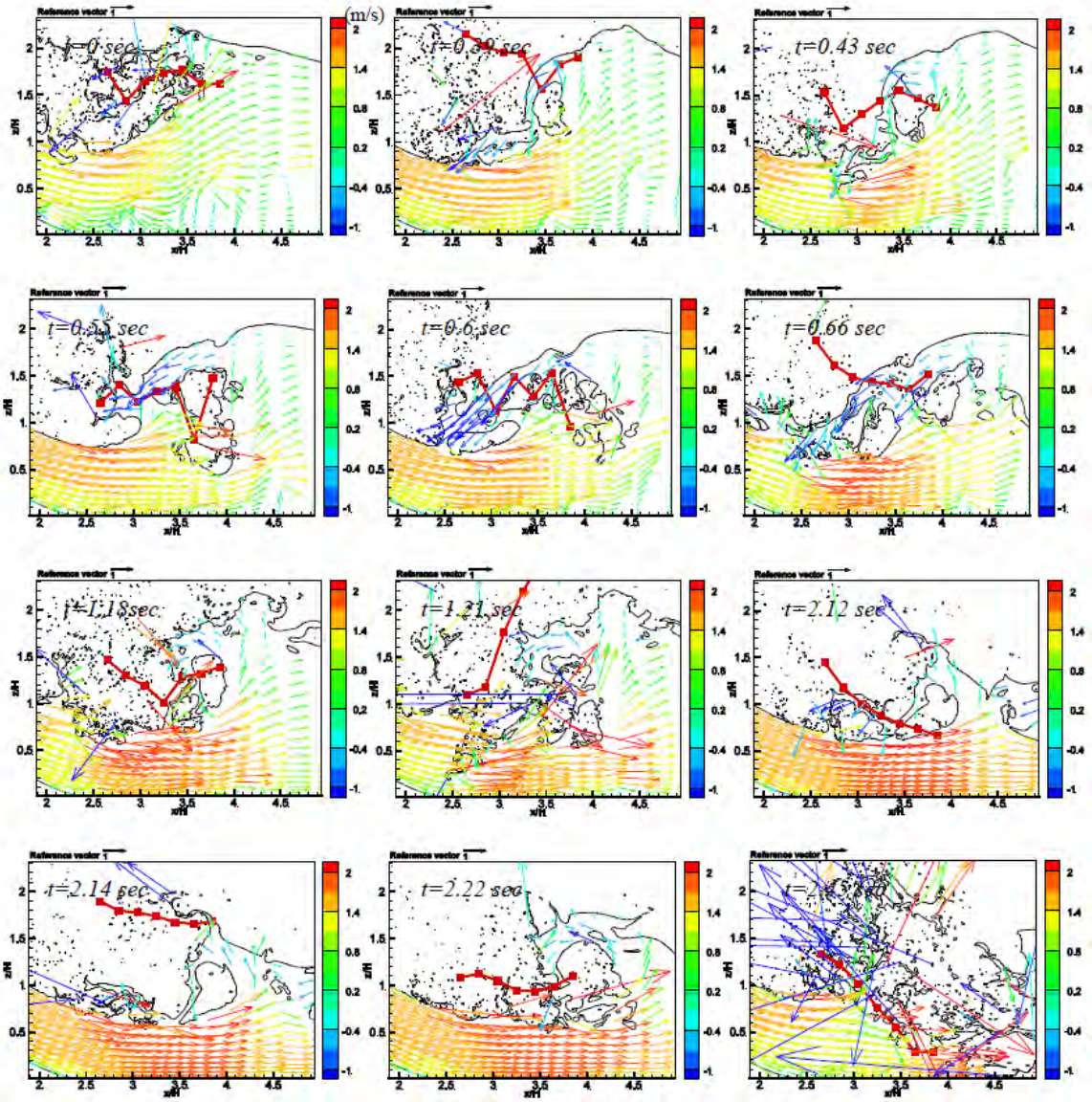

Figure B.8 CFD with overlaid vector field and water height normalized by bump height describing breaking events (OG1)

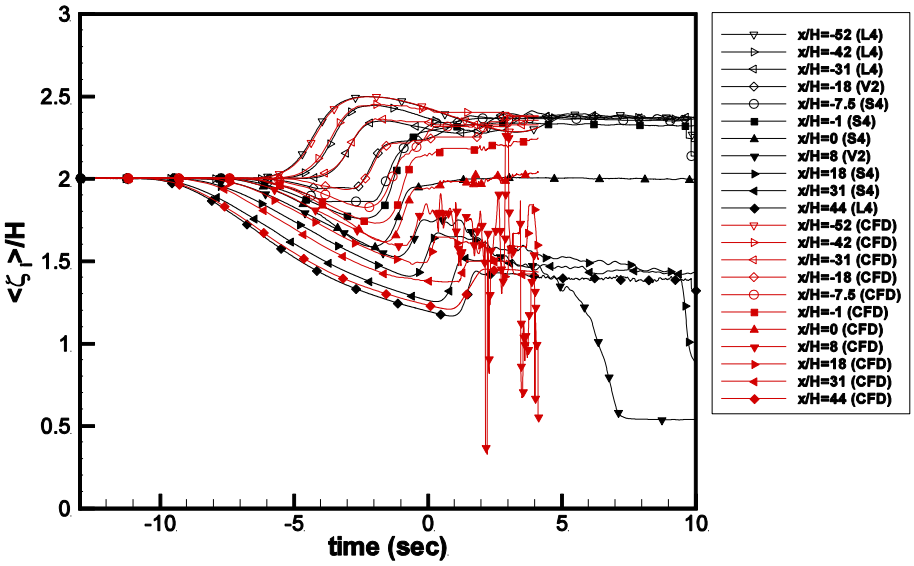

(a)

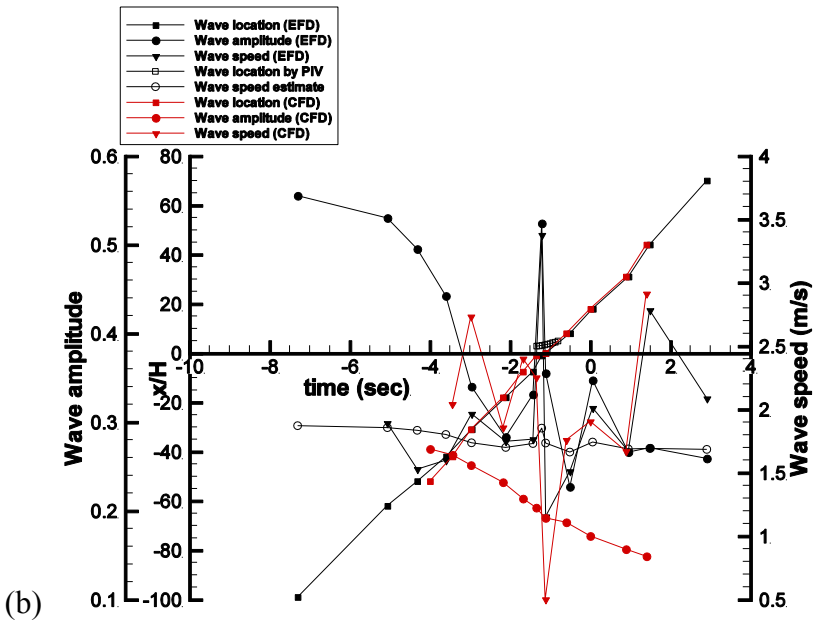

(b)

Figure B.9 Time history: (a) water elevations; (b) acceleration wave location, speed, and amplitude (OG2)

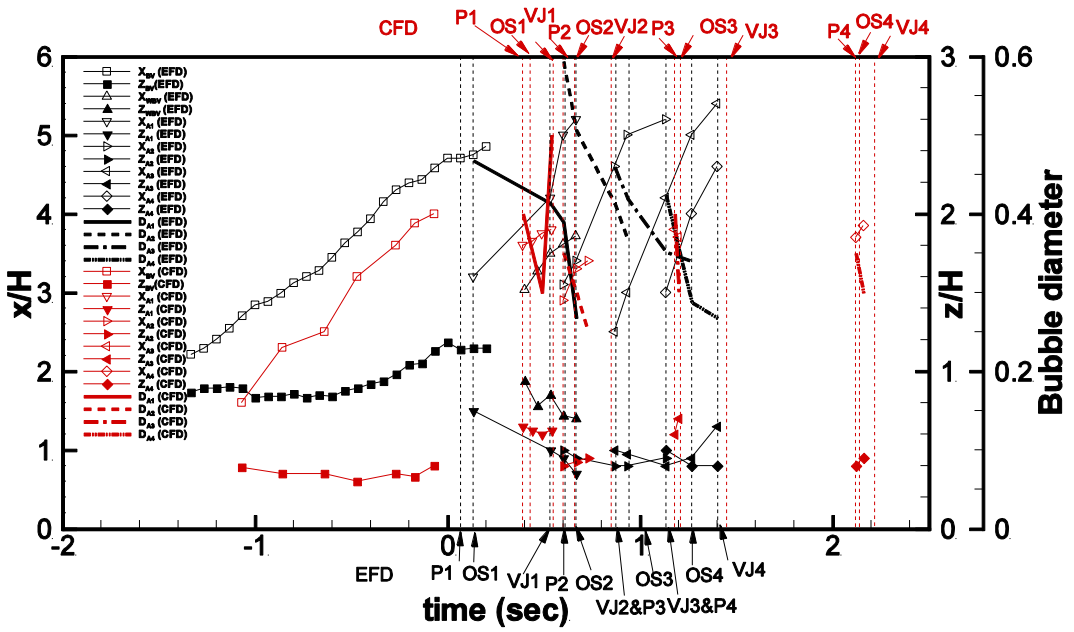

Figure B.10 Time history of vortex and air entrainment paths, and air bubble size. Red: CFD; black: EFD (OG2)

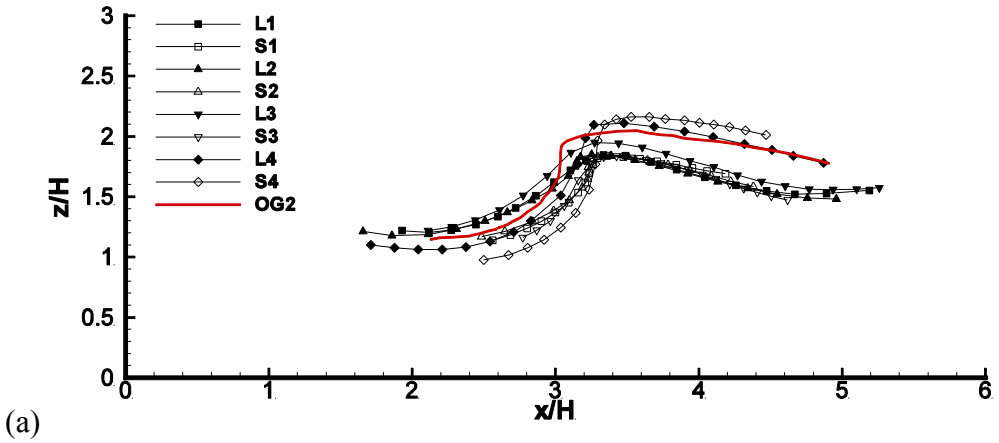

(a)

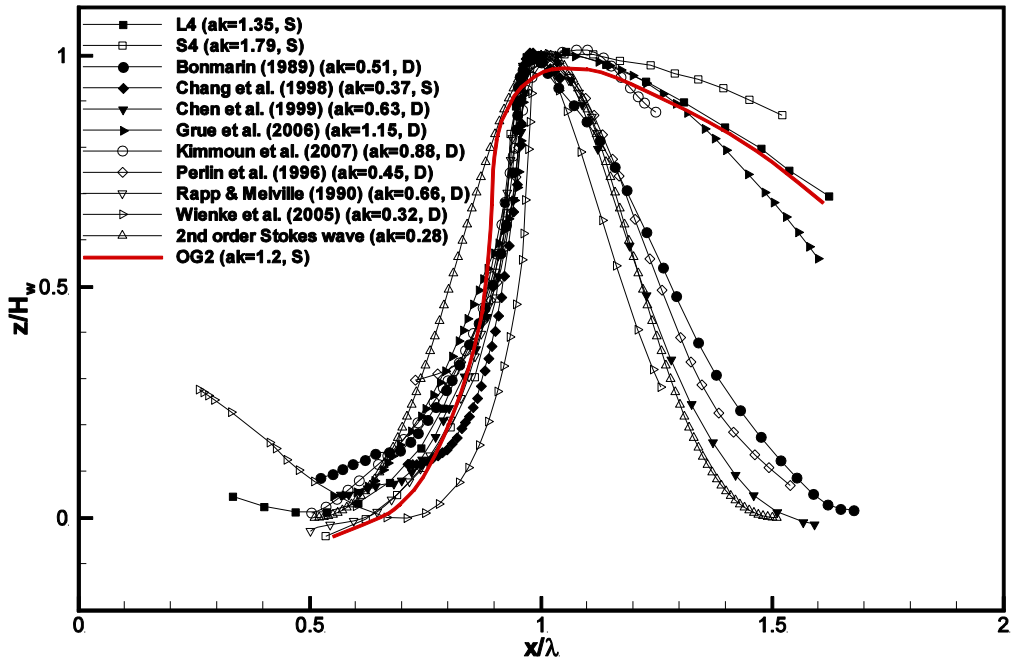

(b)

Figure B.11 Wave profile comparison with EFD. (a) CFD profile; (b) non-dimensional with wave length (λ) and wave height (H_w) at t_b in X, Z, respectively (OG2)

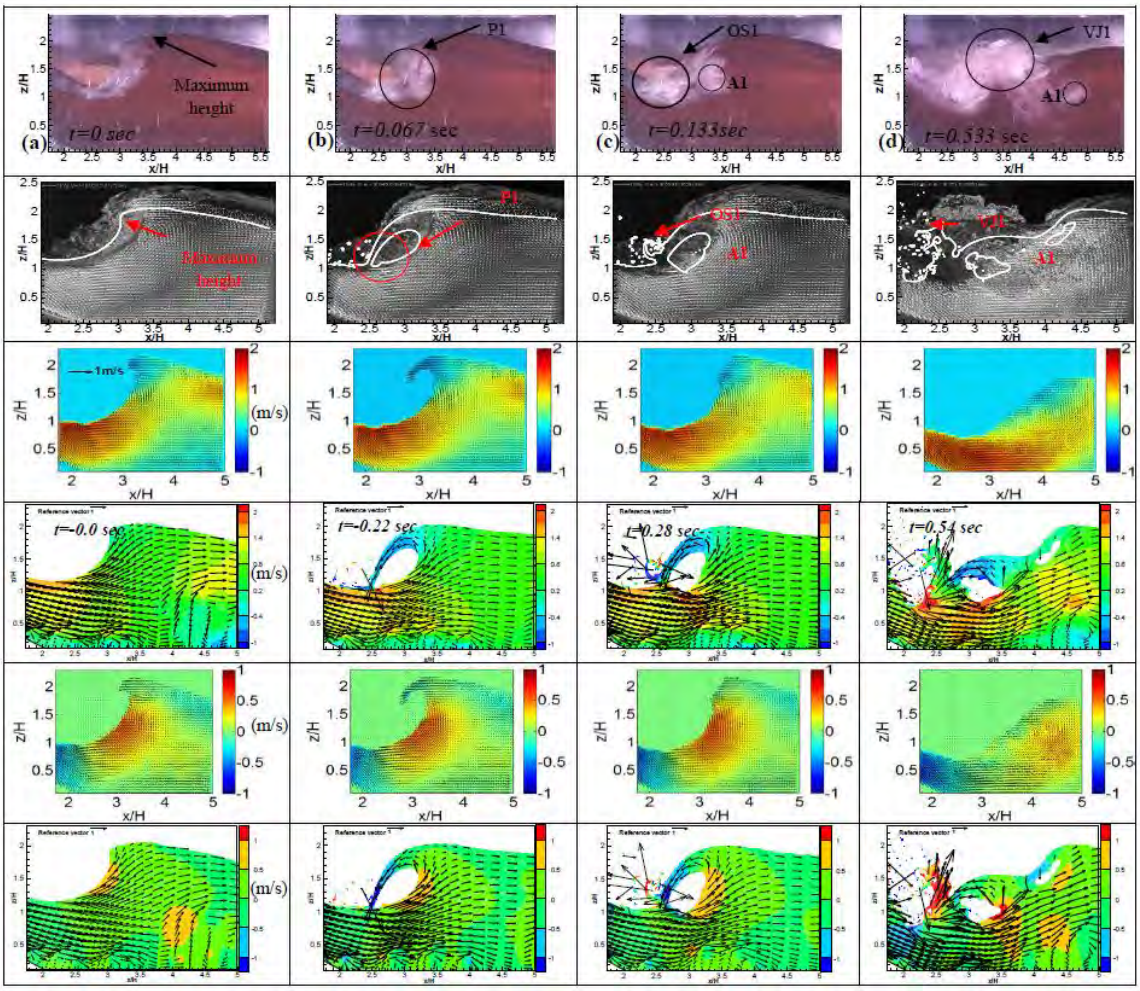

Figure B.12 Video images (Reins, 2008); PIV image with CFD; EFD U velocity contours; CFD U velocity contours; EFD W velocity contours; CFD W velocity contours (OG2)

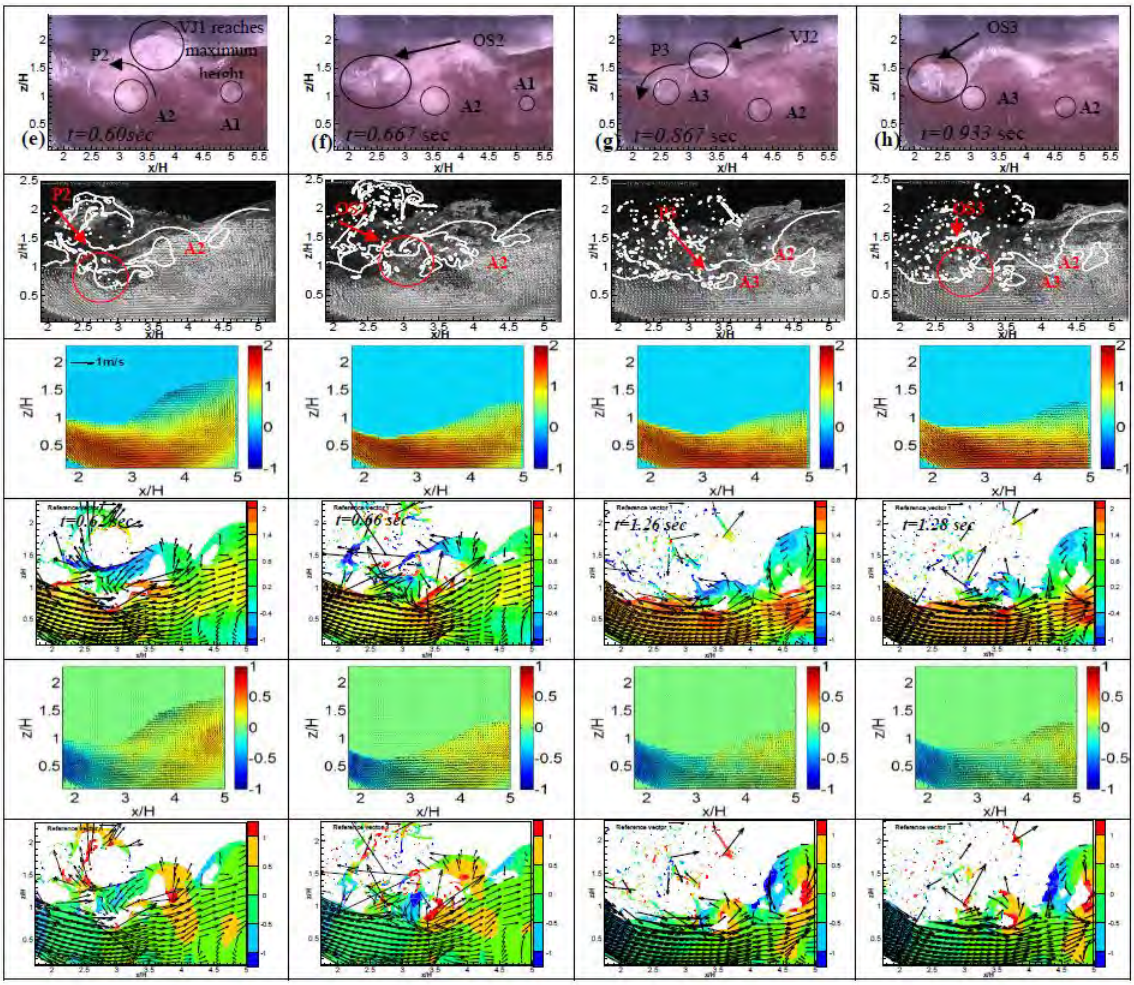

Figure B.12 (continued)

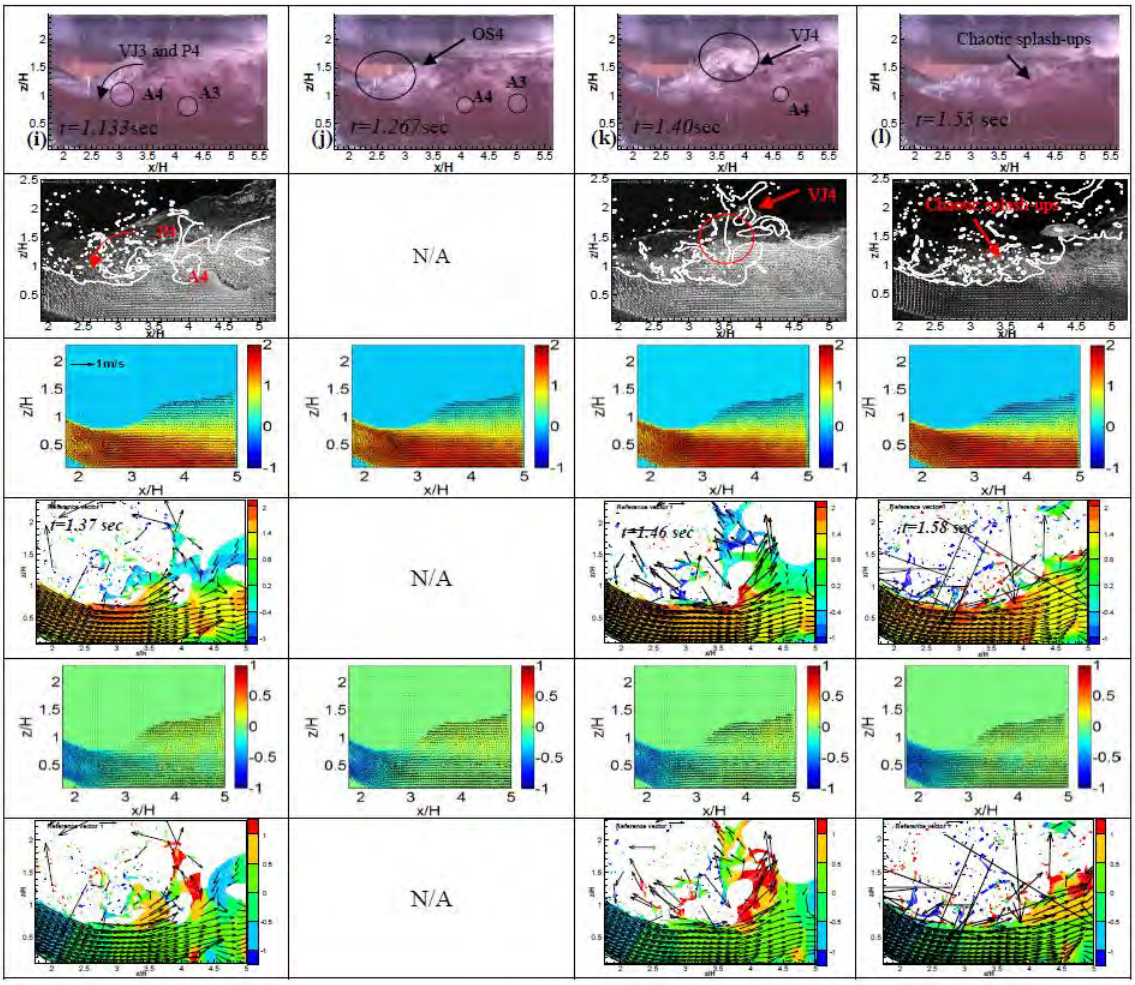

Figure B.12 (continued)

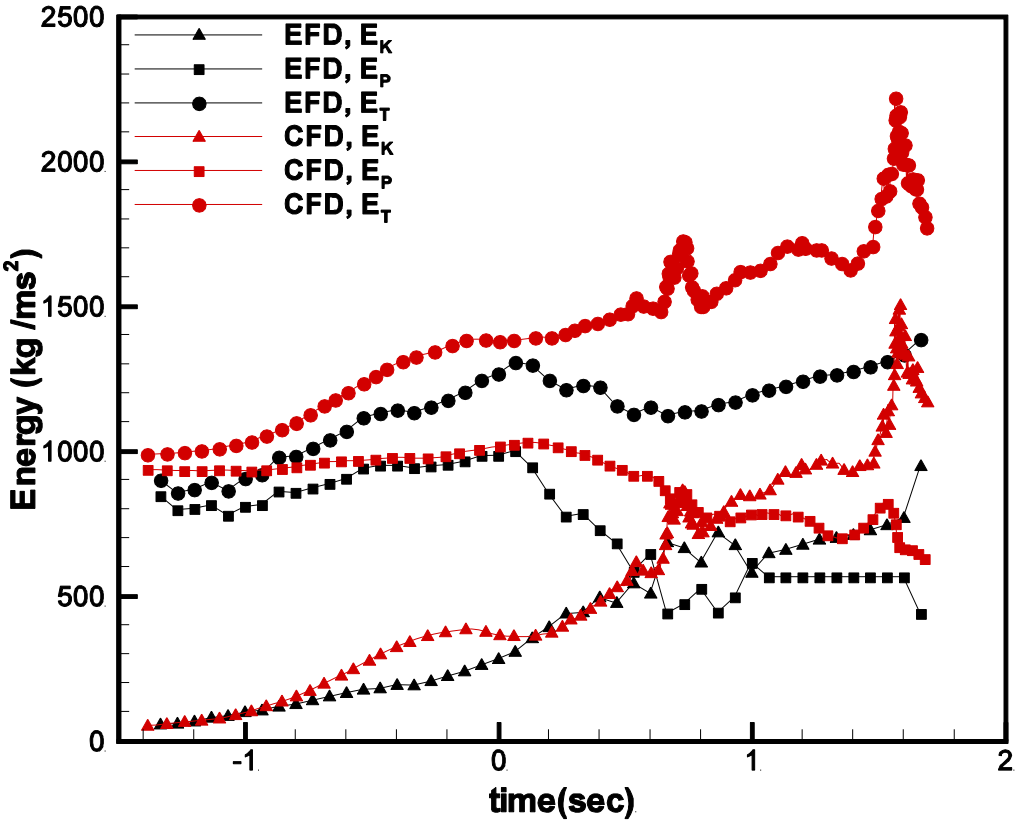

Figure B.13 Time evolutions of the total energy, the wave kinetic energy, the wave potential energy (OG2)

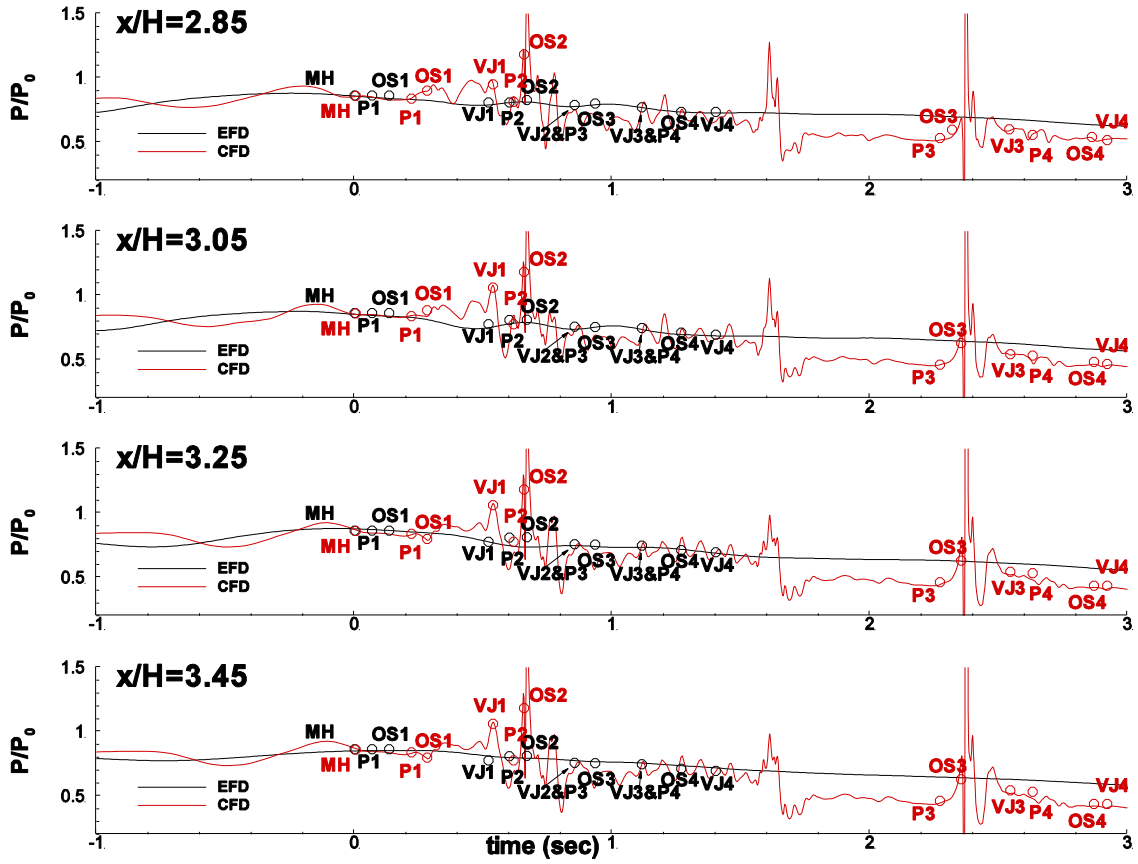

Figure B.14 Average pressure time series for EFD and CFD at various stream-wise positions (OG2)

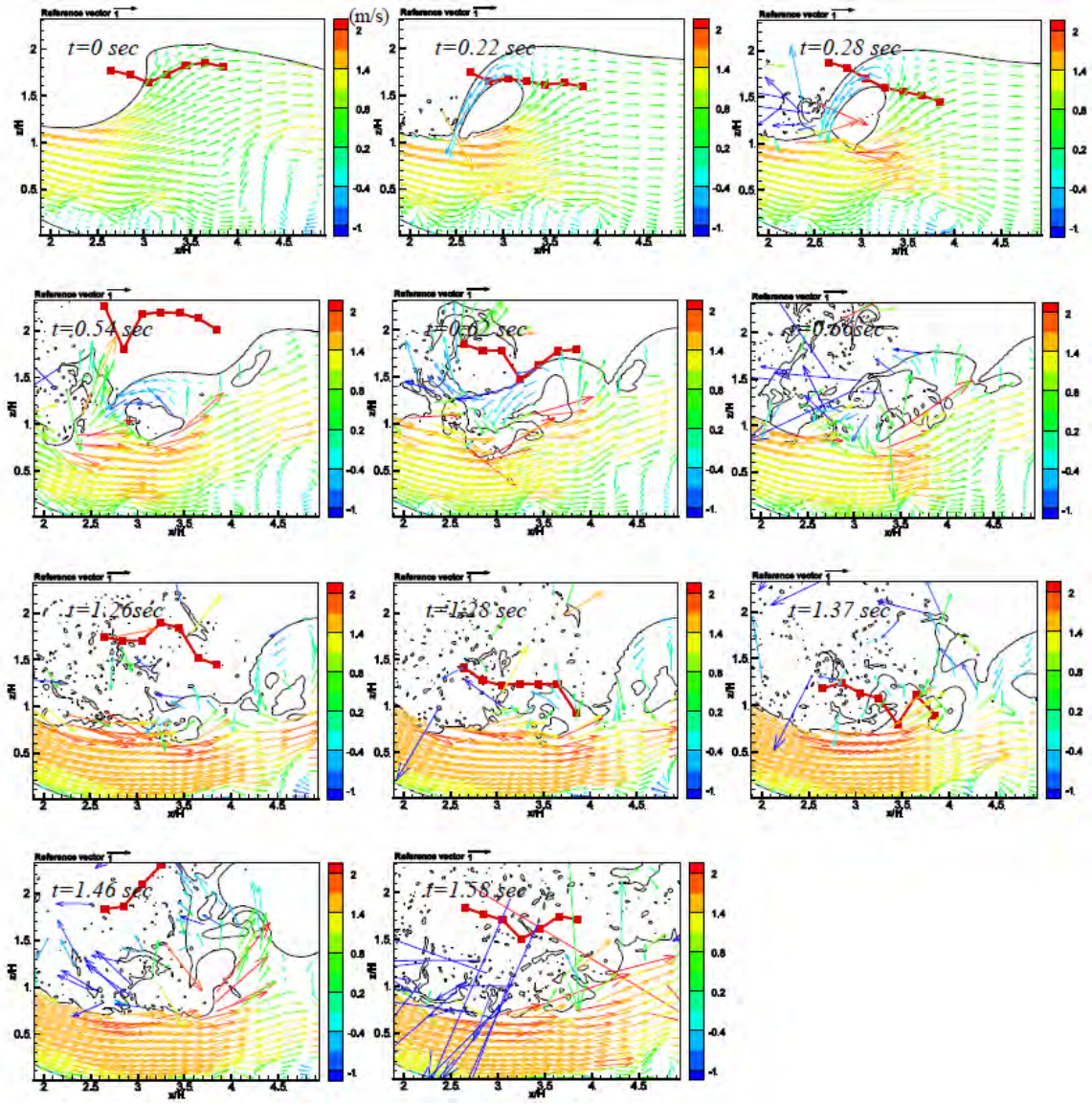

Figure B.15 CFD with overlaid vector field and water height normalized by bump height describing breaking events (OG2)

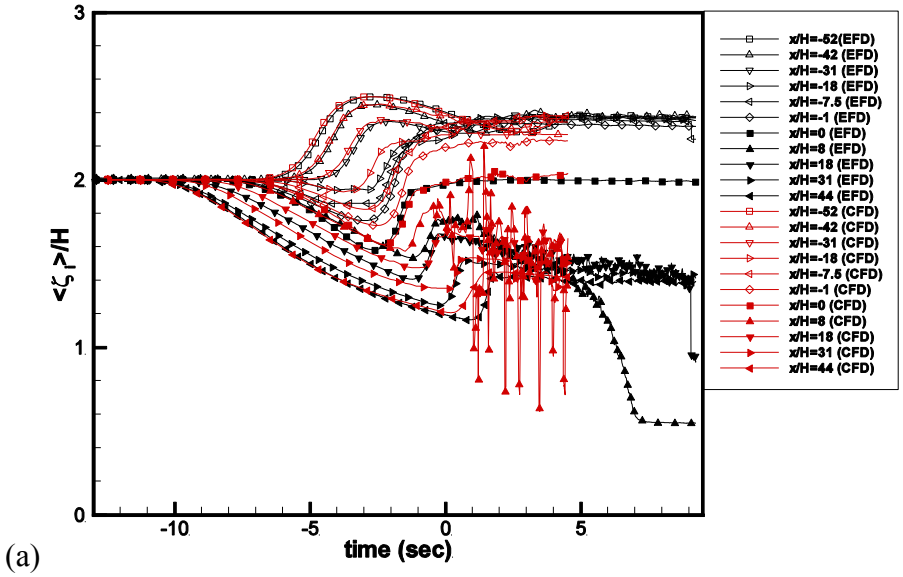

(a)

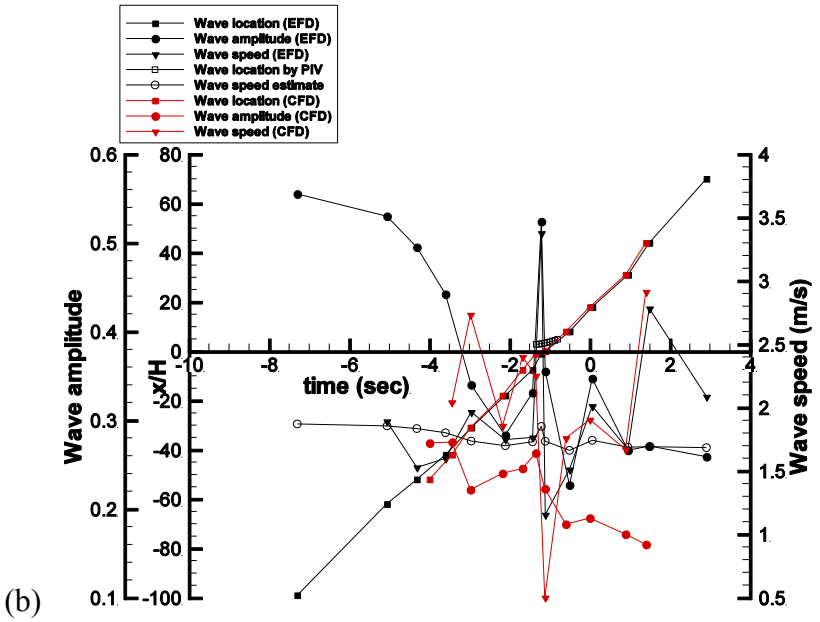

(b)

Figure B.16 Time history: (a) water elevations; (b) acceleration wave location, speed, and amplitude (OG3)

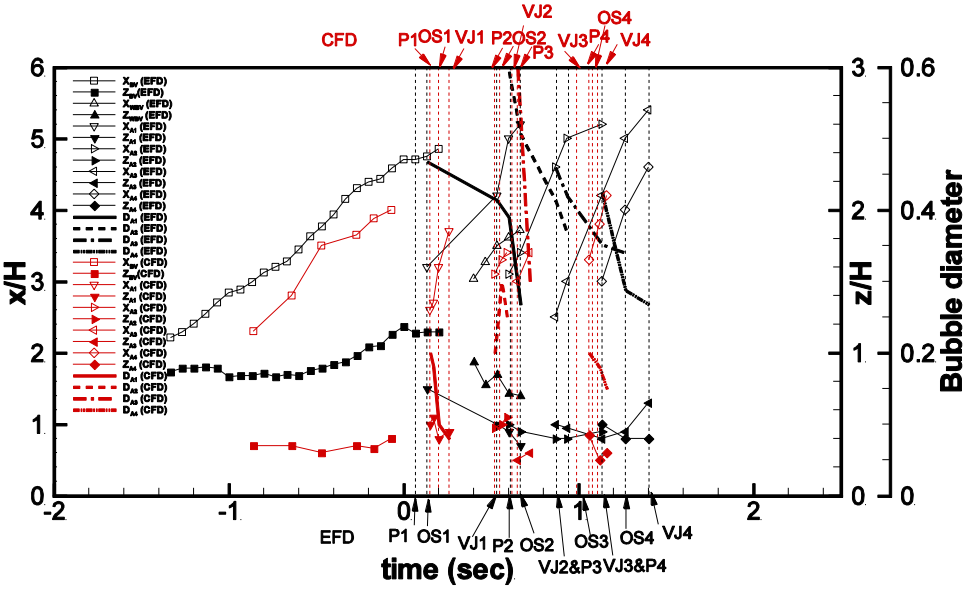

Figure B.17 Time history of vortex and air entrainment paths, and air bubble size. Red: CFD; black: EFD (OG3)

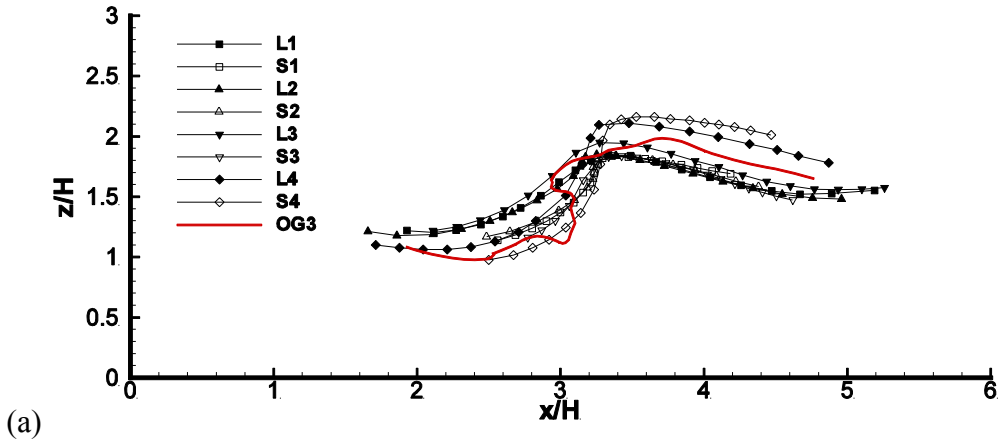

(a)

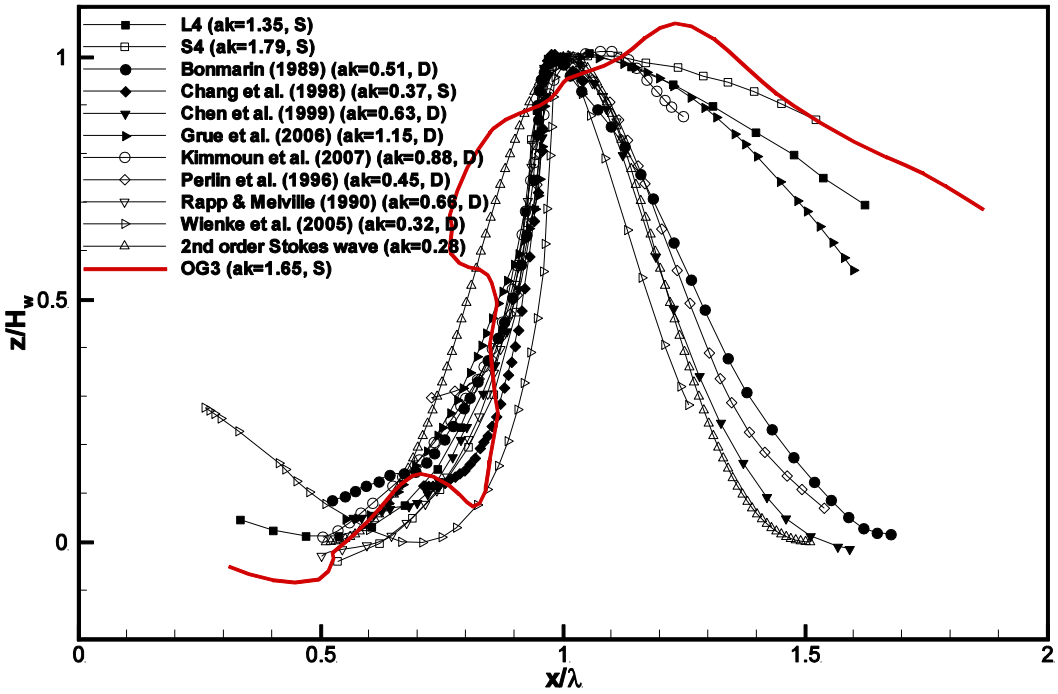

(b)

Figure B.18 Wave profile comparison with EFD. (a) CFD profile; (b) non-dimensional with wave length (λ) and wave height (H_w) at t_b in X, Z, respectively (OG3)

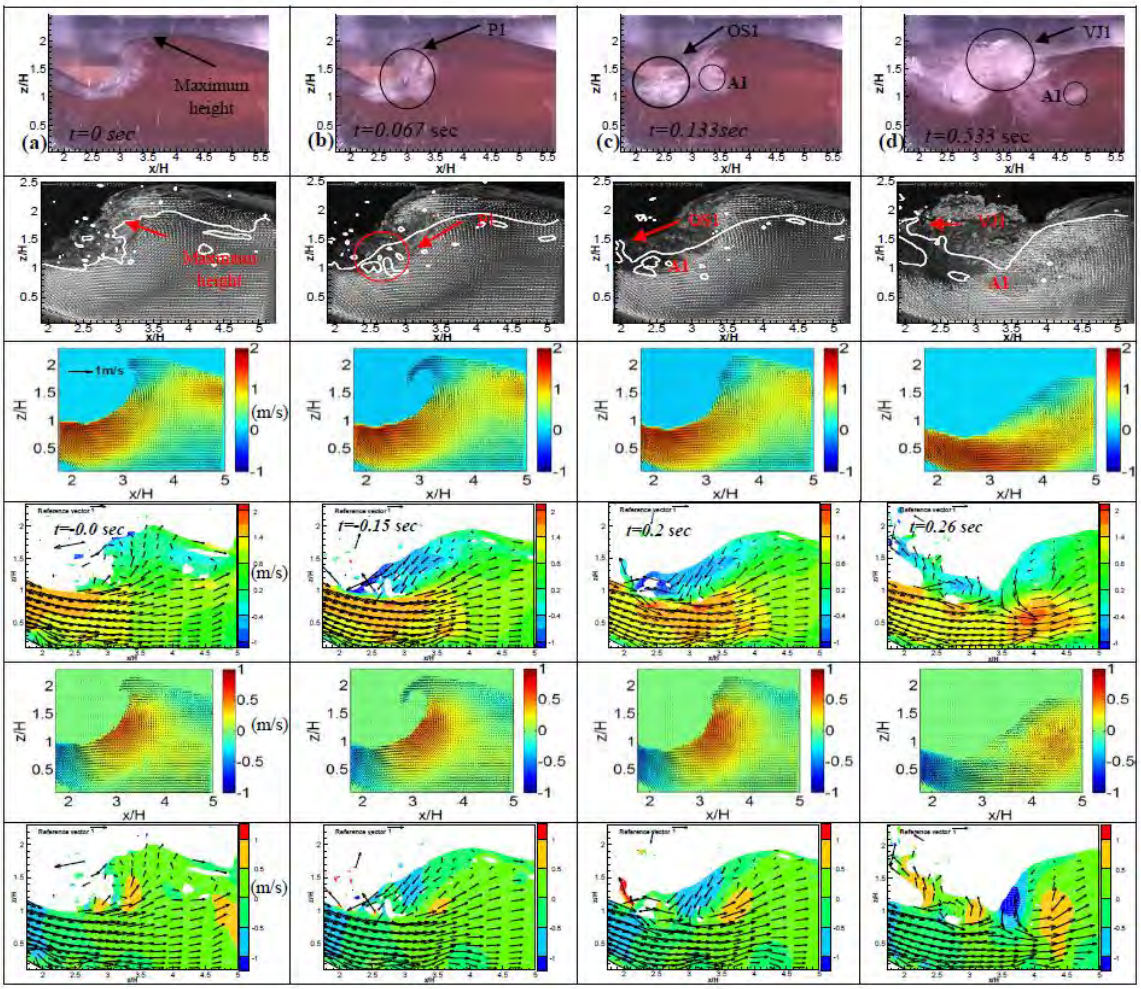

Figure B.19 Video images (Reins, 2008); PIV image with CFD; EFD U velocity contours; CFD U velocity contours; EFD W velocity contours; CFD W velocity contours (OG3)

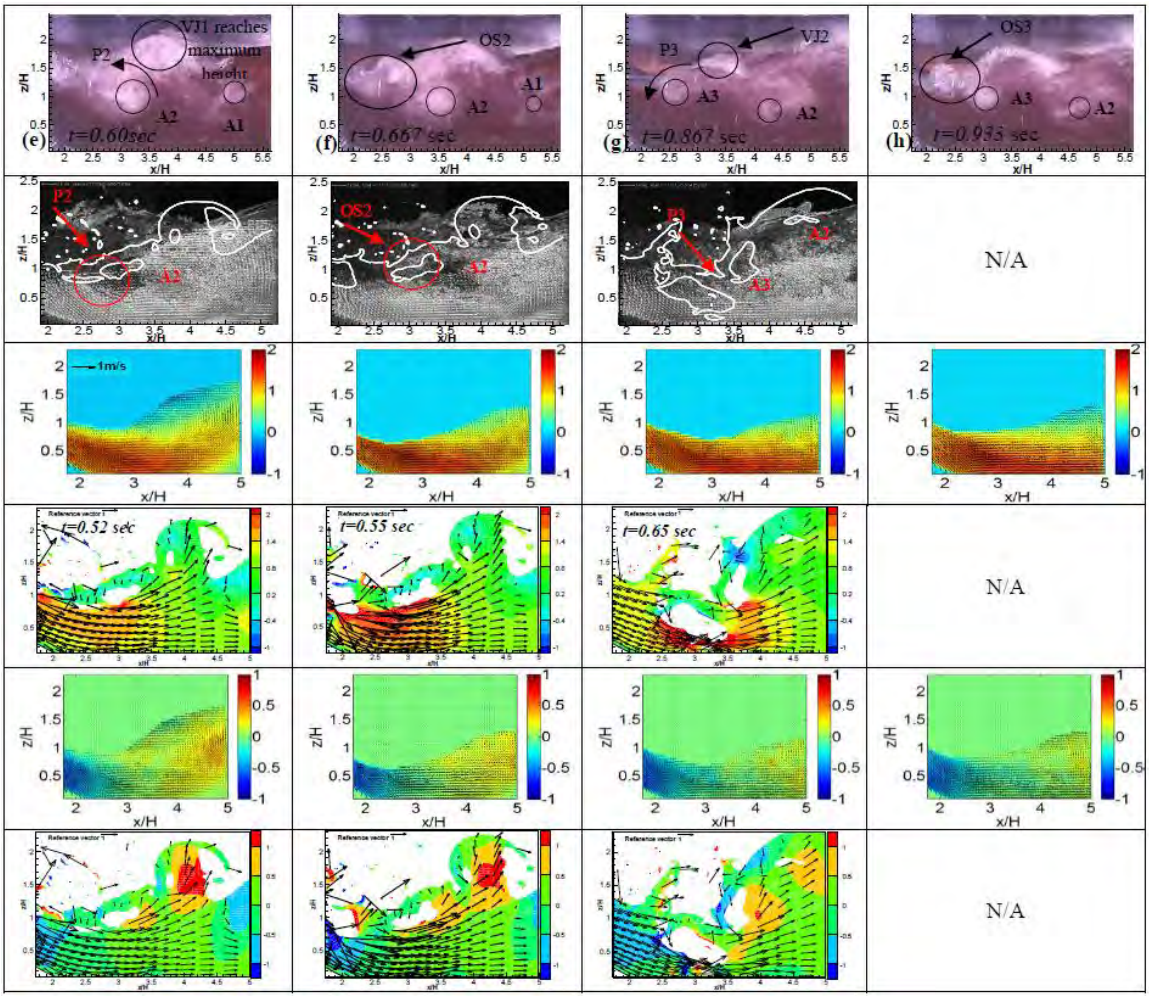

Figure B.19 (continued)

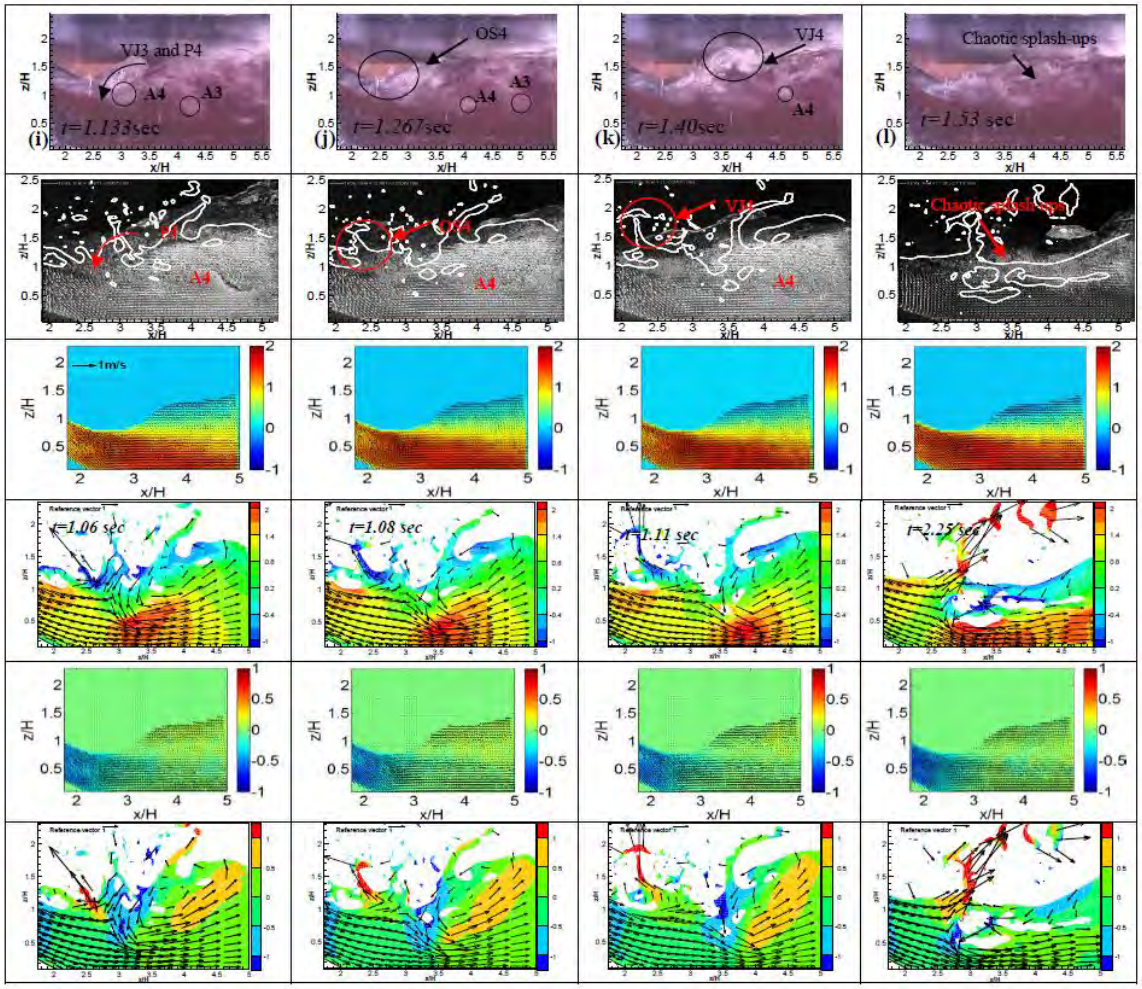

Figure B.19 (continued)

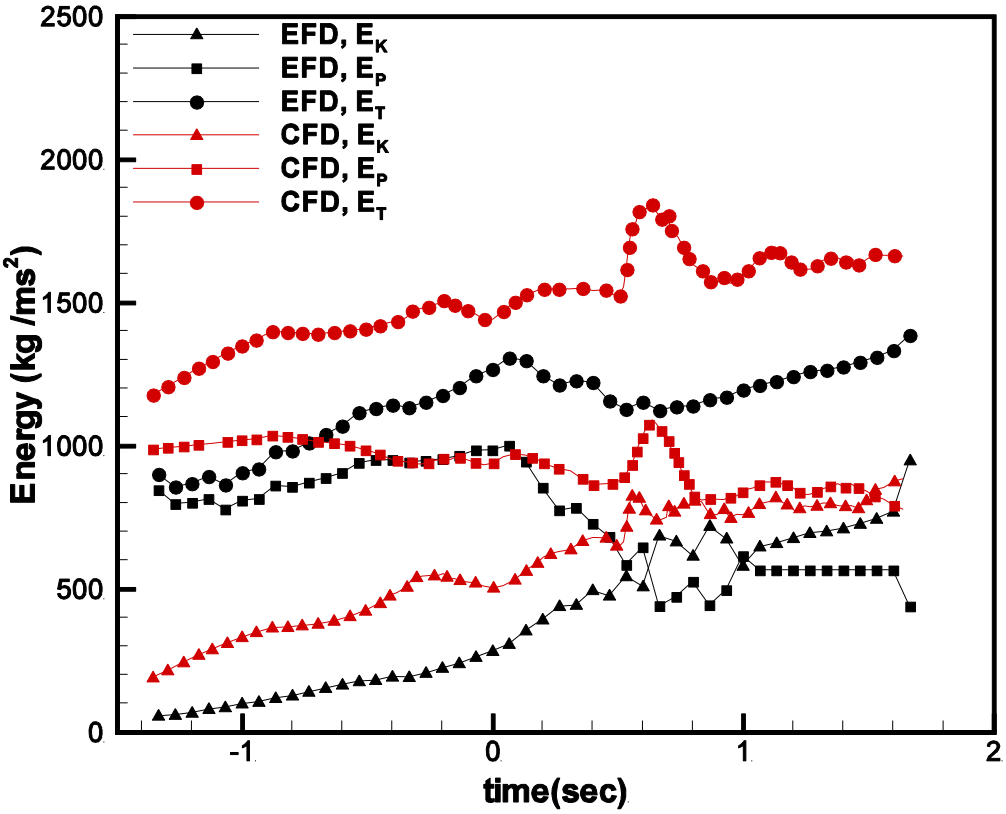

Figure B.20 Time evolutions of the total energy, the wave kinetic energy, the wave potential energy (OG3)

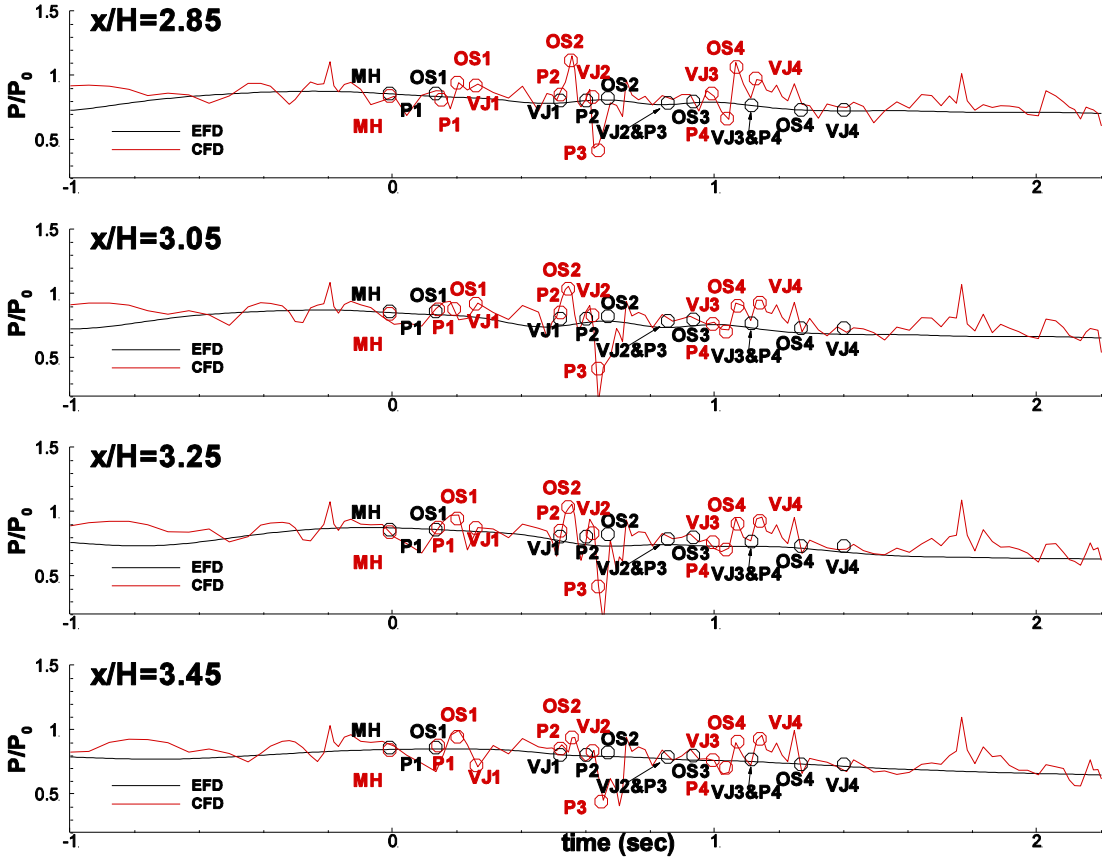

Figure B.21 Average pressure time series for EFD and CFD at various stream-wise positions (OG3)

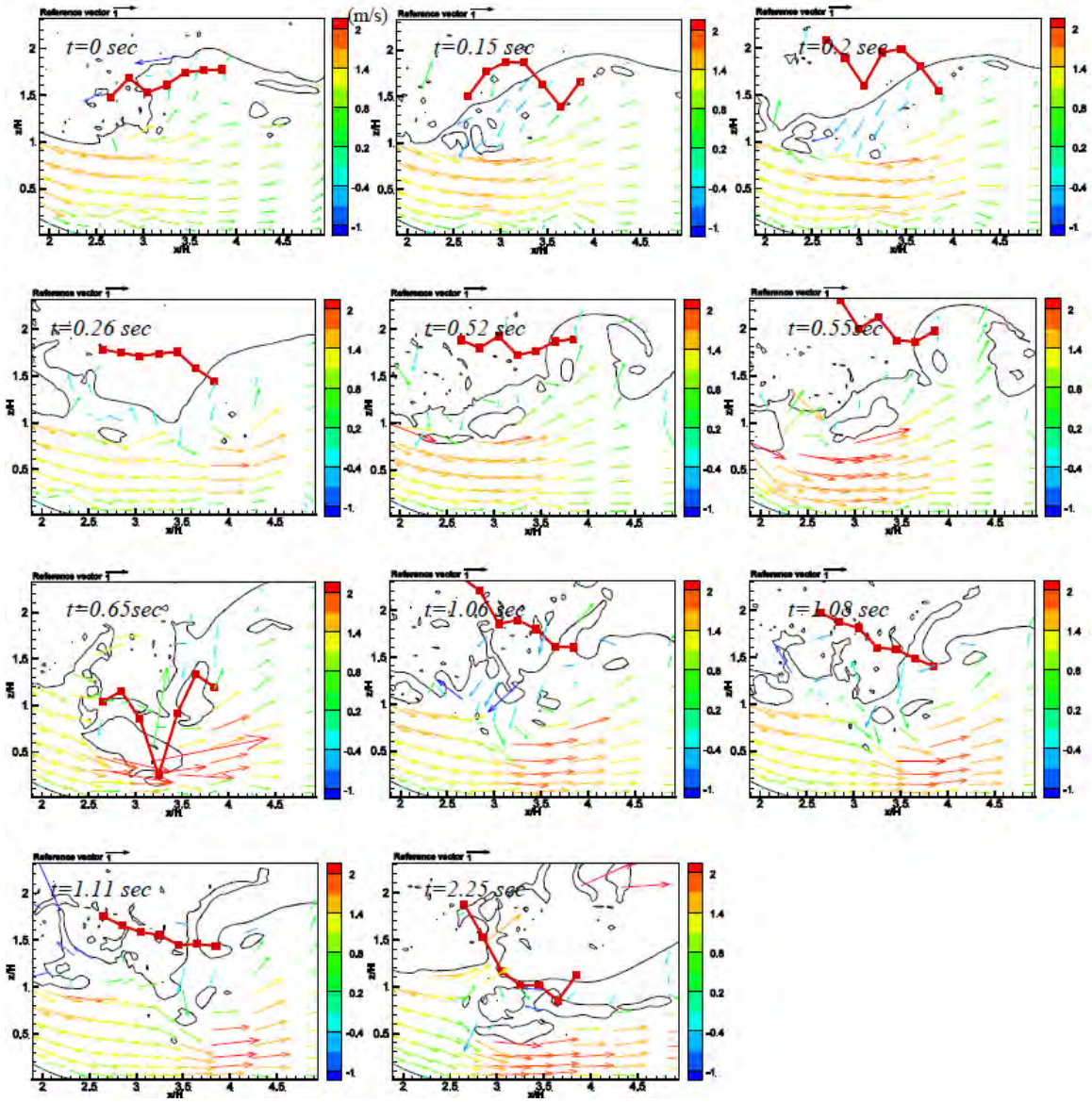

Figure B.22 CFD with overlaid vector field and water height normalized by bump height describing breaking events (OG3)